Uncovering the molecular basis of compartmentalization as a principle of neuronal organization

Inaugural-Dissertation
to obtain the academic degree
Doctor rerum naturalium (Dr. rer. nat.)

submitted to the Department of Biology, Chemistry, Pharmacy
of Freie Universität Berlin

by

Jakob Rentsch

2024

This doctoral study was conducted from October 2018 to March 2024 under the supervision of Prof. Dr. Helge Ewers in the Department of Biology, Chemistry and Pharmacy of the Freie Universität Berlin.

1. reviewer: Prof. Dr. Helge Ewers, Freie Universität Berlin
2. reviewer: Prof. Dr. Stephan Sigrist, Freie Universität Berlin
Date of defense: 22.07.2024

Declaration of authorship

I hereby declare that I alone am responsible for the content of my doctoral dissertation and that I have only used the sources or references cited in the dissertation.

Berlin, 18.03.2024 Jakob Rentsch

Acknowledgements

First of all, I would like to thank my entire family for their emotional support and security. Many thanks to my mother, Karina Rentsch and my grandparents Annemarie and Günter Uebe for their financial support from my bachelor's degree until today. You have given me the luxury of being able to concentrate on my studies without financial worries.

Thank you to Helge Ewers for being an inspirational mentor since my master studies. Thank you for your guidance, for letting me explore so many projects over the years, for sending me all around the world and for shielding me from the injustices that this profession can bring with it. Thank you for letting me grow into a scientist in your lab.

Thank you to Ria Thielhorn. We started this sitting next to each other and we finish this sitting next to each other. Thank you for comparing notes, studying together, practicals, internships, for publishing together, for proofreading all three of my theses. Thank you for being a great friend through all the ups and downs of the last decade! Hopefully, we do get to open that lab together at some point.

Thank you to Dragomir Milovanovic for taking me on an exciting journey through liquid liquid phase separation and for being a great mentor.

Thank you to Purba Kashyap for proofreading this thesis and so many other things. Thank you for all the long talks about SPT, science, the world, life and our futures.

Thank you to Ella de Gaulejac for proofreading this thesis. For our time in Berlin and beyond. Thank you for keeping me sane by bringing me into the world of yoga.

Thank you to all members of the Ewers lab for insightful scientific feedback and for the fun!

Thank you to Nico Went for accompanying me most of the way and thank you to Jordi Serrano Berbel for being with me at the final stretch and whatever exciting things our future together holds.

Table of contents

List of figures

List of abbreviations

AIS	Axon initial segment
AnkG	Ankyrin G
CaMKI	Calmodulin-dependent protein kinase
CD44	Cluster of differentiation 44
DIV	Day *in vitro*
DMSO	Dimethyl sulfoxide
dSTORM	Direct stochastic optical reconstruction microscopy
EM	Electron microscopy
FRAP	Fluorescence recovery after photobleaching
GFP	Green fluorescent protein
GPI	Glycosylphosphatidylinositol
IgG	Immunoglobulin G
KO	Knock-out
KV1.2	voltage gated potassium channel 1.2
MINFLUX microscopy	Minimal photon fluxes microscopy
MOI	Molecule of interest
MPS	Membrane-associated periodic skeleton
MSD	Mean squared displacement
PALM	Photoactivated localization microscopy
PM	Plasma membrane
PSF	Point spread function
PTM	Post-translational modification
QD	Quantum dot nanocrystal
SMLM	Single molecule localization microscopy
SMT	Single molecule tracking
SNARE	N-ethylmaleimide-sensitive-factor attachment receptor
SPT	Single particle tracking
STED microscopy	Stimulated emission depletion microscopy
STORM	Stochastic optical reconstruction microscopy
SV	Synaptic vesicle
Swin A	Swinholide A

UV light	Ultraviolet light
VAMP2	Vesicle-associated membrane protein 2
VGLUT1	Vesicular glutamate transporter 1
WT	Wild type

1. Zusammenfassung

Zellen müssen unzählige, gleichzeitige, teilweise gegensätzliche biochemische Reaktionen koordinieren. Dies gilt insbesondere für Neuronen, die die komplexe Aufgabe der Neurotransmission koordinieren. Eine Lösung für dieses Problem ist die Bildung spezialisierter Kompartimente. Um die molekulare Funktionsweise solcher Kompartimente zu verstehen, werden in dieser Arbeit zwei Systeme in neuronalen Zellen untersucht: i. die Plasmamembran und das darunterliegende Zytoskelett und ii. synaptische Vesikel-Cluster in Boutons. Zu diesem Zweck, wurde ein kombinatorischer Ansatz aus Computermodellierung, Einzelpartikelverfolgung und superauflösender Mikroskopie verwendet.

Periodische Aktinringe im neuronalen Axoninitialsegment schränken die Bewegung von Membranproteinen ein. Jedoch liefert eine lokale Anreicherung von Ionenkanälen eine alternative Erklärung. Durch Computermodellierung wird in dieser Arbeit nun gezeigt, dass Ionenkanäle keine Einschränkung der Membranmolekülbewegung bewirken. Darüber hinaus wird durch Einzelpartikelverfolgung und superauflösende Mikroskopie gezeigt, dass Aktinringe nahe der Plasmamembran sind und dass Aktinringe Membranproteine in verschiedenen neuronalen Zelltypen in ihrer Bewegung einschränken. Weiterhin wird gezeigt, dass die Zerstörung der Aktinringe Membrankompartmentalisierung reduziert.

Synaptische Boutons im Axon sind der Ort der Freisetzung synaptischer Vesikel. Synaptische Vesikel bilden dichte Cluster in Boutons, welche für die Funktion der Präsynapse essenziell sind. *In vitro* Experimente haben gezeigt, dass das lösliche Phosphoprotein Synapsin 1 das Clustern durch Flüssig-Flüssig-Phasentrennung steuert, der Mechanismus *in vivo* ist jedoch unklar. Diese Arbeit zeigt nun mittels Zweifarben-Einzelmolekülverfolgung in lebenden Neuronen, dass Synapsin 1 das Clustern synaptischer Vesikel steuert. Anhand eines Synapsin-Knock-out-Modells wird gezeigt, dass Synapsin 1 die Mobilität synaptischer Vesikel durch seine intrinsisch ungeordnete Region kontrolliert, die für die Phasentrennung verantwortlich ist.

Durch Untersuchungen der Dynamik kompartmentalisierter Systeme in neuronalen Zellen deckt diese Arbeit zwei molekulare Mechanismen auf: Aktinringe bilden Membrandiffusionsbarrieren und Synapsin 1 steuert Clustern und Mobilität synaptischer Vesikel durch Flüssig-Flüssig-Phasentrennung. Somit macht diese Arbeit wichtige Fortschritte zum Verständnis der Funktionsweise neuronaler Zellen, indem sie aufdeckt, wie die Kompartmentalisierung der Plasmamembran und des Zytosols gesteuert wird.

2. Abstract

Cells are faced with coordinating countless, simultaneous, partly antagonistic biochemical reactions. This is especially true for neurons that must orchestrate the complex task of neurotransmission. One solution to this problem is the formation of specialized compartments. To understand the molecular mechanisms of such compartments this thesis investigates two system in neuronal cells: i. the plasma membrane and its underlying cytoskeleton and ii. synaptic vesicle clusters inside synaptic boutons. Towards this end, a combinatorial approach of computational modeling, single particle tracking and super-resolution microscopy is employed.

A periodic array of actin rings in the neuronal axon initial segment has been known to confine membrane protein motion. Still, a local enrichment of ion channels offers an alternative explanation. Using computational modeling this thesis now shows that ion channels, in contrast to actin rings, cannot mediate confinement. Furthermore, by employing single particle tracking and super-resolution microscopy, this work shows that actin rings are close to the plasma membrane and that actin rings confine membrane proteins in several neuronal cell types. Further, it is shown that actin ring disruption leads to a reduction of membrane compartmentalization.

Synaptic boutons in the axon of neurons are the location of synaptic vesicle release. Synaptic vesicles form dense clusters inside boutons, that are essential for pre-synaptic function. *In vitro* experiments have suggested that the soluble phosphoprotein synapsin 1 controls synaptic clustering via liquid liquid phase separation. However, the *in vivo* mechanism remains elusive. This work now shows via two-color single molecule tracking in live neurons that synapsin 1 drives synaptic vesicle clustering. Furthermore, using a synapsin knock-out model it is shown that synapsin 1 controls the mobility of synaptic vesicles through its intrinsically disordered region, which is responsible for phase separation.

By studying the dynamics of compartmentalized systems in neuronal cells this work uncovers two molecular mechanisms: actin rings form membrane diffusion barriers and synapsin 1 controls synaptic vesicle clustering and mobility through liquid liquid phase separation. Thus, this thesis makes important strides towards deepening the understanding of neuronal function by uncovering how compartmentalization operates in both the plasma membrane and the cytosol of neuronal cells.

3. Introduction

3.1 Compartmentalization is a guiding principle of biological organization

Cells are faced with the task of coordinating countless, complex, partly antagonistic, biochemical reactions that occur simultaneously. To solve this problem, cells form dedicated reaction volumes, so called compartments, in which a subset of molecules is concentrated to perform a specific biological function. What is the advantage of compartmentalization?

In essence compartments confer three advantages: i. they act a reaction crucible, ii. they sequester molecules and iii. they serve as an organizational hub (Figure 1).[1-6]

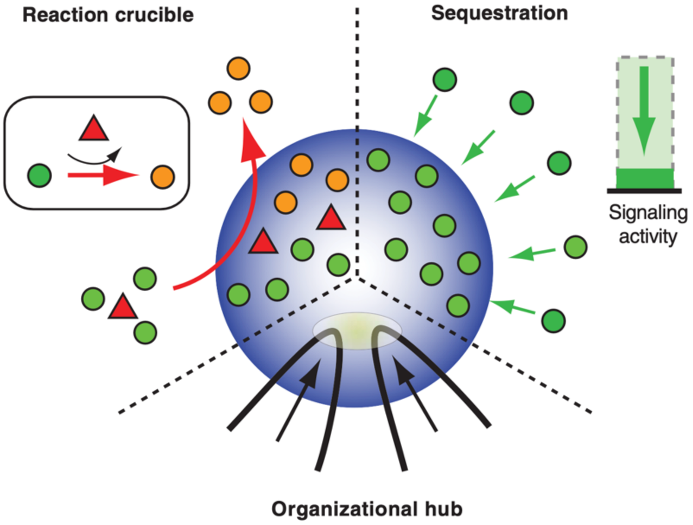

Figure 1 Compartmentalization enables biochemical reactions.

By increasing the local concentration of molecules, a reaction crucible (left) is formed in which chemical reactions can occur efficiently even between weakly interacting reactants. Additionally, reactants and products can be moved dynamically to and from compartments. To reduce off-target effects compartments can be used to sequester cellular factors from the rest of the cellular medium (right) when they are not needed. Compartments can serve as an organizational hub (bottom) by interacting with other compartments or organelles.

From Shin, Y. & Brangwynne, C. P. Liquid phase condensation in cell physiology and disease. *Science* **357** (2017). Reprinted with permission from AAAS.

Many biochemical reactions occur close to the chemical equilibrium and are therefore easily reversed in principle. Consequently, many reactions take place between weakly interacting molecules. How can these reactions still occur efficiently? Reaction rates can be increased greatly by forming reaction crucibles inside compartments that concentrate a specific subset of molecules. Furthermore, thousands of biochemical reactions can occur simultaneously inside a cell. Some having potentially opposing effects on cell physiology. How can these reactions occur without negatively interfering with one another? Compartments can play a role in sequestering away biological factors currently not needed for cellular function, thereby reducing the number of off-target effects. Additionally, compartments can serve as an organizational hub by interacting with other compartments or organelles with different specializations. In this way, compartments help orchestrate complex biological processes in which many molecular functions are involved.[1]

What is the molecular basis for compartmentalization? In this thesis, neuronal cells are used as a model system to explore the molecular organization of biological compartments in different cellular environments. In order to do so, the compartmentalization of the plasma membrane (PM) by the underlying cytoskeleton (3.2) and the compartmentalization of the cytosol through liquid-liquid phase separation in synaptic boutons (3.3) is investigated via a combinatorial approach of various super-resolution microscopy techniques (3.4).

3.2 Compartmentalization of the plasma membrane in neuronal cells

3.2.1 Proteins and lipids: The fluid mosaic model of the plasma membrane

The PM defines the boundary of the cell. It separates the interior from the exterior environment. This enables life to fine-tune the chemical environment of the cell independently of the exterior, which is a prerequisite for the complex cellular machinery to function. From the basic role as a physical barrier, all other functions of the PM follow. These include specific tasks coordinated by a complex signaling machinery consisting of receptors and other membrane proteins embedded in the PM. Furthermore, the PM is essential for maintaining a gradient of solutes and electric charge, which is achieved by protein channels and pumps.

The properties of the PM are to a large degree defined by countless non-covalent interactions of phospholipids.[7] These are most importantly hydrophobic interactions of the apolar acyl chains of lipids and polar interactions of the lipid head groups with each other and with water.[8] Biological membranes contain hundreds of different lipids but can be broadly categorized into three groups: glycerophospholipids, sphingolipids, and sterols.[9] PM lipids self-organize into a lipid bilayer of around 4 nm in diameter.[10] Both faces of the bilayer have an asymmetrical lipid composition.[9]

Around 50% of the total weight of the PM are proteins[11] that can associate with the PM as either integral or peripheral membrane proteins.[12] Integral membrane proteins contain one or more apolar stretches, that cross the lipid bilayer, surrounded by polar aromatic residues that interact with the membrane-water interphase.[13] In contrast, peripheral membrane proteins associate with the bilayer by interacting via binding to integral membrane proteins or lipids. Membrane binding mechanisms include non-specific hydrophobic interactions[14], covalently bound lipid anchors (e.g. through glycosylphosphatidylinositol, GPI)[15], recognition of specific membrane lipids[16] and electrostatic interaction between the protein and a charged lipid.[17]

How are membrane proteins organized in the bilayer? Early insights into the nature of the lipid bilayer came from Frye and Edidin in 1970. They showed that membrane proteins diffuse inside the bilayer by fusing a human and a mouse cell and observing the intermixing of membrane lipids of both cells.[18] Partly based on this observation, Singer and Nicholson developed the fluid mosaic model in 1972.[12] In this model, biological membranes are described as a matrix consisting of phospholipids interspersed with integral membrane proteins, as well as peripheral membrane proteins (Figure 2).

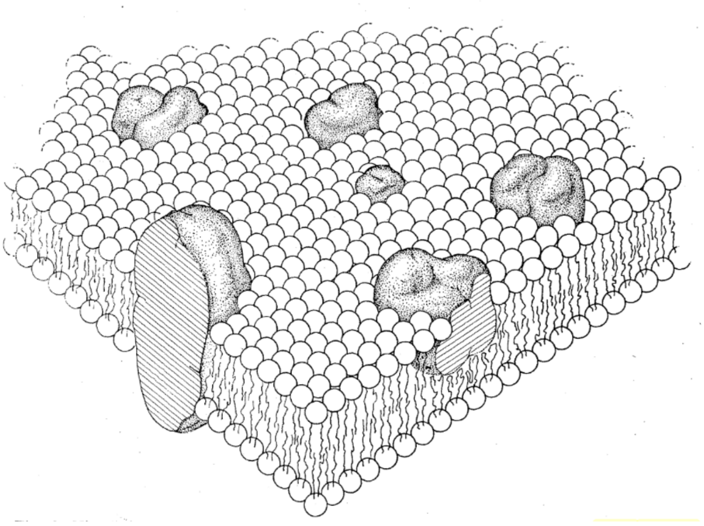

Figure 2 The fluid mosaic model.

Biological membranes are a matrix consisting of phospholipids interspersed with integral membrane proteins and peripheral membrane proteins. Proteins and lipids diffuse freely in the two-dimensional liquid generating a fluid mosaic.

From Singer, S. J. J. & Nicolson, G. L. L. The fluid mosaic model of the structure of cell membranes. *Science* **175**, 720-731 (1972). Reprinted with permission from AAAS.

Both proteins and lipids diffuse freely through the bilayer, generating a continuous two-dimensional liquid without any long-range order. The reduction of dimensionality of the PM in comparison to the cytosol is of utmost importance for the interactions of biomolecules, as this enables many orders of magnitude faster reaction rates. This is caused by the shorter time it takes for molecules to meet in a two-dimensional versus a three-dimensional space.[19]

Based on the work of Singer and Nicholson, Saffman and Delbrück developed in 1975 a quantitative model to describe the motion of proteins in the lipid bilayer.[20] Here, the diffusive behavior of the protein depends on the geometry of the membrane and the protein, as well as the viscosity of the membrane and the surrounding solvent. The Saffman-Delbrück model predicts the motion of proteins suspended in artificial lipid bilayers remarkably well.[21] However, the model does not accurately predict the behavior of proteins in biological membranes. Resolving these discrepancies led to the development of the picket-fence model, which will be discussed in detail in the following chapter.

3.2.2 The cytoskeleton compartmentalizes the plasma membrane

Given that the fluid mosaic model predicts no long-range order, proteins diffusing in the PM of a cell and those diffusing in an artificial lipid bilayer should diffuse with similar speeds. In practice, proteins in biological membranes diffuse at speeds of an order of magnitude slower than in artificial membranes.[6] Additionally, when signaling complexes are formed in the PM their diffusion rates are greatly reduced or molecules are immobilized.[4,5,22] This begs the question: What are receptor complexes immobilized onto if the membrane is a continuous liquid?

A promising candidate for the reduction of diffusion of proteins in biological membranes is the cytoskeleton. Koppel *et al*. could show using fluorescence recovery after photobleaching (FRAP) that the diffusion coefficients of integral membrane proteins were increased in cells not expressing the ubiquitous cytoskeletal protein spectrin.[23] Importantly, FRAP measurements are ensemble measurements and can give no information about the individual movement of single membrane molecules. Insights on the behavior of single membrane molecules were later found by Kusumi *et al.* They performed single particle tracking (SPT, 3.4.4) of membrane receptors in epithelial cells and observed confined diffusion of the receptor on short time scales (milliseconds) inside microscopic domains of around 300 nm.[24] This type of motion, in which molecules are confined inside a nanometer-sized compartment for several milliseconds before they jump to the next compartment, was coined hop diffusion.[25] Importantly, hop diffusion only appears confined on microscopic time scales, while manifesting as Brownian motion at macroscopic time scales. Therefore, it is compatible on large scales with the fluidity and continuity requirement of the PM of the fluid mosaic model.[26] Hop diffusion was later observed also for lipids[27] and for many membrane proteins and in many cells types[25,28-32] The observed compartmentalization of the PM into nanometer-sized domains was speculated to be caused by the underlying cytoskeleton,[24] which led to the development of the picket-fence model by Kusumi *et al*. In this model the PM is compartmentalized by the cytoskeleton directly (fences) and by transmembrane proteins immobilized onto the cytoskeleton (pickets). Membrane molecules are trapped inside the compartments for several milliseconds, thus giving rise to hop diffusion (Figure 3).[6]

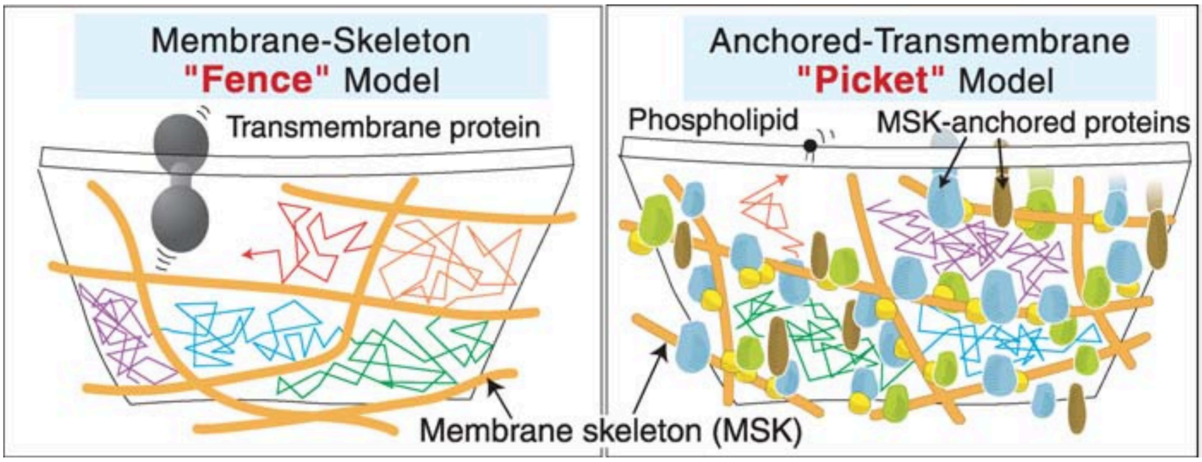

Figure 3 The picket-fence model of membrane compartmentalization.

The PM is compartmentalized by the membrane cytoskeleton at the inner leaflet of the bilayer (“Fence”) as well as by membrane-skeleton-anchored proteins. (“Picket”.) Membrane molecules undergo short-term confined diffusion within compartments and long-term hop diffusion between compartments.

From Kusumi, A. *et al.* Paradigm Shift of the Plasma Membrane Concept from the Two-Dimensional Continuum Fluid to the Partitioned Fluid: High-Speed Single-Molecule Tracking of Membrane Molecules. *Annual Review of Biophysics and Biomolecular Structure* **34**, 351-378 (2005). Reprinted with permission by Annual Reviews, Inc. conveyed through Copyright Clearance Center.

Of note, the anchored transmembrane protein pickets “communicate” membrane-skeleton fences to the outer leaflet of the PM, explaining the observed hop diffusion of phospholipids. Using Monte-Carlo-simulations Fujiwara *et al.* could show that 30% coverage of cytoskeletal fences with transmembrane proteins would be sufficient to reliably trap lipids in the outer membrane leaflet.[27]

What is the molecular identity of the fences? Next to the above-mentioned protein spectrin, another promising candidate is the ubiquitous cytoskeletal protein actin. Actin filaments form an intricate network of nanometer-scale compartments below the PM, so-called cortical actin.[33] Cortical actin is generally close to the PM (10-20 nm),[34] but there is likely local variability in the distance to the PM and density of the filaments depending on the state of the cell (e.g. direction of migration).[35] Interestingly, Fujiwara *et al.* could show using electron microscopy (EM) and SPT that the compartment size of the actin meshwork is comparable to the size of the compartments observed during hop diffusion for both membrane proteins and lipids.[31] While this is an important observation, the SPT experiments and the EM experiments were performed in different cells. It is therefore impossible to establish a direct causal link between the organization of the actin cytoskeleton and membrane compartments. Further evidence, for the picket-fence model was provided by Andrade *et al.* using stimulated emission depletion fluorescence correlation spectroscopy (STED-FCS)[36], a method in which fluctuations in fluorescence intensity are used to infer diffusion parameters of a fluorophore (in this case tagged to lipids).[32] The authors detected hop diffusion of membrane lipids. Furthermore, they found that diffusion coefficients (3.4.4) of lipids increased when the actin effector protein actin-related protein 2/3 complex (involved in promoting branching of cortical actin)[37] is inhibited. While this is strong evidence for the involvement of cortical actin in compartmentalizing the PM, the cortical actin itself could not be imaged in this study, due to limitations in axial resolution. Direct evidence of membrane-proximal actin forming a diffusion barrier was provided by Li *et al.*[38] They were able to pull magnetic nanoparticles along the surface of the cell. Afterwards, they fixed and stained the same cell for membrane-proximal actin filaments using direct stochastic optical reconstruction microscopy (dSTORM, 3.4.2), thereby detecting a membrane protein moving along an f-actin filament. Importantly, it remains an open question if this is truly a global effect, since the authors were only able to observe membrane proteins moving along actin filaments in a few instances. Performing correlative experiments on cortical actin is an inherently complicated undertaking, since these actin structures are highly dynamic and constantly remodeled.[39] As a consequence, the actin organization changes even on the time scale of the membrane molecule tracking measurement, which makes *post hoc* correlation with the actin cytoskeleton challenging.

To summarize, biological membranes behave as a fluid mosaic without long-range order on macroscopic scales. On microscopic scales however, lipids and membrane proteins are confined into nanometer-sized domains for short periods (hop diffusion). There is evidence for membrane-proximal cortical actin being the cause of the observed membrane compartmentalization. Crucially, direct correlative evidence has been difficult to obtain since cortical actin is highly dynamic. To overcome this issue, it is useful to investigate model systems with a more stable actin structure. A system with such properties is the cytoskeleton of neurons, which will be discussed in more detail in the following chapter.

3.2.3 The membrane-associated periodic skeleton in neurons

The cytoskeleton of neurons is unlike that of most other cell types. The cell body of neurons is lined with a hexagonal meshwork of sub-membranous spectrin and actin similar to that of erythrocytes.[40,41] However in axons, actin forms a periodic arrangement of ~200 nm spaced actin rings, interspaced by spectrin tetramers.

This organization was first detected by Xu *et al.* via STORM microscopy.[42] To this day, it remains one of the major findings of the super-resolution microscopy field, as this pattern had never been observed with other techniques such as EM, likely because of the susceptibility of the actin rings toward detergents.[43] The specific organization of the neuronal cytoskeleton has been termed membrane-associated periodic skeleton (MPS)[44] and has been confirmed independently using a wide range of super-resolution microscopy techniques.[30,45-53] Though the MPS was first discovered in axons,[42] it was later also found in a subpopulation of dendrites[41,49] and inside dendritic spines (Figure 4).[54]

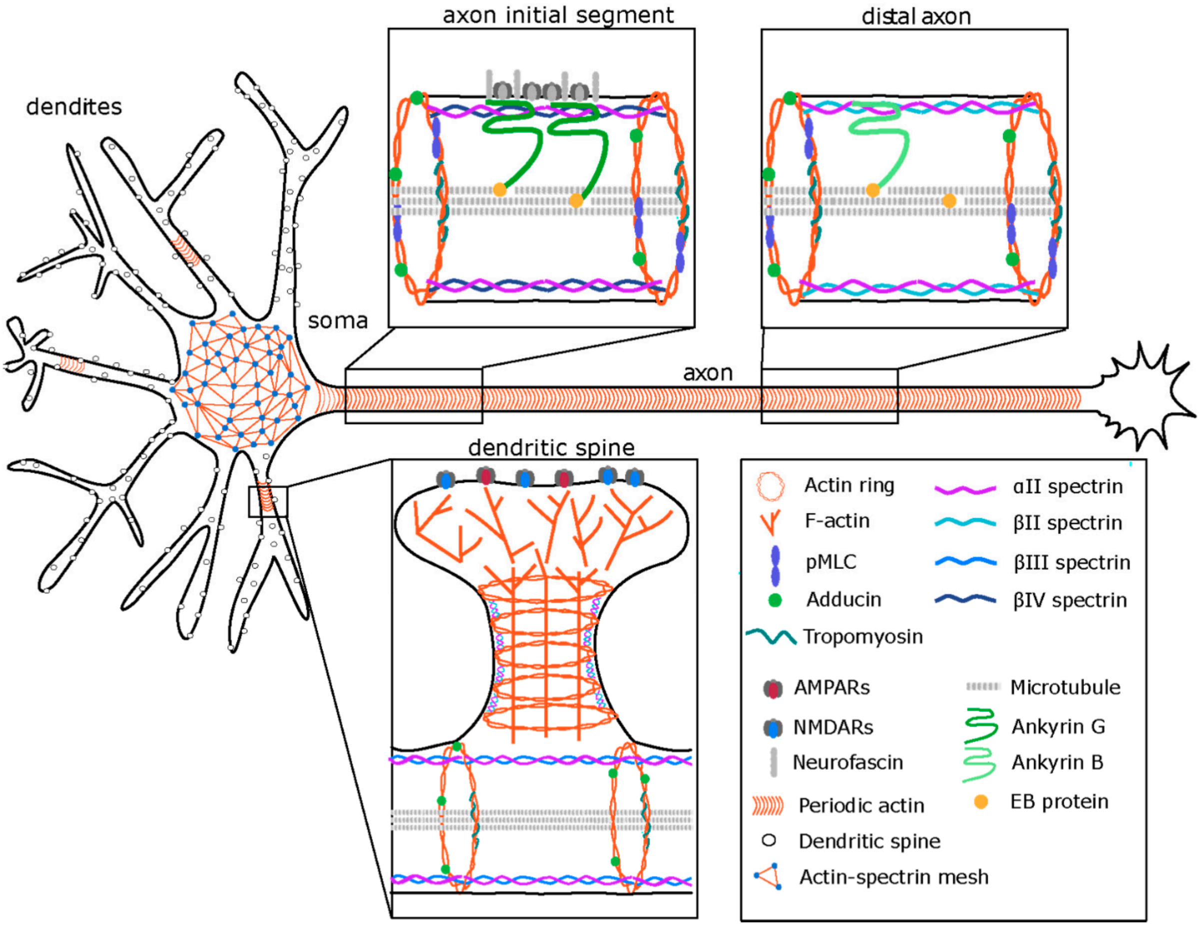

Figure 4 The organization of the cytoskeleton in neurons.

A hexagonal actin-spectrin meshwork spans the soma. A periodic membrane-associated periodic skeleton is located in axons, some dendrites and at the neck of dendritic spines, consisting of actin rings at a periodicity of ~ 200 nm, interspersed by spectrin tetramers. Each actin ring is formed by two braided actin filaments and stabilized by adducin and by tropomyosin. Spectrin tetramers consist of two αII spectrins and two cell compartment-specific isoforms of β-spectrin. Depending on the cell compartment, other specialized proteins associate with the MPS. Notably, the axon initial segment contains large voltage-gated ion channels located between actin rings bound to the scaffold protein ankyrin G.

From Mikhaylova, M., Rentsch, J. & Ewers, H. Actomyosin Contractility in the Generation and Plasticity of Axons and Dendritic Spines. *Cells* **9**, 1-14 (2020). Reprinted with permission under CC BY 4.0 DEED. creativecommons.org/licenses/by/4.0/deed.de

Furthermore, the MPS is conserved in many species from humans to worms[44] and has been found all throughout the nervous system including excitatory and inhibitory neurons,[44,50] as well as in oligodendrocytes and astrocytes.[52] In contrast to other cellular actin structures in the cell (e.g. cortical actin), actin rings of the MPS are highly stable in their location for long periods (days to weeks)[30,39] and are even resistant to some actin depolymerization drugs.[46] Though Swinholide A (Swin A), a small molecule from the marine sponge Theonella swinhoei,[55] has been shown to sever actin filaments, inhibit actin polymerization[56-58] and to efficiently disrupt actin rings[47].

Next to actin, the other major component of the MPS is spectrin, as it connects the actin rings via tetramers.[46] In neurons, spectrin dimers are formed by the lateral association of αII and β spectrin monomers. The dimers then associate head-to-head to produce a tetramer. Interestingly the β isoform of the tetramers varies between neuronal compartments. βIV spectrin is located at the beginning of the axon (axon initial segment, AIS), while βII spectrin is located at the distal axon and in dendrites and βIII in dendrites.[41,42,46,59] What is the role of spectrin for the MPS? Spectrins are required for the assembly of the MPS.[41] Furthermore, they seem to be essential for the mechanical stability of the axon. In spectrin knock-out (KO) animals axons tear easily due to mechanical stress.[60] This and similar findings have led Dubey *et al.* to develop a model in which spectrin acts as a tension buffer by reversibly unfolding spectrin domains in response to mechanical stress.[61]

What other proteins associate with the MPS? Xu *et al.* observed co-localization of adducin with actin rings. They hypothesized that actin rings consist of short filaments that are capped and stabilized via binding to adducin.[42] Recent work by Vassilopoulos *et al.* using platinum replica EM however revealed that actin rings consist of braids of intertwined actin filaments with a diameter of around only 20 nm. Here adducin was suggested to enhance the binding between actin and βII-spectrin.[47] While further work to illuminate the role of adducin is needed, the findings of Vassilopoulos *et al.* are highly significant as they could for the first time visualize the organization of actin rings using EM. Other proteins that associate with the MPS include non-muscle tropomyosin. It likely has a stabilizing function as inhibition of tropomyosin leads to a reduction in the periodicity of actin rings.[62]

While the basic structure of the MPS is ubiquitous in neurons, a specialized MPS is present in the first 50-100 µm of the axon, the so-called AIS. The AIS acts as a barrier between the somatodendritic and the neuronal compartment and plays an important role in action potential generation.[63,64] The MPS can be detected in the AIS early in neuronal development (day *in vitro* 2, DIV2), preceding all AIS markers.[30,42] One of the key proteins of the AIS is the scaffolding protein ankyrin G (AnkG). AnkG is essential for AIS integrity, as knock-down of AnkG leads to rapid degradation of the AIS and subsequent loss of axonal function.[65,66] AnkG associates directly with the MPS by binding to βIV spectrin. It is therefore located between the actin rings[46] (Figure 4). AnkG is essential for the targeting of membrane proteins to the AIS. These include large voltage gated ion channels, necessary for action potential generation[67] as well as adhesion molecules such as neurofascin.[68]

To summarize, the neuronal cytoskeleton is unique in its stability and regularity. It consists of periodic ~200 nm spaced actin rings, interspersed by spectrin tetramers (MPS) and adhesion and adaptor proteins that can vary depending on the neuronal compartment. A specialized version of the MPS is present in the AIS, where it has an essential role as a platform for action potential generation. Furthermore, the AIS has an important function in maintaining the molecular composition of the axon by acting as a diffusion barrier between the axonal and the somatodendritic compartment. The role of the AIS as a diffusion barrier and the involvement of the MPS will be discussed in more detail in the next chapter.

3.2.4 The membrane-associated periodic skeleton is a diffusion barrier

Neurons are exceptionally polarized cells. This means that the composition of the somatodendritic and axonal compartments is highly specialized and varies greatly between compartments. Loss of polarity is often catastrophic, as it can result in the overall loss of function of the neuron.[66] Such loss of polarity might be implicated in many neurological diseases such as schizophrenia, epilepsy, multiple sclerosis and stroke.[69-71] Consequently, understanding the establishment and maintenance of neuronal polarity has been an important ongoing pursuit for many decades.

Early insights into the establishment of neuronal polarity were gained by Dotti *et al*. They ectopically expressed viral glycoproteins in mature neurons and found that they are differentially sorted between compartments in a manner reminiscent of epithelial cells.[72] They could later also show that the GPI-anchored protein Thy-1 preferentially localized to axons.[73] How is the preferential localization of axonal membrane proteins maintained? One possible explanation is the establishment of a diffusion barrier that prohibits somatodendritic proteins from entering the axon and *vice versa*. Such a barrier was first observed for phospholipids[74] and later also for membrane proteins.[75] Additional evidence for the establishment of a diffusion barrier was provided by Nakada *et al*. They could show that a diffusion barrier for membrane proteins is established between DIV4 and DIV10 and that the slowdown of membrane proteins coincided with an increase in AnkG immunostaining intensity. They hypothesized under the picket-fence model (3.2.2) that transmembrane proteins are recruited to the AIS by AnkG, forming an increasingly dense meshwork over time.[76] While the observations of Nakada *et al*. are an important contribution, they predate the development of STORM microscopy[77] (3.4.2) and the discovery of the MPS in neurons.[42] Investigations into the role of the MPS in the establishment of a diffusion barrier were later performed by Albrecht and Winterflood *et al*.[30] They performed SPT of GPI-anchored GFP in the AIS of developing neurons and found a strong reduction in diffusion coefficient early in neuronal development (DIV3-DIV7). Interestingly, they observed that localizations of GPI-GFP formed a pattern of ~200 nm periodicity, very similar to the one observed for actin rings.[42] Furthermore, they could show using correlative SPT of GPI-GFP and STORM of the MPS that the GPI-GFP pattern alternates with actin rings (Figure 5).[30]

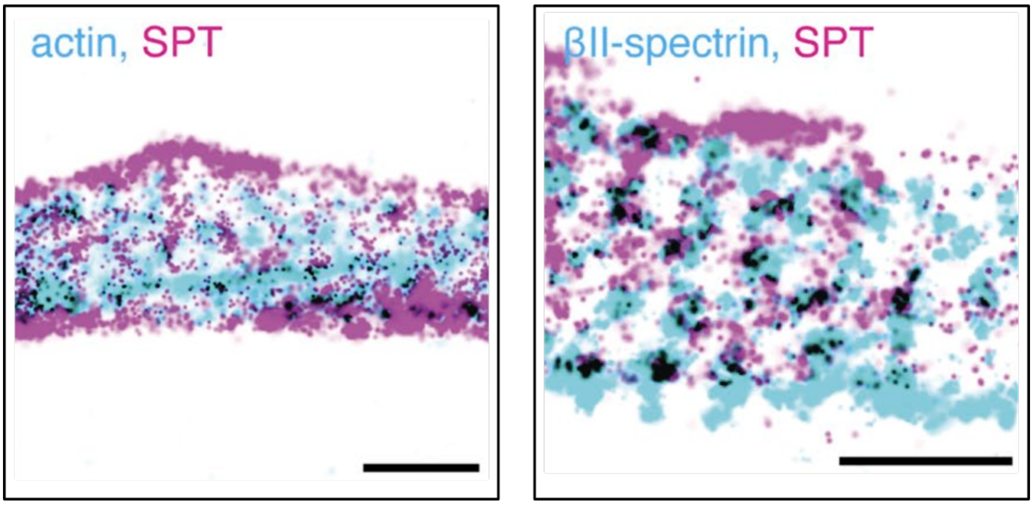

Figure 5 GPI-GFP accumulations in the AIS form a periodic pattern that alternates with actin rings and co-localizes with spectrin.

Shown are correlative reconstructions of localizations of SPT of GPI-GFP (magenta) and of STORM (cyan) of actin (left) or βII-spectrin (right). Scalebars are 500 nm.

From Albrecht, D. et al. Nanoscopic compartmentalization of membrane protein motion at the axon initial segment. Journal of Cell Biology 215, 37-46 (2016). Adapted with permission from Rockefeller University Press conveyed through Copyright Clearance Center.

As mentioned above, Nakada *et al.* originally proposed that transmembrane proteins immobilized by AnkG are the cause of the barrier.[76] Importantly, AnkG co-localizes with spectrin to form a periodic pattern (Figure 4).[46] In this view, GPI-GFP would be immobilized by a dense meshwork of transmembrane proteins (like large voltage-gated channels). In contrast Albrecht and Winterflood *et. al.* hypothesized that actin rings cause the barrier. In this view, actin rings (and immobilized membrane proteins on it) would restrict the motion of membrane proteins directly.

Crucially, the model proposed by Nakada *et al.* is compatible with the work of Albrecht and Winterflood *et al.*, because a periodic channel density that traps membrane molecules could equally explain the observed pattern of GPI-GFP localizations. The molecular basis of the membrane diffusion barrier at the AIS therefore remains elusive. To elucidate which of the described models (channel proteins anchored to AnkG or actin rings as barrier) is correct will be a major focus of this thesis. To that end, it will be essential to investigate whether the observed membrane compartmentalization by actin rings is specific to the AIS or rather a global phenomenon, wherever actin ring structures are present. Recently, Hauser *et al*. have shown that the MPS is present in progenitor-derived neuronal cells like astrocytes and oligodendrocytes.[52] Importantly, these cells lack an AIS and therefore also the AIS-specific density of AnkG. Consequently, these cells provide the opportunity to investigate the compartmentalization of actin rings by the PM in a system without a density of membrane proteins anchored to AnkG. Therefore, progenitor-derived neuronal cells will be one of the main cellular systems explored in this thesis.

To summarize, the AIS acts as a diffusion barrier between the somatodendritic and the axonal compartment of the neuron. The diffusion barrier arises early during maturation and is essential for neuronal function. The molecular mechanism behind the barrier remains elusive but two competing hypotheses have emerged: i. transmembrane proteins anchored to AnkG or ii. actin rings. To elucidate which hypotheses is true, the membrane compartmentalization of progenitor-derived neuronal cells, a system with periodic actin rings but without AnkG densities, is explored in this thesis (4).

3.3 Compartmentalization of the cytosol in neuronal cells

3.3.1 Liquid-liquid phase separation is ubiquitous in nature

The cytosol is the inside of the cell, embedding everything that is located below the PM. As such, the cytosol is the stage for all cellular processes that are not sequestered away within membrane-bound organelles. These include some of the most fundamental biochemical functions such as protein synthesis and folding, intracellular transport and a host of enzymatic reactions. The cytosol should not be thought of an aqueous solution in which proteins diffuse freely but rather a dense gel crowded with macromolecules and organelles, in which diffusion is highly restricted by steric hinderance and a plethora of low affinity interactions.[78] Investigations into the structure and organization of the cytosol have long been on the forefront of understanding cell biology. E.B. Wilson proposed in 1899 that the cytosol is compartmentalized into a mixture of chemically active liquids forming emulsions with different properties.[79] In the following decades the existence of such emulsions (also known as membrane-less compartments) in the cytosol was experimentally verified in many biological systems.[3,80-87]

Recent studies have revealed that the compartments are formed by liquid-liquid phase separation (LLPS).[1] LLPS is a process in which one or multiple liquids spontaneously unmix from the surrounding medium. In terms of cells, it can be thought of as the spontaneous separation of biochemical polymers from an aqueous solution (e.g. cytosol, nucleosol) to form condensates.[2] LLPS can occur when a critical concentration of condensate-forming molecules is reached.[88] Even though condensates lack a surrounding membrane they are often thought of as organelles as they form highly specialized functional units.[89] Condensates are round and typically a few micrometer in size [1,3,83] The defining features of liquid condensates in contrast to other dense biomolecular structures (e.g. protein aggregates) is that the inside of the condensate remains fluid and in rapid exchange with the surrounding medium. This can be shown by bleaching condensates in FRAP experiments, where bleached regions will recover in seconds to minutes.[3,90,91] Even though exchange with the surrounding medium is highly dynamic, condensate structures can be stable for tens of minutes.[85,92] Importantly, it has been reported that condensates exhibit metastability i.e. initial liquid structures transition over time into solid like aggregates.[86,87] This feature of condensates could have important implications for the pathology of many protein aggregation diseases (e.g. Alzheimer, amyotrophic lateral sclerosis, Parkinson's).[1] Furthermore, condensates exhibit other typical properties of liquids, such as coalescence of multiple droplets into a single condensate upon contact[82] and showing "wetting behavior" (covering a surface with a liquid film upon interaction).[92]

What is the structural basis for LLPS? Condensates often contain a mixture of protein organelles and RNA molecules.[3,93] Here, RNA has been shown to reduce the critical concentration needed to make a given protein undergo LLPS.[87] The properties of liquid condensates arise from the weak interaction of many molecules.[1] Therefore, multivalent interactions play a crucial role in the formation of liquid condensates. Many condensate-forming proteins contain several repeats of the same domains or multiple domains that interact with other components.[94] One example of such domains are repeats of the SH3 domain, which interact with proline-rich motifs. Li, Banjade and Cheng *et al.* showed that repeats of three or more SH3 domains form condensates with proline-rich motifs in an *in vitro* system.[95] The critical concentration for condensation decreased with the number of SH3 domain repeats, highlighting the importance of multivalency for LLPS. Furthermore, many proteins involved in LLPS contain stretches without a stable secondary or tertiary structure, so-called intrinsically disordered regions (IDRs).[3,87,96] These stretches typically lack hydrophobic residues but contain polar and charged amino acids[97] or aromatic residues.[88] These residues enable the polypeptide backbone to engage in many low-affinity interactions (charge-charge, charge-π, π-π).[88]

Since condensates are metastable[86] they have to be tightly controlled by biological activity. Some of these mechanisms include targeted phosphorylation of proteins, which can lead to condensate assembly,[98] release from the condensate,[99] and even to the dissolution of the entire phase.[100] It is likely that many other post-translational modifications (PTMs) have a direct influence on condensate dynamics. For example, Nott *et al.* have shown that arginine methylation led to an order of magnitude increase in critical concentration.[101] Additionally, PTMs have been shown to act as a seed for condensation by attaching a highly negatively charged adenosine 5-diphosphate-ribose to target proteins (similar to how negatively charged RNA reduces critical concentration).[102]

In summary, LLPS is the main mechanism by which the compartmentalization of the cytosol into functional membranelles organelles is achieved. One such organelle, that has been proposed to form through LLPS, is located in the pre-synapse of neurons: synaptic vesicle clusters.[3] The relevance of this system for neuronal activity and it's molecular constituents will be discussed in the following chapters.

3.3.2 Synaptic vesicle clusters organize pre-synaptic composition and activity

Neurons must orchestrate the very complex task of neurotransmission, which entails integrating signals they receive from neighboring neurons into their somatodendritic compartment and subsequently signaling to other neurons via their axonal compartment. This is achieved by a collection of highly specialized organelles inside a signaling hub called the chemical synapse.

An example of such organelles are synaptic vesicles (SVs) located on the axonal (pre-synaptic) side of the synapse, so-called synaptic boutons. SVs contain neurotransmitters that are released into the synaptic cleft after fusion of SVs with the PM. Neurotransmitters move across the synaptic cleft, interacting with the post-synapse, which ultimately leads to inhibition or activation of the post-synapse. After neurotransmitter release SVs are retrieved from the PM and are turned over into newly fusion-competent SVs.[103] This process is called SV recycling.[104] Interestingly SVs are not equally distributed inside boutons but rather form so called SV clusters.[105] What is the function of SV clusters? SV clusters act as a reservoir of neurotransmitters that can be released during a high-frequency stimulation.[104] However, the number of SVs within synaptic clusters appears to exceed what is strictly necessary for maintaining synaptic activity.[106] Therefore, it is likely that the high number of SVs inside clusters servers other functions as well.

SVs bind to many soluble proteins inside the pre-synapse, therefore they might act as a localized storage for soluble factors required for SV recycling.[107] In this way a more active synapse, which contains more SVs,[108] would also contain the required high number of soluble factors bound to SVs. Furthermore, SVs might also regulate components of the PM by interacting with adhesion complexes (e.g. N-ethylmaleimide-sensitive-factor attachment receptor, SNARE proteins) or by changing the composition of the PM by fusing with it.[109] Additionally, SVs likely play a role in regulating the synaptic cytoskeleton. The major scaffolding protein in the synaptic bouton is actin[110,111] and SVs have been shown to affect the polymerization kinetics *in vitro*[112]. Actin has been shown to form distinct nanostructures inside synaptic boutons. These include a dense actin meshwork at the PM of the active zone, actin rails inside boutons and actin corrals surrounding SV clusters, while actin rings are absent.[113] The functional role of these nanostructures remains underexplored, though they have been hypothesized to be involved in speeding up endocytosis in the pre-synapse (Figure 6).[114]

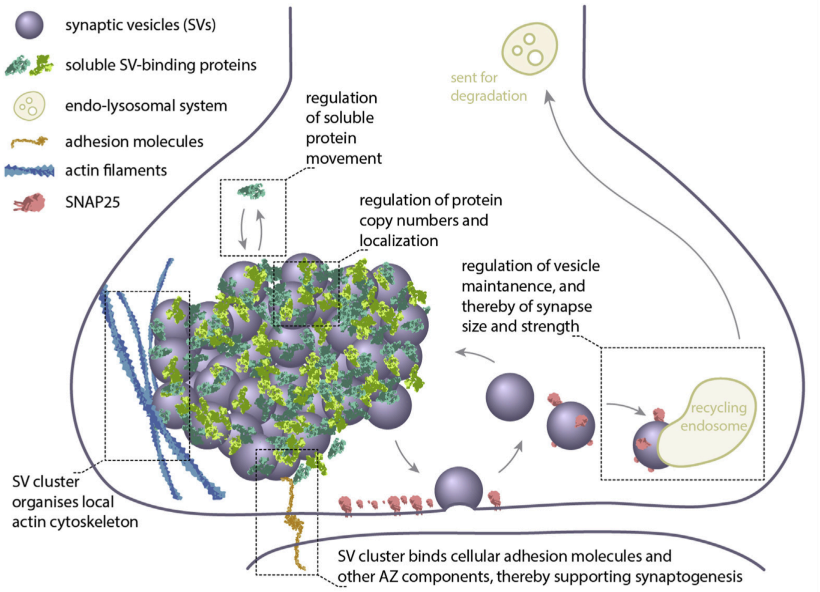

Figure 6 SV clusters organize pre-synaptic composition and activity.

SVs control the movement and regulate the abundance of soluble factors. Furthermore, SVs control the polymerization of the cytoskeleton (e.g. actin). The PM is influenced by the binding of adhesion molecules by SVs. SV number is kept in homeostasis by SNARE proteins (e.g. SNAP25) accumulation which needs to fusion with recycling endosomes.

From Reshetniak, S. & Rizzoli, S. O. The vesicle cluster as a major organizer of synaptic composition in the short-term and long-term. *Curr Opin Cell Biol* **71**, 63-68 (2021). doi.org/10.1016/j.ceb.2021.02.007. Reprinted with permission under CC BY-NC-ND 4.0 DEED. creativecommons.org/licenses/by-nc-nd/4.0

Taken together, SV clusters are essential for neurotransmission and play an important role in maintaining composition and activity of the pre-synapse. As such, SV clusters are under the tight control of many biological factors, some of which will be discussed in the next chapter.

3.3.3 Synaptic vesicle clusters are tightly regulated

Synaptic boutons contain a number of highly concentrated soluble proteins that have been shown to effect SV clustering.[2] Examples include a family of phosphoproteins called synapsins.[115] Synapsins are of singular importance for SV clustering and therefore deserve their own chapter (3.3.4). Another abundant family of soluble proteins inside boutons are synucleins (α, β, γ).[116] Interestingly, synucleins lack tertiary structure, but α-synuclein shows a high affinity for negatively charged lipids, changing its structure to an alpha-helix upon binding (a possible mechanism for its recruitment to SV clusters).[117] Triple KO of synucleins produces a phenotype in which nerve terminal size is reduced and packing density of SVs is increased.[118] Furthermore, injection of anti-α-synuclein antibodies leads to a dose-dependent disruption of SV clusters, that nevertheless does not lead to a complete abolishment of SV clusters.[119] Synucleins have been hypothesized to forms oligomers on the SV surface, thereby accelerating fusion reactions during neurotransmitter release.[120]

Interestingly, SV clusters are largely void of other organelles.[121] How is the specificity achieved? A possible explanation are cytosolic tails of integral SV proteins that modulate the overall valency and affinity of SV clusters. For example, vesicle-associated membrane protein 2 (VAMP2) is an interaction partner of α-synuclein. VAMP2 and α-synuclein have been shown to cluster liposomes in tandem.[122] Another example is the vesicular glutamate transporter 1 (VGLUT1), which contains a negatively charged cytoplasmic tail that regulates SV density.[123] Furthermore, there are three major families of tetra-span membrane proteins in the SV membrane (synaptophysins, synaptogyrins and secretory-carrier membrane proteins) that play a role in SV cluster regulation. The most important member is synaptophysin 1, which is highly enriched in SVs (10% of total SV protein content).[124] The physiological effect of the KO of tetra-span proteins is small, as only the knockout of four major tetra-span proteins (synaptophysin 1, synaptophysin 2, synaptogyrin 1, and synaptogyrin 3) leads to an increased release frequency under mild stimulation.[125] This finding likely indicates that many of the tetra-span membrane proteins have redundant roles in the regulation of SV clustering.[2] For a summary of SV cluster regulators see Figure 7.

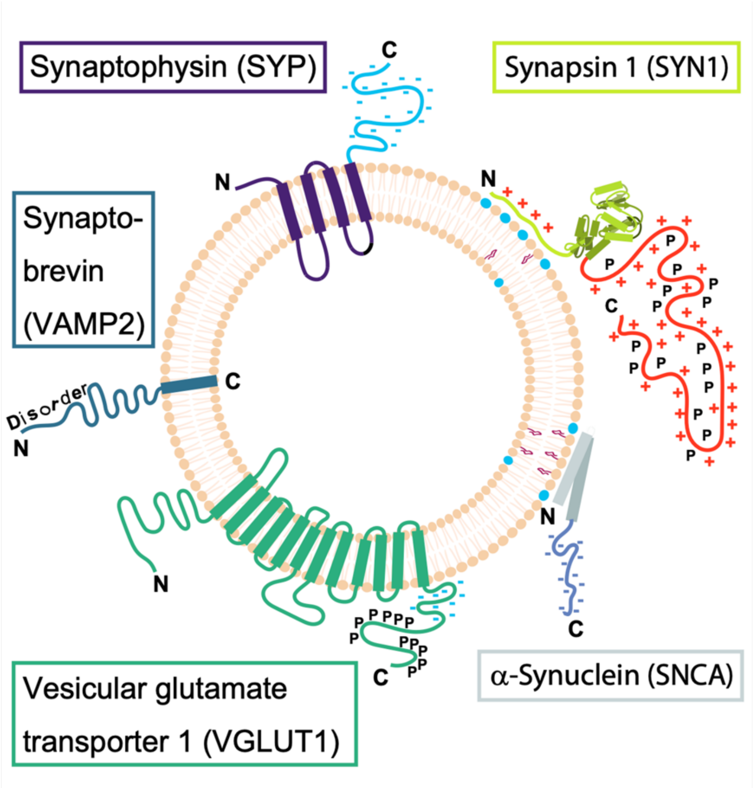

Figure 7 SV clusters are regulated by soluble proteins and resident SV transmembrane proteins.

Shown are important members of each group. Note that the master regulator of SV condensation synapsin can directly interact with charged and unsaturated lipids present in the SV membrane.

From Sansevrino, R., Hoffmann, C. & Milovanovic, D. Condensate biology of synaptic vesicle clusters. Trends Neurosci 46, 293-306 (2023). doi.org:10.1016/j.tins.2023.01.001. Adapted with permission under CC BY-NC-ND 4.0 DEED. creativecommons.org/licenses/by-nc-nd/4.0

In summary, SV clusters are under tight control by a complex protein machinery. It is critical to note, however, that none of the here mentioned proteins (e.g. α-synuclein, VAMP2, synaptophysin, VGLUT1) are sufficient to trigger SV clustering alone. How is clustering of SVs achieved then? Synapsins have been hypothesized to be the master regulator of SV clustering. The role of synapsins in the organization of the synaptic bouton will be discussed in the next chapter.

3.3.4 Synapsins control synaptic vesicle clustering

Synapsins are exceptionally enriched inside synaptic boutons (120 µM).[126] They are a key regulator of neurotransmitter release.[127] Mutations in synapsins have been associated with epilepsy.[128] Furthermore, synapsins show a lower expression level in patients with schizophrenia.[129] In mammals three genes encode for synapsins (I, II, III).[130] Through alternative splicing multiple synapsin variants have been observed (Figure 8).

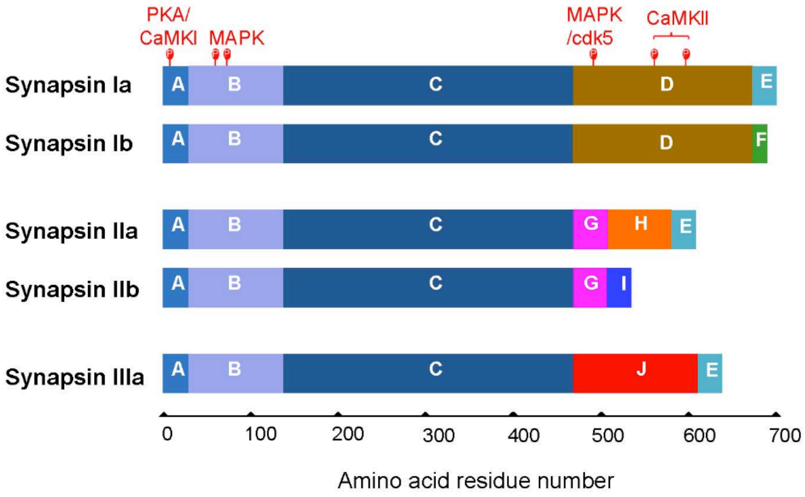

Figure 8 Multiple synapsin isoforms are generated of three genes via alternative splicing.

Shown here are protein domains of synapsins ordered by their amino acid residue number. Some phosphorylation sites of human synapsin 1 that are implicated in neurotransmission are highlighted in red.

From Song, S.-H. & Augustine, G. Synapsin Isoforms and Synaptic Vesicle Trafficking. *Molecules and cells* **38**, 936-940 (2015). Doi.org/10.14348/molcells.2015.0233. molcells.org. Reprinted with permission under CC BY-NC 4.0 DEED. creativecommons.org/licenses/by-nc/4.0

Synapsins I is the most expressed isoform of all synapsins, with synapsin Ia being the dominant splice variant.[131] All synapsin splice variants show high homology at the n-terminus (domains A-C), while they show more variability at the c-terminus (domains D-J).[132] Domain A controls the association with SVs via binding to phospholipids[115,133]. Domain B is a conserved linker[132], likely involved in regulating interactions of synapsins with actin.[134] Domain C is governing ATP-binding, making synapsins likely act as phosphotransferase for targets on the surface of SVs.[135] Domain E is involved in oligomerization of synapsins.[136] Domains F and I are poorly understood.[132] Domains D, G, H, and J contain long IDRs, which share structural similarities such as repetitive proline sequence elements, a positive net charge and serine-, glycine- , glutamine-rich regions. Importantly, the IDR of synapsin I is around 2-fold longer than the IDR of synapsin II and III.[115,137,138]

Synapsins contains several important phosphorylation sites that are partly conserved between family members and species. Site S9 is conserved in vertebrates and invertebrates, while site S568 and S605 are specific to mammalian synapsin I.[115,139] During neuronal transmission, synapsin I cycles between two main phosphorylation states. At rest, sites S62, S67 and S551 are constitutively phosphorylated by mitogen-activated protein kinase under the control of brain-derived neurotrophic factor.[140,141] After neuronal stimulation, calcium release leads to activation of calcineurin, in turn dephosphorylating S62, S67, S551.[142] Simultaneously, site S9 is phosphorylated by Ca^{2+}/calmodulin-dependent protein kinase I (CaMKI) or protein kinase a and sites S568 and S605 are phosphorylated by CamKII. The change in phosphorylation pattern ultimately leads to a reduction in SV binding by synapsin I.[143]

Critically, synapsins have been found to affect the organization of SV clusters using EM. This is clearly indicated by genetic data where triple KO of all mammalian synapsins shows a reduction in the number of SVs as well as a reduction in the overall packing density.[3,144] Additionally, the acute perturbation of SV clustering induced by injection of anti-synapsin antibodies leads to a complete dispersion of SVs.[145] Interestingly, antibodies against the IDR of synapsin I led to a loss of SV clustering even in the absence of any stimulation (Figure 9).[146]

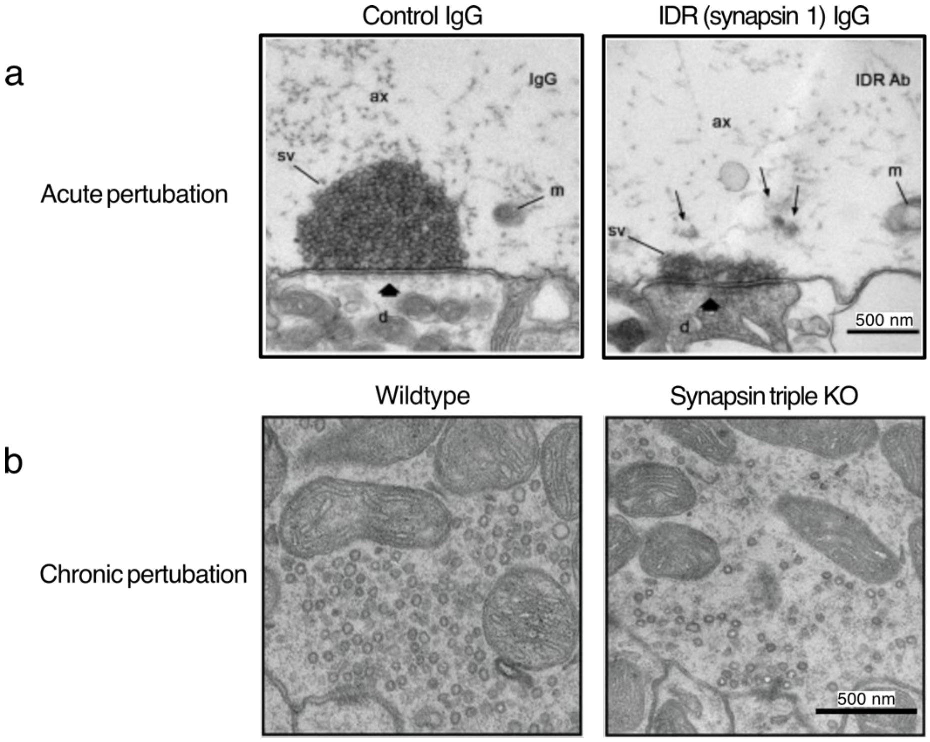

Figure 9 Perturbation of synapsin leads to loss of SV clustering.

(a) Electron micrographs of lamprey synapses microinjected with an inactive control immunoglobulin G (IgG, left) or an IgG against the IDR of synapsin 1 (IDR AB, right). SV (sv) clustering in the active zone (thick arrows) is lost upon injection with anti synapsin 1 IgGs. Thin arrows point at dispersed SVs. d, dendrite; ax, axonal cytosol; m, mitochondrion. **(b)** Electron micrographs of synapses of wildtype (left) or synapsin I, II, III KO (right) of adult mice. SV clusters are absent in synapsin triple KO mice.

a) from Pechstein, A. *et al.* Vesicle Clustering in a Living Synapse Depends on a Synapsin Region that Mediates Phase Separation. *Cell Reports* **30**, 2594-2602.e2593 (2020). Adapted with permission under CC BY-NC 4.0 DEED. creativecommons.org/licenses/by-nc/4.0

b) from Milovanovic, D., Wu, Y., Bian, X. & De Camilli, P. A liquid phase of synapsin and lipid vesicles. *Science* **361**, 604-607 (2018). Reprinted with permission from AAAS. Modified with permission from Dragomir Milovanovic, Laboratory of Molecular Neuroscience, German Center for Neurodegenerative Diseases (DZNE), 10117 Berlin, Germany.

Importantly, EM of both the triple KO of synapsin and the acute perturbation of synapsin by antibodies are end-point measurements that highlight the significance of synapsins for the organization of SVs, however, they cannot provide information on the dynamics of the system. Therefore, the exact mechanism by which synapsins control SV clustering remains elusive.

SV clusters are a tightly packed structure without any restraining boundary.[147] SVs are mobile inside clusters[148] and can be exchanged between clusters.[149] Still SVs need to be highly concentrated inside synaptic boutons to prevent dispersal along the axon. So how is a local density of SVs in proximity to the PM achieved, while maintaining high mobility of individual SVs? Synapsins have been proposed to solve this issue by acting as a rigid scaffold for SVs and their interaction partners.[111] However, the high concentration of synapsins[126] and the high mobility of SVs inside clusters[148] shed doubt on this view.

Alternatively, LLPS has been proposed to play role in SV clustering.[147] Synapsins I and II can form biomolecular condensates that show all properties of a liquid phase.[3] Of note is the ability of synapsins to homo- and heterodimerize, which reduces the critical concentration for condensation.[150,151] Specifically, the IDR of synapsin I has been shown to be necessary and sufficient for condensate formation.[3] Scaffolding proteins can be recruited into the condensate phase via SH3-domain interactions with proline rich motifs inside the IDR but are not necessary for droplet formation.[152,153] In addition, other soluble synaptic bouton resident proteins have been shown to be recruited to synapsin condensates. For examples, α-synuclein (3.3.3) is present in synapsin-condensates in living neurones.[91] This finding is significant, since triple KO of synucleins has the opposite effect as triple KO of synapsins on SV clustering (higher SV cluster density[118] versus abolishment of SV clusters[3]), likely indicating that synapsins and synucleins fine tune SV cluster density in tandem.[2]

Crucially, synapsin 1 liquid condensates can cluster small liposomes *in vitro* by recruiting them into the liquid phase. Could a similar mechanism explain SV clustering *in vivo?* The electric charge of lipids plays a critical role in liposome clustering, as negatively charged lipids are required for the recruitment by the synapsin condensate.[3,154] This finding is important, since SVs have been shown to have a negative surface charge.[155] Furthermore, the SV resident protein synaptophysin (3.3.4) can be recruited into the synapsin condensate via it's c-terminal region of low complexity and high acidity.[156] Interestingly, ectopic co-expression of synaptophysin 1 and synapsin 1 is sufficient to form vesicular condensates that are SV cluster like.[157]

Synapsin 1 has been shown to sense membrane curvature.[158] SVs are highly curved due to their small diameter (45 nm).[124] Thus, the high curvature of SVs could possibly explain their recruitment to the synapsin condensate. Importantly, neither negative electric charge, nor high membrane curvature are specific features of SVs. The possible recruitment of SVs into the synapsin phase is therefore likely to not be conferred by a single property but rather by the unique combination of features of the SVs membrane (lipid composition, membrane protein composition, membrane curvature).[2] Vitaly, while *in vitro* experiments clearly suggest recruitment of SVs into the synapsin condensate, this so far has not been shown conclusively *in vivo*.

In summary, synapsins control the clustering of SVs, however the exact mechanism remains elusive. While EM has corroborated the important role of synapsins for SV clustering, it cannot provide any insights into the dynamics and by extend the exact molecular mechanism of SV clustering. *In vitro* investigations of the synapsin condensate clearly show the recruitment of SV-like liposomes into the liquid phase, however if SVs are clustered by synapsins *in vivo* remains unclear. Therefore, this work now aims to use a combinatorial approach of super-resolution techniques (3.4) to scrutinize the dynamics of synapsin 1 and SVs in living neurons to address whether SV / synapsin condensate formation through LLPS is sufficient to explain SV clustering at synaptic boutons (4).

3.4 Super-resolution microscopy as a tool to study biological compartmentalization

3.4.1 Microscopy beyond the diffraction limit

In the pursuit of understanding biology, microscopy has been one of the most prolific tools, as it enables the direct observation of processes in living systems. Therefore, advances in microscopy have always been accompanied by new biological insights. Advances in microscopy are often related to an improvement in both spatial and temporal resolution. While the resolution of optical microscopes has steadily improved in the centuries since their inception, one fundamental barrier remained insurmountable: the diffraction limit.

Due to diffraction, when photons leave the aperture of the microscope, they do not propagate in a straight line. Instead, photons spread in a radial pattern. Therefore, the minimal focal point size is limited and leads to a point-like light source appearing spread out in the image (point-spread function, PSF). The PSF defines the physical resolution limit of conventional optical microscopes, the so-called diffraction limit, which Ernst Abbe famously formulized in 1873[159]:

$$d = \frac{\lambda}{2\,NA} \qquad \text{Equation 1}$$

Equation 1 states that any point-like light source with the wavelength λ traveling through an objective of an optical microscope will have a minimum resolvable distance d that is inversely proportional to twice the numerical aperture NA. The numerical aperture is a measure of an objective's ability to "gather" light, specifically, it characterizes the range of incendiary angles the objective can collect light at. Numerical apertures of modern objectives are ~1.4. Therefore, a single green fluorescent protein (GFP) with an emission wavelength of ~500 nm can only be resolved to a spot with a diameter of ~250 nm. The size of a GFP molecule is around 3-4 nm.[160] This means that the diffraction-limited spot that the molecule can be imaged as, is almost two orders of magnitude larger than the actual dimensions of the protein. This poses obvious challenges to understanding the dynamics of proteins at the single molecule level. To investigate the nature of the compartmentalization of the PM or the cytosol, it is necessary to observe the constituent molecules at a resolution that is approaching the dimensions of those molecules.

Importantly, Equation 1 only holds under specific conditions. One of these conditions is that the excitation light uniformly illuminates the sample.[161] So using structured illumination light, opens up the possibility to achieve a resolution beyond the diffraction limit. Gustafsson *et al.* first implemented structured illumination microscopy (SIM) in 2000 and achieved a resolution of ~130 nm, almost half the diffraction limit of 250 nm.[162] While SIM remains useful because of its accessibility and acquisition speed, it has been surpassed by other techniques in terms of spatial resolution.[77,161] Beginning in the 1990s, Hell *et al.* developed an approach that would enable spatial resolutions far beyond the diffraction limit. They implemented a second donut-shaped depletion laser, selectively switching off fluorophores near the periphery of the excitation volume of the illumination laser (stimulated emission depletion microscopy (STED) microscopy), achieving a spatial resolution of ~30 nm.[163]

Importantly, SIM and STED are ensemble measurements. This means that the emission of many millions of fluorophores is observed at the same time. To be able to observe the interactions of proteins directly, it is necessary to detect proteins individually. A significant step towards this goal was taken by Moerner *et al.* by measuring the optical absorption spectrum of a single pentacene molecule, albeit at cryonic temperatures.[164] This discovery led to the development of a whole single molecule imaging field, culminating in the development of many single molecule localization microscopy (SMLM) techniques. All SMLM techniques aim to selectively “activate” a limited number of fluorophores, that can be individually localized with high resolution. SMLM techniques include photoactivated localization microscopy (PALM) using photo-switchable proteins developed by Betzig *et al.*,[165] STORM exploiting dark state photochemistry of organic dyes developed by Rust *et al.*[77] and DNA points accumulation for imaging in nanoscale topography (DNA-PAINT) employing transient binding of fluorophore-tagged short DNA fragments developed by Jungmann *et al.*[166] SMLM achieves spatial resolutions even beyond STED microscopy in biological samples of as high as 20 nm.[167]

Recently, Balzarotti, Eilers, Gwosch *et al.* developed a technique combining the detection of single fluorophores reminiscent of SMLM with the donut-shaped illumination of STED microscopy. Here, a low intensity excitation laser (not the depletion laser as in STED microscopy) is shaped into a “donut” in the focal plane of the objective lens. The excitation beam is then deflected and modulated in such a way, that the center of the donut is placed at the location of an emitting fluorophore. Every photon emitted by the fluorophore essentially guides the center of the donut closer to the location of the fluorophore. Detected photons are then counted at the specific position of the donut, enabling up to 1 nm spatial resolution. Because this technique only requires minimal photon emissions of the fluorophore i.e., minimal photon flux (MINFLUX) it was termed MINFLUX microscopy.[168]

SMLM techniques can be applied in live cells to study cellular dynamics in great detail. A technique called single particle tracking (SPT) developed by Geerts *et al.* in 1987 (originally termed nanovid microscopy)[169] follows the motion of a biological molecule of interest by tagging it with an easily resolvable fluorescence or light-scattering tag. From the movement of the observed tag, important information about the molecule of interest's type of motion and interactions with other molecules can be inferred.[170,171] Due to the low intensity of the excitation laser, MINFLUX is also compatible with imaging in live cells. Recently, MINFLUX has been applied in live cells, tracking the motion of kinesin molecules at unprecedented resolution both spatially and temporally (1.7 nanometer per millisecond), opening exciting new avenues for the study of cellular dynamics.[172]

To summarize, optical microscopy has always been at the forefront of biological discovery, but for a long time was held back by a physical resolution barrier: the diffraction limit. In recent years, this limit has been surpassed by ingenious new microscopy techniques. Some of the techniques are applied in this thesis to study the compartmentalization of the PM and the cytosol. These techniques (dSTORM, PALM (3.4.2), STED microscopy (3.4.3) and SPT (3.4.4)) will be discussed in detail in the following chapters.

3.4.2 Single molecule localization microscopy

All SMLM techniques aim at temporarily isolating individual fluorophores. This idea was first conceived by Eric Betzig.[173] They later implemented their idea using photoconvertible fluorescent proteins. One of the used proteins was Eos-FP, which converts from green fluorescence to red by cleavage of the Nα-C-bond in His-62 inside the chromophore backbone (His-62, Tyr-63 and Gly-64).[174,175] The rate of conversion is enhanced by irradiation with ultraviolet (UV) light, since His-62 is transiently protonated via photoexcitation.[175] Consequently, by changing the laser power of the UV-laser, the fluorophore density in red can be fine-tuned to isolate individual conversion events.

At the same time as Betzig developed PALM, a similar approach using a pair of organic dyes was developed by Rust *et al.*[77] Here, the cyanine dye Cy5 is switched into a stable dark state (so-called because it cannot emit photons) by high-intensity red laser irradiation. Exposure to low-intensity green light then converts a small subset of Cy5 molecules back to the fluorescent state. Importantly, the recovery from the dark state critically depends on the proximity of a second dye (Cy3). Excitation of Cy3 by a green laser leads to radiation-less energy transfer to Cy5, leading to the recovery of the fluorescent state of Cy5. While STORM in its first iteration was an important breakthrough, since it enabled SMLM using organic dyes, it had several drawbacks for its practical application in biological samples. These include the requirement of a dye-pair and the cycling between green and red irradiation of the samples. Later, Heilemann *et al.* developed an iteration of STORM, which only requires a single conventional organic fluorophore (direct STORM, dSTORM).[167]

In dSTORM, the dark state of the fluorophore is stabilized by a thiol-containing reducing buffer. Many commonly used dyes (Alexa Flour and Atto dyes) are rhodamines and oxazines, which are reduced by electron donors. The reduction reaction can be induced by irradiation with light. Employing a weaker electron donor such as R-mercaptoethylamine (MEA) ensures that the reduction of the first excited singlet state of the fluorophore is negligible. But importantly, when applying a high laser power in the excitation range of the dye, a significant number of dyes enter a triplet dark state by interaction with molecular (triplet) oxygen. Effectively the singlet excited dye and triplet molecular oxygen exchange spin states, in a process called intersystem crossing. Crucially, the triplet dark state of the dye can be efficiently reduced by forming a corresponding dye radical anion, with a lifetime of several hundred milliseconds to seconds. For some dyes (thiazine and oxazine dyes, e.g. Atto 655) the dye radical anion can be further reduced to form a reduced leuco dye. Both reduced forms of the dye are returned to the ground state via oxidation by molecular oxygen. Oxidation of the reduced dye and return to the excitable singlet ground state can be facilitated by irradiation with UV light (Figure 10a).[176]

By stabilizing the dark state of the dye, a sufficiently low emitter density is achieved. The remaining fluorescent dyes can be localized with high accuracy. Hundreds of thousands of localizations are collected in this way during the acquisition of thousands of camera frames. The resulting localization can then be reconstructed to generate a super-resolving image of the sample (Figure 10b).[176]

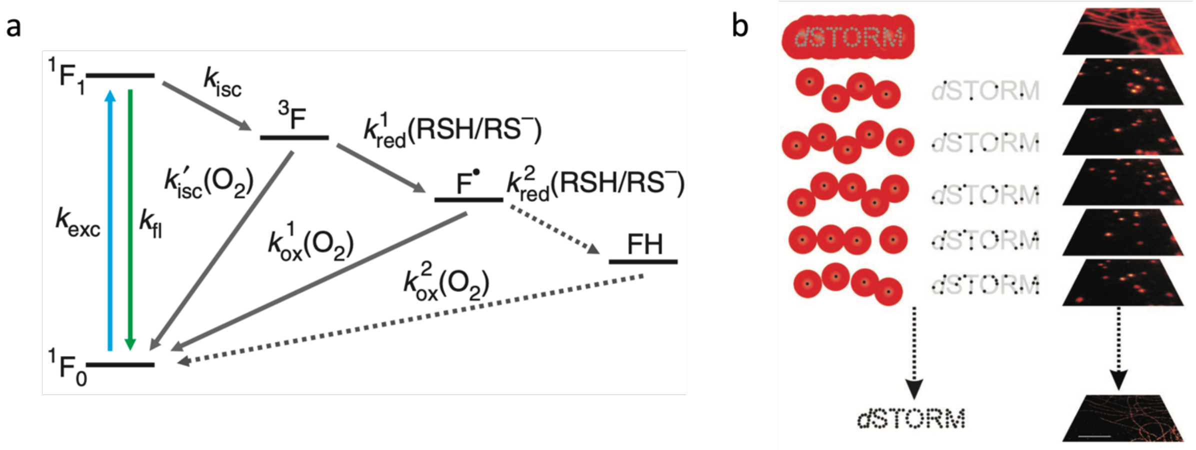

Figure 10 dSTORM enables SMLM with a single conventional fluorophore.

(a) A fluorophore (F) is excited by irradiation with light in its excitation range (F_0 → F_1, where k_{exc} is the rate of excitement). k_{exc} depends on the intensity of the exciting laser, so a high laser power leads to a higher rate. The excited state (F_1) of the dye returns to its ground state (F_0) by emitting a photon (fluorescence, F_1 → F_0, where k_{fl} is the rate of fluorescence). The singlet exited state $^1F_1$ can be converted into a non-fluorescent triplet dark state ^3F (intersystem crossing, where k_{isc} is the rate of intersystem crossing). ^3F can be reduced by a thiolate (RSH/RS$^-$) and thereby converted into a more stable dye radical F• or leuco dye FH (where k_{red} is the rate of reduction). $^1F_0$ can be recovered by the reaction of F• or FH with molecular oxygen (where k_{ox} is the rate of oxidation). Irradiation with UV light promotes recovery of $^1F_0$. **(b)** Stabilizing the dark state of the dye leads to a sufficiently low emitter density. Consequently, dyes can be localized with high accuracy. Localizations can then be reconstructed to generate a super-resolving image of the sample.

From van de Linde, S. *et al.* Direct stochastic optical reconstruction microscopy with standard fluorescent probes. *Nature Protocols* **6**, 991-1009 (2011). Reproduced with permission from Springer Nature conveyed through Copyright Clearance Center.

To summarize, SMLM aims at temporarily isolating single fluorophores. This can be achieved by controlling the conversion rate of photo-switchable proteins (PALM). Alternatively, in dSTORM the excitation of organic dyes effectively pumps them into a triplet dark state, that is reduced and stabilized by thiolates. Excitation of the reduced dyes with UV light facilitates the recovery of the ground state. While SMLM techniques achieve very high resolutions (around 20 nm)[167], the long acquisition times make it difficult to apply these techniques in a live-cell setting, where cells are constantly moving.

In contrast to SMLM, STED microscopy can be applied more easily *in vivo.* STED microscopy achieves the recording of a sub-diffraction sized area by employing a laser scanning confocal fluorescence microscope, equipped with a depletion laser. Since only a single image is recorded, acquisition speeds are much faster than for SMLM.[161] STED microscopy will be discussed in detail the following chapter.

3.4.3 Stimulation emission depletion microscopy

In optical microscopy, the size of the illumination PSF is a major limiting factor in determining the resolution of the final image. If it would be possible to limit the area of the illumination PSF, dyes could be isolated spatially in a sub-diffraction area, thereby greatly increasing resolution. One such technique, which achieves the reduction of the size of the illumination PSF, is STED microscopy.[163] In STED microscopy, fluorophores near the periphery of the excitation volume are selectively switched off. This is facilitated by a process called stimulated emission first described by Albert Einstein in 1916.[177] During spontaneous emission a fluorophore in its first excited state falls back to its ground state by emitting a photon (fluorescence, Figure 10a). This process occurs spontaneously and at a constant rate. However, when the excited molecule is irradiated again with a photon that is part of its emission spectrum, it relaxes to the ground state by the emission of two identical photons (stimulated emission). Importantly, the probability that a stimulated photon is emitted scales exponentially with the intensity of the stimulating beam. Therefore, by using a sufficiently intense stimulation laser, spontaneous emission can be efficiently depleted.[178] Furthermore, STED requires the PSF of the depletion laser to have an intensity profile with a central minimum. This is achieved by destructive interference at the center of the depletion beam, generating a typically donut-shaped intensity region.[179] Although, other depletion patterns have been used as well.[180] The central depletion minimum generates a sub-diffraction limited area. Therefore, by overlaying a Gaussian-shaped excitation beam with a donut-shaped depletion laser, fluorescence in a sub-diffraction-sized area can be recorded.[181] Importantly, the depletion pulse is delayed relative to the excitation pulse (typically by hundreds of picoseconds) to avoid higher-state excitations (Figure 11).[182]

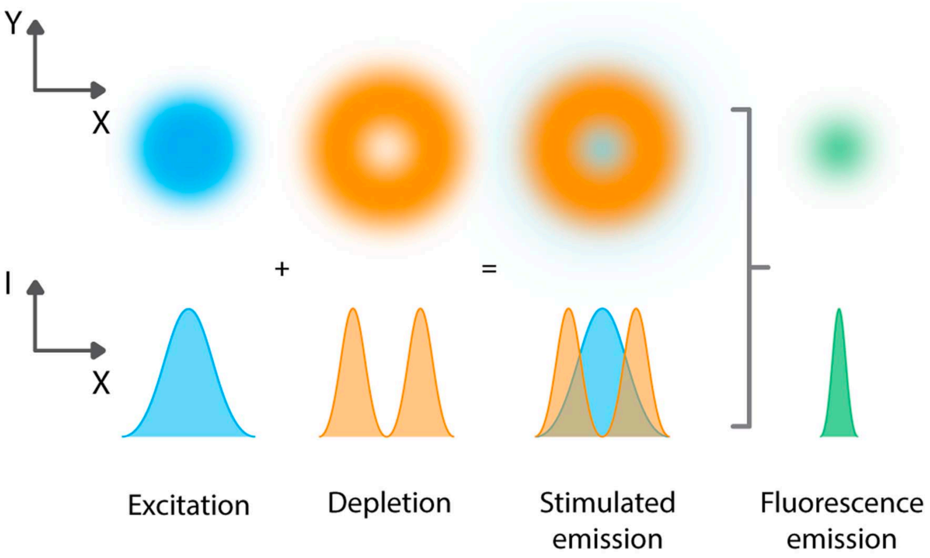

Figure 11 The principle of STED microscopy.

The confocal Gaussian-shaped excitation beam is overlayed with a donut-shaped (central region of zero intensity) depletion beam. After the stimulated emission of dyes in the donut region, the fluorescence of dyes in the sub-diffraction-sized center of the donut is recorded. The depletion pulse is delayed relative to the excitation pulse by hundreds of picoseconds to avoid higher-state excitations.

From Vangindertael, J. *et al.* An introduction to optical super-resolution microscopy for the adventurous biologist. *Methods and Applications in Fluorescence* **6** (2018). Adapted and reprinted with permission under CC BY 3.0 DEED. creativecommons.org/licenses/by/3.0/

A typical STED setup is a laser-scanning confocal with an additional depletion laser. This allows the fast (seconds) scanning of the sample by the sub-diffraction-sized excitation PSF, thereby creating a super-resolved image of the sample.[179] Due to its imaging speed and no special buffer condition requirements, STED microscopy has been used extensively *in vivo* in cell systems[34,49,183] but also in animals.[184,185]

In summary, STED microscopy aims at spatially separating fluorophores. This is achieved by generating a sub-diffraction area of excitation, in which fluorescence is recorded. To that end, an excitation beam is overlayed with a depletion laser, containing a central minimum. By scanning the sample with the resulting illumination pattern, a super-resolution image is then recorded. While STED microscopy is much faster in its image acquisition speed than many SMLM techniques (like PALM, dSTORM)[163,165,167] it still lacks the temporal resolution that is required to observe the dynamics of cellular processes in the cytosol and the PM directly. These processes often take place in the millisecond range and below.[27,29,171] A technique that achieves such temporal resolution is SPT and will therefore be discussed in the next chapter.

3.4.4 Single particle /-molecule tracking

The goal of SPT is the direct observation of the motion of a biological molecule of interest (MOI). Hence, the MOI must be attached to a sufficiently resolvable reporter molecule (label). Crucially, the density of the label must be so sparse, that the position of individual labels can be determined with high precision by fitting of the PSF of the label. Localizations stemming from the same molecule over time are then algorithmically connected to generate trajectories. From the trajectories, important information concerning the molecular dynamics of the MOI can be extracted by analysis with appropriate statistical methods (Figure 12).[170]

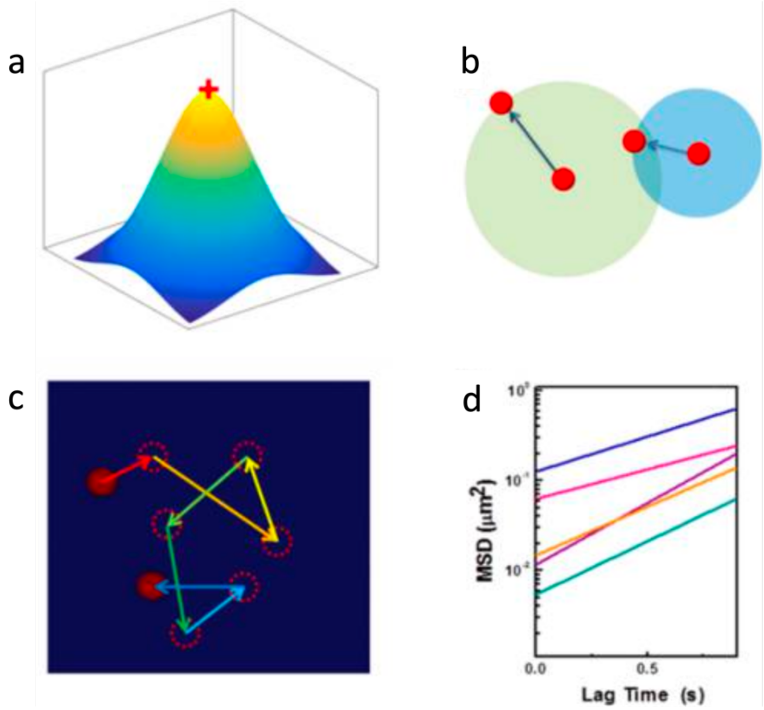

Figure 12 A typical SPT experiment.

(a) Localizations are generated by fitting the PSF of a label attached to a MOI. **(b)** Localizations stemming from the same molecule are connected algorithmically **(c)** Trajectories are generated from the connected localization that describe the path of a single molecule over time. **(d)** Statistical analysis of the trajectories reveals important dynamic information about the MOI.

From Shen, H. et al. Single Particle Tracking: From Theory to Biophysical Applications. Chemical Reviews 117, 7331-7376 (2017). Adapted with permission from American Chemical Society conveyed through Copyright Clearance Center.

Importantly, the properties of the employed label are crucial to the success of SPT experiments. The ideal label must achieve the following things: i. be small enough not to significantly interfere with the dynamics of the MOI ii. be chemically inert and non-toxic iii. be clearly identifiable by some optical microscopy technique and iv) be efficiently deliverable to the MOI. No label performs equally well on all dimensions, so tradeoffs between different label qualities must be considered, which highly depend on the specific MOI. Some labels and their advantages and drawbacks will be discussed in the following.

The earliest labels used for SPT were colloidal gold particles coated with antibody fragments or lectins to target MOIs in the outer leaflet of the PM.[24,169,186] Here, the colloidal gold particles were localized using their phase contrast, which can render it challenging to distinguish the label from cellular background.[169] Furthermore, to achieve a sufficiently high contrast, gold particles have to be large (~40 nm in diameter)[169] in comparison to the MOIs (compare with the diameter of a SV ~45 nm[124] or a single GFP ~5 nm[160]), this poses challenges to the delivery of gold particles to intracellular targets. Additionally, due to their large size, gold particles might affect the dynamics of the MOI.

Fluorescent molecules offer an alternative labelling approach that can alleviate problems related to label size. Modern organic fluorophores are very small (< 1 nm), offer high brightness, high quantum yield and relatively high photostability.[187,188] Since in contrast to gold or other nanoparticles, only a single fluorophore is used, this method is also referred to as single molecule tracking (SMT).[189] It is important to consider how the fluorescent label interacts with the cellular environment. For example, many water-soluble dyes bind to lipid-bilayers due to their hydrophobicity. Therefore, the right fluorophore has to be chosen carefully to reduce unspecific background binding.[190]

Additionally, the fluorophore must be targeted to the MOI in some way. This is commonly achieved by labeling of antibodies against MOIs with organic dyes. Importantly, antibodies are relatively big (10 nm) so this again introduces complications related to the influence on the motion of the MOI and delivery into cells.[191] Recently, small nanobodies (single domain antibodies from camelids) have been used to track the motion of extracellular proteins,[192] that have a similar affinity to their target while alleviating some of the problems related to antibody size.[191] Additionally, some proteins that bind intracellular MOIs have been labeled with fluorescent dyes and delivered into cells.[193] Furthermore, fluorophores can be delivered to the MOI by the use of self-labeling peptides in conjunction with membrane-permeable dyes. For example the Halo-Tag is a haloalkane dehalogenase which interacts with a chloroalkane linker (Halo-ligand) by covalently attaching the Halo-ligand to itself.[194] Importantly, self-labelling peptides require genetic modification of the MOI that might affect its function. Additionally, photoactivable proteins employed in PALM, can also be used for SPT. This method is sometimes referred to as sptPALM.[195] Here, sparse labelling of the MOI is achieved by photoconversion of a small subset of fluorophores. While this provides the advantage of fine-tuning the labeling density precisely, it requires genetic tagging of the MOI. Furthermore, fluorescent proteins are generally less bright und less photostable than organic dyes.[188,196]

Brightness and photostability are important considerations for the efficient detection of fluorophores, as they determine how many photons can be captured per fluorophore, thus influencing localization precision. Recently, quantum dot nanoparticles (QDs) have been developed that are very bright and very photostable.[197-199] QDs consist of a metallic semiconducting core with a surrounding shell (e.g. ZnS), which improves optical properties and solubility of the QDs. Additionally, the shell can be modified by biomolecules to further improve cytocompatibility or to target a MOI via antibodies or nanobodies.[30,200] In semiconductors, the valence band and the conductance band of electronic states are separated by a band gap. If an electron in the valence band is excited, it can enter the conductance band. If the electron falls subsequently back to band gap, energy is released by emitting a photon.[201] QD fluorescence is based on their core size (2-10 nm in diameter)[200] by exploiting the quantum confinement effect. The effect occurs when the size of a nanostructure is comparable to the wavelength of the electron. As a consequence, the fluorescence emission spectrum of QDs is quantized and brightness and wavelength are highly size dependent.[197] QDs are comparable in size to gold nanoparticles,[169,202] this renders it non-trivial to deliver them into cells (though they have been used to track intracellular targets)[203-210]. Nevertheless, their exceptionally high quantum yield and their high photostability makes QDs excellent tools for SPT of extracellular targets.[30,198,211-214]

How can dynamic information of the MOI be extracted from SPT data? One important metric is the mean square displacement (MSD), which is a measure of the area that a MOI explores per unit of time. First, consider the displacement of a particle (a measure of the distance that a particle traveled between two time points):

$$d(t_1, t_2) = r(t_1) - r(t_2) \qquad \text{Equation 2}$$

Where d is the displacement, t_1 and t_2 are consecutive time points and r particle positions at t_1 and t_2. Importantly, d as described in Equation 2 can be both negative and positive. For considerations of the dynamics of a particle the direction of motion is often irrelevant. Therefore, it can be useful to consider the squared displacement instead:

$$sd(t_1, t_2) = (r(t_1) - r(t_2))^2 \qquad \text{Equation 3}$$

Where sd is the squared displacement. In SPT, the acquisition speed of the experiment is determined by the exposure time of the camera, which “quantizes” time into discrete intervals (lags). Here, t_1 and t_2 are assumed to be consecutive camera frames (frame 1 and frame 2) and therefore are separated by the smallest possible time interval (lag 1) observable for this experiment. To study the dynamics of the MOI it is often useful to consider all time intervals of the same length (in this case all consecutive frames i.e. frame 1 and 2, frame 2 and 3, frame 3 and 4 etc.) To that end, the mean of all squared displacement for the same lag (which is the MSD) is calculated. The MSD for lag 1 can be calculated as follows:

$$msd(\Delta t_1) = \frac{\sum_{i=1}^{N-1}(r(t_i) - r(t_{i+1}))^2}{N-1} \qquad \text{Equation 4}$$

Where msd is the mean squared displacement of lag 1 (Δt_1), N is the total number of time points and i is the frame index. Equation 4 can be generalized to lags of any frame interval:

$$msd(\Delta t_n) = \frac{\sum_{i=1}^{N-n}((r(t_i) - r(t_{i+n}))^2}{N-n} \qquad \text{Equation 5}$$

Where Δt_n is the lag of a frame interval n. Now, the MSD can be used to calculate the diffusion coefficient, which is a measure of the speed of the MOI. In contrast to the cytosol, the PM is a quasi two-dimensional system, since membrane molecules are embedded in the bilayer and can only move along the cell surface. Therefore, in many SPT applications of membrane molecules only two-dimensional motion is considered.[170] However, due to their tubular shape, neuronal processes are an inherently three dimensional system. Hence, in this work calculations of diffusive parameters were performed considering three spatial dimensions for tracking molecules in the cytosol and the PM of neuronal cells. According to the Einstein relationship[215] for a MOI moving in three spatial dimensions the diffusion coefficient can be calculated as follows:

$$msd_{xyz}(\Delta t) = 6D\Delta t \qquad \text{Equation 6}$$

Where msd_{xyz} is the three-dimensional MSD, D is the diffusion coefficient and Δt the lag. Equation 6 holds true for a MOI that is performing a random walk (Brownian motion[216]). Here, the MSD increases linearly with time. As discussed above many proteins do not perform simple Brownian motion (3.2.2). Indeed, many membrane proteins are found to show long term-confined diffusion.[6] Here, the motion of the MOI is restricted by a surrounding barrier. Therefore, the MSD does not change linearly with time, since the MOI can only explore a smaller area as compared to an unrestricted molecule. To describe confined motion, an additional exponent must be introduced to Equation 6:

$$msd_{xyz}(\Delta t) = 6D\Delta t^{\alpha} \qquad \text{Equation 7}$$

Where α is the exponent of confinement. For Brownian motion α is equal or close to 1. For confined diffusion α is smaller than one. In contrast, for active vesicular transport processes α is bigger than 1.[217] This type of motion is also called directed motion (Figure 13a). Both the diffusion coefficient and the exponent of confinement can be calculated by determining the MSD from experimentally determined particle positions. This is often done by linear fit of the logarithmized version of Equation 7:

$$\log\left(msd_{xyz}(\Delta t)\right) = \log(6D\Delta t^{\alpha}) \qquad \text{Equation 8}$$

$$\log\left(msd_{xyz}(\Delta t)\right) = \alpha\log(\Delta t) + \log(6D) \qquad \text{Equation 9}$$

Here, α is the slope of a linear function and the term $\log(6D)$ the y-axis intercept. Importantly, small lags include more data points. This is because a small lag can “fit” more times into a given trajectory than a greater lag. Therefore, the error of the MSD increases with greater lags. In practice this means, that often α and D are determined for the initial lags only ($\Delta t < 4$, Figure 13b).[218]

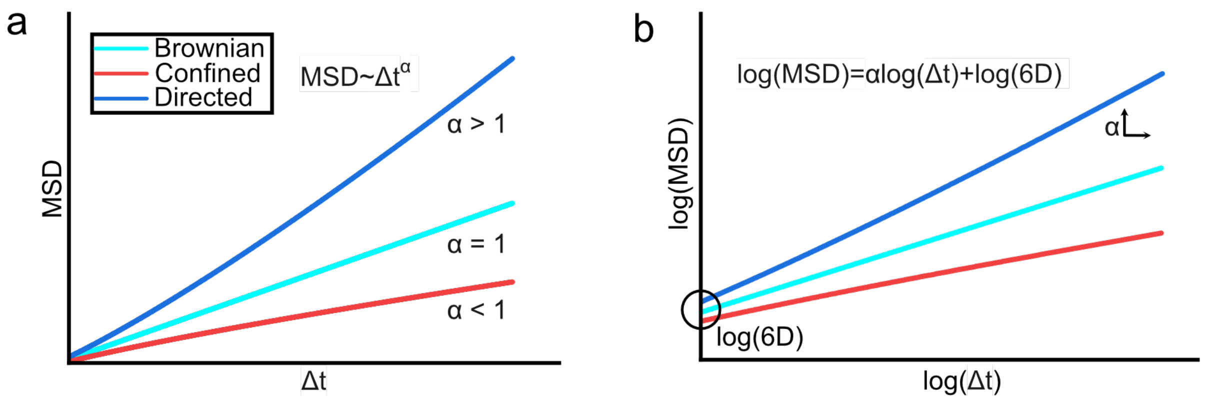

Figure 13 Retrieving the diffusion coefficient and the exponent of confinement from experimentally determined particle positions.

(a) Shown are typical MSD-lag-plots of particles undergoing Brownian (cyan), confined (red) and directed (blue) motion. The MSD is directly proportional to the lag (Δt) to the power of the exponent of confinement (α). For Brownian motion $\alpha=1$, resulting in a straight line. For confined motion $\alpha<1$, resulting a downward facing curve. For directed motion $\alpha>1$, resulting in an upward facing parabola. **(b)** Logarithmic linearization of plot shown in (a). The diffusion coefficient (D) can be calculated from the y-axis intercept and α from the slope of the resulting lines.

To summarize, SPT aims at the direct observation of the motion of a biological molecule by following the motion of an attached optic label. From the motion of the particle important dynamic information can be deduced like the diffusion coefficient and exponent of confinement. Optimal SPT labels should be stable and not interfere with the target. Of exceptional use due to their small size are membrane-permeable fluorescent dyes in combination with self-labeling peptides like the Halo-tag. These are used in this work to track the motion of intracellular targets in both the cytosol and the PM. Additionally, bright and photostable QDs are excellent tools for extracellular targets and are used in this thesis for such targets in the PM. To what end these labels and SPT and super-resolution microscopy in general are employed in the work, will be discussed in the next section.

4. Scientific aims

Compartmentalization is an important organizational principal in biology, as it enables the generation of functionally specialized reaction hubs (3.1).[1] Neurons are highly polarized cells that serve a wide array of functions. Neurons therefore make heavy use of compartmentalization principles in both the cytosol (3.3) and the PM (3.2), though the molecular constituents and the dynamics of these compartments have been underexplored. Therefore, two such compartmentalized systems are investigated in this work: i. the PM of neuronal cells and the underlying cytoskeletal actin rings and ii. SV clusters inside synaptic boutons of neuronal axons (Figure 14).

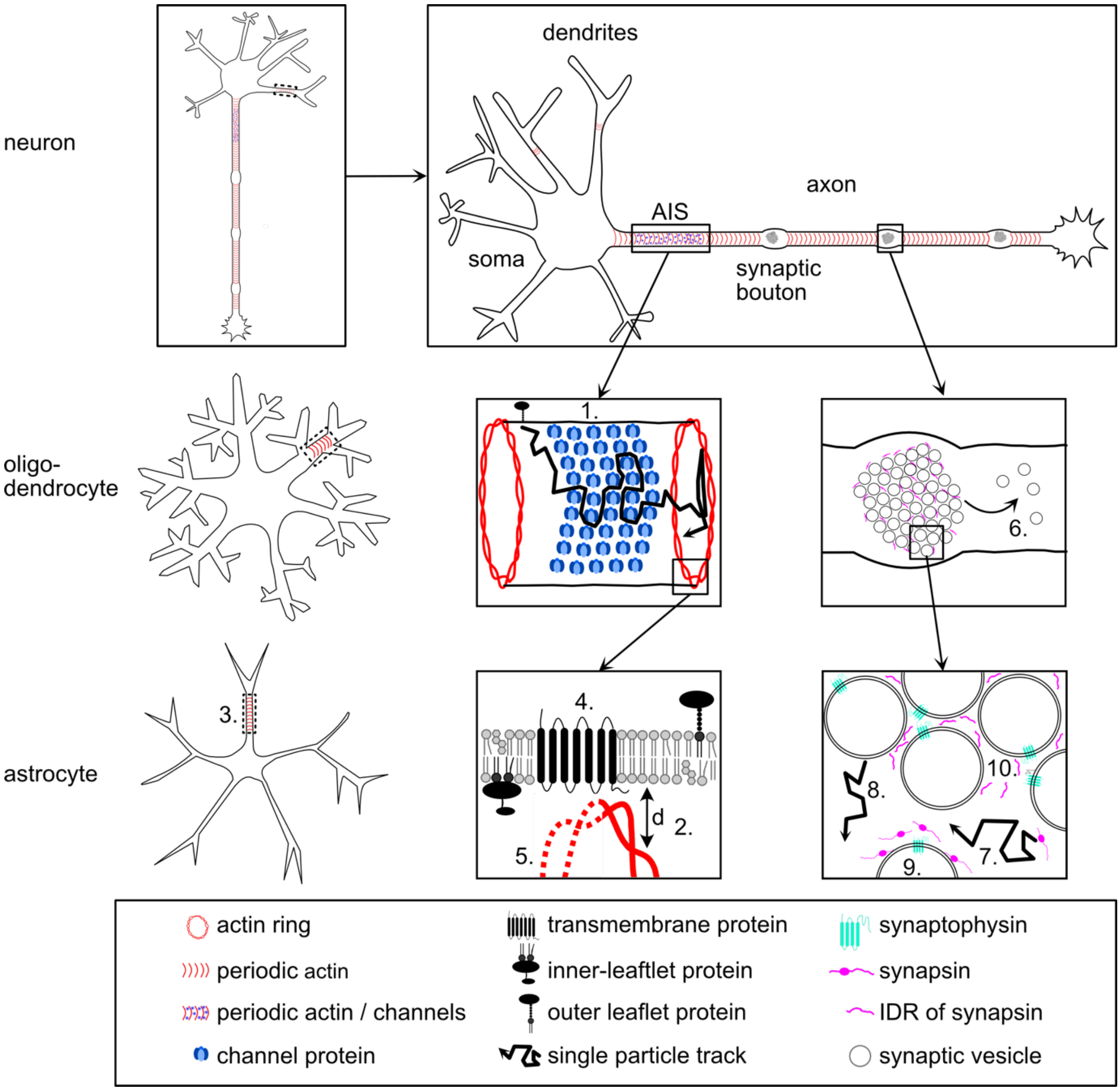

Figure 14 Uncovering the molecular basis of membrane and cytosolic compartmentalization in neuronal cells.

4. Scientific aims

The cytoskeleton of neurons is unique in that is consists of ~200 nm spaced actin rings. These rings are prominent in the AIS. Here, the rings are also interspersed with large voltage-gated channel proteins. In the AIS, compartmentalization of membrane proteins has been observed, which confines molecules between actin rings. The molecular cause of the compartments remains unclear. Therefore, this works aims to address: 1. Are large voltage-gated channels or actin rings the cause of the membrane compartmentalization in the AIS. If actin rings are the cause of the membrane compartmentalization, it follows they must be near the PM. Therefore, this work investigates: 2. What is the distance between actin rings and PM? Furthermore, periodic actin rings are also present in other cells of the neuronal lineage (astrocytes, oligodendrocytes). Importantly, these cells lack voltage-gated channel protein densities. Therefore, these cells are excellent model systems to study the influence of actin on membrane compartmentalization: 3. Are membrane compartments between actin rings present in other cells of the neuronal lineage (see dashed boxes)? And if so: 4. Can compartments also be detected for inner-leaflet and transmembrane proteins? And: 5. Are actin rings required for membrane compartmentalization? Synaptic boutons in the axon of neurons are the location of SV release. SVs form dense clusters inside the pre-synapse that are essential for pre-synaptic function. SV clusters are controlled by the soluble phosphoprotein synapsin. The mechanism of how clustering is achieved however, remains elusive. *In vitro* experiments suggest that synapsin controls SV clustering by forming a distinct liquid phase that recruits SVs, but it remains unclear if this is true *in vivo*. Therefore, this work asks: 6. Is SV / synapsin condensate formation sufficient to explain the concentration of SV clusters at synaptic boutons? Crucially, studies on the nature of SV condensates have so far been performed in fixed cells or as assembly measurements. Therefore, this works aims at addressing: What is the mobility of 7. synapsin and 8. SVs (synaptophysin) inside *in vivo* condensates? Furthermore, since synapsin is the master regulator of SV cluster formation: 9. Does synapsin control the dynamics of SVs inside *in vivo* liquid condensates? Further, this thesis aims at addressing 10. Is SV / synapsin condensate formation through LLPS (conferred by the IDR of synapsin 1) sufficient to explain wildtype SV mobility at synaptic boutons?

Towards i.: The cytoskeleton of neuronal cells consist of ~200 nm spaced actin rings, interspersed by spectrin tetramers.[42] The actin rings are prominent in the AIS of neurons, but are also present in other neural compartments and cells of the neuronal lineage.[50,52] Specifically in the AIS, actin rings are also interspersed with large voltage-gated channel proteins. Here, membrane compartmentalization of proteins has been observed between actin rings, although the molecular cause of the compartments remains unclear (3.2.4).[30] Therefore, this works aims to address: 1. Are large voltage-gated channels or actin rings the cause of the membrane compartmentalization in the AIS of neurons. To answer this question a combinatorial approach of SPT of membrane molecules in the AIS of neurons *in silico* and *in vivo* is employed. SPT is the tool of choice, as it provides the sufficient temporal and spatial resolution to observe membrane compartmentalization (3.4.4.).[30,42] *In vivo* SPT experiments are performed using QDs in rat hippocampal neurons, the system in which membrane compartmentalization in the AIS was first discovered.[30] QDs are an exceptionally useful tool for extracellular targets, because of their high brightness and photostability.[214] *In silico* SPT experiments are performed using FluoSim, a software that enables simulation of molecules diffusing over defined geometries,[219] thereby, allowing for the mathematical exploration of the channel versus the actin ring model.

If actin rings are the cause of the membrane compartmentalization, it follows that the rings must be near the PM. Therefore, this work investigates: 2. What is the distance between actin rings and PM? To this end, STED microscopy[163] of actin in neuronal cells is employed. STED is used here, as it can be implemented in a straightforward manner in a live-cell setting (3.4.3).

Importantly, other cells of the neuronal lineage (astrocytes, oligodendrocytes) lack voltage-gated channel protein densities, while sharing the same cytoskeletal organization with neurons.[52] Therefore, these cells are excellent model systems to study the influence of actin rings on membrane compartmentalization. If membrane compartmentalization can be observed here, this would provide evidence for actin rings being the cause of the membrane compartmentalization. Therefore, this work addresses: 3. Are membrane compartments between actin rings present in other cells of the neuronal lineage? Peltier *et. al* recently published a pipeline to generate many cell types of the neuronal lineage from adult rat hippocampal progenitor cells.[220] This work makes use of these cells for SPT of outer-leaflet membrane proteins using QDs.

Furthermore, if membrane compartments can be detected for outer-leaflet membrane proteins in cells of the neuronal lineage, it follows that transmembrane proteins and inner-leaflet membrane proteins should also experience this barrier. This is especially likely, since transmembrane and inner-leaflet probes should be in direct contact with the actin rings on the cytosolic side. Consequently, this thesis investigates: 4. Can membrane compartments also be detected for inner-leaflet and transmembrane proteins? Accordingly, SPT is performed in progenitor-derived neuronal cells, via QDs for transmembrane proteins and using Halo-tagged[194] inner-leaflet proteins. Membrane-permeable dyes are used to label the Halo-tag, since due to their small size, they are easy to deliver to intracellular targets and will not interfere with the dynamics of the target significantly.[202]

Furthermore, this work investigates: 5. Are actin rings required for membrane compartmentalization? Consequently, correlative dSTORM[176] (3.4.2) of actin rings and SPT of outer-leaflet membrane probes is employed to elucidate the nanoscopic location of the membrane compartments in relation to the actin rings. Additionally, correlative analysis of SPT of membrane proteins before and after treatment with the actin disrupting drug Swin A[56] is performed.

Towards ii.: Synaptic boutons in the axon of neurons are the location of SV release. SVs form dense clusters that are essential for pre-synaptic function[221] (3.3.2). SV clustering is controlled by the soluble phosphoprotein synapsin. The mechanism of how clustering is achieved however, remains elusive. *In vitro* experiments suggest that synapsin controls SV clustering by forming a distinct liquid phase that recruits SVs (3.3.4),[3] but it remains unclear if this is true *in vivo*. This work now addresses this lack of mechanistic understanding by asking: 6. Is SV / synapsin condensate formation sufficient to explain the concentration of SV clusters at synaptic boutons? This question is addressed by comparing the nanoscopic organization of synapsin 1 and of the SV marker synaptophysin (3.3.3) in live hippocampal neurons in different genetic background (3.4.2). Genetic backgrounds include wild type (WT) and synapsin triple knockout (KO) neurons and synapsin triple knockout neurons expressing full length synapsin 1 (full length rescue) and neurons expressing only the IDR of synapsin 1 (differential rescue, the IDR is known to be necessary and sufficient to induce LLPS[3]). Towards this goal, PALM (3.4.2) of synapsin 1 and synaptophysin 1 is performed in live axons of mouse hippocampal neurons. Synapsin 1 is visualized by genetic labelling with the Halo-tag in combination with membrane permeable organic dyes, while synaptophysin 1 is genetically tagged with the photo-switchable protein mEos.[196]

Crucially, studies on the nature of SV condensates have so far been performed *in vitro* or in assembly measurements,[3,91,145] leaving many questions about the dynamics of *in vivo* synapsin condensates unanswered. Therefore, this works seeks to expand the understanding of *in vivo* liquid condensates by asking: What is the mobility of 7. synapsin and 8. SVs inside *in vivo* condensates? To this end, dual-color SMT of Halo-synapsin 1 and of synaptophysin 1-mEos is performed in mouse hippocampal neurons.

Synapsin has been shown to be the master regulator of SV cluster formation, as KO of synapsins leads to loss of SV clustering and to a reduction of the overall number of SVs (3.3.4).[3,144] However, it remains unclear how and if synapsin influences the dynamics of SVs directly. Consequently, this work investigates: 9. Does synapsin control the dynamics of SVs inside *in vivo* liquid condensates? To this end, SPT of SVs (synaptophysin 1-mEos) is performed in mouse hippocampal neurons in different genetic backgrounds of synapsin 1 (WT, KO, full length rescue) to compare the diffusive behavior of SVs in the presence and absence of synapsin 1. Furthermore, this works investigates 10. Is SV / synapsin condensate formation through LLPS sufficient to explain wildtype SV mobility at synaptic boutons? This question is addressed by comparing the mobility of SVs in the full length recue system with the mobility of SVs in the differential rescue system (where only the IDR of synapsin 1 expressed).

In summary, this work employs a combination of different super-resolution microscopy techniques (STED, dSTORM, SPT) to investigate compartmentalized systems in both the PM and the cytosol of neuronal cells. Two overarching questions are addressed in this work: i. Do actin rings compartmentalize the plasma membrane in cells of the neuronal lineage and ii. Is condensate formation through LLPS by synapsins sufficient to explain SV clustering inside synaptic boutons?

5. Publications

5.1 Sub-membrane actin rings compartmentalize the plasma membrane

Journal: Journal of Cell Biology

DOI: 10.1083/jcb.202310138

Authors: Jakob Rentsch, Selle Bandstra, Batuhan Sezen, Philipp Sigrist, Francesca Bottanelli, Bettina Schmerl, Sarah Shoichet, Frank Noé, Mohsen Sadeghi and Helge Ewers

Author contributions: Jakob Rentsch performed all SPT experiments in rat hippocampal neurons and CV-1 cells, in silico SPT experiments, STED experiments, correlative SPT / immunostainings and correlative SPT / dSTORM experiments. Batuhan Sezen and Jakob Rentsch cloned constructs and performed SPT experiments in progenitor-derived neuronal cells. Batuhan Sezen peformed AnkG immunostainings in rat hippocampal neurons. Philipp Sigrist and Jakob Rentsch performed correlative SPT experiments under actin disruption. Selle Bandstra, Mohsen Sadeghi and Frank Noé developed the Stripefinder analysis tool. Jakob Rentsch developed all other analysis tools. All analyses related to the Stripefinder were perfomed by Selle Bandstra. All other data was analyzed by Jakob Rentsch. Francesca Bottanelli provided training, equipment and reagents related to STED microscopy. Bettina Schmerl, Sarah Shoichet provided neuronal cell material. Jakob Rentsch prepared all figures. Helge Ewers and Jakob Rentsch wrote the paper. Helge Ewers designed research. All authors read and approved the final manuscript.

JCB Journal of Cell Biology

ARTICLE

Sub-membrane actin rings compartmentalize the plasma membrane

Jakob Rentsch[1], Selle Bandstra[2], Batuhan Sezen[1], Philipp Sigrist[1], Francesca Bottanelli[1], Bettina Schmerl[3], Sarah Shoichet[4], Frank Noé[2], Mohsen Sadeghi[2], and Helge Ewers[1]

The compartmentalization of the plasma membrane (PM) is a fundamental feature of cells. The diffusivity of membrane proteins is significantly lower in biological than in artificial membranes. This is likely due to actin filaments, but assays to prove a direct dependence remain elusive. We recently showed that periodic actin rings in the neuronal axon initial segment (AIS) confine membrane protein motion between them. Still, the local enrichment of ion channels offers an alternative explanation. Here we show, using computational modeling, that in contrast to actin rings, ion channels in the AIS cannot mediate confinement. Furthermore, we show, employing a combinatorial approach of single particle tracking and super-resolution microscopy, that actin rings are close to the PM and that they confine membrane proteins in several neuronal cell types. Finally, we show that actin disruption leads to loss of compartmentalization. Taken together, we here develop a system for the investigation of membrane compartmentalization and show that actin rings compartmentalize the PM.

Introduction

The plasma membrane (PM) is, according to the Singer-Nicolson fluid mosaic model (Singer and Nicolson, 1972), a continuous membrane bilayer in which membrane proteins are suspended. Saffman and Delbrück (Saffman and Delbrück, 1975) offered a quantitative model to describe the two-dimensional free diffusion of membrane proteins in fluid membranes, which depends on the viscosity of the membrane and the surrounding solvent as well as the geometry of the protein and the membrane, and very well describes the motion of transmembrane proteins in artificial bilayers (Weiß et al., 2013). However, in cellular membranes, proteins mostly do not seem to undergo unhindered lateral diffusion. Rather, they exhibit diffusion coefficients about an order of magnitude lower than measured in artificial membranes (Kusumi et al., 2005). Based on such observations, it has been proposed that membrane proteins are confined to membrane subdomains formed by the cytoskeleton (Kusumi et al., 2005). Here, transmembrane proteins may be corralled by a mesh of submembrane actin filaments that act as physical obstacles to the motion of their intracellular portion and form small domains according to the "fence" model of membrane partitioning (Kusumi et al., 2005). On the other hand, lipids and lipid-anchored proteins, which are also found to exhibit subdiffusive motion, cannot be confined in this way. However, their confinement may be explained by an array of transmembrane proteins anchored along the actin filaments in the meshwork that by occupying a fraction of membrane space act as obstacles and are sufficient to confine molecules to compartments in the "picket" model (Kusumi et al., 2005).

However, due to the dynamic nature of the submembrane actin meshwork, no tractable model for the mechanistic investigation of the "fence" or picket model is available. This problem may be overcome after the discovery of a periodic network of actin rings spaced every 200 nm along neuronal axons (Xu et al., 2012). In contrast to cortical actin, which is highly dynamic (Gowrishankar et al., 2012), these rings are stable in their location (Albrecht et al., 2016) and exist for longer periods of time even in the presence of some actin-depolymerizing drugs (Leterrier et al., 2015). Indeed, we could previously show that the diffusion coefficient of a lipid-anchored molecule is abruptly reduced over the time course of establishment of these actin rings in the axon initial segment (AIS) of developing neurons (Albrecht et al., 2016). Strikingly, in areas of reduced diffusion coefficient, correlative high-density single particle tracking (SPT) of membrane proteins and super-resolution microscopy of actin revealed that membrane protein motion was confined between actin rings in the AIS (Albrecht et al., 2016). However,

---

[1]Institute for Chemistry and Biochemistry, Freie Universität Berlin, Berlin, Germany; [2]Department of Mathematics and Computer Science, Freie Universität Berlin, Berlin, Germany; [3]Picower Institute for Learning and Memory, Massachusetts Institute of Technology, Cambridge, MA, USA; [4]Charité—Universitätsmedizin Berlin, Berlin, Germany.

Correspondence to Helge Ewers: helge.ewers@fu-berlin.de.

Rockefeller University Press
J. Cell Biol. 2024 Vol. 223 No. 4 e202310138

https://doi.org/10.1083/jcb.202310138

JCB Journal of Cell Biology

ARTICLE

Sub-membrane actin rings compartmentalize the plasma membrane

Jakob Rentsch[1], Selle Bandstra[2], Batuhan Sezen[1], Philipp Sigrist[1], Francesca Bottanelli[1], Bettina Schmerl[3], Sarah Shoichet[4], Frank Noé[2], Mohsen Sadeghi[2], and Helge Ewers[1]

The compartmentalization of the plasma membrane (PM) is a fundamental feature of cells. The diffusivity of membrane proteins is significantly lower in biological than in artificial membranes. This is likely due to actin filaments, but assays to prove a direct dependence remain elusive. We recently showed that periodic actin rings in the neuronal axon initial segment (AIS) confine membrane protein motion between them. Still, the local enrichment of ion channels offers an alternative explanation. Here we show, using computational modeling, that in contrast to actin rings, ion channels in the AIS cannot mediate confinement. Furthermore, we show, employing a combinatorial approach of single particle tracking and super-resolution microscopy, that actin rings are close to the PM and that they confine membrane proteins in several neuronal cell types. Finally, we show that actin disruption leads to loss of compartmentalization. Taken together, we here develop a system for the investigation of membrane compartmentalization and show that actin rings compartmentalize the PM.

Introduction

The plasma membrane (PM) is, according to the Singer-Nicolson fluid mosaic model (Singer and Nicolson, 1972), a continuous membrane bilayer in which membrane proteins are suspended. Saffman and Delbrück (Saffman and Delbrück, 1975) offered a quantitative model to describe the two-dimensional free diffusion of membrane proteins in fluid membranes, which depends on the viscosity of the membrane and the surrounding solvent as well as the geometry of the protein and the membrane, and very well describes the motion of transmembrane proteins in artificial bilayers (Weiß et al., 2013). However, in cellular membranes, proteins mostly do not seem to undergo unhindered lateral diffusion. Rather, they exhibit diffusion coefficients about an order of magnitude lower than measured in artificial membranes (Kusumi et al., 2005). Based on such observations, it has been proposed that membrane proteins are confined to membrane subdomains formed by the cytoskeleton (Kusumi et al., 2005). Here, transmembrane proteins may be corralled by a mesh of submembrane actin filaments that act as physical obstacles to the motion of their intracellular portion and form small domains according to the "fence" model of membrane partitioning (Kusumi et al., 2005). On the other hand, lipids and lipid-anchored proteins, which are also found to exhibit subdiffusive motion, cannot be confined in this way. However, their confinement may be explained by an array of transmembrane proteins anchored along the actin filaments in the meshwork that by occupying a fraction of membrane space act as obstacles and are sufficient to confine molecules to compartments in the "picket" model (Kusumi et al., 2005).

However, due to the dynamic nature of the submembrane actin meshwork, no tractable model for the mechanistic investigation of the "fence" or picket model is available. This problem may be overcome after the discovery of a periodic network of actin rings spaced every 200 nm along neuronal axons (Xu et al., 2012). In contrast to cortical actin, which is highly dynamic (Gowrishankar et al., 2012), these rings are stable in their location (Albrecht et al., 2016) and exist for longer periods of time even in the presence of some actin-depolymerizing drugs (Leterrier et al., 2015). Indeed, we could previously show that the diffusion coefficient of a lipid-anchored molecule is abruptly reduced over the time course of establishment of these actin rings in the axon initial segment (AIS) of developing neurons (Albrecht et al., 2016). Strikingly, in areas of reduced diffusion coefficient, correlative high-density single particle tracking (SPT) of membrane proteins and super-resolution microscopy of actin revealed that membrane protein motion was confined between actin rings in the AIS (Albrecht et al., 2016). However,

[1]Institute for Chemistry and Biochemistry, Freie Universität Berlin, Berlin, Germany; [2]Department of Mathematics and Computer Science, Freie Universität Berlin, Berlin, Germany; [3]Picower Institute for Learning and Memory, Massachusetts Institute of Technology, Cambridge, MA, USA; [4]Charité—Universitätsmedizin Berlin, Berlin, Germany.

Correspondence to Helge Ewers: helge.ewers@fu-berlin.de.

Rockefeller University Press
J. Cell Biol. 2024 Vol. 223 No. 4 e202310138

Check for updates

https://doi.org/10.1083/jcb.202310138

since the AIS is the site of a strong developmental accumulation of ion channels between the actin rings (Brachet et al., 2010; Garrido et al., 2003; Zhang et al., 1998; Hedstrom et al., 2008; Gasser et al., 2012), it remains uncertain whether the membrane compartmentalization is due to the actin rings or the high local density of transmembrane ion channels (Huang and Rasband, 2016; Leterrier, 2018).

Importantly, since then, actin rings have been reported over a large variety of cell types across the neuronal lineage (Hauser et al., 2018; He et al., 2016; D'Este et al., 2015, 2016; Zhong et al., 2014). They may thus present a tractable experimental system for the investigation of membrane compartmentalization by the cytoskeleton. The answer to this open question is fundamental to our understanding of membrane compartmentalization in neurons and PMs in general.

Here, we ask if the submembrane actin rings alone can partition the PM using computational modeling and high-density, high-speed SPT in a variety of cell types. We find that wherever in the neuronal lineage we observe periodic actin rings, these compartmentalize the motion of membrane proteins. Stimulated emission depletion (STED) microscopy in live cells shows that actin rings are closely apposed to the PM. Using molecular inhibitors, we find that acute actin disruption in live cells abolishes membrane compartmentalization. Taken together, our results establish actin rings as causative to membrane compartmentalization in a variety of cell types, suggesting a global mechanism for the regulation of membrane protein motion in cells.

Results

We first aimed to answer whether the observed membrane partitioning in the AIS was due to actin rings or the local density of ion channels. To do so, we performed 3D high-speed, high-density SPT of GPI-GFP (glycophosphatidylinositol green fluorescent protein) in day in vitro 7 (DIV7) rat hippocampal neurons using anti-GFP nanobody (NB) conjugated quantum dots (QDs). When we plotted all individual detection events, they clearly exhibited a periodic 200-nm spaced pattern, resembling stripes perpendicular to the direction of propagation of the axon (Fig. 1, b–e), similar to what we previously observed (Albrecht et al., 2016). These stripes line the perimeter of the axon and appear especially striking when observed in a 3D rendering of the GPI-GFP localizations (Video 1). We hypothesize that the observed pattern can be explained by either of two possible mechanisms: (i) the periodic actin rings could cause membrane compartmentalization, and (ii) the enrichment of large ion channels at the AIS may trap and accumulate membrane proteins between actin rings (Fig. 1 f).

We investigated three models for the location of the diffusion barrier: actin rings (Fig. 1 g), a sparse (Fig. 1 h), and a dense accumulation of channel proteins (Fig. 1 i).

To address which of these models best explains our experimental observations, we performed simulations of single-particle motion using the simulation software Fluosim (Lagardère et al., 2020). We used this software to generate synthetic time-series of images of single molecule peaks using parameters as found in cell experiments. We then added noise and motion blur to the level measured in real experiments and used single-molecule localization microscopy software to analyze the resulting image stacks. We found that the synthetic data strongly resembled real measurements (Videos 2 and 3), giving us confidence that this system would allow us to ask specific questions concerning compartmentalization of membrane molecule motion by obstacles. We went on to investigate three simulated scenarios mimicking the developmental time course of axon initial segment establishment (Fig. 1 a), where first actin rings appear, and subsequently ion channels become highly enriched over the following days. We thus first created a model geometry consisting of 20 nm thick lines that created 200 nm sized compartments between them to represent the actin rings (Xu et al., 2012). When we generated artificial SPT movies of molecules diffusing over the model geometry, we found compartmentalization between the actin rings as repetitive peaks in an autocorrelation function beginning at a 70% probability for molecules to cross the actin rings (Fig. S1). This is consistent with previous work, suggesting that membranes can be compartmentalized even by incomplete "palisades" of transmembrane proteins anchored to submembrane actin filaments (Fujiwara et al., 2002). Furthermore, we simulated single-molecule localization microscopy (SMLM) reconstructions of the actin rings and correlated the resulting pattern with the reconstructions of the simulated SPT data from the same simulation (Fig. 1 g). In this first simulation, we observed a clear pattern of SPT localizations, spaced between adjacent actin staining like we found in our experimental data before (Compare Fig. 1, b–e and g; and Albrecht et al., 2016). Secondly, we generated model geometries consisting of a randomly spaced accumulation of circular exclusions zones with a diameter of 15 nm located between the periodic actin rings, the exclusion zones here mimicking large ion channels anchored at spectrin/ankyrin between actin rings in the AIS. These exclusion zones reject molecules in 100% of encounters, but in this case, actin was 100% permeable. To simulate the increasing enrichment in the AIS over time (Jones et al., 2014), we performed simulations with 10 and 100 ion channels confined in this manner. When we then performed simulated SPT experiments of membrane molecules and SMLM experiments of actin as described above for these conditions, we could not detect an accumulation of membrane protein localizations between actin rings (Fig. 1, h and i). Strikingly in the scenario with 100 ion channels, molecules rather became accumulated on simulated actin staining (Fig. 1 i). Taken together, our simulations show that even very dense arrays of transmembrane proteins will not trap transmembrane proteins, but rather exclude them. Our simulations indeed support a model where the PM is compartmentalized by submembrane actin rings.

We next aimed to determine whether the actin rings were indeed located in close proximity to the PM (Fig. 2 d). To do so, we performed line-scans across the equator of processes in live progenitor-derived neuronal cells labeled with SiR-actin and GPI-GFP (Fig. 2, a–c). We imaged SiR-actin in STED and GPI-GFP in confocal microscopy. When we quantified the distance between the peaks representing the GPI-GFP in the bilayer and the

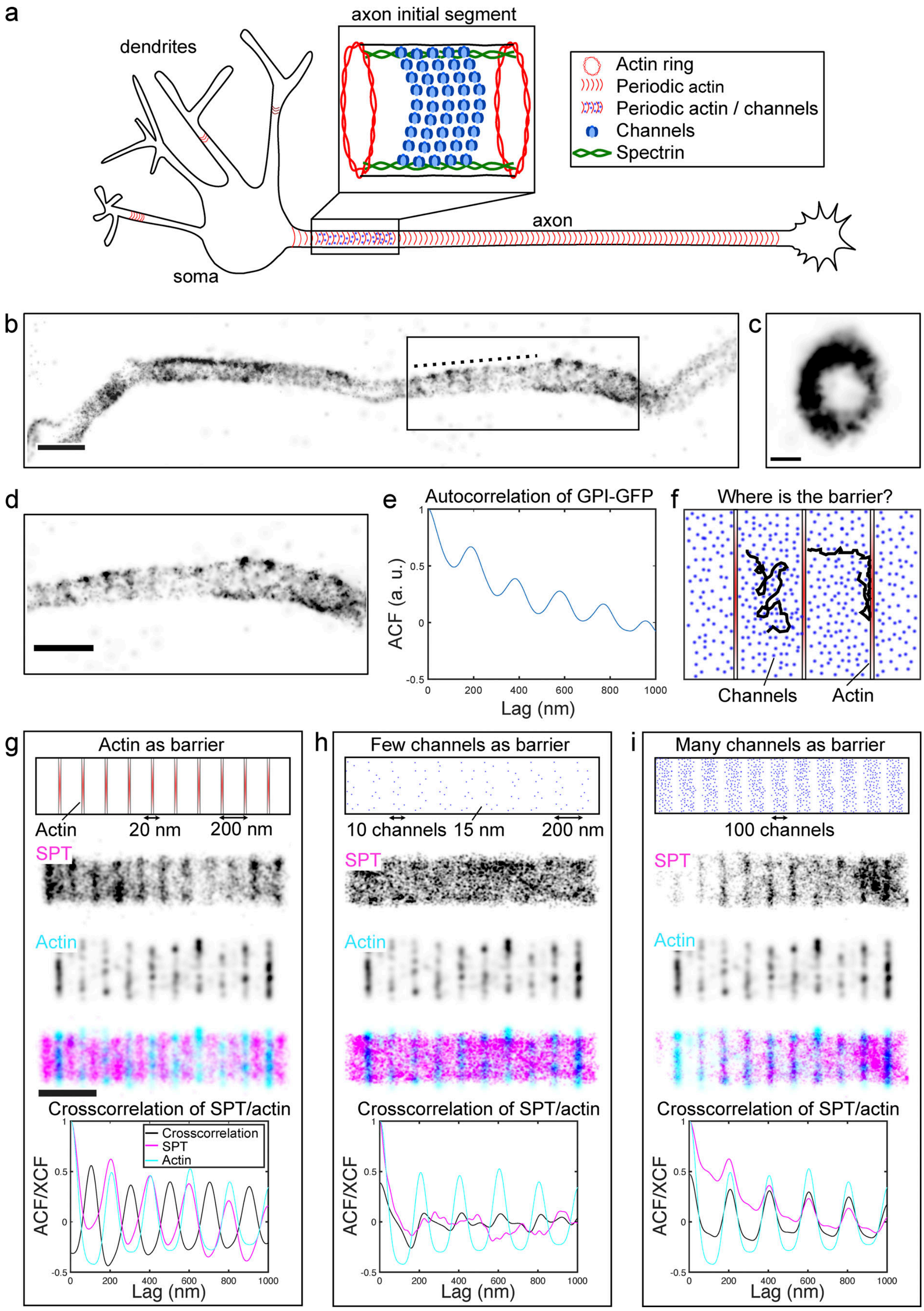

Figure 1. **Simulations of SPT experiments reveal that actin rings act as a diffusion barrier. (a)** Schematic representation of the cytoskeleton in neurons: the axon initial segment contains periodically organized actin rings (~200 nm), which are interspersed by accumulations of channel proteins. **(b)** GPI-GFP forms

membrane domains in DIV7 rat hippocampal neurons. Reconstruction of localizations of SPT experiment of GPI-GFP tagged with QDs (5,000 frames, 200 Hz). **(c)** Projection along the dotted line in (b). Scale bar is 100 nm. **(d)** Zoom in of box shown in (b). **(e)** Autocorrelation along the neuronal process shown in (c) reveals periodicity of GPI-GFP domains at ∼200 nm. **(f)** Schematic representation of the two competing hypotheses: Actin acts as a diffusion barrier or channel proteins act as a diffusion barrier. **(g)** Simulations of SPT experiments in Fluosim. Top: Model geometry mimicking the organization of actin rings. Middle top: Reconstruction of localizations of in silico SPT experiments over the geometry. Middle: In silico STORM reconstruction of actin rings. Middle bottom: Merge of SPT reconstruction and STORM of actin. Bottom: Crosscorrelation function (XCF) and individual autocorrelation functions (ACF) of SPT of GPI-GFP and STORM of actin reveals that GPI-GFP forms domains located between actin rings. **(h)** Same as (g) but with few channel proteins as a model geometry: No periodic pattern of GPI-GFP can be observed. **(i)** Same as (g) but with many channel proteins as model geometry: Periodic patterns of GPI-GFP can be observed but are localized on top of actin rings (in contrast to experimental data). If not otherwise indicated, scale bars are 500 nm.

actin rings (SiR-actin) in many cells, we found that they were on average separated by around 30 nm. At the same time, when we measured the distance between membrane stainings by GPI-GFP and cholesterol-Abberior Star Red, we found a distance of around 13 nm. The localizations of multicolor fluorescent beads measured in the same assay yielded an accuracy of ∼2 nm (Fig. 2 e). This suggests that the actin rings are indeed very close to the PM, possibly close enough to anchor transmembrane proteins as pickets that act as obstacles to lateral membrane molecule motion.

Next, we aimed to ask, whether an AIS is required for membrane compartmentalization. To do so, we used adult hippocampal neuronal progenitor cells (AHNPCs). They can be induced to differentiate into different types of cells of the neuronal lineage that all exhibit periodic actin rings (Hauser et al., 2018). Indeed, when we differentiated AHNPCs as described (Peltier et al., 2010), neuronal cells did not show an AnkG accumulation characteristic for an intact axon initial segment after DIV7 or DIV14 (Fig. S2). Since AnkG is required to target voltage-gated channels to the AIS (Garrido et al., 2003; Leterrier et al., 2017; Gasser et al., 2012) positioned by spectrin C-termini between the actin rings (Xu et al., 2012), we conclude here that neuronal cells derived from AHNPCs do not contain voltage-gated ion channel proteins in the characteristic dense organization present in the AIS. If membrane protein motion is compartmentalized between the periodic actin rings in these cells, it can thus not be controlled by an ion channel density. When we tracked GPI-GFP diffusion via QDs in these cells (Fig. 3 a), we still found that they formed repetitive ∼200 nm size domains. (Fig. 3, b and c) Strikingly, the observed membrane domains seemed to be stable over time as the same areas were visited multiple times during the observation period (Fig. 3 e). GPI-GFP in membrane domains remained mobile ($D = 0.04\ \mu m^2\ s^{-1}$) and exhibited only slightly subdiffusive motion ($\alpha = 0.9$, Fig. S3).

Next, we investigated whether the membrane compartmentalization we detected for the peripheral outer leaflet membrane protein GPI-GFP could also be observed for the inner leaflet lipid-anchored Src family kinase Src-Halo (Boggon and Eck, 2004; Zhou et al., 2019) or the multispanning transmembrane cannabinoid receptor CB1 (Howlett et al., 2002; Zhou et al., 2019) coupled to YFP (Fig. 4 a). Indeed, after high-speed, high-density SPT, we could observe membrane compartmentalization for both molecules in the characteristic 200 nm spacing (Fig. 4, b and c), showing that also inner leaflet and multispanning proteins are sensitive to the barriers located at the actin rings.

Submembrane actin rings spaced by spectrin tetramers have been described in a variety of cell types, including progenitor-derived astrocytes and oligodendrocytes (Hauser et al., 2018). If our hypothesis was correct, these cells should thus also compartmentalize the motion of membrane proteins between actin rings. We thus differentiated progenitor cells into neuronal cells, astrocytes, and oligodendrocytes (Fig. 4 d) and performed SPT experiments of GPI-GFP in all three cell types that were a priori identified via their morphology. After SPT experiments, cells were fixed and stained with markers of their respective lineage to confirm their cellular identity (βIII-tubulin for neurons, glial fibrillary acidic protein [GFAP] for astrocytes, myelin basic protein [MBP] for oligodendrocytes). When we analyzed SPT localizations using autocorrelation analysis, we detected compartmentalization of GPI-GFP motion with a period of ∼200 nm for all cell types investigated here (Fig. 4, e–g). We concluded that membrane compartments are bounded by actin rings in many cell types.

We went on to perform correlated high-speed, high-density SPT of GPI-GFP and subsequent direct stochastical optical reconstruction microscopy (dSTORM) super-resolution imaging of actin in the same region of cells. When we overlayed the SPT and SMLM data from such experiments, we found that GPI-GFP molecules explored areas free from actin (Fig. 5 and Video 4).

Finally, we decided to test, whether the actin rings, the location of membrane compartment boundaries, were indeed causing the membrane compartmentalization. To do so, we performed high-speed, high-density SPT experiments in live progenitor-derived neuronal cells before and after actin disruption by SwinholideA (SWIN A), a small molecule that cleaves actin filaments and inhibits actin polymerization (Spector et al., 1999; Klenchin et al., 2005; Vassilopoulos et al., 2020; Fig. S4). We reasoned that to detect compartmentalization in regions of neurons before treatment, but not after treatment, we would need an automated means of detecting such patterns to avoid bias due to insufficient sampling in our experiments or due to arbitrary choice of region of interest. To do so, we developed a software (Stripefinder) that would detect patterns in our simulated compartmentalized SPT data as in Fig. 1 g, but not in data generated from random walks (Fig. S5 a). With our software, we did not detect such patterns in accumulated high-speed, high-density SPT localizations in CV1 fibroblast cells that lack visible periodic actin structures (Fig. S5 b). Our software could, however, reliably detect regions in which autocorrelation analysis picked up stripes from accumulated high-speed, high-density SPT localizations (Fig. S5 c).

When we analyzed accumulated high-speed, high-density SPT localizations from neuronal cells before and after treatment, we found many areas with periodic compartmentalization

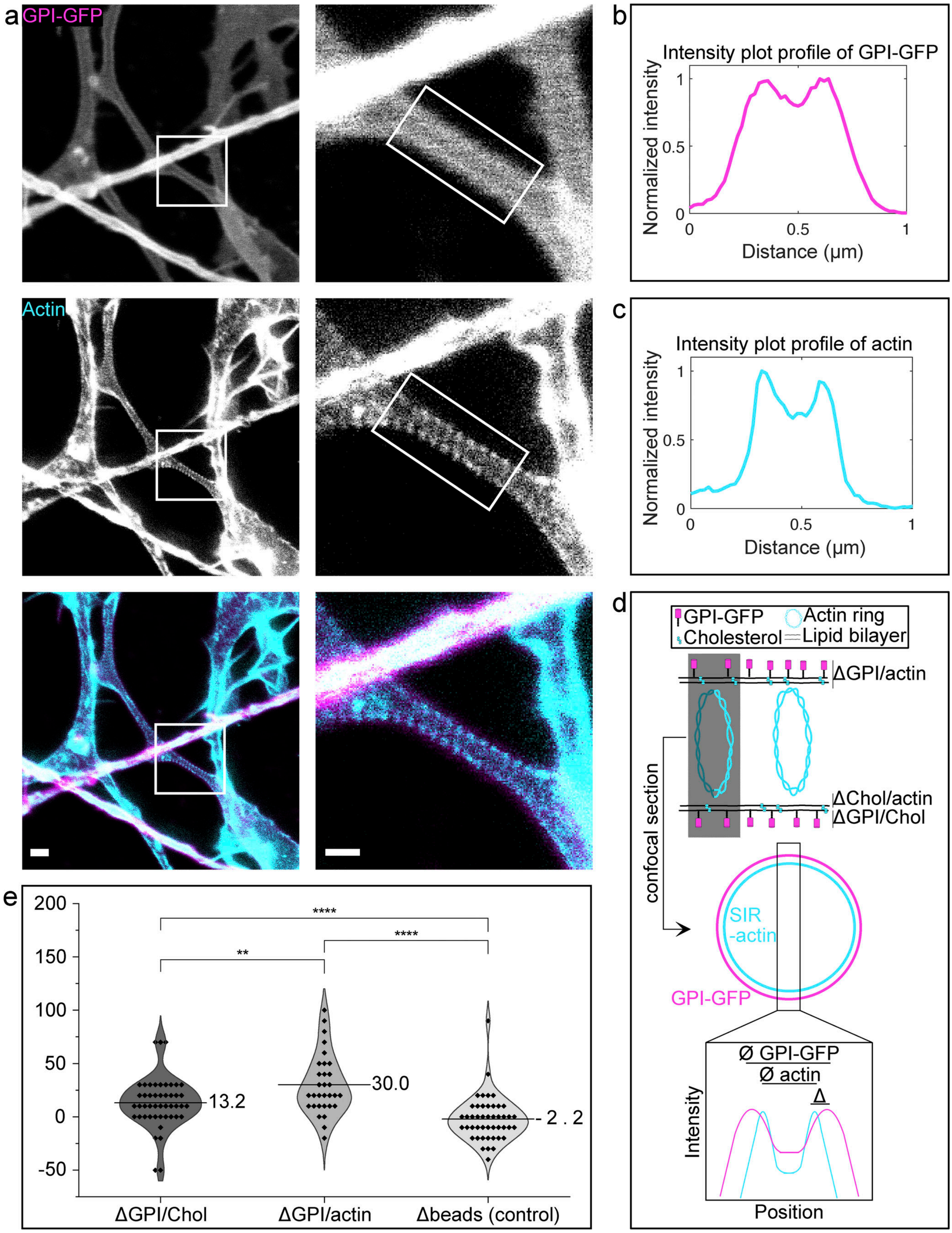

Figure 2. **Actin rings are close to the plasma membrane. (a)** Top: Confocal image of GPI-GFP; middle: live-STED image of actin rings in progenitor-derived neuronal cells; bottom: merge of actin and GPI-GFP. Right images are zoom-ins of box on the left. Scale bars on the left are 1 µm. Scale bars on the right are

500 nm. **(b)** Line profile of box of confocal image of GPI-GFP shown in (a) on the right. **(c)** Line profile of box of live-STED image of actin rings shown in (a) on the right. **(d)** Schematic representation of the calculation of the distance between GPI-GFP and actin rings: The distance of the peaks shown in (b) and (c) is measured. The difference between the distances is used to calculate the distance between actin rings and GPI-GFP. **(e)** Violin plot of the measured distances between GPI-GFP and the PM stained via Cholesterol-Star Red (ΔGPI/Chol, n = 47 regions from eight images), GPI-GFP and actin rings stained via SIR-actin (ΔGPI/actin, n = 31 regions from 12 images), and a bead control (beads, n = 46 regions from seven images). Lines indicate mean. Normality was tested using Shapiro–Wilk Test and rejected (ΔGPI/Chol P = 0.00054***, ΔGPI/actin P = 0.076 ns, Δbeads P = 3.6E-5****). Significance was tested using Mann–Whitney Test (ΔGPI/Chol versus ΔGPI/actin P = 0.0098**, ΔGPI/actin versus beads P = 8.7E-8****, ΔGPI/Chol versus beads P = 2.2E-5****).

of GPI-GFP motion before treatment. We here specifically made sure that only areas that exhibited sufficient sampling density to make detection of rings possible in terms of localizations per area before and after drug addition were included in the analysis. However, in contrast, regions in which we detected stripes did not exhibit them after SWIN A treatment (Fig. 6, a–c). Similarly, we could not detect periodic localizations using autocorrelation analysis after SWIN A treatment when we reanalyzed areas in which stripes were detected before treatment (Fig. 6 d). We concluded that the disruption of actin rings by SWIN A reduces compartmentalization in the PM of progenitor-derived neuronal cells.

Discussion

We here used periodic actin rings in a variety of cell types as an experimental paradigm to test the hypothesis that submembrane actin structures can compartmentalize membrane protein motion. We find that actin rings compartmentalize the motion of transmembrane and peripheral membrane proteins linked to either leaflet of the PM by lipid anchors. This compartmentalization is independent of the presence of large clusters of immobilized membrane proteins between the actin rings such as found in the axon initial segment. We find that the actin rings are located a few nanometers below the PM and that their disruption leads to loss of compartmentalization. Taken together, our results establish actin rings are a tractable experimental paradigm for the investigation of membrane compartmentalization.

We find that these actin rings, which are interconnected by spectrin tetramers in many neuronal cell types, are indeed closely apposed to the PM. Many transmembrane molecules are immobilized in the PM by cytoskeletal association and such submembrane actin rings, when spiked with many transmembrane domains may significantly obstruct the motion of molecules across them (Fujiwara et al., 2002; and Figs. 1 and S1). Such an arrangement is the basis of the transmembrane picket model for membrane compartmentalization (Kusumi et al., 2005). This model was proposed decades ago; however, it has been hard to prove experimentally as cortical actin in live mammalian cells is very dynamic (Gowrishankar et al., 2012; Goswami et al., 2008) and in the presence of a thick actin cortex and stress fibers, membrane-apposed actin filaments are nearly impossible to detect (Clausen et al., 2017; Clark et al., 2013). However, we recently succeeded in pulling transmembrane proteins across the dorsal PM of cultured cells and found them to become stuck at the location of actin filamentous structures (Li et al., 2020). Indeed, it has long been observed that actin disruption influences membrane protein motion in cells (Andrade et al., 2015; Suzuki et al., 2005; Fujiwara et al., 2002) and lipids exhibit higher diffusion coefficients in blebs in which no actin cortex is associated with the PM (Hiramoto-Yamaki et al., 2014).

Our work opens several important questions. We find that lipid-anchored molecules in the inner (Src-Halo) as well as the outer leaflet (GPI-GFP) become confined between actin rings, likewise transmembrane proteins (CB1). Importantly, molecules remain mobile and unconfined inside compartments (Fig. S3). A recent high-speed diffusion mapping study showed that lipophilic dyes exhibit relatively lower motility at ER–PM contact sites. As the dyes did not exhibit a shift in their spectrum, it was concluded that increased lipid order was not responsible for this reduction (Yan et al., 2020). Instead, it was speculated that local protein density may be responsible. Indeed, lateral protein density can influence membrane protein diffusion at very high concentrations of membrane proteins (Hartel et al., 2016); however, this would be expected to be a global effect on the membrane rather than a local effect. Also, our simulations show that densities of immobilized proteins between the action rings as seen in Fig. 1 do not create striped patterns as we observe them. In the periodic structures we observe, however, the lipid environment has not been probed yet, and it remains to be investigated whether the closely apposed actin rings influence lipid packing or motion in the inner or outer PM leaflet. Renner et al. have shown that tracking in 2D and under low acquisition speeds can lead to an underestimation of the observed diffusion coefficients due to the inherently three-dimensional geometry of neurites (Renner et al., 2011). We are, however, confident in the diffusion coefficients reported here since all tracking data have been acquired under high acquisition speeds (5–10 ms) in 3D using a total internal reflection fluorescence (TIRF) microscope equipped with a biplane module.

Taken together, our observations support the transmembrane picket model. What could be the pickets serving as obstacles on actin rings? Recently, CD44 has been put forward to serve as picket to transmembrane diffusion in macrophages (Freeman et al., 2018); however, it is unclear if it is expressed in our cells. Recent mass spectrometric investigation of the periodic actin rings unfortunately did not produce novel actin ring–associated membrane proteins (Zhou et al., 2022). The only transmembrane protein reported to localize to actin rings is the potassium channel KV1.2 (D'Este et al., 2017); however, it localizes to axons in neurons, but not astrocytes or oligodendrocytes. In the future, it will be important to identify transmembrane proteins that may serve as pickets.

What instead confines the molecules at the location of actin rings? Actin disruption via SWIN A led to a reduction in membrane compartmentalization. This reduction was not complete; however, the loss of periodic actin rings was neither underlining

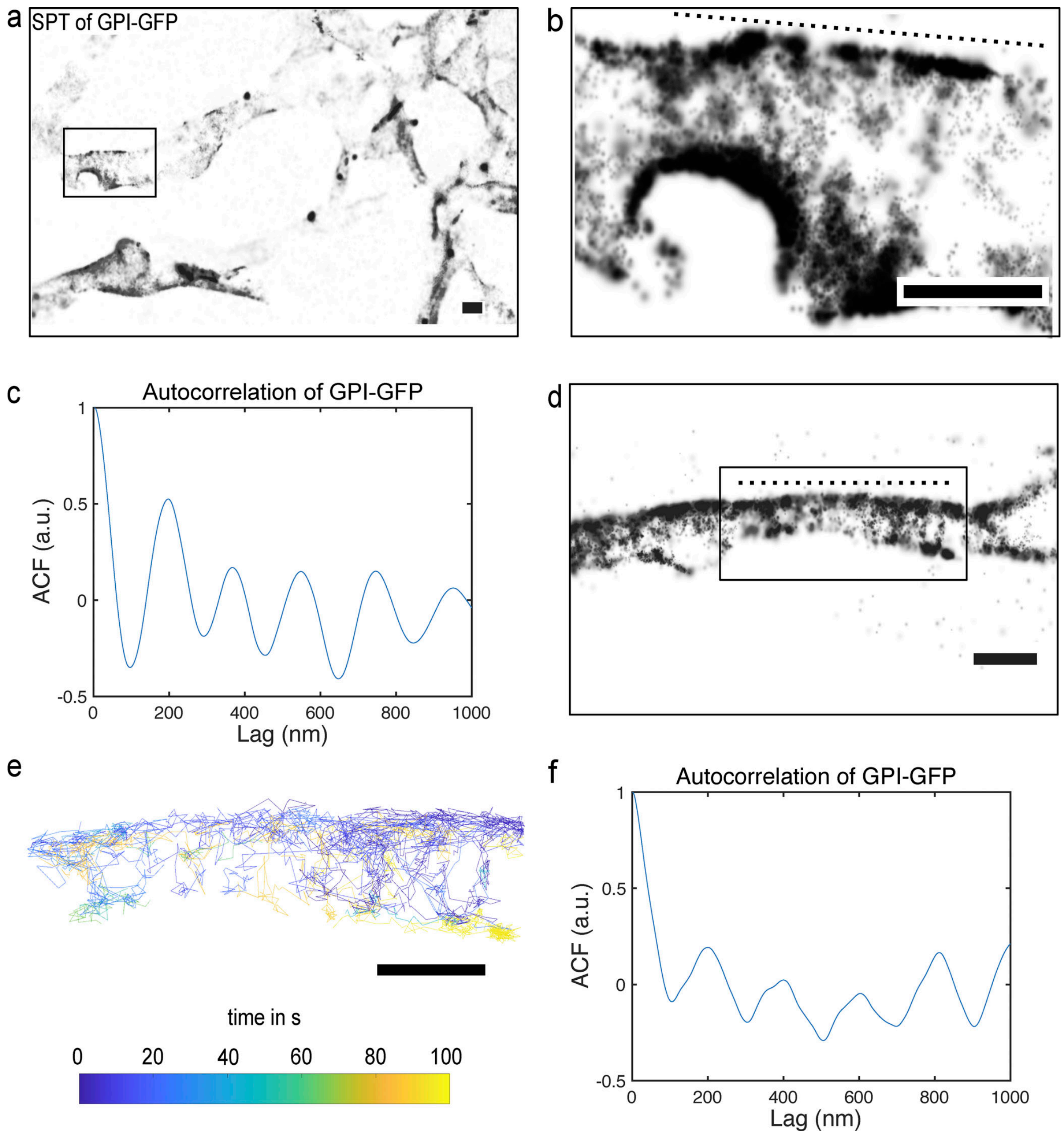

Figure 3. **Membrane domains can be detected in progenitor-derived neuronal cells. (a)** Reconstruction of SPT experiment (20,000 frames, 200 Hz) of GPI-GFP tagged with QDs in progenitor-derived neuronal cells. **(b)** Zoom-in of box shown in (a) showing GPI-GFP forming membrane domains. **(c)** Autocorrelation function (ACF) along the dotted line along the neuronal process shown in (b) reveals periodicity of GPI-GFP domains at ∼200 nm. **(d)** Like (a) but different neuronal cell. **(e)** Single particle tracks color-coded for time of GPI-GFP motion of box shown in (d) reveals GPI-GFP membrane domains. **(f)** Like (c) but for neuron shown in (d). Scale bars are 500 nm.

again the exceptional stability of these structures. The actin rings remain exciting structures for further investigation. It was recently shown that they are formed from a particular, braided actin filament structure (Vassilopoulos et al., 2020) and that they are capable of changing their diameter to accommodate for large cargo (Wang et al., 2020), a capability that is likely mediated by non-muscle myosin II located to the rings (Berger et al., 2018; Zhou et al., 2022; Mikhaylova et al., 2020; Costa et al., 2020). Clearly, the actin rings influence membrane protein motion, but it remains to be shown how such a ubiquitous

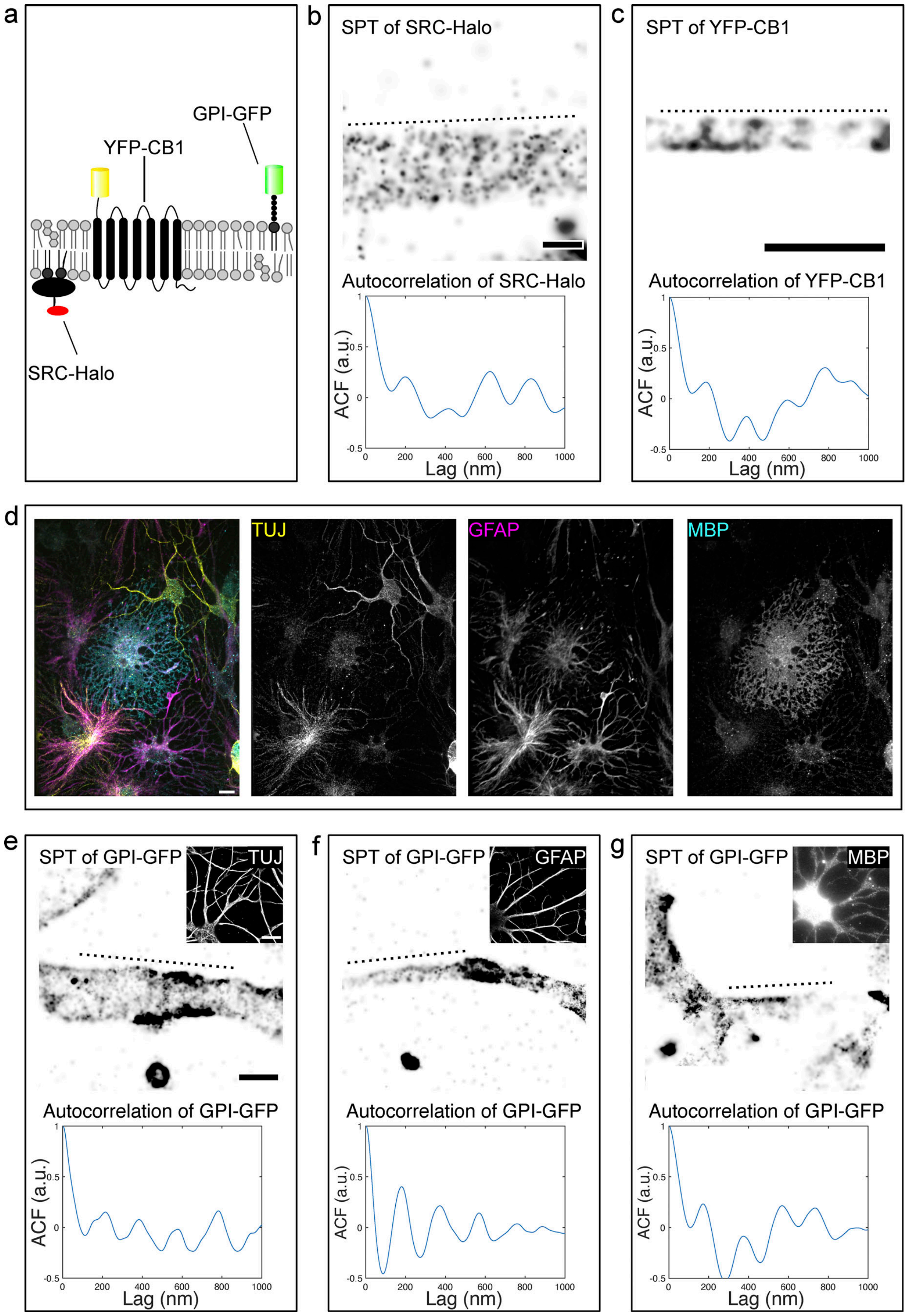

Figure 4. **Membrane domains can be detected for different membrane molecule species and in several cell types of the neuronal lineage.** **(a)** Schematic representation of molecule species that were investigated: The inner leaflet peripheral membrane protein SRC-Halo, the transmembrane protein

YFP-CB1, and the outer leaflet peripheral membrane protein GPI-GFP. **(b)** Top: Reconstruction of SPT experiment (20,000 frames, 100 Hz) of SRC-Halo tagged JF635; bottom: autocorrelation function (ACF) along the dotted line along the neuronal process shown on top reveals periodicity of SRC-Halo domains at ~200 nm. **(c)** Top: Reconstruction of SPT experiment (20,000 frames, 200 Hz) of YFP-CB-1 tagged with QDs in progenitor-derived neuronal cells. Bottom: Autocorrelation function (ACF) along the dotted line along the neuronal process shown on top reveals the periodicity of YFP-CB1 domains at ~200 nm. **(d)** Confocal images of progenitor-derived neuronal cells stained for their lineage marker: (left) merge, (middle left) neurons stained for TUJ, (middle right) astrocytes stained for GFAP, (right) oligodendrocytes stained for MBP. **(e)** Top: Reconstruction of SPT experiment (20,000 frames, 200 Hz) of GPI-GFP tagged with QDs in progenitor-derived neurons. Inset shows microscopy image of tracked cell stained for TUJ. Scale bar of inset is 10 µm. Bottom: Autocorrelation function (ACF) along the dotted line along the neuronal process shown on top reveals periodicity of GPI-GFP domains at ~200 nm. **(f)** Like (e) but for an astrocyte stained for GFAP. **(g)** Like (e) but for an oligodendrocyte stained for MBP. If not otherwise indicated, scale bars are 500 nm.

method to compartmentalize membrane protein motion influences the biology of membrane proteins. Since diffusion of membrane proteins is a principal biophysical property that strongly affects the kinetics of membrane protein reactions and the rings are evolutionarily conserved at least in axons (He et al., 2016), their presence likely has significant functional consequences. It has been shown that receptor tyrosine kinase signaling is dependent on the periodic actin rings (Zhou et al., 2019); however, the mechanism behind this requirement remains unclear. Likewise, neuronal adhesion molecules assume a periodic organization between actin rings in progenitor-derived oligodendrocytes (Hauser et al., 2018), and the rings are aligned between neighboring processes (Hauser et al., 2018; Zhou et al., 2022). The disruption of actin rings by spectrin knockdown leads to reduced axon bundling (Zhou et al., 2022), adhesion of dendrites to axons, and even synapse formation, but it remains to be shown if this is a specific effect or indeed the compartmentalization allows for more efficient lateral

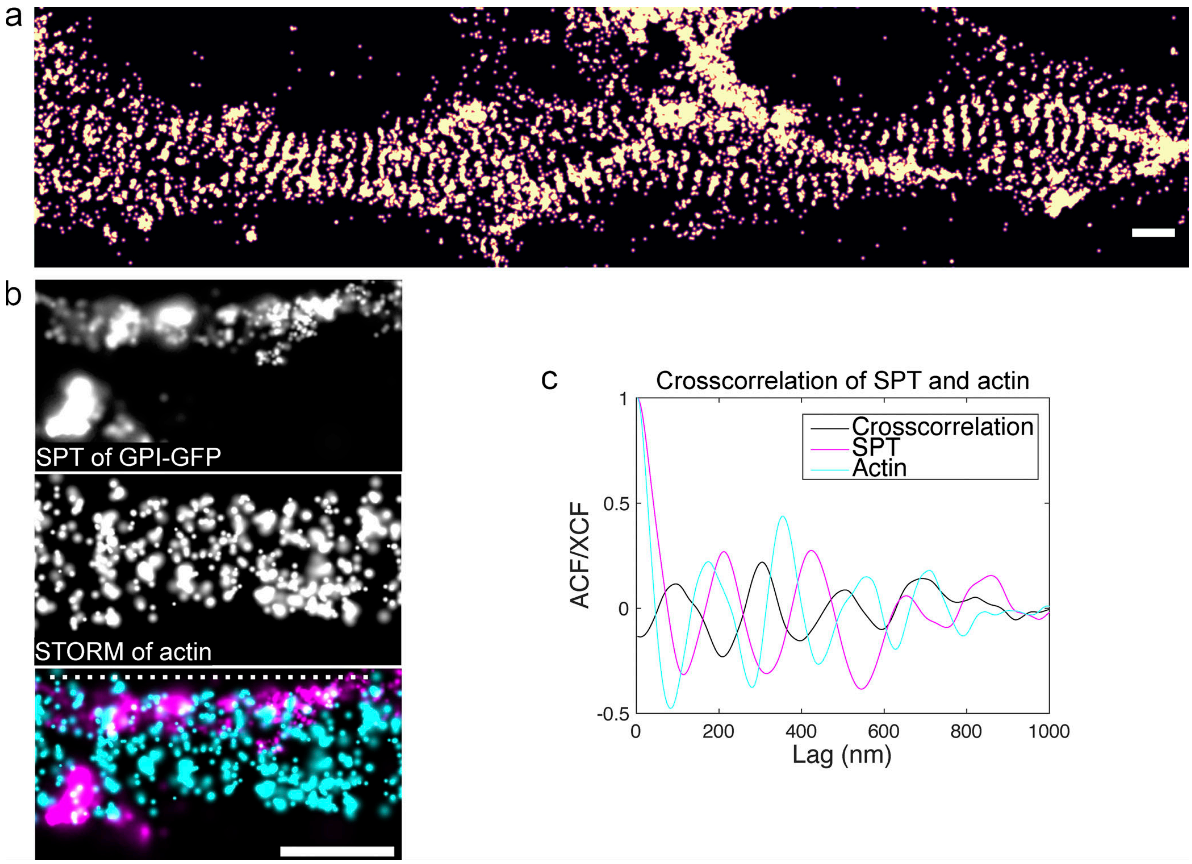

Figure 5. **GPI-GFP is more likely to be localized between actin rings in progenitor-derived neuronal cells. (a)** dSTORM reconstruction of actin in progenitor-derived neuronal cells stained with phalloidin. **(b)** Correlative SPT of GPI-GFP tagged with QDs and dSTORM of actin experiments in progenitor-derived neuronal cells. Top: GPI-GFP was tracked using QDs (5,000 frames, 200 Hz). Middle: Cells were subsequently fixed and stained for actin using phalloidin. Bottom: Overlay of SPT and STORM reconstructions. GPI-GFP is more likely to be localized between actin rings. **(c)** Autocorrelation function (ACF) along the dotted line in (b) reveals periodicity ~200 nm of actin rings and GPI-GFP domains. Crosscorrelation function (XCF) of GPI-GFP domains and actin rings reveals that GPI-GFP is more likely to be localized between actin rings. Scale bars are 500 nm.

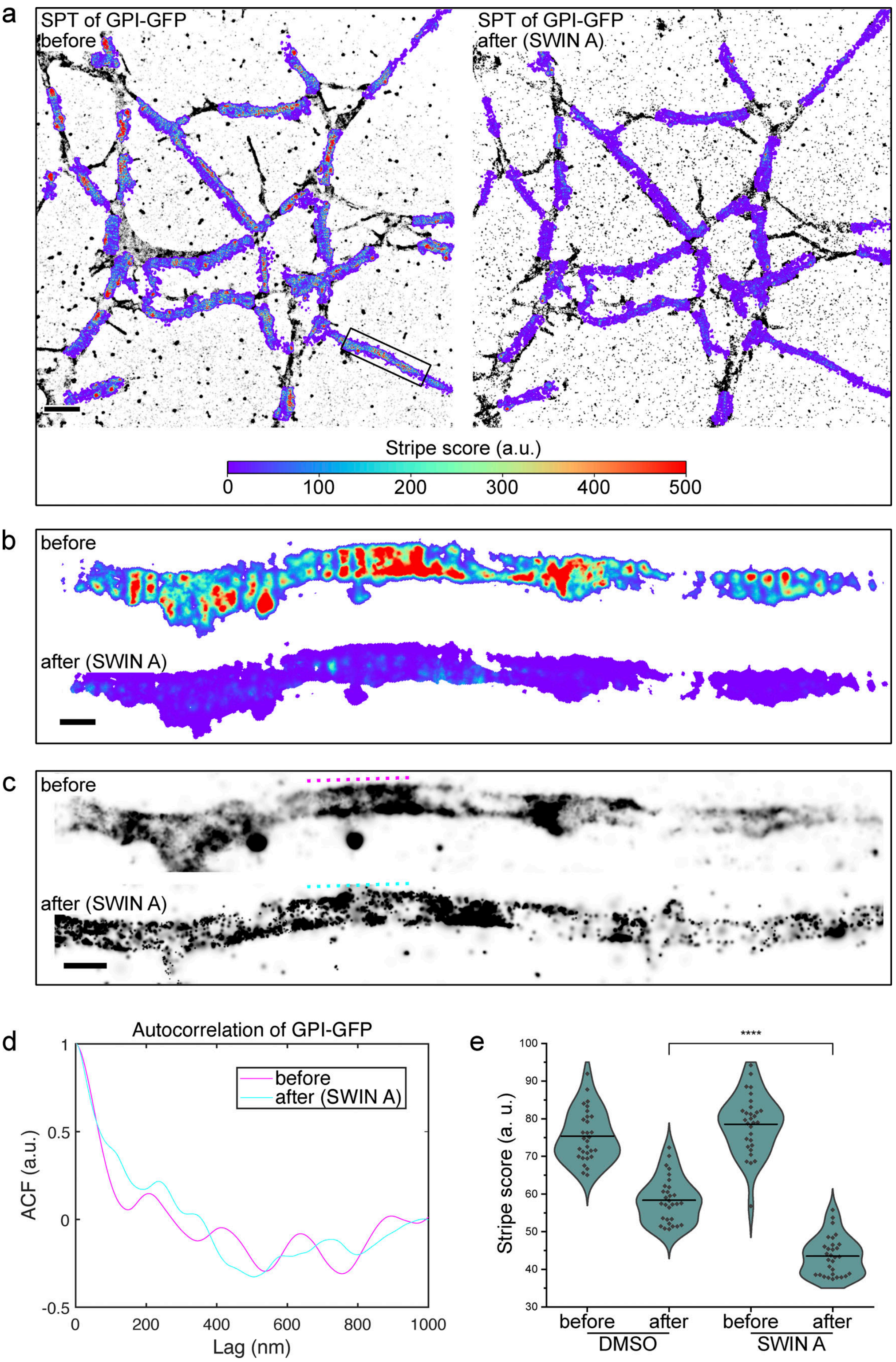

Figure 6. **Actin disruption leads to loss of GPI-GFP periodicity. (a)** Correlative SPT of GPI-GFP of progenitor-derived neuronal cells before and after SWIN A treatment. GPI-GFP was tracked using anti-GFP-NB-conjugated QDs (5,000 frames, 200 Hz). Cells were then treated with 1 µM SWIN A for 30 min. Afterward,

the same cell was tracked again. A local "stripe score" was then calculated based on the localizations via a Fourier-filter-based algorithm to detect periodicity at 200 nm. Shown are reconstructions of SPT experiments overlayed with heat maps of the local stripe score. After treatment, cells show a clear reduction in periodicity at 200 nm. Scale bar is 5 µm. **(b)** Heat map of stripe score of box in (a) before and after SWIN A treatment. **(c)** Reconstructions of SPT experiments of box in (a) before and after SWIN A treatment. **(d)** Autocorrelation function (ACF) of periodic area in (c) as indicated with dotted lines before and after SWIN A treatment. Periodicity ∼200 nm is lost after SWIN A treatment. **(e)** Experimental procedure as described in (a). Violin plot of stripe scores of cells before and after SWIN A treatment (n = 30 per condition from three independent experiments). Lines indicate means. Normality was tested using Shapiro–Wilk test and rejected (DMSO after P = 0.072 ns, SWIN A after P = 0.022*). Significance was tested using Mann–Whitney test. SWIN A treated cells show a significantly reduced stripe score compared to the control cells (DMSO after versus SWIN A after P = 4.2E-10****). Scale bars are 500 nm if not otherwise indicated.

association of processes via transcellular adhesive protein interaction (Zhou et al., 2022).

Taken together, our work establishes the causal role of actin rings in membrane protein compartmentalization and offers a tractable experimental paradigm to investigate the control of membrane protein motion. In the future, new extremely high-speed single-molecule tracking methods (Fujiwara et al., 2023) or MINFLUX microscopy (Balzarotti et al., 2017) will allow more insight into nanoscopic membrane protein compartmentalization.

Materials and methods

Simulated SPT experiments

Simulated SPT experiments were generated using Fluosim (Lagardère et al., 2020). Model geometries were generated using custom Python scripts (see Data availability for script). Movies of five particles diffusing over the geometry were then generated using parameters similar to those observed in real data for either the actin model (crossing probability 30%, fluorophore spot size 150 nm, intensity 200, switch on/off rate 0.5 Hz, and 5,005 frames) or the channel model (crossing probability 0%, fluorophore spot size 150 nm, intensity 200, switch on/off rate 0.5 Hz, and 5,005 frames). Motion blur and Poisson noise were added to the movies using custom Python code (see Data availability for script). Picasso (Schnitzbauer et al., 2017) was then used to generate localizations and to render super-resolved reconstructions from the movies.

Additionally, to test the effect of different crossing probabilities on compartmentalization, super-resolved reconstructions were generated in Fluosim. The same parameters as described above were used for the actin model with varying crossing probabilities (0, 0.01, 0.1, 0.2 … 1). 10 reconstructions were generated per condition. The mean autocorrelation peak at 200 nm was then calculated from all reconstructions per condition using a custom MATLAB (RRID: SCR_001622; MathWorks) script (see Data availability for script).

Cell culture

Wild-type *Cercopithecus aethiops* kidney fibroblasts (CV-1, Cat# 605471/p715_CV-1, RRID: CVCL_0229; CLS) were a kind gift from the Helenius laboratory (Eidgenössische Technische Hochschule Zürich, Switzerland) and cultured as described previously (Li et al., 2020): Cells were grown in DMEM without phenol red (#31053028; Thermo Fisher Scientific)/10% (vol/vol) fetal bovine serum (FBS; #A5256701; Thermo Fisher Scientific)/1% (vol/vol) GlutaMAX (#35050061; Thermo Fisher Scientific) at 37°C in a CO_2-controlled humidified incubator.

Neuronal cell culture

Rat hippocampal neurons were cultured as described previously (Schmerl et al., 2022): Rat E18 Wistar (RRID: RGD_13792727) pups were decapitated and hippocampi were isolated and collected in ice-cold DMEM (#BE15-604K; Lonza). The fetal tissue was partially digested (5 min at 37°C) with 2.5% Trypsin/EDTA (#CC-5012; Lonza) prior to addition of 10% FBS (#S0615; Biochrom) in DMEM (#BE15-604K; Lonza) to stop the digest, followed by two washes with DMEM (#BE15-604K; Lonza; 10 rcf for 3 min at room temperature). Tissue was resuspended in neuron culture medium (Neurobasal A, #10888022; Thermo Fisher Scientific supplemented with B27, #7504044; Thermo Fisher Scientific and 500 µM *L*-glutamine #25030081; Thermo Fisher Scientific) and mechanically dissociated. Neurons were then plated at ∼10^5 cells/cm^2 on coverslips coated with 0.2 mg/ml poly-*D*-lysine (#P6403; Sigma-Aldrich) and 2 µg/ml laminin (#11243217001; Sigma-Aldrich). 1 h after plating, medium was exchanged and thereby cell debris removed. The cultures were maintained in a humidified incubator at 37°C with 5% CO_2. All procedures were in accordance with the Directive 2010/63/EU of the European Parliament on the protection of animals used for scientific purposes. Protocols for animal sacrifice were approved by the Regional Office for Health and Social Affairs in Berlin ("Landesamt für Gesundheit und Soziales; LaGeSo") and the animal welfare committee of the Charité and carried out under permits T0280/10 and T-CH 0002/21. Rat hippocampal neurons were transfected on DIV1 with GPI-GFP using Lipofectamin 3000 (#L3000001; Thermo Fisher Scientific) following the manufacturer's instructions.

AHNPCs were cultured and differentiated into progenitor-derived neuronal cells as described previously (Hauser et al., 2018; Peltier et al., 2010). Cell culture flasks and coverslips were coated with 10 µg/ml ornithine (#P3655-100MG; Sigma-Aldrich)/phosphate-buffered saline (PBS) overnight and subsequently with 5 µg/ml lamine (#23017015; Thermo Fisher Scientific)/PBS overnight. Cell culture flasks and coverslips were washed thrice with PBS. AHNPCs were cultured on coated T75 (#90076; TPP) flasks in DMF12/1% (vol/vol; #35050061; Thermo Fisher Scientific)/N2 supplement (#17502048; Thermo Fisher Scientific)/20 ng/ml fibroblast growth factor 2 (#AF-450-33; Peprotech). AHNPCs were maintained at <80% confluence. All experiments were performed on cells grown in a double layer in 35 × 10 mm coated plastic dishes (#627160; Cellstar) containing 25-mm coated coverslips (#631-1072; VWR). 300,000 AHNPCs were seeded onto the plastic dishes (#631-1072; VWR) and 200,000 cells on top of the coverslip (#631-1072; VWR). Differentiation was induced in DMF12/1% (vol/vol; #35050061; Thermo Fisher Scientific)/N2 supplement (#17502048; Thermo

Fisher Scientific)/1 µM retinoic acid (Cay14587-10; Biomol) to generate progenitor-derived neuronal cells.

Progenitor-derived neuronal cells were transfected on DIV1 with YFP-CB1 using Lipofectamin 3000 (#L3000001; Thermo Fisher Scientific) following the manufacturer's instructions.

SPT

Lag16 anti-GFP-NB (Fridy et al., 2014) was labeled with biotin as described previously (Li et al., 2020): α-Biotin-ω-(succinimidyl propionate)-24(ethylene glycol) (#PEG4250; Iris Biotech) at twofold molar excess was added to Lag16 anti-GFP-NB. Afterward, conjugates were purified thrice via 7 kD MWCO Zeba Spin Desalting Columns (#89882; Thermo Fisher Scientific). QD655-Streptavidin (#Q10121MP; Thermo Fisher Scientific) was incubated with biotinylated anti-GFP nanobodies in a 1:1 M ratio for 10 min. Cells (DIV7 rat hippocampal neurons, DIV5–DIV14 progenitor-derived neuronal cells, CV-1) expressing either GPI-GFP or YFP-CB1 were then incubated with increasing amounts of QD-NB conjugates (between 0.1 and 1 nM) in live cell imaging solution (#A14291DJ; Thermo Fisher Scientific) until desired QD density was reached depending on cell density and transfection efficiency. Cells were then washed with 1 ml live cell imaging solution. Imaging was performed at a laser-power density of 0.6 kW^*cm^{-2} using a 637 nm laser. Typically, 20,000 frames were acquired per measurement at an exposure time of 5 ms.

Progenitor-derived neuronal cells (DIV5–DIV14) expressing SRC-Halo were incubated with 0.25 nM JF635 in live cell imaging solution for 10 min. Afterward, cells were washed with 1 ml live cell imaging solution. Imaging was performed at a laser-power density of 1.3 kW^*cm^{-2} using a 637 nm laser. Typically, 20,000 frames were acquired per measurement at an exposure time of 10 ms.

All samples were imaged at room temperature using a Vutara 352 super-resolution microscope (Bruker) equipped with a Hamamatsu ORCA Flash4.0 sCMOS camera for super-resolution imaging and a 60× oil immersion TIRF objective with a numerical aperture of 1.49 (Olympus). Immersion Oil 23°C (#1261; Cargille) was used.

Acquired raw data were localized using SRX (Bruker). Localizations were estimated by fitting single emitters to a 3D experimentally determined point spread function (PSF) under optimization of maximum likelihood. The maximum number of localization iterations performed before a given non-converging localization was discarded was set to 40. PSFs were interpolated using the B-spline method. For reconstructions, localizations were rendered according to their radial precision. For single molecule tracking analysis, localizations were exported using SRX (Bruker) and tracked in 3D using the FIJI (RRID: SCR_002285) Mosaic tracker plugin (Linkrange: 3, Displacement: 2; Sbalzarini and Koumoutsakos, 2005). Diffusion coefficients and alpha exponents were calculated in Mosaic. Tracks were filtered according to their α exponent ($2 > \alpha > 0$).

Autocorrelation and crosscorrelation were calculated using custom MATLAB (RRID: SCR_001622; MathWorks) scripts employing the built-in autocorr() and crosscorr() functions. For crosscorrelation, the mean of SPT and actin; actin and SPT was calculated (see Data availability for script).

Correlative SPT/immunostainings

The sample holder containing samples of progenitor-derived neuronal cells (DIV5–DIV14) stably expressing GPI-GFP was fixated on the microscope using a two-component adhesive (Picodent Twinsil; Picodent) using the manufacturer's instructions to avoid sample drift during the staining process. Cells were tracked as described under section SPT and subsequently fixed on the microscope in 4% PFA (#E15710; ScienceServices; vol/vol)/PBS for 15 min. Then, samples were quenched in 50 mM NH_4Cl/PBS for 30 min. Afterward, permeabilization/blocking was performed with 1% BSA (wt/vol)/0.05% saponin (wt/vol)/4% horse serum (vol/vol; #16050130; Thermo Fisher Scientific)/PBS for 45 min. Then, samples were incubated in a drop of Image-iT (#R37602; Thermo Fisher Scientific) for 30 min. Samples were then stained with either rat anti-myelin basic protein (1:100, #ab7349, RRID: AB_305869; Abcam), rabbit anti-GFAP (1:1,000, #ab7260, RRID: AB_305808; Abcam), or mouse anti-Tuj (1:300, #SAB4700544, RRID: AB_10898725; Sigma-Aldrich) for 2 h in 1% BSA (wt/vol)/0.05% saponin (wt/vol)/4% horse serum (vol/vol; #16050130; Thermo Fisher Scientific)/PBS. Afterward, samples were washed five times with 1 ml 1% BSA (wt/vol)/0.05% saponin (wt/vol)/PBS. Then, samples were incubated with donkey anti-mouse AF647 (1:500, #A31571, RRID: AB_162542; Invitrogen), goat anti-rabbit AF647 (1:500, #A21246RRID: AB_1500778; Invitrogen), or goat anti-rat AF647 (1:500, #A21247, RRID: AB_10563558; Invitrogen) for 1 h in 1% BSA (wt/vol)/0.05% saponin (wt/vol)/4% horse serum (vol/vol; #16050130; Thermo Fisher Scientific)/PBS. Subsequently, samples were washed thrice with 1 ml PBS and then the same cells were imaged there were tracked previously. Imaging was performed in PBS at room temperature.

Correlative SPT experiments under actin disruption

The sample holder containing coverslips of progenitor-derived neuronal cells (DIV5–DIV14) stably expressing GPI-GFP were fixated on the microscope (Picodent Twinsil, Picodent) using the manufacturer's instructions to avoid sample drift during drug incubation time. Afterward, cells were tracked as described under section SPT ($n = 30$ from 3 independent experiments). Cells were then treated with either 1% DMSO or 1 µM SWIN A for 30 min. Subsequently, the same cells were tracked again without addition of new QD-NB conjugates. SPT data were analyzed using custom Stripefinder software (see section Stripefinder software, see Data availability for script). A violin plot was generated and statistical tests were performed in OriginPro (RRID: SCR_014212; OriginLab). Normality was tested for stripe scores using Shapiro–Wilk Test and rejected (DMSO after $P = 0.072$ ns, SWIN A after $P = 0.022$*). Significance was tested using Mann–Whitney Test (DMSO after versus SWIN A after $P = 4.2E-10$****).

Correlative SPT/dSTORM experiments

The sample holder containing samples of progenitor-derived neuronal cells (DIV5–DIV14) stably expressing GPI-GFP were fixated on the microscope (Picodent Twinsil; Picodent) using the manufacturer's instructions to avoid sample drift during the staining process. Cells were tracked as described under section SPT. Afterward, cells were fixed and stained for actin as described under section dSTORM. The cells that were previously tracked were then imaged for actin.

Triple-color immunostainings

Samples of progenitor-derived neuronal cells (DIV5–DIV14) were fixed in 4% PFA (#E15710; ScienceServices; vol/vol)/PBS for 15 min. Then, samples were quenched in 50 mM NH_4Cl/PBS for 30 min. Afterward, permeabilization/blocking was performed with 1% BSA (wt/vol)/0.05% saponin (wt/vol)/4% horse serum (vol/vol; #16050130; Thermo Fisher Scientific)/PBS for 45 min. Then, samples were incubated in a drop of Image-iT (#R37602; Thermo Fisher Scientific) for 30 min. Samples were then stained with rat anti-myelin basic protein (1:100#ab7349, RRID: AB_305869; Abcam), rabbit anti-GFAP (1:1,000, #ab7260, RRID: AB_305808; Abcam), and mouse anti-Tuj (1:300, #SAB4700544, RRID: AB_10898725; Sigma-Aldrich) overnight at 4°C in 1% BSA (wt/vol)/0.05% saponin (wt/vol)/4% horse serum (vol/vol; #16050130; Thermo Fisher Scientific)/PBS. Afterward, samples were washed thrice with 1 ml 1% BSA (wt/vol)/0.05% saponin (wt/vol)/PBS for 5 min on a shaker. Then, samples were incubated with donkey anti-mouse AF647 (1:500, #A31571; RRID: AB_162542; Invitrogen), goat anti-rabbit AF568 (1:500, #A11036, RRID: AB_10563566; Invitrogen), and goat anti-rat AF488 (1:500, #A11006, RRID: AB_2534074; Invitrogen) for 1 h in 1% BSA (wt/vol)/0.05% saponin (wt/vol)/4% horse serum (vol/vol; #16050130; Thermo Fisher Scientific)/PBS. Subsequently, samples were washed thrice with 1 ml PBS and imaging was performed in PBS on an inverted Olympus IX71 microscope equipped with a Yokogawa CSU-X1 spinning disk at room temperature. A 60×/1.42 NA oil Olympus objective and a sCMOS camera (Hamamatsu) was used.

AnkG immunostainings

DIV7 rat hippocampal neurons and DIV7 or DIV14 progenitor-derived neuronal cells were fixed, blocked, and imaged as described under section Triple-color immunostainings but were incubated with mouse anti-AnkG (1:200, #AB_10675130, RRID: AB_10675130; Neuromab) overnight at 4°C and subsequently with donkey anti-mouse AF647 (1:800, #A31571, RRID: AB_162542; Invitrogen) for 1 h.

Generation of lentiviruses

Lentiviral transfer vectors containing the coding sequence for GPI-GFP (#BLV-1633a) or GFP-P2A-SRC-Halo (#BLV-1639a) and corresponding lentiviruses were generated at the Viral Core Facility (Charité).

Generation of stable cell lines

For coating of dishes and culturing of AHNPCs, see section Neuronal cell culture. 1 ml of supernatant containing lentivirus (GPI-GFP, or GFP-P2A-SRC-Halo) was added to 100,000 AHNPCs growing on coated 6-well plates (#92406; TPP). Plates were centrifuged at 1,000 rcf for 30 min. After 72 h of incubation, cells were washed thrice with 1 ml PBS. Cells were then extended and frozen.

Cloning of LYN-Halo-pEGFP-N1

GPI-Halo-pEGFP-N1 was a gift from Akihiro Kusumi (Okinawa Institute of Science and Technology, Okinawa, Japan). pEGFP-N1 was a gift from Antony K Chen (plasmid # 172281; https://n2t.net/addgene:172281; RRID: Addgene_172281; Addgene). A DNA fragment (BamHI-LYN-Halo-BsrGI) was generated by performing a PCR (forward primer: 5′-AAAAAGGATCCGCCACCATGGGCTGCATCAAGAGCAAGCGCAAGGACAACCTGAACGACGACGGCGTGGACACCGGTTTTTT-3′, reverse primer: 5′-AAAAATGTACACTAGCCGGAAATCTCGAGCGTCG-3′) using GPI-Halo-pEGFP-N1 as a template. The DNA fragment and the pEGFP-N1 backbone were digested using BsrGI-HF (#R3575SVIAL; NEB) and BamHI-HF (#R3136SVIAL; NEB) following the manufacturer's instructions. The digested backbone and the digested fragment were then ligated and transformed into TOP10. Plasmid sequences were confirmed by Sanger sequencing.

Cloning of SRC-Halo-pEGFP-N1

SRC-EGFP-pEGFP-N1 was a gift from Terence Dermody and Bernardo Mainou (plasmid # 110496; https://n2t.net/addgene:110496; RRID: Addgene_110496; Addgene). A DNA fragment (BamHI-Src(c-term)-Halo(n-term)) was generated by performing a PCR (forward primer: 5′-AAAGGATCCACCGGTCGCCACCATGGCAGAAATCG-3′, reverse primer: 5′-AAAAATGTACACTAGC-3′) using LYN-Halo-pGFPN1 as a template. The DNA fragment and the SRC-EGFP-pEGFP-N1 backbone were digested using BsrGI-HF (#R3575SVIAL; NEB) and BamHI-HF (#R3136SVIAL; NEB) following the manufacturer's instructions. The digested backbone and the digested fragment were then ligated and transformed into TOP10. Plasmid sequences were confirmed by Sanger sequencing.

Cloning of YFP-CB-1-pcDNA3

CB1-pcDNA3 was a gift from Mary Abood (plasmid #13391; https://n2t.net/addgene:13391; RRID: Addgene_13391; Addgene). L-YFP-GT46 was a gift from P. Keller (Max Planck Institute for Cell Biology and Genetics, Dresden, Germany). The eYFP coding region containing a signal sequence was amplified from L-YFP-GT46 by performing a PCR using a primer pair of YFP_GT46_fwd (5′-CAAGCTTGGTACCGAGCTCGGCCACCATGGAGCTCTTTTG-3′) and YFP_GT46_rev (5′-GGCCGTCTAAGATCGACTTCATGCCACTACTACTACTTCCACTACTACTACTTCCCTTGTACAGCTCGTCCATGCC-3′). To assemble DNA fragment YFP_GT46_fwd-YFP_GT46_rev into CB-1-pcDNA3, primers were also designed to have 25-bp overlap at the junction regions. Afterward, CB-1-pcDNA3 was digested with BamHI-HF (#R3136SVIAL; NEB). To ligate the PCR product of YFP_GT46_fwd-YFP_GT46_rev into digested CB-1, Gibson Assembly Kit (#E5510S; NEB) was used following the manufacturer's instruction. The resulting plasmid was transformed into TOP10. Plasmid sequences were confirmed by Sanger sequencing.

STED microscopy

Progenitor-derived neuronal cells stably expressing GPI-GFP aged between DIV5 and DIV14 were stained live for actin using 1 μM SIR-actin (#SC001; Spirochrome) for 1 h at 37°C or stained for the PM using 10 nM Cholesterol-Starred (#STRED-0206; Abberior) for 10 min. For control experiment, cells were simultaneously incubated with Tetraspeck beads (1:500, #T7279; Invitrogen) for 1 h at 37°C. Cells were washed thrice with Live

Cell Imaging Solution (#A14291DJ; Invitrogen). Then, samples were imaged in 1 ml Live Cell Imaging Solution (#A14291DJ; Invitrogen). STED microscopy was performed at 37°C on an Abberior STED system with a 100×/1.4 NA oil uPlanSApo Olympus objective. STED imaging of SIR was performed with a 645 nm excitation and a 775 nm depletion pulsed laser. Detection was carried out with an avalanche photodiode (APD) with a 650–756 nm detection window. GFP was excited with a 485 nm laser and detected with an APD (498–551 nm). A single focal plane in the center of neuronal processes was imaged. Pixel size was set to 20 nm and pixel dwell time to 10 µs.

Distance calculation between GPI-GFP and actin rings/PM

To measure the distance between actin rings and GPI-GFP ($n = 31$ regions from 12 images) or between the PM and GPI-GFP ($n = 47$ regions from 8 images), plot profiles along neuronal processes were taken in both the GPI-GFP channel (confocal) and the SIR/Starred channel (STED). The plot profiles were analyzed and plotted using custom MATLAB (RRID: SCR_001622; MathWorks) scripts (see Data availability for script). In the plot profiles, two peaks are apparent for the two sides of the PM/actin rings/GPI-GFP. The plot profiles were smoothed slightly by applying a moving mean. Afterwards, the left and right peaks in the plot profiles were identified by finding the maxima in the smoothed profiles. The diameter of the PM/actin rings/GPI-GFP was then calculated from the difference of the peaks. Half the difference of GPI-GFP and actin rings and half the difference of GPI-GFP and the PM was then used to calculate the corresponding distances. To control the accuracy of the distance calculation, the same analysis was performed on the distance of Tetraspeck (#T7279; Invitrogen) beads imaged in the green channel (confocal) and the far-red channel (STED; $n = 46$ regions from seven images). A violin plot was generated and statistical tests were performed in OriginPro (RRID: SCR_014212; Originlab). Normality was tested using Shapiro–Wilk-Test and rejected (ΔGPI/PM P = 0.00054**, ΔGPI/actin P = 0.076 ns, Δbeads P = 3.6E-5****). Significance was tested using Mann–Whitney-Test (ΔGPI/Chol versus ΔGPI/actin P = 0.0098**, ΔGPI/actin versus beads P = 8.7E-8****, ΔGPI/Chol versus beads P = 2.2E-5****).

dSTORM

Progenitor-derived neuronal cells (DIV5–DIV14) were fixed in 4% PFA (#E15710; ScienceServices)/PBS for 15 min at 37°C. Then, samples were quenched in 50 mM NH4Cl/PBS for 30 min. Samples were subsequently stained with 2 µM Phalloidin-AF647 (#A22287; Thermo Fisher Scientific) in 1% BSA (wt/vol)/0.05% saponin (wt/vol)/4% horse serum (vol/vol; #16050130; Thermo Fisher Scientific)/PBS for 1 h. Afterward, samples were washed five times with PBS. All samples were imaged using a Vutara 352 super-resolution microscope (Bruker) equipped with a Hamamatsu ORCA Flash4.0 sCMOS camera for super-resolution imaging and a 60× oil immersion TIRF objective with a numerical aperture of 1.49 (Olympus). Immersion Oil 23°C (#1261; Cargille) was used. Samples were mounted onto the microscope in GLOX buffer (1.5% β-mercaptoethanol, 0.5% (vol/wt) glucose, 0.25 mg/ml glucose oxidase and 20 µg/ml catalase, 150 mM Tris-HCl, pH 8.8). All imaging was performed at room temperature at a laser-power density of $3.5\ \mathrm{kW{*}cm^{-2}}$ using a 637 nm laser. 10,000 frames were acquired per measurement at an exposure time of 20 ms.

Stripefinder software

We have developed a software pipeline for processing and segmentation of SMLM reconstructions and identifying periodic structures within. The pipeline has been implemented using Python and depends on NumPy (Harris et al., 2020), Pandas (McKinney, 2010), and SciPy (Virtanen et al., 2020) packages for computations and data analysis. Additionally, we have used the Scikit-Image (van der Walt et al., 2014) package for image processing operations.

Our designed pipeline is compatible with localizations from SMLM experiments in the form of sets of (x, y) coordinates with corresponding information on the point spread functions.

Matching similar regions: We implemented a convenient method for finding the required translations that result in the optimal match between two corresponding SMLM reconstructions (before SWINA treatment/after SWINA treatment). Reconstructions are loaded and rasterized into high-resolution bitmaps. This is followed by smoothing with identical Gaussian filters and segmentation using the Otsu's thresholding method (van der Walt et al., 2014; Otsu, 1979). The resulting binary masks are superimposed and shifted in the x and y directions. Optimal shift in both directions is obtained via numerical minimization of the sum of absolute pixel-wise differences between the two images.

Segmentation of the region of interest: We have been interested in a functionality to automatically select features such as the edge regions of axons. Towards this goal, we start with the binary masks obtained from the previous step and transform them back into a sparse point-cloud. To reduce the number of points, we first find the skeletons of the binary masks via morphological operations. We sample the x and y coordinates of the remaining points and calculate their pairwise distance matrix. Nearest neighbors of each point are then found by applying a cutoff to the pairwise distances. We use the number of nearest neighbors of each point to assign a measure of connectivity to it. We consequently use the point-wise connectivity measure to construct a connectivity graph with highly connected points as nodes. This allows us to segment the connectivity graph into regions of interest (ROIs) with a criterion that selects nodes belonging to an intact region and relates the highlighted ROIs back to the original image. We have used the regioncrops function of the Scikit-Image (van der Walt et al., 2014) package to uniquely label ROIs in the final image.

We store the resulting information including coordinates of the point clouds and the per-point ROI labels in a data structure for subsequent analysis. By iterating over the labels, we could select edges of neuronal processes and (i) determine their orientation by measuring the slope of a simple least-squares linear fit, and (ii) apply appropriate scaling and cropping operations to focus on a region for further processing.

Identifying periodic structures via two-dimensional convolutions: To identify regions of the SMLM reconstructions that contain periodically occurring structures, we devised an approach based on two-dimensional convolution with a periodic kernel. The kernel comprises a series of elongated bivariate Gaussian functions that are positioned on a one-dimensional lattice, all oriented with a tilt angle θ with respect to the abscissa. Separation between the Gaussians is an input parameter of the method, and was chosen to mirror the expected separation between structures in the analyzed images.

Convolving this periodic kernel with the SMLM reconstructions results in local maxima for pixels around which the periodic tilted Gaussians best resemble the features in the image. To improve performance of the convolution operation, especially for large images, we implemented the convolution via Fourier transform. The well-known convolution theorem of the Fourier transform states that multiplication of signals in Fourier space corresponds to their convolution in real space. With the aid of fast Fourier transform (Cooley and Tukey, 1965), the sequence of forward transform, pixel-wise multiplication with the kernel, and inverse transform has still better performance than the direct convolution in real space.

We processed the resulting convolved image further via a sweep with the discrete Laplace operator, which emphasizes the contrast in highlighted regions. By repeating the whole process for different values of the kernel tilt angle θ, we identified regions of the image containing periodic structures posed at different orientations. See Data availability for the script.

Online supplemental material

Fig. S1 investigates the permeability of the actin barrier using simulations of SPT data. Fig. S2 shows that progenitor-derived neuronal cells do not exhibit AnkG accumulations. Fig. S3 shows that GPI-GFP in membrane domains remains mobile and unconfined. Fig. S4 shows that the actin inhibitor SWIN A disrupts actin rings in progenitor-derived neuronal cells. Fig. S5 demonstrates the functionality of the Stripefinder software, which enables automated detection of periodicity at 200 nm. Video 1 is a 3D reconstruction of localizations of GPI-GFP in the axon. Video 2 is typical raw data of an SPT experiment of GPI-GFP tagged with QDs. Video 3 is typical synthetic data of an SPT experiment generated in Fluosim. Video 4 is an animation of GPI-GFP localizations of a SPT experiment on top of dSTORM localizations of actin rings, showing that GPI-GFP is more likely to be localized between actin rings in progenitor-derived neuronal cells.

Data availability

Data and all scripts are available under https://zenodo.org/records/10386831, except super-resolution microscopy files. Files are available upon reasonable request. Stripefinder software can be found under https://github.com/selleban/stripe_finder.

Acknowledgments

We thank all members of the Ewers laboratory for helpful discussions, especially Purba Kashyap for input regarding data analysis and cloning and Jia Hui Li for input regarding data analysis and experimental procedures. We thank Thorsten Trimbuch and the team of the Viral Core Facility (Charité, Berlin, Germany) for the generation of the lentiviruses.

This work was supported by Deutsche Forschungsgemeinschaft through SFB958/A04, SFB 958/Z02, SFB1114/C03, and TRR 186 (project number 278001972) and by the European Research Council through CoG 772230 "ScaleCell" and the Federal Ministry of Education and Research Germany through the grant "Deep-learning for XRM of organelle connectomics."

Author contributions: H. Ewers designed research. J. Rentsch, B. Sezen, and P. Sigrist performed research. S. Bandstra, J. Rentsch, M. Sadeghi, and F. Noé developed analysis tools. J. Rentsch and S. Bandstra analyzed data. F. Bottanelli provided training, equipment, and reagents related to STED microscopy. B. Schmerl and S. Shoichet provided neuronal cell material. H. Ewers and J. Rentsch wrote the paper. All authors read and approved the final manuscript.

Disclosures: The authors declare no competing interests exist.

Submitted: 27 October 2023
Revised: 20 December 2023
Accepted: 4 January 2024

References

Albrecht, D., C.M. Winterflood, M. Sadeghi, T. Tschager, F. Noé, and H. Ewers. 2016. Nanoscopic compartmentalization of membrane protein motion at the axon initial segment. *J. Cell Biol.* 215:37–46. https://doi.org/10.1083/jcb.201603108

Andrade, D.M., M.P. Clausen, J. Keller, V. Mueller, C. Wu, J.E. Bear, S.W. Hell, B.C. Lagerholm, and C. Eggeling. 2015. Cortical actin networks induce spatio-temporal confinement of phospholipids in the plasma membrane--a minimally invasive investigation by STED-FCS. *Sci. Rep.* 5: 11454. https://doi.org/10.1038/srep11454

Balzarotti, F., Y. Eilers, K.C. Gwosch, A.H. Gynnå, V. Westphal, F.D. Stefani, J. Elf, and S.W. Hell. 2017. Nanometer resolution imaging and tracking of fluorescent molecules with minimal photon fluxes. *Science.* 355: 606–612. https://doi.org/10.1126/science.aak9913

Berger, S.L., A. Leo-Macias, S. Yuen, L. Khatri, S. Pfennig, Y. Zhang, E. Agullo-Pascual, G. Caillol, M.-S. Zhu, E. Rothenberg, et al. 2018. Localized myosin II activity regulates assembly and plasticity of the axon initial segment. *Neuron.* 97:555–570.e6. https://doi.org/10.1016/j.neuron.2017.12.039

Boggon, T.J., and M.J. Eck. 2004. Structure and regulation of Src family kinases. *Oncogene.* 23:7918–7927. https://doi.org/10.1038/sj.onc.1208081

Brachet, A., C. Leterrier, M. Irondelle, M.-P. Fache, V. Racine, J.-B. Sibarita, D. Choquet, and B. Dargent. 2010. Ankyrin G restricts ion channel diffusion at the axonal initial segment before the establishment of the diffusion barrier. *J. Cell Biol.* 191:383–395. https://doi.org/10.1083/jcb.201003042

Clark, A.G., K. Dierkes, and E.K. Paluch. 2013. Monitoring actin cortex thickness in live cells. *Biophys. J.* 105:570–580. https://doi.org/10.1016/j.bpj.2013.05.057

Clausen, M.P., H. Colin-York, F. Schneider, C. Eggeling, and M. Fritzsche. 2017. Dissecting the actin cortex density and membrane-cortex distance in living cells by super-resolution microscopy. *J. Phys. D Appl. Phys.* 50: 064002. https://doi.org/10.1088/1361-6463/aa52a1

Cooley, J.W., and J.W. Tukey. 1965. An algorithm for the machine calculation of complex fourier series. *Math. Comput.* 19:297–301. https://doi.org/10.2307/2003354

Costa, A.R., S.C. Sousa, R. Pinto-Costa, J.C. Mateus, C.D. Lopes, A.C. Costa, D. Rosa, D. Machado, L. Pajuelo, X. Wang, et al. 2020. The membrane periodic skeleton is an actomyosin network that regulates axonal diameter and conduction. *Elife.* 9:e55471. https://doi.org/10.7554/eLife.55471

D'Este, E., D. Kamin, F. Balzarotti, and S.W. Hell. 2017. Ultrastructural anatomy of nodes of Ranvier in the peripheral nervous system as revealed by STED microscopy. *Proc. Natl. Acad. Sci. U S A*. 114:E191–E199. https://doi.org/10.1073/pnas.1619553114

D'Este, E., D. Kamin, F. Göttfert, A. El-Hady, and S.W. Hell. 2015. STED nanoscopy reveals the ubiquity of subcortical cytoskeleton periodicity in living neurons. *Cell Rep*. 10:1246–1251. https://doi.org/10.1016/j.celrep.2015.02.007

D'Este, E., D. Kamin, C. Velte, F. Göttfert, M. Simons, and S.W. Hell. 2016. Subcortical cytoskeleton periodicity throughout the nervous system. *Sci. Rep*. 6:22741. https://doi.org/10.1038/srep22741

Freeman, S.A., A. Vega, M. Riedl, R.F. Collins, P.P. Ostrowski, E.C. Woods, C.R. Bertozzi, M.I. Tammi, D.S. Lidke, P. Johnson, et al. 2018. Transmembrane pickets connect Cyto- and pericellular skeletons forming barriers to receptor engagement. *Cell*. 172:305–317.e10. https://doi.org/10.1016/j.cell.2017.12.023

Fridy, P.C., Y. Li, S. Keegan, M.K. Thompson, I. Nudelman, J.F. Scheid, M. Oeffinger, M.C. Nussenzweig, D. Fenyö, B.T. Chait, and M.P. Rout. 2014. A robust pipeline for rapid production of versatile nanobody repertoires. *Nat. Methods*. 11:1253–1260. https://doi.org/10.1038/nmeth.3170

Fujiwara, T., K. Ritchie, H. Murakoshi, K. Jacobson, and A. Kusumi. 2002. Phospholipids undergo hop diffusion in compartmentalized cell membrane. *J. Cell Biol*. 157:1071–1081. https://doi.org/10.1083/jcb.200202050

Fujiwara, T.K., S. Takeuchi, Z. Kalay, Y. Nagai, T.A. Tsunoyama, T. Kalkbrenner, K. Iwasawa, K.P. Ritchie, K.G.N. Suzuki, and A. Kusumi. 2023. Development of ultrafast camera-based single fluorescent-molecule imaging for cell biology. *J. Cell Biol*. 222:e202110160. https://doi.org/10.1083/jcb.202110160

Garrido, J.J., P. Giraud, E. Carlier, F. Fernandes, A. Moussif, M.-P. Fache, D. Debanne, and B. Dargent. 2003. A targeting motif involved in sodium channel clustering at the axonal initial segment. *Science*. 300:2091–2094. https://doi.org/10.1126/science.1085167

Gasser, A., T.S.-Y. Ho, X. Cheng, K.-J. Chang, S.G. Waxman, M.N. Rasband, and S.D. Dib-Hajj. 2012. An ankyrinG-binding motif is necessary and sufficient for targeting Nav1.6 sodium channels to axon initial segments and nodes of Ranvier. *J. Neurosci*. 32:7232–7243. https://doi.org/10.1523/JNEUROSCI.5434-11.2012

Goswami, D., K. Gowrishankar, S. Bilgrami, S. Ghosh, R. Raghupathy, R. Chadda, R. Vishwakarma, M. Rao, and S. Mayor. 2008. Nanoclusters of GPI-anchored proteins are formed by cortical actin-driven activity. *Cell*. 135:1085–1097. https://doi.org/10.1016/j.cell.2008.11.032

Gowrishankar, K., S. Ghosh, S. Saha, R. C, S. Mayor, and M. Rao. 2012. Active remodeling of cortical actin regulates spatiotemporal organization of cell surface molecules. *Cell*. 149:1353–1367. https://doi.org/10.1016/j.cell.2012.05.008

Harris, C.R., K.J. Millman, S.J. van der Walt, R. Gommers, P. Virtanen, D. Cournapeau, E. Wieser, J. Taylor, S. Berg, N.J. Smith, et al. 2020. Array programming with NumPy. *Nature*. 585:357–362. https://doi.org/10.1038/s41586-020-2649-2

Hartel, A.J.W., M. Glogger, N.G. Jones, W. Abuillan, C. Batram, A. Hermann, S.F. Fenz, M. Tanaka, and M. Engstler. 2016. N-glycosylation enables high lateral mobility of GPI-anchored proteins at a molecular crowding threshold. *Nat. Commun*. 7:12870. https://doi.org/10.1038/ncomms12870

Hauser, M., R. Yan, W. Li, N.A. Repina, D.V. Schaffer, and K. Xu. 2018. The spectrin-actin-based periodic cytoskeleton as a conserved nanoscale scaffold and ruler of the neural stem cell lineage. *Cell Rep*. 24:1512–1522. https://doi.org/10.1016/j.celrep.2018.07.005

He, J., R. Zhou, Z. Wu, M.A. Carrasco, P.T. Kurshan, J.E. Farley, D.J. Simon, G. Wang, B. Han, J. Hao, et al. 2016. Prevalent presence of periodic actin-spectrin-based membrane skeleton in a broad range of neuronal cell types and animal species. *Proc. Natl. Acad. Sci. USA*. 113:6029–6034. https://doi.org/10.1073/pnas.1605707113

Hedstrom, K.L., Y. Ogawa, and M.N. Rasband. 2008. AnkyrinG is required for maintenance of the axon initial segment and neuronal polarity. *J. Cell Biol*. 183:635–640. https://doi.org/10.1083/jcb.200806112

Hiramoto-Yamaki, N., K.A.K. Tanaka, K.G.N. Suzuki, K.M. Hirosawa, M.S.H. Miyahara, Z. Kalay, K. Tanaka, R.S. Kasai, A. Kusumi, and T.K. Fujiwara. 2014. Ultrafast diffusion of a fluorescent cholesterol analog in compartmentalized plasma membranes. *Traffic*. 15:583–612. https://doi.org/10.1111/tra.12163

Howlett, A.C., F. Barth, T.I. Bonner, G. Cabral, P. Casellas, W.A. Devane, C.C. Felder, M. Herkenham, K. Mackie, B.R. Martin, et al. 2002. International union of pharmacology. XXVII. Classification of cannabinoid receptors. *Pharmacol. Rev*. 54:161–202. https://doi.org/10.1124/pr.54.2.161

Huang, Y.-M., and M.N. Rasband. 2016. Organization of the axon initial segment: Actin like a fence. *J. Cell Biol*. 215:9–11. https://doi.org/10.1083/jcb.201609084

Jones, S.L., F. Korobova, and T. Svitkina. 2014. Axon initial segment cytoskeleton comprises a multiprotein submembranous coat containing sparse actin filaments. *J. Cell Biol*. 205:67–81. https://doi.org/10.1083/jcb.201401045

Klenchin, V.A., R. King, J. Tanaka, G. Marriott, and I. Rayment. 2005. Structural basis of swinholide A binding to actin. *Chem. Biol*. 12:287–291. https://doi.org/10.1016/j.chembiol.2005.02.011

Kusumi, A., C. Nakada, K. Ritchie, K. Murase, K. Suzuki, H. Murakoshi, R.S. Kasai, J. Kondo, and T. Fujiwara. 2005. Paradigm shift of the plasma membrane concept from the two-dimensional continuum fluid to the partitioned fluid: High-speed single-molecule tracking of membrane molecules. *Annu. Rev. Biophys. Biomol. Struct*. 34:351–378. https://doi.org/10.1146/annurev.biophys.34.040204.144637

Lagardère, M., I. Chamma, E. Bouilhol, M. Nikolski, and O. Thoumine. 2020. FluoSim: Simulator of single molecule dynamics for fluorescence live-cell and super-resolution imaging of membrane proteins. *Sci. Rep*. 10:19954. https://doi.org/10.1038/s41598-020-75814-y

Leterrier, C. 2018. The axon initial segment: An updated viewpoint. *J. Neurosci*. 38:2135–2145. https://doi.org/10.1523/JNEUROSCI.1922-17.2018

Leterrier, C., N. Clerc, F. Rueda-Boroni, A. Montersino, B. Dargent, and F. Castets. 2017. Ankyrin G membrane partners drive the establishment and maintenance of the axon initial segment. *Front. Cell. Neurosci*. 11:6. https://doi.org/10.3389/fncel.2017.00006

Leterrier, C., J. Potier, G. Caillol, C. Debarnot, F. Rueda Boroni, and B. Dargent. 2015. Nanoscale architecture of the axon initial segment reveals an organized and robust scaffold. *Cell Rep*. 13:2781–2793. https://doi.org/10.1016/j.celrep.2015.11.051

Li, J.H., P. Santos-Otte, B. Au, J. Rentsch, S. Block, and H. Ewers. 2020. Directed manipulation of membrane proteins by fluorescent magnetic nanoparticles. *Nat. Commun*. 11:4259. https://doi.org/10.1038/s41467-020-18087-3

McKinney, W. 2010. Data structures for statistical computing in Python. In Proceedings of the 9th Python in Science Conference. S. van der Walt and J. Millman, editors. 56–61. https://doi.org/10.25080/Majora-92bf1922-00a

Mikhaylova, M., J. Rentsch, and H. Ewers. 2020. Actomyosin contractility in the generation and plasticity of axons and dendritic spines. *Cells*. 9:2006. https://doi.org/10.3390/cells9092006

Otsu, N. 1979. A threshold selection method from gray-level histograms. *IEEE Trans. Syst. Man Cybern*. 9:62–66. https://doi.org/10.1109/TSMC.1979.4310076

Peltier, J., S. Agrawal, M.J. Robertson, and D.V. Schaffer. 2010. In vitro culture and analysis of adult hippocampal neural progenitors. In Protocols for Adult Stem Cells. I.M. Conboy, D.V. Schaffer, M.H. Barcellos-Hoff, and S. Li, editors. Humana Press, Totowa, NJ. 65–87. https://doi.org/10.1007/978-1-60761-063-2_5

Renner, M., Y. Domanov, F. Sandrin, I. Izeddin, P. Bassereau, and A. Triller. 2011. Lateral diffusion on tubular membranes: Quantification of measurements bias. *PLoS One*. 6:e25731. https://doi.org/10.1371/journal.pone.0025731

Saffman, P.G., and M. Delbrück. 1975. Brownian motion in biological membranes. *Proc. Natl. Acad. Sci. USA*. 72:3111–3113. https://doi.org/10.1073/pnas.72.8.3111

Sbalzarini, I.F., and P. Koumoutsakos. 2005. Feature point tracking and trajectory analysis for video imaging in cell biology. *J. Struct. Biol*. 151:182–195. https://doi.org/10.1016/j.jsb.2005.06.002

Schmerl, B., N. Gimber, B. Kuropka, A. Stumpf, J. Rentsch, S.A. Kunde, J. von Sivers, H. Ewers, D. Schmitz, C. Freund, et al. 2022. The synaptic scaffold protein MPP2 interacts with GABAA receptors at the periphery of the postsynaptic density of glutamatergic synapses. *PLoS Biol*. 20:e3001503. https://doi.org/10.1371/journal.pbio.3001503

Schnitzbauer, J., M.T. Strauss, T. Schlichthaerle, F. Schueder, and R. Jungmann. 2017. Super-resolution microscopy with DNA-PAINT. *Nat. Protoc*. 12:1198–1228. https://doi.org/10.1038/nprot.2017.024

Singer, S.J., and G.L. Nicolson. 1972. The fluid mosaic model of the structure of cell membranes. *Science*. 175:720–731. https://doi.org/10.1126/science.175.4023.720

Spector, I., F. Braet, N.R. Shochet, and M.R. Bubb. 1999. New anti-actin drugs in the study of the organization and function of the actin cytoskeleton. *Microsc. Res. Tech*. 47:18–37. https://doi.org/10.1002/(SICI)1097-0029(19991001)47:1<18:AID-JEMT3>3.0.CO;2-E

Suzuki, K., K. Ritchie, E. Kajikawa, T. Fujiwara, and A. Kusumi. 2005. Rapid hop diffusion of a G-protein-coupled receptor in the plasma membrane as revealed by single-molecule techniques. *Biophys. J*. 88:3659–3680. https://doi.org/10.1529/biophysj.104.048538

Vassilopoulos, S., S. Gibaud, A. Jimenez, G. Caillol, and C. Leterrier. 2020. Ultrastructure of the axonal periodic scaffold reveals a braid-like organization of actin rings. *Nat. Commun.* 10:5803. https://doi.org/10.1038/s41467-019-13835-6

Virtanen, P., R. Gommers, T.E. Oliphant, M. Haberland, T. Reddy, D. Cournapeau, E. Burovski, P. Peterson, W. Weckesser, J. Bright, et al. 2020. SciPy 1.0: Fundamental algorithms for scientific computing in Python. *Nat. Methods.* 17:261–272. https://doi.org/10.1038/s41592-019-0686-2

van der Walt, S., J.L. Schönberger, J. Nunez-Iglesias, F. Boulogne, J.D. Warner, N. Yager, E. Gouillart, T. Yu, and scikit-image contributors. 2014. scikit-image: Image processing in Python. *PeerJ.* 2:e453. https://doi.org/10.7717/peerj.453

Wang, T., W. Li, S. Martin, A. Papadopulos, M. Joensuu, C. Liu, A. Jiang, G. Shamsollahi, R. Amor, V. Lanoue, et al. 2020. Radial contractility of actomyosin rings facilitates axonal trafficking and structural stability. *J. Cell Biol.* 219:e201902001. https://doi.org/10.1083/jcb.201902001

Weiß, K., A. Neef, Q. Van, S. Kramer, I. Gregor, and J. Enderlein. 2013. Quantifying the diffusion of membrane proteins and peptides in black lipid membranes with 2-focus fluorescence correlation spectroscopy. *Biophys. J.* 105:455–462. https://doi.org/10.1016/j.bpj.2013.06.004

Xu, K., G. Zhong, and X. Zhuang. 2012. Actin, spectrin, and associated proteins form a periodic cytoskeletal structure in axons. *Science.* 339: 452–456. https://doi.org/10.1126/science.1232251

Yan, R., K. Chen, and K. Xu. 2020. Probing nanoscale diffusional heterogeneities in cellular membranes through multidimensional single-molecule and super-resolution microscopy. *J. Am. Chem. Soc.* 142: 18866–18873. https://doi.org/10.1021/jacs.0c08426

Zhang, X., J.Q. Davis, S. Carpenter, and V. Bennett. 1998. Structural requirements for association of neurofascin with ankyrin. *J. Biol. Chem.* 273:30785–30794. https://doi.org/10.1074/jbc.273.46.30785

Zhong, G., J. He, R. Zhou, D. Lorenzo, H.P. Babcock, V. Bennett, and X. Zhuang. 2014. Developmental mechanism of the periodic membrane skeleton in axons. *Elife.* 3:e04581. https://doi.org/10.7554/eLife.04581

Zhou, R., B. Han, R. Nowak, Y. Lu, E. Heller, C. Xia, A.H. Chishti, V.M. Fowler, and X. Zhuang. 2022. Proteomic and functional analyses of the periodic membrane skeleton in neurons. *Nat. Commun.* 13:3196. https://doi.org/10.1038/s41467-022-30720-x

Zhou, R., B. Han, C. Xia, and X. Zhuang. 2019. Membrane-associated periodic skeleton is a signaling platform for RTK transactivation in neurons. *Science.* 365:929–934. https://doi.org/10.1126/science.aaw5937

JCB

Supplemental material

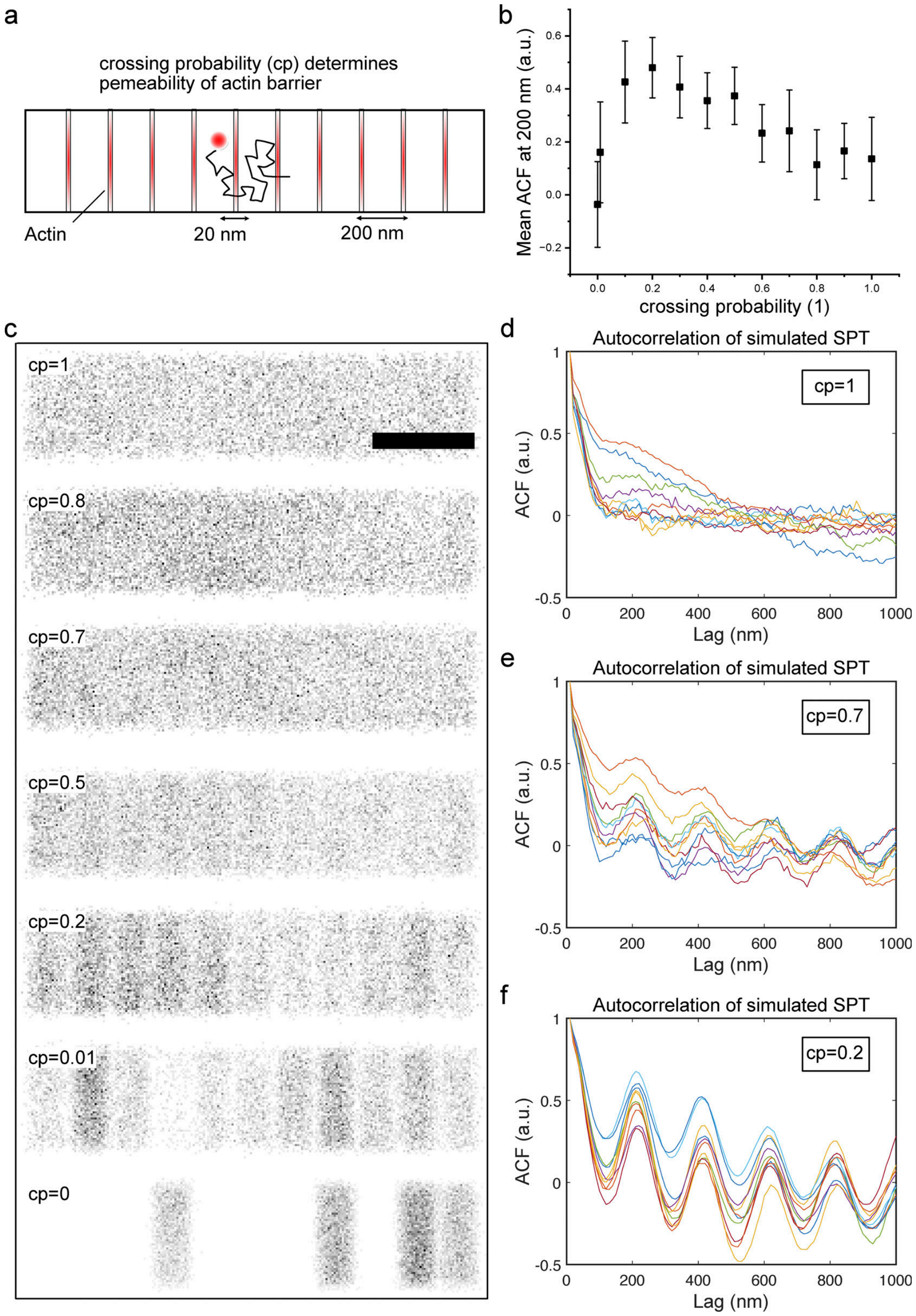

Figure S1. **Simulation of SPT experiments to investigate the permeability of the actin barrier. (a)** Schematic representation of the model geometry that was used. The crossing probability (cp) is a measure of the likelihood that a particle will be able to pass through the actin barrier. **(b)** Single-molecule localization reconstructions were generated using Fluosim from simulations of particles moving randomly over the model geometry in (a). 10 reconstructions per cp were used to determine the mean peak at 200 nm of the autocorrelation function. Error bars indicate standard deviation. **(c)** Exemplary reconstructions of simulated SPT experiments for varying cp's. Note that domains become apparent at cp = 0.7. Very low cp leads to confinement of molecules, prohibiting the exploration of the geometry. **(d)** Autocorrelation function (ACF) of reconstruction described in (a) for cp = 1. Since actin is fully permeable, no peaks in the autocorrelation function can be detected. **(e)** Like (d), but for cp = 0.7. A periodicity of ~200 nm is clearly apparent in all reconstructions. **(f)** Like (d), but for cp = 0.2. Scale bar is 500 nm.

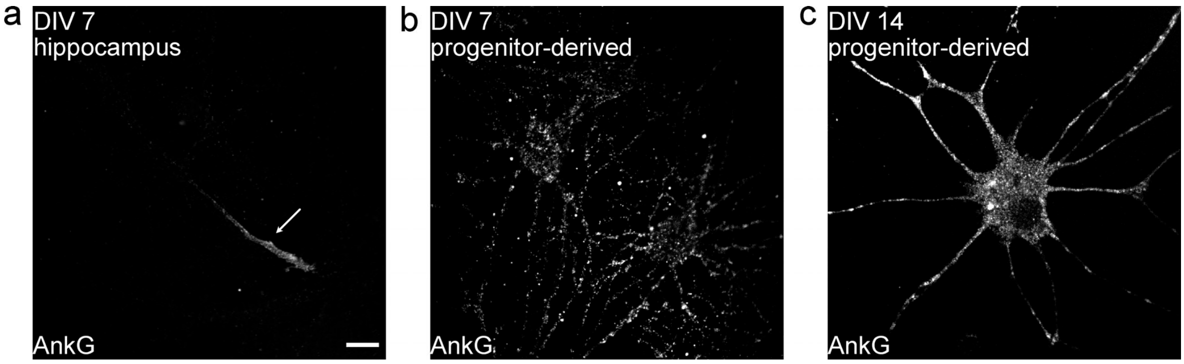

Figure S2. **Progenitor-derived neuronal cells do not show AnkG accumulation required for targeting of large channel proteins to the AIS. (a)** Confocal image of a DIV7 rat hippocampal neuron stained for AnkG. Image shows characteristic AnkG accumulation in the AIS (see arrow). **(b)** Same as (a) but for DIV7 progenitor-derived neuronal cells. No AnkG accumulation. **(c)** Same as (a) but for DIV14 progenitor-derived neuronal cells. Even at DIV14 no AnkG accumulation can be detected. Scale bar is 10 µm.

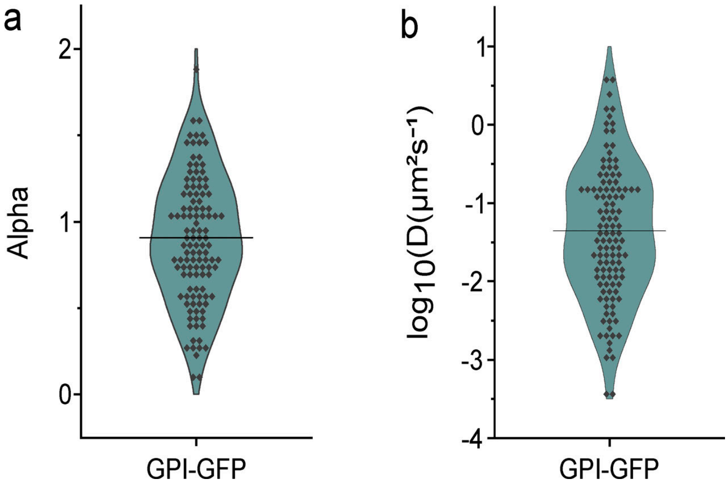

Figure S3. **GPI-GFP in membrane domains remains mobile and unconfined. (a)** Violin plot of alpha exponents in Fig. 3 e. Lines indicated mean. Mean alpha = 0.9. **(b)** Like (a) but for diffusion coefficients. Geometric mean D = 0.04 µm^2 s^{-1}.

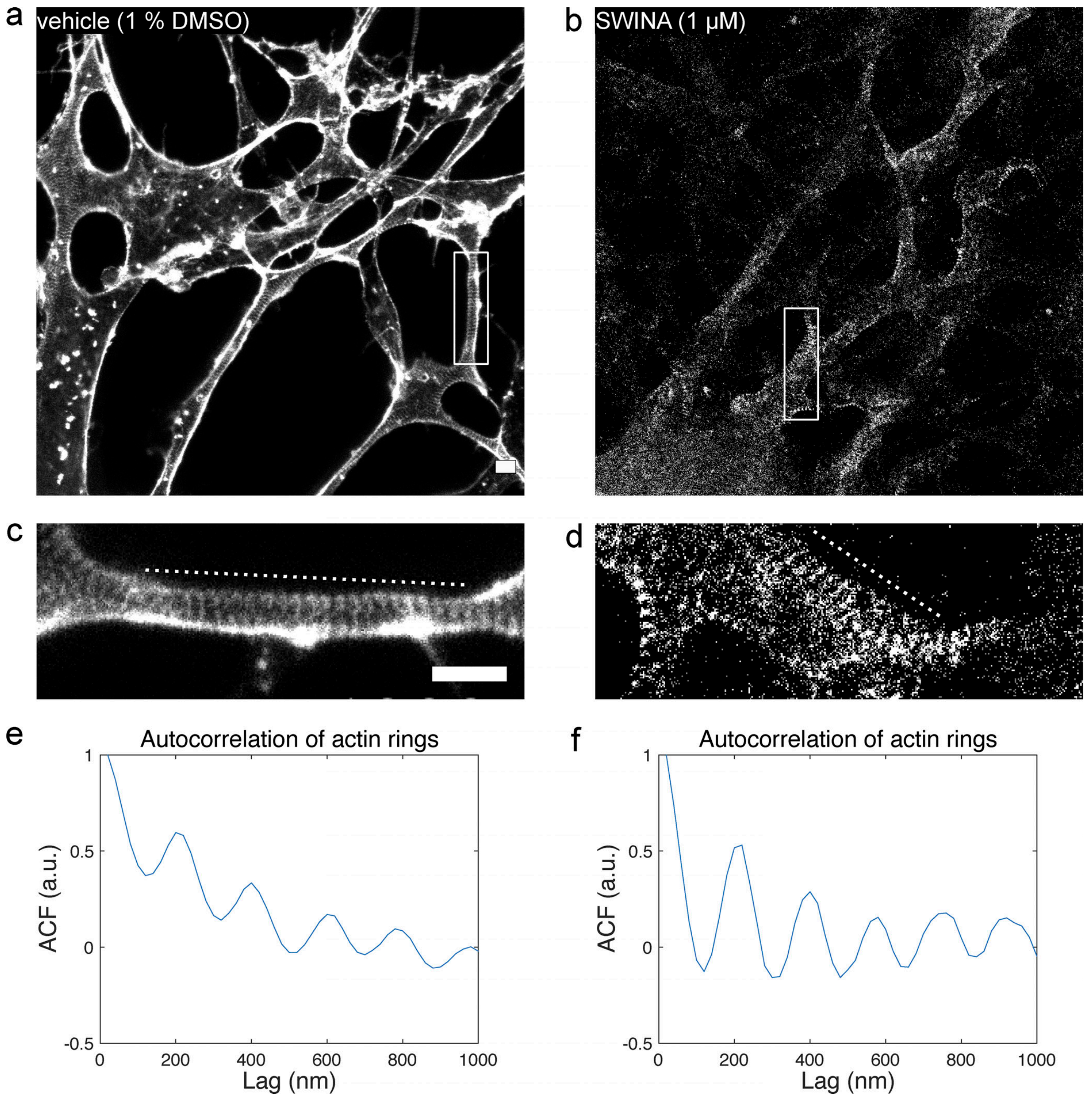

Figure S4. **SWIN A disrupts actin rings in progenitor-derived neuronal cells. (a)** STED image of DIV6 progenitor-derived neuronal cells treated with 1% (vol/vol) DMSO for 30 min and subsequently fixed and stained for actin using phalloidin. **(b)** Like (a), but neuronal cells were treated with 1 µM SWIN A for 30 min. **(c)** Zoom-in of box in (a). Actin rings are ubiquitous in control cells. **(d)** Zoom-in of box in (b). Actin rings are disrupted in SWIN A treated cells. **(e)** Autocorrelation function (ACF) along dotted line in (c) shows periodicity of actin rings ~200 nm. **(f)** Like (e), but for dotted line in (d). Even though actin rings are disrupted in SWIN A treated cells, they remain partially intact. Scale bars are 1 µm.

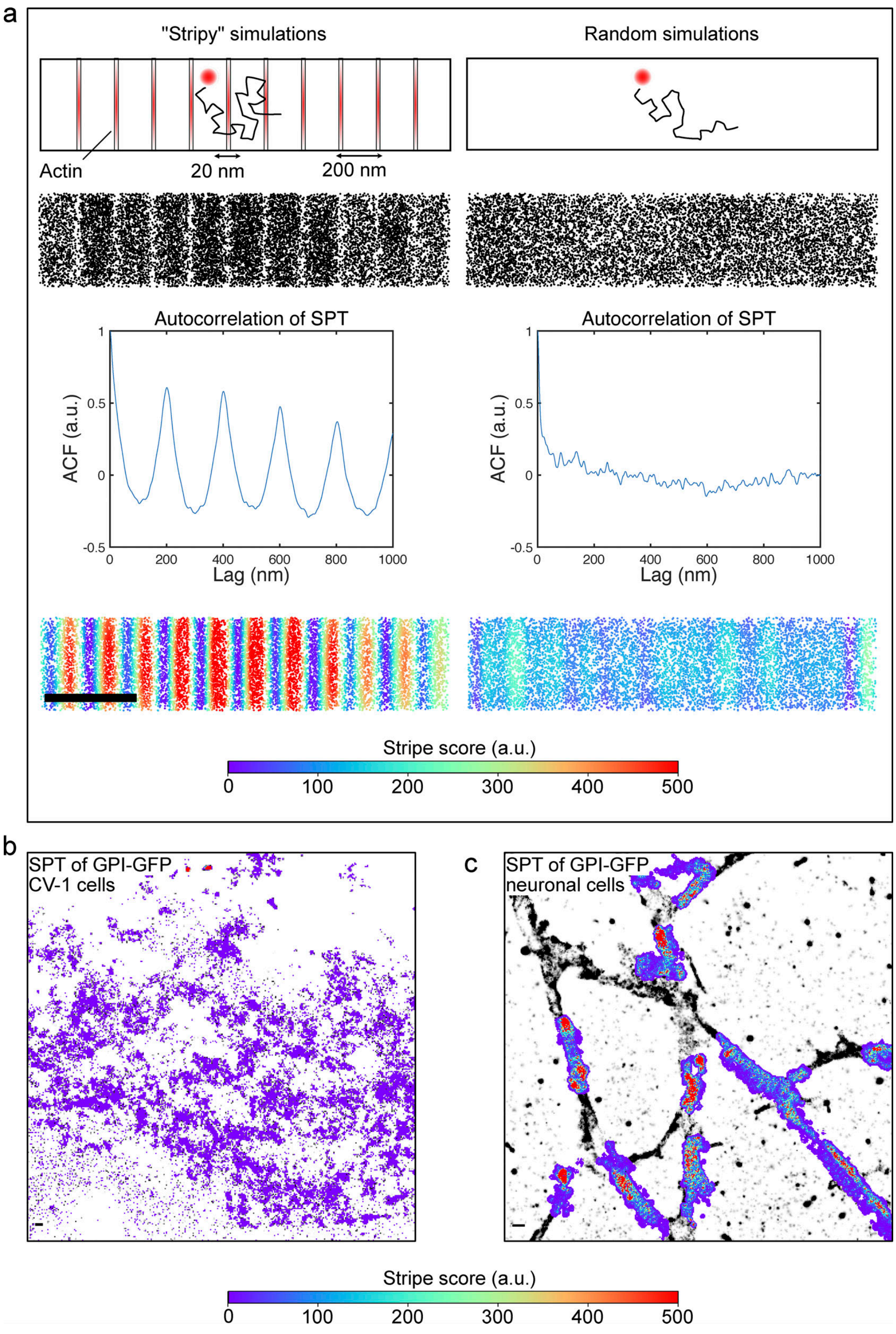

Figure S5. **Automated detection of periodicity at 190 nm via Stripefinder. (a)** Single molecule localizations were generated using Fluosim from particles moving Brownian over the model geometries (top) to generate either "stripy" or random datasets. Middle top: Stripes are apparent in the stripy reconstructions of the localizations, absent for random datasets. Middle bottom: Autocorrelation function (ACF) reveals periodicity of ~200 nm for stripy datasets and not for random datasets. Bottom: Localizations were analyzed using a Fourier transformation–based custom software (Stripefinder) to calculate a local stripe score that was lower, when no stripes were detected. **(b)** Stripefinder finds no stripes in localizations of GPI-GFP in CV-1 cells. GPI-GFP was tracked using anti-GFP-NB-conjugated QDs (20,000 frames, 200 Hz). **(c)** Stripefinder finds stripes in localizations of GPI-GFP in progenitor-derived neuronal cells. GPI-GFP was tracked using anti-GFP-NB-conjugated QDs (5,000 frames, 200 Hz). Scale bars are 500 nm.

Video 1. **GPI-GFP forms membrane domains around the circumference of the axon.** 3D reconstruction of localizations of SPT experiment of GPI-GFP tagged with QDs (5,000 frames, 200 Hz frame rate) in DIV7 rat hippocampal neurons of the area shown in Fig. 1 d. Scale bar is 500 nm.

Video 2. **Raw data of SPT experiment of GPI-GFP in neurons.** SPT experiment of GPI-GFP tagged with QDs (5,000 frames, 200 Hz frame rate) in DIV7 rat hippocampal neurons of area shown in Fig. 1 d. Scale bar is 500 nm.

Video 3. **Synthetic raw data of SPT experiment.** Synthetic SPT data was generated in Fluosim of particles diffusing over the geometry shown in Fig. 1 g. Parameters were chosen to mimic experimental data (crossing probability 30%, fluorophore spot size 150 nm, intensity 200, switch on/off rate 0.5 Hz, 5,005 frames, 200 Hz frame rate) and motion blur and Poisson noise were added. Scale bar is 500 nm.

Video 4. **GPI-GFP is more likely to be localized between actin rings in progenitor-derived neuronal cells.** GPI-GFP was tracked (5,000 frames, 200 Hz frame rate) in progenitor-derived neuronal cells. Cells were subsequently fixed and stained for actin using phalloidin. Shown is an overlay of a STORM reconstruction of actin (magenta) and a movie of accumulated GPI-GFP localizations during 1 s (cyan) of area shown in Fig. 5 b. Scale bar is 500 nm.

5.2 Synapsin condensation controls synaptic vesicle sequestering and dynamics

Journal: Nature Communications

DOI: 10.1038/s41467-023-42372-6

Authors: Christian Hoffmann, Jakob Rentsch, Taka A. Tsunoyama, Akshita Chhabra, Gerard Aguilar Perez, Rajdeep Chowdhury, Franziska Trnka, Aleksandr A. Korobeinikov, Ali H. Shaib, Marcelo Ganzella, Gregory Giannone, Silvio O. Rizzoli, Akihiro Kusumi, Helge Ewers and Dragomir Milovanovic

Author contributions: Jakob Rentsch, Christian Hoffmann and Taka A. Tsunoyama contributed equally to the work. Jakob Rentsch performed all single molecule tracking experiments in live cells (CV-1 cells and mouse hippocampal neurons), analyzed data and prepared figures relating to those experiments. Helge Ewers supervised all single molecule tracking experiments in live cells. Christian Hoffman performed all reconstitution experiments, analyzed related data and created related figures. Christian Hoffmann cloned constructs. Taka A. Tsunoyama and Akihiro Kusumi performed *in vitro* single molecule tracking, analyzed related data and created related figures. Rajdeep Chowdhury, Ali H. Shaib, and Silvio O. Rizzoli performed 3D STED microscopy and analyzed related data. Gregory Giannone advised on single molecule microscopy. Christian Hoffmann, Akshita Chhabra, Aleksandr A. Korobeinikov and Marcelo Ganzella performed partitioning measurements, analyzed related data and generated related figures. Gerard Aguilar Perez and Franziska Trnka performed other experiments in neurons. Christian Hoffmann, Jakob Rentsch, Taka A. Tsunoyama, Akihiro Kusumi, Helge Ewers, and Dragomir Milovanovic wrote the paper. Dragomir Milovanovic conceptualized the study. All the authors read and approved the final version of the paper.

nature communications

Article

https://doi.org/10.1038/s41467-023-42372-6

Synapsin condensation controls synaptic vesicle sequestering and dynamics

Received: 23 February 2023

Accepted: 9 October 2023

Christian Hoffmann[1,7], **Jakob Rentsch**[2,7], **Taka A. Tsunoyama**[3,7], **Akshita Chhabra**[1], **Gerard Aguilar Perez**[1], **Rajdeep Chowdhury**[4], **Franziska Trnka**[1], **Aleksandr A. Korobeinikov**[1], **Ali H. Shaib**[4], **Marcelo Ganzella**[5], **Gregory Giannone**[6], **Silvio O. Rizzoli**[4], **Akihiro Kusumi**[3], **Helge Ewers**[2] & **Dragomir Milovanovic**[1] ✉

Neuronal transmission relies on the regulated secretion of neurotransmitters, which are packed in synaptic vesicles (SVs). Hundreds of SVs accumulate at synaptic boutons. Despite being held together, SVs are highly mobile, so that they can be recruited to the plasma membrane for their rapid release during neuronal activity. However, how such confinement of SVs corroborates with their motility remains unclear. To bridge this gap, we employ ultrafast single-molecule tracking (SMT) in the reconstituted system of native SVs and in living neurons. SVs and synapsin 1, the most highly abundant synaptic protein, form condensates with liquid-like properties. In these condensates, synapsin 1 movement is slowed in both at short (i.e., 60-nm) and long (i.e., several hundred-nm) ranges, suggesting that the SV-synapsin 1 interaction raises the overall packing of the condensate. Furthermore, two-color SMT and super-resolution imaging in living axons demonstrate that synapsin 1 drives the accumulation of SVs in boutons. Even the short intrinsically-disordered fragment of synapsin 1 was sufficient to restore the native SV motility pattern in synapsin triple knock-out animals. Thus, synapsin 1 condensation is sufficient to guarantee reliable confinement and motility of SVs, allowing for the formation of mesoscale domains of SVs at synapses in vivo.

Neurons are highly polarized cells with the axonal length being orders of magnitude larger than the diameter of a cell body. SVs are often clustered in specific three-dimensional regions within synaptic boutons along the axons[1–3]. However, SV diffusion goes against their localization[4,5]: The volume of an axon is much larger than the volume of a bouton, implying that there needs to be a mechanism allowing for SVs to accumulate and remain at the synapses.

Decades of research have established that SVs are clustered by synapsin 1, an SV-associated phosphoprotein abundant at synapses[6]. The genetic data strongly support a synapsin-dependent mechanism of SV clustering. Analyses of synapses in situ[7] and in culture[8] indicate that both the total number and the packing of SVs drop significantly in synapsin knock-out animals. Furthermore, an acute antibody-mediated perturbation of synapsin abolishes SV

---

[1]Laboratory of Molecular Neuroscience, German Center for Neurodegenerative Diseases (DZNE), 10117 Berlin, Germany. [2]Institute of Chemistry and Biochemistry, Freie Universität Berlin, 14195 Berlin, Germany. [3]Membrane Cooperativity Unit, Okinawa Institute of Science and Technology Graduate University (OIST); Onna-son, Okinawa 904-0495, Japan. [4]University Medical Center Göttingen, Institute for Neuro- and Sensory Physiology, Germany; Biostructural Imaging of Neurodegeneration (BIN) Center, Göttingen, Germany; Excellence Cluster Multiscale Bioimaging, 37073 Göttingen, Germany. [5]Department of Neurobiology, Max Planck Institute for Multidisciplinary Sciences, 37077 Göttingen, Germany. [6]Interdisciplinary Institute for Neuroscience, University of Bordeaux, UMR 5297, F-33000 Bordeaux, France. [7]These authors contributed equally: Christian Hoffmann, Jakob Rentsch, and Taka A. Tsunoyama. ✉e-mail: dragomir.milovanovic@dzne.de

clusters in the lamprey giant axons both at rest[9] and upon stimulation[10].

The classical view postulates that synapsins crosslink SVs together in a "scaffold" of protein-protein interactions between synapsin and its binding partners[11,12]. Yet, the exceptionally high concentrations of synapsins in boutons (i.e., 120 μM)[13] suggests them being more than just a modifiable scaffold for SVs[14]. Recent studies showed that synapsin 1 alone can cluster lipid vesicles via liquid-liquid phase separation (LLPS)[7,15]. While LLPS is an intrinsic property of synapsins, the synapsin condensates recruit SV integral proteins (e.g., synaptophysin[16], VGLUT1[17]) and soluble synaptic proteins (intersectin[7], alpha-synuclein[18]) through multivalent interactions. However, key questions remain unanswered, including what is the nature of accumulation and motility of SVs in synaptic boutons, and—just as important—does the region of synapsin 1 responsible for LLPS suffice to give rise to the specific diffusion properties and confinement of SVs in synaptic boutons? To address these questions, we scrutinize the dynamics of synapsin 1 and SVs both in a minimal reconstitution system and in living neurons capitalizing on the (ultrafast) single-molecule imaging.

Results

Reconstitution of synaptic vesicle/synapsin condensates

We first pursued a minimalist approach to reconstitute synaptic vesicle (SV)/synapsin condensates. Untagged, EGFP- and Halo7-tagged synapsin 1, hereafter referred to as synapsin 1, were purified using a mammalian expression system (Supplementary Fig. 1). Untagged synapsin 1 formed condensates similarly to tagged chimeric versions of the protein, as visualized by phase contrast microscopy. Native SVs were isolated from murine brains (Supplementary Fig. 2) and co-assembled with synapsin 1-driven condensates, as visualized upon the addition of FM 4–64 dyes to visualize SV lipid bilayer (Fig. 1a). SV/synapsin 1 condensates readily underwent fusion/fission, relaxing in round structures minimizing their surface tension (Fig. 1b). Note that doping the SV condensates with lipophilic FM 4–64 dye sometimes indicated a stronger signal at the periphery in several independent reconstitutions, presumably due to the penetration of dye or the local uneven distribution of SVs.

Next, we wanted to determine whether the presence of SVs affects the ability of synapsin 1 condensates to accumulate small solutes. To achieve this, we prepared the condensates and incubated them with fluorescently-tagged dextran[19,20]. This is further facilitated when the average mesh size of the pores within synapsin 1 condensates is larger than the hydrodynamic radius of dextran. Homogenous synapsin 1-only condensates accumulated 4.4 kDa (hydrodynamic radius ~2 nm) and 65.85 kDa dextran (hydrodynamic radius ~6 nm) while excluding 155 kDa dextran (hydrodynamic radius ~10 nm) (Supplementary Fig. 3). However, SV/synapsin 1 condensates could incorporate only 4.4 kDa while readily excluding 65.85 and 155 kDa dextran (Fig. 1c, d). To accommodate dextran, the loss of the enthalpy by the breakage of the synapsin-synapsin interactions needs to be compensated by the sum of the enthalpy of synapsin-dextran interaction and the increase in the mixing entropy. Thus, from our data, we can conclude that the presence of SVs (~40 nm diameter) increases the enthalpy of synapsin-dextran and decreases the mixing entropy thereby reducing the effective molecular weight cut-off from ~6 nm to ~2 nm (Fig. 1e). That SVs modulate the meshwork pore size of synapsin condensates was further confirmed by incubating the condensates with a mixture of fluorescently-tagged nanobody and primary/secondary antibody conjugates (Supplementary Fig. 4). While small nanobodies are readily enriched within condensates, the presence of SVs prevents larger primary/secondary antibody conjugates from penetrating inside the synapsin/SV condensates.

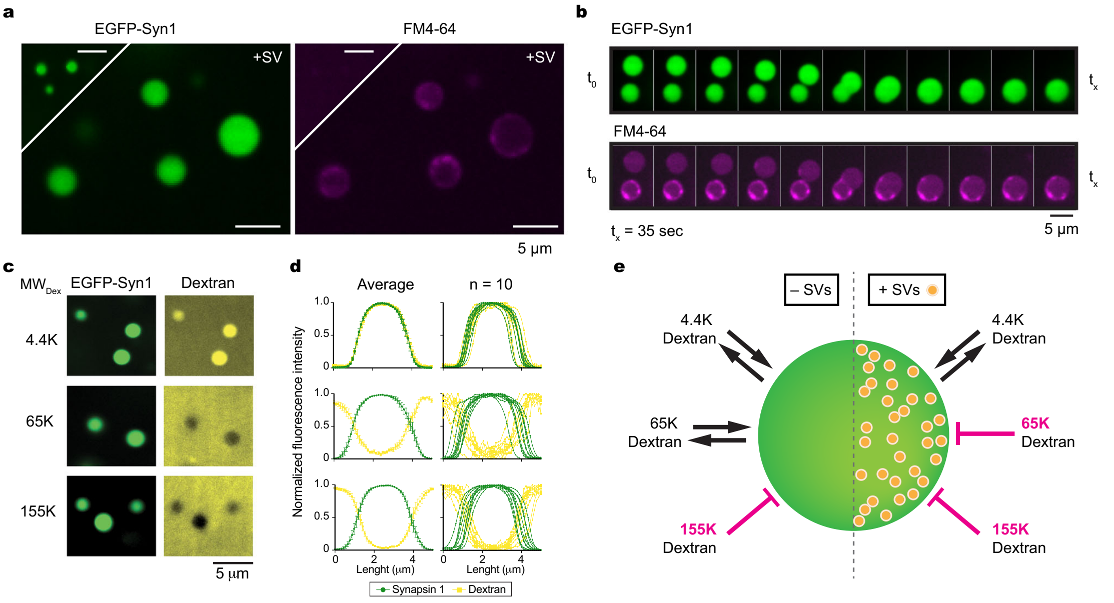

Fig. 1 | Synapsin 1 and synaptic vesicles (SVs) form condensates. a Confocal image of reconstituted EGFP-synapsin 1 (10 μM) in the absence (top) or presence (bottom) of natively isolated SVs (3 nM) doped with FM 4-64 dye to visualize the lipid bilayer. **b** Timelapse of synapsin 1/SV condensates fusing over a period of 35 s. **c** Confocal images of synapsin 1/SV condensates upon incubation with fluorescently-labeled dextran of 4.4 kDa (top), 65.85 kDa (middle), and 155 kDa (bottom) panels. **d** Line profiles indicating either enrichment or exclusion of fluorescently-labeled dextran of different molecular weights in synapsin 1/SV condensates. Left, an average ± SEM; right, exemplary line profiles. For each condition ten condensates of similar size from three independent reconstitutions are analyzed. **e** Scheme summarizing the effects of SVs on the average diameter of meshwork pore size in synapsin-driven condensates. Scale bars, 5 μm. Source data are provided as a Source Data file.

Single-molecule detection of synapsin 1 in the condensates in vitro

Ensemble measurements of protein dynamics inside condensates, such as recovery after photobleaching, are quite useful for homogenous media but fail to distinguish short-range and long-range interactions and dynamics in non-homogeneous mixtures. To address this challenge, we turned to single-molecule tracking (SMT) coupled with total internal reflection fluorescence (TIRF) microscopy, which allowed us to obtain both high spatial (tens of nm) and temporal (ms) resolution of tracking. We reconstituted SV/synapsin 1 condensates that contained 1% of EGFP-tagged synapsin 1 (for visualizing the condensates), and 0.1% of Halo7(JF549)-synapsin 1 (for single-molecule tracking) on the cover-glass, and imaged the condensates with diameters between 2 ~ 4 μm on the cover-glass with a focus near their equatorial planes (Fig. 2a, b). The presence of 1% EGFP-tagged synapsin 1 hardly affected the diffusion properties of Halo7-synapsin 1 (Supplementary Fig. 5a).

We investigated the behaviors of Halo7-synapsin 1 at the level of single molecules projected onto the two-dimensional x–y plane (for single-molecule localization precisions at 60-, 250-, and 1000-Hz observations, see Supplementary Fig. 5b, Supplementary Movie 1). First, we found that Halo7-synapsin 1 molecules in the condensate exchange with those in the bulk solution (Fig. 2b). For semi-quantitative analysis of the exchange rate, we identified synapsin 1 molecules that newly arrived at the condensate surface within the focal plane from the medium and measured the durations until they either left the condensate or became photobleached. Approximately 3 ~ 7% of Halo7-synapsin 1 molecules entered/disappeared from the field of view by diffusion in the z-direction, and we did not include these molecules in our quantitative analysis, since we concentrated our efforts on the analysis of the behaviors of Halo7-synapsin 1 molecules in the x–y plane, the percentages of these molecules were quite limited, and the z-direction behaviors would be the same as those in x–y planes in the core volume of the condensate, which was defined as regions >500 nm away from the surface. The distributions of dwell durations revealed the presence of two populations of synapsin 1 molecules with the shorter (≈0.76 s) and longer (≈27.1 s) dwell lifetimes in both condensates without and with SVs. As the shorter and longer dwell lifetimes were quite similar for the condensates, regardless of the SV presence, we use the average lifetimes to describe the shorter and longer fractions. These lifetimes were corrected for the photobleaching lifetime of JF549 dye (for statistical parameters, see Fig. 2c and Methods). The presence of SVs led to a 21% increase in the longer component (with a corresponding reduction in the shorter dwell lifetime component, Fig. 2c). These findings suggest that SVs interact with synapsin 1, consequently modulating its dynamics within the condensates.

SVs globally suppress synapsin 1 diffusion in the condensates in vitro

Next, we examined the single-molecule movements of Halo7(JF549)-synapsin 1 in the core region of the condensates, projected onto the x–y plane (Fig. 2d). To avoid the strong edge effect caused by the projection, we selected synapsin 1 molecules located >500 nm away from the edge. Synapsin molecules exhibited rapid diffusion, both in the absence and presence of SVs. The analysis of single-molecule trajectories can be conveniently performed by plotting the mean-square displacement (MSD) against the elapsed time (Δt) (ensemble averaged over many observed molecules; Fig. 2e; Supplementary Fig. 5c; Methods). Such MSD-Δt plots could be simply analyzed by the equation, $\mathrm{MSD} = 4D_\alpha(\Delta t)^\alpha$, where D_α represents the diffusion coefficient near $\Delta t = 0$ and α represents the anomaly parameter. The anomaly parameter indicates the deviation of the observed diffusion from simple Brownian diffusion ($\alpha = 1$) and becomes smaller ($0 \le \alpha < 1$) as the diffusion is more suppressed (subdiffusion).

We evaluated the single-molecule behaviors over a very broad range of time intervals, from a few milliseconds up to 3.2 s, to observe the possible long-range orders of synapsin 1 interaction and dynamics within the condensates and the effects of SVs, which are sparsely distributed in our SV-synapsin 1 reconstituted condensates, on synapsin 1 movements across various spatial ranges. To achieve this, we employed three different camera frame rates: 60, 250, and 1000 Hz (frame times of 16.7, 4, and 1 ms, respectively). Additionally, we generated 15-Hz and 30-Hz single-molecule trajectories (frame times of 67 and 33.3 ms, respectively) by re-sampling longer 60-Hz trajectories. Observations at various frame rates were necessary because, while ideal, 1000-Hz observations for up to 3.2 s (3200 frames) are impossible due to photobleaching. The MSD-Δt plots for 50 steps are presented for all the frequencies (Fig. 2e; note that the actual time in the x-axis is 50x the camera frame time and that the y-axis scales were varied accordingly), whereas the plot for 300 steps at 60-Hz (5 s) confirmed that the MSD-Δt plots based on 15- and 30-Hz re-sampled data were adequate (Fig. 2f).

The anomaly parameters (α's) obtained from the MSD-Δt plots in Fig. 2e are plotted against the total observation durations (the full x-axis scales in Fig. 2e) in Fig. 2g. Since all α values are <1, this result indicates that synapsin 1 diffusion within the condensate is suppressed from that expected for the simple-Browinan case, often called subdiffusion, even in the absence of SVs. This is likely to represent that the synapsin 1 condensates provide environments like a crowded and/or porous medium for the diffusion of synapsin 1 molecules that form the condensates, consistent with the dextran incorporation data (Fig. 1c–e). Smaller α values in the presence of SVs for the same observation duration indicate that the synapsin 1 diffusion is more suppressed in the condensates with SVs.

The plots in Fig. 2g demonstrate that the diffusion anomaly increases with longer observation durations for both condensates without and with SVs and that the reduction of α values slowly levels off in the duration range >0.83 s. To the best of our knowledge, such α dependences on the observation duration in protein condensates have not been reported thus far and are quite interesting. Such α dependences on the observed time duration are related to the diffusion suppression as a function of the diffused area. For instance, during a duration of 0.83 s, in the absence and presence of SVs, synapsin 1 molecules exhibited diffusion on the order of 2.7 and 1.7×10^{-2} μm^2 in MSD (60-Hz data in Fig. 2e) corresponding to ranges of (160- and 130-nm)^2, which are equivalent to ~16 and 13 molecules of synapsin 1 and to 4 and 3.3 SVs, respectively. Further reductions of α-values for longer observation durations, 1.67 s and 3.3 s, for both condensates without and with SVs would indicate that there exist longer-range correlation lengths in the condensates than those covered here up to the observation time scale of 3.3 s (the space scales greater than a few tens of synapsin 1 molecules). This dependence of α on the observed time duration suggests that direct but multiple synapsin 1-synapsin 1 interactions propagate at least to a few tens of synapsin 1 molecules, which is consistent with the network mechanisms that protein condensates are considered to form[21]. Meanwhile, at all the temporal (and thus spatial) scales examined here, the SV-induced further suppression of synapsin 1 diffusion is evident.

Importantly, the SV-induced slowdown of synapsin 1 diffusion was also observed at a much shorter time scale of ≈3 ms (Fig. 2h). The diffusion coefficients for individual Halo7-synapsin 1 molecules were determined from their MSD-Δt plots in the range of 2 ~ 4 ms (without ensemble averaging) using 1000-Hz data ($D_{3\mathrm{ms}}$), and their distributions are shown in Fig. 2h. In the presence of SVs in the condensates, both the mean and median $D_{3\mathrm{ms}}$ values were smaller than those in the condensate without SVs. The distributions indicate a shift of the major peak toward smaller $D_{3\mathrm{ms}}$ values, rather than the emergence of a secondary smaller peak for lower $D_{3\mathrm{ms}}$ values, in the condensates containing SVs. This shift suggests that the presence of SVs broadly

https://doi.org/10.1038/s41467-023-42372-6

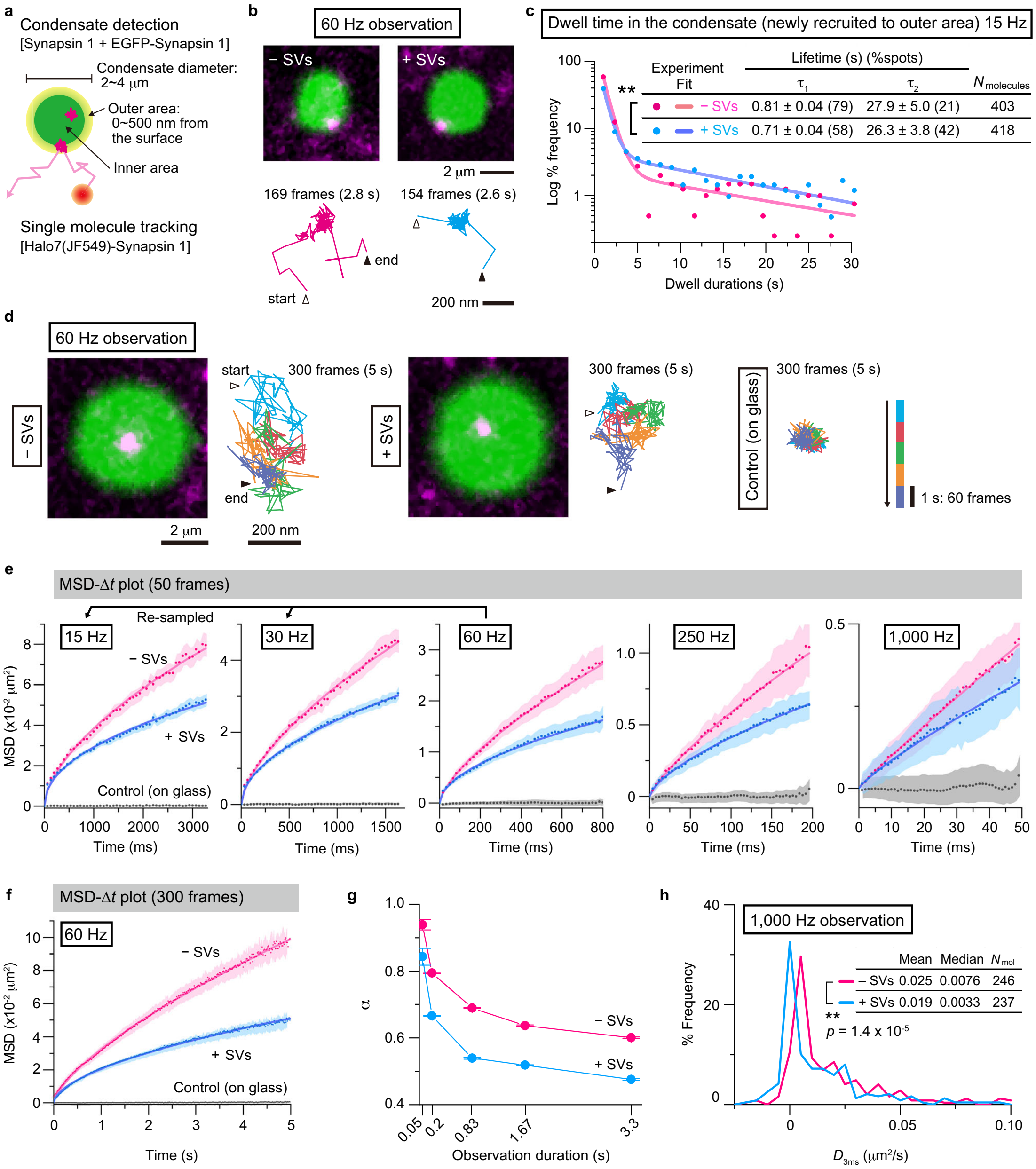

Fig. 2 | Ultrafast SMT of synapsin 1 revealed the liquid properties of the SV/synapsin condensates. a Schematic drawing showing the design of synapsin 1 SMT experiments in the condensates in vitro. **b** Typical (among 314 and 356 Halo7(JF549)-synapsin 1 molecules in the experiments with and without SVs, respectively) fluorescence microscopy images of the synapsin 1 condensates marked by EGFP-synapsin 1 (green), recruiting a single Halo7(JF549)-synapsin 1 molecule (magenta), (top) and the representative trajectories of single Halo7(JF549)-synapsin 1 molecules (bottom). The images were recorded at 60 Hz in the absence (left) and presence (right) of SVs. **c** Distributions of the dwell durations of single Halo7-synapsin 1 molecules in the condensates; $p = 9.81 \times 10^{-14}$. **d** Representative (among 276 and 328 Halo7(JF549)-synapsin 1 molecules in the experiments with and without SVs, respectively) microscopy images including the Halo7-synapsin 1 molecules in the core regions, together with their trajectories in the condensates core region. Control for immobile Halo7-synapsin 1 is also shown. The colors indicate the passage of time (see the time scale on the right). **e** The MSD-Δ*t* plots for Halo7-synapsin 1 molecules located in the inner volume (mean ± SEM). The full x-scales of all plots are 50 steps (50 frames). The number of observed molecules: 237, 237, 276, 317, and 246 (without SV, magenta); 307, 307, 328, 327, and 237 (with SV, cyan); and 242, 242, 476, 397, and 239 (on glass, gray), for frame rates of 15, 30, 60, 250, and 1000 Hz, respectively. For the offset value of the MSD, see Supplementary Fig. 5c. **f** The long-term MSD-Δ*t* plots (300 frames, 60 Hz; mean ± SEM). **g** The diffusion anomaly parameter (α) depends on the total observation durations (mean ± SEM). **h** The distributions of the diffusion coefficients determined in the range of 2 - 4 ms, called $D_{3\text{ms}}$, evaluated from the trajectories obtained at 1000 Hz. $p = 1.41 \times 10^{-5}$; $^{**}P < 0.01$, using Brunner-Munzel test for (**c**) and (**h**). Source data are provided as a Source Data file.

impacts the synapsin 1 diffusion in the condensate, rather than merely slowing the movement of synapsin 1 molecules bound on the surfaces of the SVs.

Considering that SVs occupy only a minor fraction of the volume in our reconstituted condensates (vesicle-to-protein ratio = 1:3000) mimicking a mere few percent of the synapse's total volume, the findings presented in Fig. 2g (α dependences on the observed time duration) and 2 h (D_{3ms} distributions) imply that SVs suppress the diffusion of synapsin 1 located on the SV surfaces through direct molecular interactions, and this slowing effect propagates quite far to exert a global effect, likely due to the synapsin 1 interactions that are indeed responsible for the condensate formation. Since the SVs are sequestered into condensates by the interaction with synapsin 1 molecules, it would be reasonable to conclude that this interaction reciprocally slows the dynamics of synapsin 1, although synapsin molecules continue to exchange rapidly between the condensates and the surrounding medium.

In addition, we examined the diffusion of the free JF549 dye in the synapsin 1 condensates without and with SVs in case that the unbound dye dominated the results described here (Supplementary Fig. 5d). From the MSD-Δt plots, the diffusion of free dye is clearly much faster than those incubated with Halo7-synapsin 1. However, interestingly, the free dye also exhibited more suppressed diffusion (smaller anomaly parameter) in the condensates with SVs. This might be due to the small size of the dye, which allows its transient local accumulation in the condensates.

Single-molecule imaging of synapsin 1 and SVs in live neurons

We then aimed to scrutinize the motility of synapsin and SVs in living neurons. We co-transfected primary hippocampal neurons with Halo7-synapsin 1 (synapsin 1) and synaptophysin-mEos3.2 (synaptophysin), a bona-fide SV marker, and synapsin 1 was labeled with fluorogenic dye Janelia Fluor 635 (JF635). Single-molecule localization in live neurons showed a clear accumulation of synapsin 1 in synaptic boutons and its colocalization with SVs (Fig. 3a, Supplementary Movie 2). This stereotypical localization allowed us to separately assess the motility of synapsin 1 and SVs within and between boutons by performing two-color SMT experiments along the axon (Fig. 3b). In contrast to synaptophysin-mEos3.2 which is almost exclusively confined inside boutons (Fig. 3b, c), synapsin 1 is present along the entire axons (Fig. 3b, d). Although enriched at the synaptic boutons, synaptophysin remains mobile with a mean diffusion coefficient of 0.049 ± 0.005 $\mu m^2 s^{-1}$ and the anomaly parameter α of 0.65 ± 0.014 (Fig. 3f,g). For an integral membrane protein, the surprisingly high apparent diffusion of synaptophysin may result from its oligomerization in the membrane of SVs[22], the pronounced membrane fluidity of SV bilayer[23], and the motion of SV as a whole. Given that the spatial resolution achieved in the live tracking experiments (~15 nm) is in the same range as the average radius of SVs (~20 nm[24]), it is not possible to distinguish between the movement of individual synaptophysin molecules in the SV membrane and the overall movement of SVs. Rather, we use the motility of synaptophysin here as a proxy for the relative motility of SVs. Interestingly, we identified two populations of synapsin 1 (Fig. 3e, h, i): the first is confined at synaptic boutons (geometric mean diffusion = $0.051\,\mu m^2 s^{-1}$ and $\alpha = 0.65 \pm 0.024$), while the second is much less confined (geometric mean diffusion = $0.18\,\mu m^2 s^{-1}$ and $\alpha = 0.84 \pm -0.044$) and exhibits high diffusivity between boutons (Fig. 3e, h, i) resembling the motility of mEos3.2 tag alone (Supplementary Fig. 7). Calculated from the number of trajectories, we observed a ~3-fold enrichment of synapsin 1 molecules inside versus outside boutons. This pattern of synapsin 1 diffusion remains independent of expression levels, as indicated in our measurements of synapsin 1 on one- and 2 days post-transfection (Supplementary Fig. 6). To delineate synapsin 1 confinement driven by LLPS from diffusion occurring outside the condensates in the boutons and in between the boutons due to non-specific crowding, we compared the motion of mEos3.2 alone with that of mEos3.2-synapsin 1 (Supplementary Fig. 7). Indeed, mEos3.2-synapsin 1 was more confined and less mobile inside boutons than soluble mEos3.2 despite their molecular weight being within the same order of magnitude. This indicates that the confinement of synapsin 1 in boutons is a specific effect independent of molecular crowding.

To avoid selection bias, we repeated the entire experimental pipeline and filtered the acquired trajectories not by location (e.g., inside or outside synaptic boutons) but rather by the level of confinement with 0–0.75 for confined motion and >1.25 for directed motion (Supplementary Fig. 8). Importantly, we identify a similar pattern with two population of synapsin 1 molecules with a largely confined and mobile population inside synaptic boutons. The trajectories of synapsin 1 that followed directed motion were only appearing between neighboring boutons.

Additionally, we generated synapsin 1 condensates in non-neuronal cells, where synapsin is not endogenously expressed. Functionally, these synapsin 1 condensates actively recruit SVs and SV-like vesicles in the reconstituted systems[16]. Specifically, we co-transfected CV-1 cells with plasmids encoding synapsin 1 and a concatemer of SH3 domains of intersectin. Intersectin is a cytoplasmic membrane-associated protein, which contains multiple SH3-domains essential for the generation of liquid-liquid phase separated condensates[25]. Indeed, we observed the formation of condensates in CV-1 cells reminiscent to synapsin 1 condensates in primary neurons. In these ectopically-formed condensates synapsin 1 was accumulated and confined irrespectively whether the condensates were induced by co-expression of mEos3.2-synapsin 1 with the SH3 concatemer, Grb2, or synaptophysin (Supplementary Fig. 9), strongly suggesting that synapsin 1 has the capacity to form condensates irrespectively of SVs both in vitro, in neurons and in ectopic systems. However, the presence of other components in the system and local differences in ion and protein composition may regulate the viscoelastic properties of these condensates[20].

IDR of synapsin 1 is crucial for SV motility and confinement in vivo

To complement our analysis in synapses in cultured neurons of wild-type mice, we turned to a murine model where all three synapsin genes are deleted (i.e., synapsin triple knock-out mice, SYN-TKO). Here, the number of SVs and their packing in the synapses were shown to be significantly lower both in neurons in culture and in brain slices[7,8]. We investigated the motility and level of confinement of SVs in SYN-TKO neurons (Fig. 4 a–c, Supplementary Fig. 10). Indeed, SVs were significantly more mobile and less confined in SYN-TKO than in wild-type neurons (Fig. 4 e, f). Importantly, we fully rescued both the confinement and motility of SVs in SYN-TKO neurons expressing full-length mEos3.2-synapsin 1 (Fig. 4 d–f). Synapsin 1 diffusion is independent of the type of tag used for tracking, mEos3.2 or Halo7 (Supplementary Fig. 7). In contrast to the clear effect of synapsin 1 on SV motion in SYN-TKO neurons, there was no effect of co-expression of synaptophysin on synapsin 1 motility or confinement in wild-type neurons (Supplementary Fig. 7). This is congruent with the genetic analysis that the number of totally available SVs remains unaltered by the expression levels of synaptophysin[26].

Synapsin 1 contains a large intrinsically disordered region (IDR)[27]. IDRs are sequences of amino acids that do not fold into any stable secondary or tertiary structure. IDR of synapsin 1 (a.a., 416-705, syn1-IDR) was shown to be necessary and sufficient for triggering LLPS in vitro[7,10]. Thus, we suspected that syn1-IDR is sufficient for the unique diffusion signature of SVs. To test this, we purified syn1-IDR (Supplementary Fig. 1) and reconstituted it with natively isolated SVs. Indeed, the condensates of syn1-IDR were able to sequester SVs similar to the full-length proteins (Supplementary Fig. 11). We further expressed syn1-

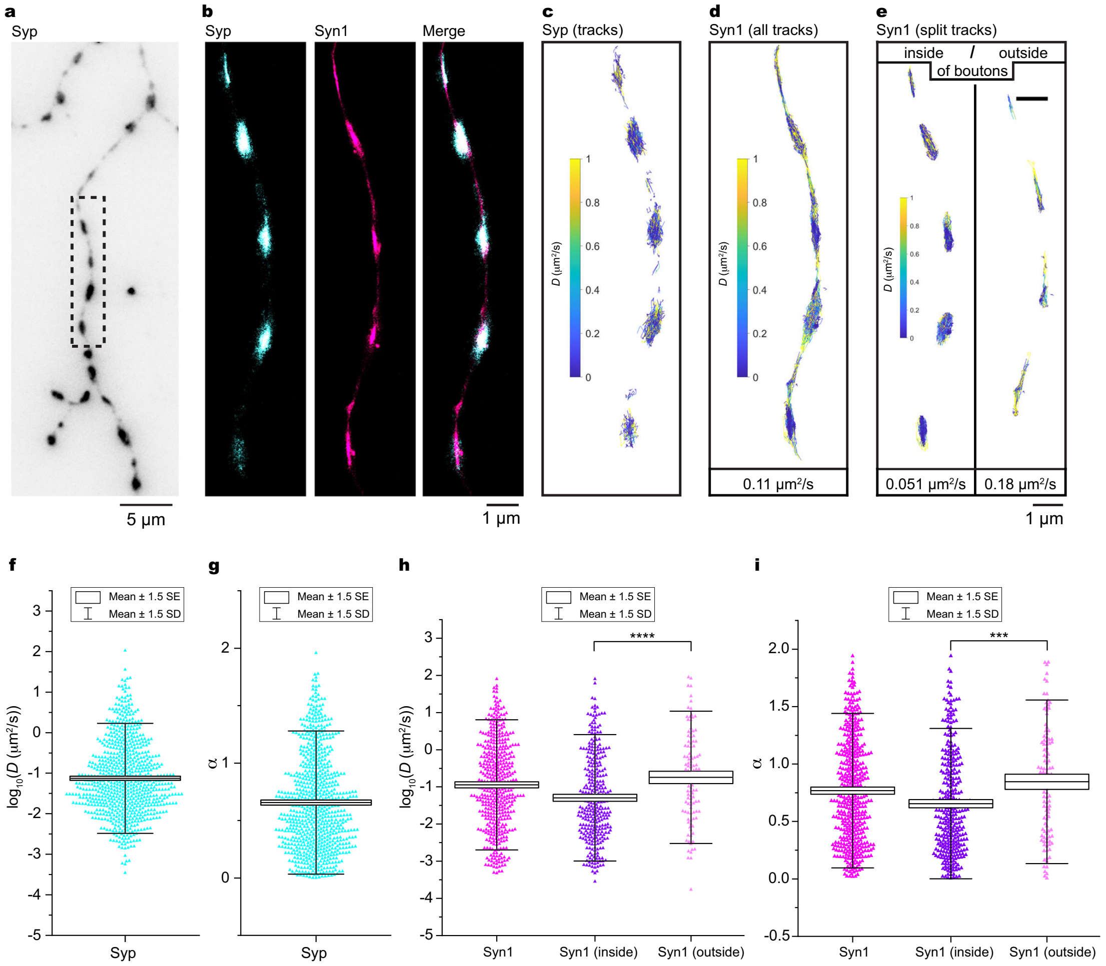

Fig. 3 | Synapsin 1 and synaptophysin are confined at synaptic boutons while maintaining their high motility. a Single-molecule localization image of a neuron expressing synaptophysin-mEos3.2. Mouse hippocampal neurons (14 days in culture) were transfected with synaptophysin-mEos3.2 (Syp) and Halo7-synapsin 1 (Syn1). **b** Single-molecule localization reconstruction of proteins localized within dashed box in (**a**). Dual-color single-molecule tracking of Syp or Syn1 coupled to JF635 were performed at 100 Hz for 50 s. **c** Map of all tracks ($n = 775$) of Syp within dashed box in (**a**) color-coded for diffusion coefficient. Note that Syp is almost exclusively confined at synaptic boutons. **d** Map of Syn1 within dashed box in (**a**) color-coded for diffusion coefficients indicating all tracks ($n = 464$). **e** Syn1 tracks inside synaptic boutons (left, $n = 337$) and between boutons (right, $n = 116$), indicating 2.9x enrichment of synapsin 1 inside boutons. Values indicate the geometric mean diffusion coefficient for each panel. Boxplots (mean ± 1.5 x SD (whiskers) and 1.5 x SEM (box)) showing diffusion coefficients (**f**) and the coefficient of confinement (α) (**g**) for all tracks of Syp shown in (**c**). Boxplots (mean ± 1.5 x SD (whiskers) and 1.5 x SEM (box)) showing diffusion coefficients (**h**) and α (**i**) for all and grouped tracks of Syn1 shown in (**d**, **e**). Significance was tested using Mann–Whitney test; asterisks, statistical significance; n.s., not significant. Note that Syn1 is significantly slowed down (**h**, $p = 1.4 \times 10^{-5}$,***) and confined (**i**, $p = 1.2 \times 10^{-4}$,****) in synaptic boutons. Source data are provided as a Source Data file.

IDR in SYN-TKO neurons. 3D stimulated depletion emission (STED) microscopy indicates that syn1-IDR is targeted to the synaptic bouton similarly to synapsin 1 full-length (Fig. 4a). The syn1-IDR not only rescued the phenotype that is, the clustering of SVs in boutons (Supplementary Fig. 12) but also led to a further reduction in motility of SVs as compared to either wild-type neuron or a rescue with a full-length synapsin 1 (Fig. 4d–f). This clearly indicates that syn1-IDR is sufficient to generate condensates and to recruit SVs to them in vivo. In addition to changes in diffusive behavior, we observed a decrease in accumulation of SVs in boutons in SYN-TKO neurons as compared to wild-type neurons, as reported previously[7,8]. This lack of accumulation was fully rescued by the expression of full-length synapsin 1. Overexpression of just syn1-IDR in SYN-TKO neurons was already sufficient to trigger an increase of SVs accumulation in synaptic boutons (Fig. 4b, c).

This raised an important question whether syn1-IDR would be sufficient to rescue the clustering of SVs in vivo. To assess this question, we turned to functional analysis of SV exocytosis by using pH-sensitive probe (i.e., the luminal domain of synaptophysin that contains pHluorin) and performed the rescue experiments in SYN-TKO neurons (Supplementary Fig. 14, Supplementary Movie 3). Excitingly, both IDR and full length of synapsin 1 rescued the SV release in SYN-TKO neurons (Fig. 4g). This is particularly interesting since synapsins 2 and 3 contain shorter IDR and no IDR, respectively[27]. In wild-type synapses, synapsins can heterodimerize through their highly-conserved, dimerization motif[28]. Yet syn1-IDR solely was sufficient to recapitulate clustering and secretion of SVs. As these are hippocampal neurons in culture and the chemical stimulation with high (90 mM) potassium chloride is comparatively strong to common physiological

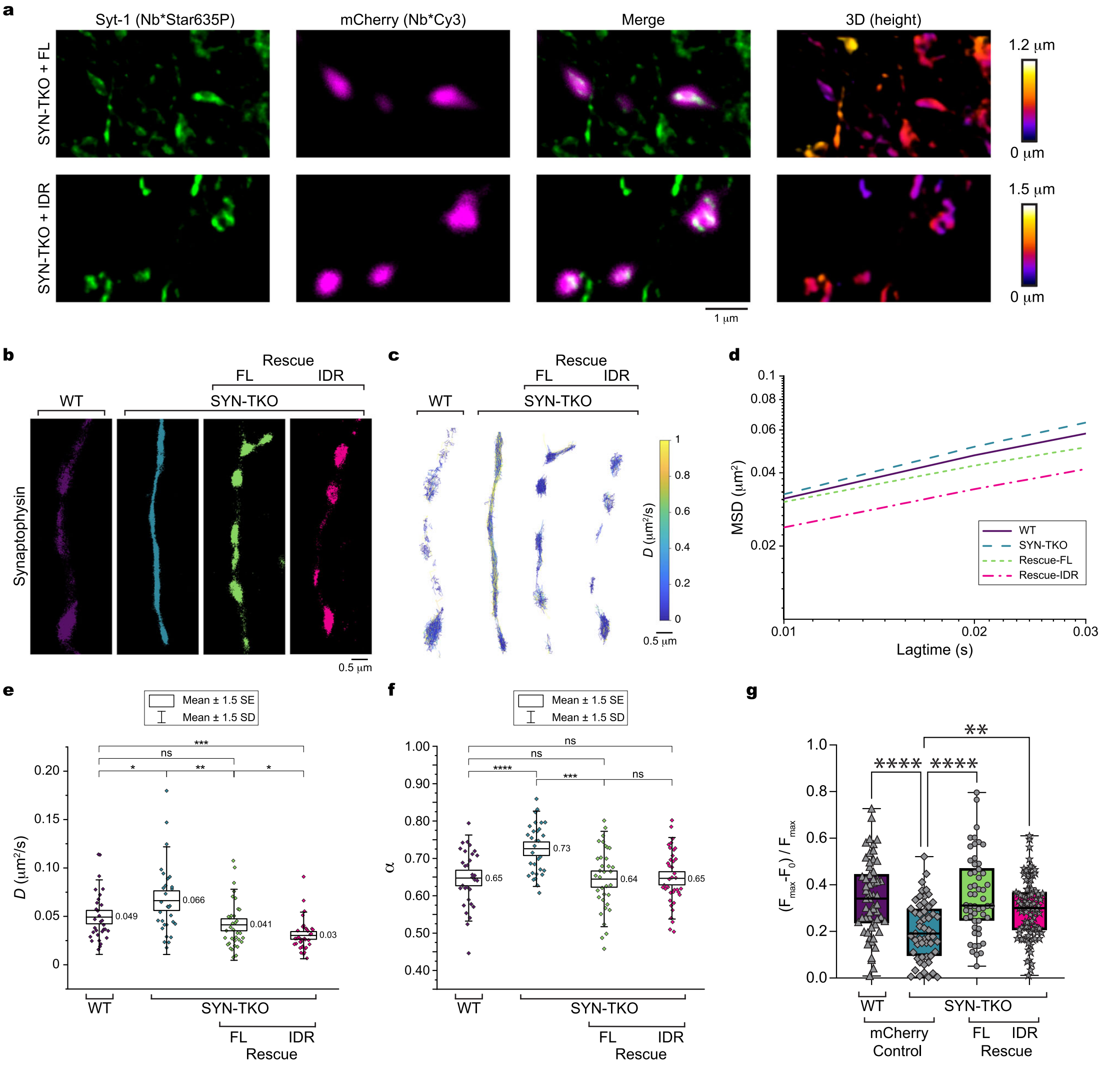

Fig. 4 | Synapsin determines the confinement and diffusion rates of SVs. a 3D-STED imaging of synapsin triple knockout (SYN-TKO) neurons expressing mCherry-tagged full-length (top) or the intrinsically disordered region (IDR; bottom) of synapsin 1. Primary hippocampal neurons were fixed and stained with fluorescently-tagged nanobodies against synaptotagmin–1, a bona fide synaptic vesicle protein (Nb*Star635P, STED channel), and against mCherry (Nb*Cy3, confocal channel). **b** Single-molecule localization reconstructions from tracking experiments of synaptophysin-mEos3.2 (Syp) performed at 100 Hz for 50 s. Mouse hippocampal neurons (14 days in culture) from wild-type or SYN-TKO animals were transfected with Syp. Rescue experiments were done by co-transfecting SYN-TKO neurons with Syp and either full-length synapsin 1 (Rescue FL) or IDR of synapsin 1 (Rescue IDR). **c** Images of all Syp tracks for each condition. **d** Mean log(MSD)-log(lag)-plot for all tracks per condition. Note that the rescue with IDR shows even greater reduction of motility than the FL rescue. **e** Boxplots (mean ± 1.5 x SD (whiskers) and 1.5 x SEM (box)) showing the geometric mean diffusion coefficients per tracking experiment of at least four independent neuronal preparations and a total of 77,675 analyzed tracks. **f** Same as in (*e*) but showing the mean coefficient of confinement (α) per tracking experiment (WT, *n* = 31; SYN-TKO, *n* = 31; Rescue-FL, *n* = 35; Rescue-IDR, *n* = 39). In *e* and *f*, the significance was tested using Mann-Whitney test; asterisks indicate significance: $^{*}p < 0.1$; $^{**}p < 0.01$; $^{***}p < 0.0001$; $^{****}p < 0.00001$; ns, not significant. Note that SVs are significantly faster and more dispersed in the absence of synapsins. **g** SV release measured as an increase in fluorescence of pH-sensitive EGFP variant tagged to the luminal region of synaptophysin upon chemical stimulation with KCl (90 mM). Wild-type or SYN-TKO neurons from three independent neuronal preparations were co-transfected with only a soluble red fluorophore, synapsin FL or the synapsin IDR.Significance was tested using one-way ANOVA test; asterisks, significance: $^{**}p < 0.01$; $^{***}p < 0.0001$. Original data are provided as a Source Data file.

stimuli, the specific protein-protein interactions or distinct synapsin isoforms might be central to regulate the secretion across different frequencies[29].

Importantly, to avoid bias by the type analysis chosen, we analyzed the data generated from single-molecule tracking experiments in three different ways: by treating each tracking experiment as a data point (Fig. 4c, e, f), by treating each track as a data point (Supplementary Fig. 13), or by calculating MSD-lagtime-curves (Fig. 4 d). Regardless of the analysis type, the observed trends of synapsin 1 and SV diffusion remained the same. Interestingly, taking the amount of synapsin 1 (ectopically expressed in the absence or presence of endogenous synapsin) as a proxy for the total protein concentration, the data suggests that the increased levels of synapsin 1 further confine and reduce the motion of SVs as reminiscent to the in vitro phase diagrams[19]. Taken together, we conclude that synapsin 1 is a master regulator of SV motility and confinement at synaptic boutons in living neurons.

Discussion

Through the quantitative characterization of synapsin 1 and SV dynamics, the findings reported here strongly support that condensation of synapsins and SVs suffices to induce SV microdomain formation without the need for a (complex) 'molecular fence' that would restrict SVs within a bouton. This does not exclude an additional role for protein–protein interactions between either integral membrane proteins or soluble proteins. In fact, these seem essential for exchanging the SVs between neighboring synapses[17] or reincorporating newly endocytosed vesicles[30,31].

The enrichment of SVs in synaptic boutons by LLPS has clear consequences for neuronal transmission. For example, our in vivo measurements show that SVs maintain their motility in synaptic boutons despite them being confined in a synapsin-dependent manner (Fig. 4). SV release can occur at a wide range of different stimulation frequencies[32]: during low-activity, docked SVs and SVs at the interface would be recruited for fusion, whereas, during prolonged activity, the synapsin 1-driven condensate will provide a reservoir of SVs[29,33]. Initially, it was proposed that synapsins act as tethers by crosslinking the vesicles together[34]. This implies that synapsins play a role in physically connecting the vesicles, thereby maintaining their clustered arrangement. The high local concentration of synapsins suggests them being more than mere crosslinkers of SVs[13,14]. We and the other showed that synapsins can form a liquid phase, effectively ensnaring the synaptic vesicles within it[7,10,18]. In this scenario, synapsins act as a cohesive medium, keeping the vesicles together in a clustered state while allowing for their high motility[4,35,36]. It is also plausible that a combination of both mechanisms occurs, as they are not necessarily mutually exclusive[12].

The diffusive behavior of SVs is completely perturbed in SYN-TKO neurons, being more mobile and less confined. Surprisingly, syn1-IDR was sufficient to restore both the diffusion pattern and the accumulation of SVs at boutons. This may be due to the last patch of amino acids within the IDR, so-called Domain E, which are well-conserved in *a*-type isoforms of all three synapsins[27,37]. We speculate that both the phase separation and the specific interactions provided by these last amino acids may allow for the coupling of SV clustering to neurotransmitter release[38].

Finally, both in vitro (0.019 $\mu m^2/s$) and in living neurons (0.051 $\mu m^2/s$), synapsins maintain their fast motility within these condensates despite their spatial confinement. This allows synapsin molecules to be rapidly phosphorylated by kinases upon the neuronal activity at the interface of condensates without the need for enzymes to fully penetrate into condensates. Thus, the size of meshwork coupled to the internal dynamics of proteins within a condensate provides an additional layer of specificity and allows for SV condensates to act as buffers of proteins and enzymes[39,40].

Collectively, our findings that SV/synapsin condensation is sufficient for vesicle sequestering and dynamics strongly support that such interactions constitute a mechanism for the formation of organelle microdomains in the cytosol by a small set of proteins. We suggest that a cooperation of mechanisms that create mesoscale domains of vesicles and proteins plays a role in other types of cellular assemblies[41,42], although the precise players implicated in such assemblies and the resulting diffusion patterns will be context-specific.

Methods

The research in this study complies with all relevant ethical regulations. All animal experiments were approved by the Institutional Animal Welfare Committees of the State of Berlin, Germany and Charité University Clinic (Berlin, DE), as well as State of Lower Saxony, Germany and Max Planck Institute for Multidisciplinary Sciences (Göttingen, DE).

Cloning

His14-SUMO_Eu1-mmSynapsin1a plasmid was created by exchanging the mScarlet-I tag of a *mScarlet-I-mmSynapsin 1a* expression vector (NM_013680.4) with the His14-SUMO_Eu1 tag cassette[43]. The His14-SUMO_Eu1 cassette was amplified from pAV0279 (*His14-SUMO_Eu1-MBP-3xFLAG)* with primers #DML0331 & #DML0332 and inserted into *mScarlet-I-mmSynapsin 1a* vector using *Age*I and *Bgl*II restriction sites.

6His-HaloTag-rnSynapsin 1 plasmid was created by exchanging the EGFP tag with Halo7Tag in an EGFP-rnSynapsin 1a expression vector[7]. The HaloTag was amplified from LYN-Halo7 with primers #DML0195 & #DML0196 and inserted into *EGFP-rnSynapsin 1a* vector using *Age*I and *Bgl*II restriction sites. For Ni-NTA affinity purification, a 6xHis tag was introduced by Annealed Oligo Cloning at the N-terminus of the HaloTag using *Nhe*I and *Age*I (#DML 0438 & 0439).

SYPH-pHluorin plasmid was created by Gibson assembly resulting in the expression of murine synaptophysin M7-A240 (NM_009305.2) with an inserted pH-sensitive GFP cassette (pHluorin[44]) between T190 and C191 under control of a CMV promoter and SV terminator (similar as in[45]). All constructs were verified by sequencing.

For primers and detailed sequences, see Supplementary Tables 1–2. pAV0286 for bacterial expression of SENP_EuB protease and pAV0279 as the template for His14-SUMO_Eu1 were from the lab of Dirk Görlich (Addgene plasmid #149333; http://n2t.net/addgene:149333; RRID:Addgene_149333 and Addgene plasmid #149688; http://n2t.net/addgene:149688; RRID:Addgene_149688)[43].

Protein purification

His14-SUMO_Eu1-mmSynapsin1a was expressed in Expi293F™cells (Thermo Fisher Scientific) for 3 days following enhancement. Cells were lysed in buffer that contained 25 mM Tris-HCl (pH 7.4), 300 mM NaCl, 0.5 mM TCEP (buffer A) supplemented with EDTA-free Roche Complete protease inhibitors, 15 mM imidazole, 10 μg/μL DNaseI and 1 mM $MgCl_2$. All purification steps were carried out at 4 °C. Debris was removed by centrifugation for 30 min at 20,000xg. For batch affinity purification, the soluble supernatant was incubated with complete His-Tag Purification resin (Roche) on a rocking platform for 1 h. Washing steps (buffer A) and elution (buffer A with 400 mM imidazole) were performed by gravity flow in a polyprep column (Biorad). Elution fractions were concentrated using a 30 K MWCO protein concentrator (Pierce) and subjected to size exclusion chromatography (Superdex™ 200 Increase 10/300, GE Healthcare, ÄKTA pure 25 M) in buffer A. Fractions containing *His14-SUMO_Eu1-mmSynapsin1a* were combined and digested overnight with SENP_EuB SUMO protease for tag-cleavage (protease:protein ratio of 1:20). For tag removal, the reaction was supplemented with 15 mM imidazole and passed 3 times over preequilibrated complete His-Tag Purification resin (buffer A). Tag-free mmSynapsin1a protein in the flow-through was concentrated with a 30 K MWCO protein concentrator and subjected to dialysis against 25 mM Tris-HCl (pH 7.4), 150 mM NaCl, 0.5 mM TCEP. Proteins were snap-frozen in liquid nitrogen and stored at -80 °C until further use.

SENP_EuB SUMO protease was recombinantly purified as described previously[43]. Specifically, SENP_EuB SUMO protease was expressed in bacteria (Rosetta (DE3) cells with plasmid pAV0286). The protein expression main culture was grown to an OD_{600} of 1.0 in LB medium containing kanamycin at 37 °C. Protein expression was induced with 0.3 mM IPTG final concentration. After overnight protein expression at 18 °C culture was supplemented with 5 mM EDTA. Cell pellets were harvested and subjected to lysis (French-press) in buffer containing 45 mM Tris-HCl (pH 7.5), 290 mM NaCl, 15 mM imidazole, 4.5 mM $MgCl_2$, 10 mM DTT (buffer B) supplemented with 10 μg/mL DNaseI and a spatula tip of lysozyme. The lysate was cleared by centrifugation for 1 h at 50,000xg (JA25.50) at 4 °C. All purification steps were carried out at 4 °C. For batch affinity purification, the cleared soluble supernatant was incubated with complete His-Tag Purification resin (Roche) on a rocking platform for 1 h. Washing steps (45 mM Tris-HCl (pH 7.5), 500 mM NaCl, 15 mM imidazole, 4.5 mM MgCl$_2$, 10 mM DTT) and elution (buffer B with 400 mM imidazole) were performed by gravity flow in a polyprep column (Biorad). SENP_EuB-containing fractions were subjected to size exclusion chromatography (HiLoad™ 16/600 Superdex™ 200 pg, Cytiva, ÄKTA pure 25 M) in 45 mM Tris-HCl (pH 7.4), 290 mM NaCl, 4.5 mM MgCl$_2$, 2 mM DTT. SENP_EuB fractions were combined and supplemented with 2.5% (v/v) glycerol for storage at -80 °C until use.

EGFP-synapsin 1, EGFP-synapsin 1 IDR (416-705) and *Halo7-synapsin 1* were expressed in Expi293F™cells (Thermo Fisher Scientific) for 3 days following enhancement. Cells were lysed in a buffer that contained 25 mM Tris-HCl (pH 7.4), 300 mM NaCl, 0.5 mM TCEP (buffer A) supplemented with EDTA-free Roche Complete protease inhibitors, 25 mM imidazole, 10 μg/mL DNaseI and 1 mM MgCl$_2$. All purification steps were carried out at 4 °C. Debris was removed by centrifugation for 1 h at 20,000xg. For affinity purification, soluble supernatant was applied on a Ni-NTA column (HisTrap™HP, Cytiva, ÄKTA pure 25 M) for binding. After a wash step (buffer A with 40 mM imidazole) and elution (buffer A with 400 mM imidazole), proteins were concentrated and subjected to size exclusion chromatography (Superdex™ 200 Increase 10/300, GE Healthcare, ÄKTA pure 25 M) in 25 mM Tris-HCl (pH 7.4), 150 mM NaCl, 0.5 mM TCEP. Proteins were snap-frozen in liquid nitrogen and stored at -80 °C until further use.

In vitro Halo7-synapsin 1 labeling

For fluorescent labeling of Halo7-synapsin 1, 250 μg purified protein (in 25 mM Tris-HCl (pH7.4), 150 mM NaCl, 0.5 mM TCEP) was incubated with 0.7 μg Janelia Fluor® HaloTag® ligand (JF549, Promega GA111A; stock: 0.13 μg/μL in DMSO) for 1 h at room temperature. The reaction was applied to PD-10 columns (Sephadex G-25, Cytiva) equilibrated with 25 mM Tris-HCl (pH7.4), 150 mM NaCl, 0.5 mM TCEP. Elution fractions containing labeled Halo7(JF549)-synapsin 1 protein fraction were concentrated using a 30 K MWCO protein concentrator (Pierce) and snap-frozen in liquid nitrogen for storage at -80 °C until use.

Synaptic vesicle preparation

Synaptic vesicles (SVs) were isolated according to previous publications[24,46,47]. Briefly, 20 rat brains (isolated from adult male rats) were homogenized in ice-cold sucrose buffer (320 mM sucrose, 4 mM HEPES-KOH, pH 7.4 supplemented with 0.2 mM phenylmethylsulfonylfluoride and 1 mg/ml pepstatin A). Cellular debris was removed by centrifugation (10 min at 900 g$_{Av}$, 4 °C) and the resulting supernatant was further centrifuged for 10 min at 12,000 g$_{Av}$, 4 °C. The pellet containing synaptosome was washed once by carefully resuspending it in sucrose buffer and further centrifuged for 15 min at 14500 g$_{Av}$, 4 °C. Synaptosomes were lysed by hypo-osmotic shock and free, released SVs were obtained after centrifugation of the lysate for 20 min at 20,000 g$_{Av}$, 4 °C. The supernatant containing the SVs was further ultracentrifuged for 2 h at 230,000 g$_{Av}$, yielding a crude synaptic vesicle pellet. SVs were purified by resuspending the pellet in 40 mM sucrose followed by centrifugation for 3 h at 110,880 g$_{Av}$ on a continuous sucrose density gradient (50–800 mM sucrose). SVs were collected from the gradient and subjected to size-exclusion chromatography on controlled pore glass beads (300 nm diameter), equilibrated in glycine buffer (300 mM glycine, 5 mM HEPES, pH 7.40, adjusted using KOH), to separate synaptic vesicles from residual larger membrane contaminants. SVs were pelleted by centrifugation for 2 hr at 230,000 g$_{Av}$ and resuspended in sucrose buffer by homogenization before being aliquoted into single-use fractions and snap frozen in liquid nitrogen. The weight/volume of SV proteins is related to the copy/number of SVs as described in (*7*).

Reconstitutions

For all reconstitutions, we co-incubated 10 μM synapsin 1 with 1% (w/v) PEG 8000. When synaptic vesicles were included in the reconstitutions, we first added FM4-64 dye to synapsin 1 and then triggered the condensate formation by the addition of 1% (w/v) PEG 8000. Synaptic vesicles (3 nM final concentration) were loaded with a low-binding pipette tips. The assay scheme is shown in Supplementary Data Fig. 2. Reconstitution reactions were performed in a buffer containing 25 mM Tris-HCl (pH 7.4), 150 mM NaCl, 0.5 mM TCEP.

Dextran-based pore size determination. All TMR-dextrans were purchased from Sigma (T1037-50MG, T1162-100MG, T1287-50MG). For pore size analysis of synapsin 1 phase, condensates were formed by incubating 10 μM EGFP-synapsin 1 with 1% (w/v) PEG 8000 on a glass bottom dish (Cellvis D35-20-1.5-N). TMR-dextrans were added to the condensates when they reached an average size of 5 μm in diameter (0.04 mg/mL TMR-dextran final concentration). The participation of dextrans in synapsin 1 phases was analysed by confocal imaging (Eclipse Ti Nikon Spinning Disk Confocal CSU-X, 2 EM-CCD cameras (AndorR iXon 888-U3 ultra EM-CCD), Andor Revolution SD System (CSU-X), objectives PL APO 60x/1.4 NA, oil immersion lens. Excitation wavelengths were: 488-nm for EGFP; 561-nm for TMR).

Nanobody/antibody-based pore size determination. For the analysis of pore size, synapsin 1 condensates were formed by incubating 10 μM synapsin 1 (9 μM non-tagged synapsin 1 + 1 μM Halo7-tagged (JF549 labeled) synapsin 1) with 1% (w/v) PEG 8000 in the presence or absence of 3 nM synaptic vesicles. The reaction was incubated on ice for 5 min before placing on a glass bottom dish. After 10 min a nanobody/antibody premix consisting of FluoTag-X2*AF488 nanobody (NanoTag Biotechnologies, N1202-AF488, anti-Mouse IgG kappa light chain sdAb), anti-LAMP1 antibody (Sigma, L1418, produced in rabbit), and goat-anti-rabbit IgG-Cy5 antibody (Cytiva, RPN999) was added to the synapsin or synapsin/SV condensates on the glass bottom dish (final nano-/antibody concentrations: 0.01 mg/mL, 0.1 mg/mL and 0.01 mg/mL respectively). To test for different partitioning of the nano-/antibodies images were taken after 10 min of incubation (Excitation wavelengths: 488-nm for FluoTag-X2*AF488 nanobody; 561-nm for Halo7-tagged (JF549 labeled) synapsin 1, 647-nm for goat-anti-rabbit IgG-Cy5 antibody).

Sequestering of synaptic vesicles by the full-length or the intrinsically disordered region of synapsin 1. 10 μM EGFP-synapsin 1 or 10 μM EGFP-synapsin 1 IDR (amino acids: 416-705) was incubated with 5% (w/v) PEG 8000 in the presence or absence of 3 nM synaptic vesicles on glass bottom dishes. SVs were preincubated for 5 min on ice with either an SV-specific AbberiorStar635P-labeled anti-Synaptotagmin nanobody (NanoTag Biotechnologies, #N2302-Ab635P-L, FluoTag-X2 anti-Synaptotagmin 1) or lipophilic FM4-64 dye (AAT Bioquest, #21487, MM 4–64 dye) before adding to synapsin condensates with a diameter in the range of 3–4 μm (final concentrations: 125 nM and 1.65 μM respectively). The presence of synaptic vesicles in the condensates was visualized by SDC microscopy (Excitation wavelength: 488-nm for EGFP, 561-nm for FM4-64 and 647-nm for Ab635P-labeled anti-Synaptotagmin 1).

Primary hippocampal neurons

Hippocampal neurons were prepared from P0/1 mice of WT (C57BL/6) or synapsin triple-knockout (SYN-TKO: B6; 129-Syn2tm1Pggd Syn3tm1Pggd Syn1tm1Pggd/Mmjax)[8] background. Brains were manually dissected and hippocampi were collected in cold Hank's balanced salt solution (HBSS, Gibco) containing 10 mM Hepes buffer (Gibco), 1 mM Pyruvic Acid (Gibco), 0.5% penicillin/streptomycin and 5.8 mM Magnesium Chloride. After dissection, hippocampi were enzymatically digested with Papaine (Sigma) in HBSS for 20 min at 37 °C. Papaine was removed with repeated HBSS washing, and plating medium was added (Gibco Neurobasal Medium A [NB-A], supplemented with 5% FBS, 1% B27, 1x Glutamax, and 1% penicillin/streptomycin). Final cell suspension was obtained through mechanical dissociation with a P1000 pipette. Cells were seeded on glass coverslips coated with 0.1 mg/mL poly-L-lysine (PLL; Sigma). Neurons were maintained at 37°C and 5% CO_2 in Neuronal Media (NB-A supplemented with 1% B27, 1% Glutamax, and 0.5% penicillin/streptomycin).

Neurons were transfected by calcium phosphate transfection (adapted from[48,49]). In brief, a coverslip with neurons was transferred to a fresh petri dish containing 1 ml growth medium supplemented with 4 mM kynurenic acid (Sigma K3375, 20 mM stock solution in NB-A, freshly prepared). Transfection mix contained 2 μg of each construct in 1x TE (10 mM Tris-HCl (pH 7.3), 1 mM EDTA) supplemented with $CaCl_2$ to a final concentration of 250 mM (stock: 10 mM HEPES (pH7.2), 2.5 M $CaCl_2$). The mix was added dropwise to 2xHEBS (42 mM HEPES (pH 7.2) 274 mM NaCl, 10 mM KCl, 1.4 mM Na_2HPO_4, 10 mM glucose) with slow vortexing between each addition and incubated for 20 min at room temperature. Transfection mix was added to neurons and dishes were incubated at 37 °C, 5% CO_2 for 1.5 h. Medium was replaced by 1 mL of NB-A with 4 mM kynurenic acid supplemented with 2.5 mM HCl. Wash was performed at 37 °C, 5% CO_2 for 15 min. After transfection coverslip was placed back in the original culture dish with own conditioned medium.

Quantifying SV release in primary hippocampal neurons

Images in two channels were taken under the spinning-disc confocal microscope using the wavelengths of 488 nm for the SYPH-pHluorin and of 561 nm for the mCherry/mCherry-synapsin 1. The coverslips containing neurons were mounted in pre-warmed low-KCl Tyrode solution (150 mM NaCl; 4 mM KCl; 2 mM $CaCl_2$; 2 mM $MgCl_2$; 10 mM HEPES; 10 mM glucose; pH at 7.4 using NaOH) before imaging them under the microscope. After an initial z-stack (F_0), high-KCl pre-warmed Tyrode solution (154 mM KCl; 2 mM $CaCl_2$; 2 mM $MgCl_2$; 10 mM HEPES; 10 mM glucose; pH at 7.4 using NaOH) was added to the coverslip to obtain a final concentration of 64 mM NaCl and 90 mM KCl; an established approach for stimulating neurons in culture coupled to live-cell imaging recordings[49]. Immediately after adding the correspondent volume, another z-stack was taken at the same position (F_{max}). Then, NH_4Cl was added to the coverslip to a final concentration of 50 mM, and a final z-stack was acquired. Images were analysed in Fiji, taking the maximum intensity of the selected ROIs for both the low-KCl and high-KCl images. Calculations were performed ($(F_{max} - F_0)/F_{max}$), averaged and plotted.

Single-molecule tracking

High-speed single-molecule tracking in neurons. All samples were imaged using a Vutara 352 super-resolution microscope (Bruker) equipped with a Hamamatsu ORCA Flash4.0 sCMOS camera for super-resolution imaging and a 60x oil immersion TIRF objective with a numerical aperture of 1.49 (Olympus). Immersion Oil (#1261, Cargille) was used for the live-cell tracing in CV-1 cells or primary mouse hippocampal neurons, 14 days in culture. All experiments were done in live cell imaging solution (Thermo Fisher, 14291DJ) at 37 °C. All data acquired in neurons was collected from at least 3 biological replicates from independent preparations. Cells transfected with mEOS3.2-contructs were briefly illuminated with a low-intensity 405 laser (0.0022 kW*cm^{-2}). Afterwards, mEOS3.2-constructs were tracked at 100 Hz for 5000 frames at a laser power of 0.49 kW*cm^{-2} with a 561 nm laser under HiLo-Illumination. Cells transfected with Halo7-constructs were incubated with 100-500 pM JF635-Halo7 for 5 min. Afterwards, cells were washed with live cell imaging solution. Then, Halo7-labeled constructs were tracked at 100 Hz for 5000 frames at a laser power of 0.57 kW*cm^{-2} with a 641 laser under HiLo-Illumination. For dual-color measurements, tracking of Halo7- and mEOS3.2- constructs was performed sequentially as described above.

Data processing of single-molecule tracking data. Acquired raw data were localized using SRX (Bruker). Localizations were estimated by fitting single emitters to a 3D experimentally determined point spread function (PSF) under optimization of maximum likelihood. The maximum number of localization iterations performed before a given non-converging localization was discarded, was set to 40. PSFs were interpolated using the B-spline method[50]. For single molecule localization reconstructions, locations were rendered according to their Thomson accuracy[50]. For single-molecule tracking analysis, localizations were exported using SRX (Bruker) and tracked in 3D using the FIJI Mosaic tracker plugin (Linkrange: 1, Displacement: 5)[51]. Diffusion coefficients and alpha exponents were calculated in Mosaic[51]. All tracks were filtered according to their α ($2 > \alpha > 0$). For further analysis the mean alpha and geometric mean diffusion coefficient of all tracks per measurement were calculated.

We analyzed the single-molecule tracks either according to their localization (i.e., regions in boutons vs. the regions outside boutons) or the filtering of the tracks according to coefficient of confinement ($0 \leq \alpha \geq 0.75$) vs super-diffuse ($1.25 \leq \alpha \geq 2$). In the latter approach, the tracks of intermediate confinement including the Brownian motion ($0.75 \leq \alpha \geq 1.25$) are filtered out completely. Statistical tests for significance (Mann-Whitney) were performed in Origin (OriginLab). Alternatively, all tracks of all measurement per conditions were pooled to calculate log(MSD):log(Δt) curves using a self-written MATLAB code (MathWorks).

In vitro ultrafast SMT of synapsin 1. Synapsin condensates were reconstituted, as described above, in the final solution containing 150 mM NaCl and 0.5 mM TCEP buffered with 25 mM Tris–HCl, pH 7.4. Final synapsin 1 concentrations were 10 μM, 100 nM, and 10 nM for non-tagged, GFP-tagged, and Halo7-tagged (JF549 labeled) molecules, respectively. After the addition of a final concentration of 1% PEG 8000 (Sigma Aldrich, P5413), the mixed solution was placed on the glass-bottom slide (Ibidi, 81507). All observations were finished within 15 min after PEG addition.

Fluorescently labeled molecules were excited by oblique-angle illumination using an objective-lens-type TIRF microscope, which was constructed on an Olympus inverted microscope (IX-83) equipped with a 100x 1.49 NA objective lens (Olympus, UApoN 100x TIRF). The incident excitation laser intensities at the sample plane were 8.2 μW/μm^2 for the 488-nm line for GFP (Coherent, Sapphire 488-300 CW), 1.4, 5.7, and 12.7 μW/μm^2 for the 561-nm line for JF549 (MPB Communications, Fiber 560-20000) for the observation frame rates of 60, 250, and 1000 Hz, respectively (note 1 μW/μm^2 = 0.1 kW/cm^2). The simultaneously-obtained two-color fluorescence images were separated into two detection arms of the microscope by a dichromatic mirror (Chroma, ZT561rdc-UF3), filtered through band-pass filters of ET525/50 m or ET600/50 m (Chroma), and the images were projected onto the high-speed camera system (Photron, mini AX200-II) described previously[52,53]. The final magnification was 250x (~80 nm/pixel; square pixels). Under these observation conditions, localization precisions were determined with dyes fixed on the glass: 22.1 and 22.5 nm for x- and y-coordinates at a frame rate of 60 Hz, 29.9 (x) and 30.0 (y) nm at 250 Hz, and 33.9 (x) and 33.0 (y) nm at 1000 Hz, respectively (for the data, see Supplementary Fig. 5b).

The shapes of the condensates were determined by averaging the EGFP-synapsin 1 images recorded at 60 Hz over 100 frames. Individual Halo7-synapsin 1 spots in the image were identified and tracked by using an in-house computer program, as described previously[54,55]. The superimposition of images in different colors obtained by two separate cameras was conducted as described previously[56].

Determination of the dwell lifetime of Halo7-synapsin 1 (JF549 labeled) in the condensate in vitro. For evaluating the diffusion properties of Halo7-synapsin 1 in the condensate, we analyzed its diffusion projected onto the 2D xy plane, assuming that synapsin 1 movements in the z-direction is the same as those in x and y-directions in the core region of the condensate. Furthermore, we characterized the general molecular behaviors before quantitatively examine the diffusion of Halo7-synapsin 1 within the condensate: we measured the dwell lifetime of Halo7-synapsin 1 (JF549 labeled) in the condensate by using a time-lapse observation (15 Hz; every 66.7 ms, but the camera exposure time and laser illumination duration was 16.7 ms for each observation), which was useful for lowering the effect of photobleaching. Under these observation conditions, the photobleaching lifetime of JF549 was 54.4 s (13.6 s at 60 Hz observation).

As the arrival of a new molecule, we only included the molecules that arrived at the edges of the condensates from the outside of the condensate in/near the focal plane (within ≈ ±200 nm from the exact focal plane because we only selected the clear spots) and excluded those that came into clear focus by diffusion in the z-direction within the condensate. This was because we intended to analyze the diffusion projected onto the 2D xy plane. Less than ~5% of Halo7-synapsin 1 molecules entered the view within the condensate this way.

Halo7-synapsin 1 molecules “departed” from the view field in the condensates by (1) the departures from the edges of the condensates into the medium that occurred in/near the focal plane (within ≈ ±400 nm from the exact focal plane), (2) by photobleaching while they were still clearly visible in the focal plane within the condensates, and (3) by diffusing out of the focal plane in the z-direction (> ±400 nm from the exact focal plane) in the condensates. The molecules that disappeared by the process (3) were not included in the analysis by the same reason that the molecules that diffused into the view field by the z-direction diffusion were not considered for newly arrived molecules. Only ≈7% and ≈3% of the total Halo7-synapsin 1 molecules we observed disappeared in this manner in the condensates without and with SVs, respectively. The small numbers of arriving and departing molecules due to diffusion in the z-direction indicate that this method of analysis would not be skewed due to the possible omission of rapidly diffusing molecules.

The distribution of the Halo7-synapsin 1 dwell durations (15 Hz time-lapse observations with 16.7 ms exposure time) was fitted by the sum of two exponential functions, providing two dwell lifetimes. Observed dwell lifetimes (τ_{observed}) were corrected for the photobleaching lifetime of the probe[57], as follows,

$$\frac{1}{\tau_{\text{true}}} = \frac{1}{\tau_{\text{observed}}} - \frac{1}{\tau_{\text{bleach}}}, \tag{1}$$

where τ_{true} and τ_{bleach} are the true dwell lifetime and photobleaching lifetime.

Analysis of the MSD-Δt plots obtained from ultrafast SMT of Halo7-synapsin 1 in the condensates in vitro. MSD-Δt plots were calculated for up to 50 and 300 frames (out of the initial 100 and 350-frame trajectories; Fig. 2e, f, respectively) and averaged over 200 ~ 500 trajectories. The 15- and 30-Hz trajectories were generated by re-sampling the 60-Hz data.

The MSD-Δt plots were evaluated based on an anomalous diffusion model using the following equation,

$$\text{MSD} = \langle r^2(t) \rangle = 4D_\alpha (t)^\alpha + C, \tag{2}$$

where r, t, D_α, α, and C are displacement, time, diffusion coefficient, the anomaly parameter, and offset due to the localization error, respectively. The MSD-Δt plots after and before the offset subtraction are shown in Fig. 2e and Supplementary Fig. 5c, respectively. In the MSD-Δt plots for Halo7-synapsin 1 bound to the glass shown in Fig. 2e, the mean of the MSD values at all the Δt points were subtracted.

Sample preparation for 3D STED microscopy. 3D STED microscopy were performed on 4 different sets of samples- wild type, Syn TKO, full-length synapsin 1 transfected and synapsin 1 IDR transfected neuronal cultures (grown on coverslips), which were fixed using 4% PFA. Transfected samples (full-length synapsin 1 or IDR) were labeled with two fluorophores. The first was introduced to identify the synapses of interest. For this purpose, transfected cells were stained with a Cy3-conjugated mCherry nanobody. The second fluorophore was introduced by immunostaining SVs using a STAR 635P-conjugated synaptotagmin 1 nanobody, which was used to acquire STED images for all sets of samples. Sample preparation for STED microscopy was done as previously described[58]. Specifically, fixed cells were blocked and permeabilized with 2.5% BSA, 2.5% NGS, 2.5% NDS and 0.1% Triton X-100 in PBS for 30 min at room temperature. Synaptotagmin 1 (Nanotag, #N2302-Ab635P-L) and m-Cherry (Nanotag, #N0404-SC3-L) nanobodies were diluted to a final concentration of 25 nM in blocking buffer before applying to the coverslips. The cells were incubated with nanobody solution for 1 h followed by washing with permeabilization buffer (5 buffer exchanges for 1 h) and two quick washes with PBS. Finally, the coverslips were mounted onto the slides using antifade mounting media (Thermo Fisher Scientific, P36980).

Acquisition and analysis of 3D-STED data. An Abberior Expert line setup (Abberior Instruments) equipped with an IX83 inverted microscope (Olympus) was employed to generate confocal and STED images. A 100X oil immersion objective (UPLXAPO, 1.45 NA; Olympus) was used to focus the excitation light into the sample plane. Star635P was excited with a 640 nm pulsed excitation laser (set to 5% of max. power, 1.5 µW, frequency of 80 MHz), while a 561 nm excitation laser (27% of max. power, 1.5 µW; 80 MHz) was used for Cy3. Fluorescence signals were detected using an avalanche photodiode (APD) that has dedicated preset ranges for the two dyes (650-720 nm for Star635P and 605-625 nm for Cy3). Stimulated depletion for StarS635P was obtained by a 775 nm depletion laser (set to 6.4% of max. power, 5 mW). 3D STED images were acquired with a step size of 50 nm in z, pixel size of 20 nm, a dwell time of 10 µs per pixel and a line accumulation of 3.

Data were analyzed using Matlab (the Mathworks, Inc.). The synapses of interest were identified by applying an empirically-derived threshold on the Cy3 images. The Star635P signals within these images were filtered using a bandpass filter, and the locations and intensities of all discernable spots were determined and analyzed statistically, as described in the respective figures.

Statistics and reproducibility

The number of biological and technical replicates and the number of analyzed molecules are indicated in the figure legends and Source Data. Curve fittings were performed using Origin 2017 (OriginLab). Statistical tests were performed using R-studio (with the lawstat package) and Prism 9 (GraphPad). Differences were considered statistically significant for p-values < 0.05. The representative images in Figs. 1a and 2d come from at least three independent reconstitutions using the material (i.e., recombinant proteins and isolated SVs) from at least three independent preparations. The STED images in Fig. 4a were repeated from three independent neuronal preparations from wild-type and SYN-TKO animals.

Reporting summary

Further information on research design is available in the Nature Portfolio Reporting Summary linked to this article.

Data availability

Source data are provided with this paper. All data generated or analyzed for this study are available within the paper and its associated Supplementary Information/Source Data file. Source data are provided with this paper.

Code availability

Superimpositions of image sequences obtained in two colors and tracking single-molecules for in-vitro ultrafast observation data were perfomed using C + +-based computer programs, produced in-house[52] and based on the well-established approaches[59]. Source codes for this have been integrated into a large, complex software package. While the software package cannot be extracted in a useful way, the entire software is available from A.K. upon reasonable request, who will provide guidance on how to use it, as its manual and comments are written in Japanese. Tracking in live cells and neurons was done using Mosaic tracker plugin[51]. The code to generate figures with corresponding data is available in Source Data file.

References

1. Ceccarelli, B., Hurlbut, W. P. & Mauro, A. Turnover of transmitter and synaptic vesicles at the frog neuromuscular junction. *J. Cell Biol.* **57**, 499–524 (1973).
2. Rizzoli, S. O. & Betz, W. J. The structural organization of the readily releasable pool of synaptic vesicles. *Science* **303**, 2037–2039 (2004).
3. Fernández-Busnadiego, R. et al. Quantitative analysis of the native presynaptic cytomatrix by cryoelectron tomography. *J. Cell Biol.* **188**, 145–156 (2010).
4. Joensuu, M. et al. Subdiffractional tracking of internalized molecules reveals heterogeneous motion states of synaptic vesicles. *J. Cell Biol.* **215**, 277–292 (2016).
5. Reshetniak, S. et al. A comparative analysis of the mobility of 45 proteins in the synaptic bouton. *EMBO J.* **39**, e104596 (2020).
6. De Camilli, P., Benfenati, F., Valtorta, F. & Greengard, P. The synapsins. *Annu Rev. Cell Dev. Biol.* **6**, 433–460 (1990).
7. Milovanovic, D., Wu, Y., Bian, X. & De Camilli, P. A liquid phase of synapsin and lipid vesicles. *Science* **361**, 604–607 (2018).
8. Gitler, D. et al. Different presynaptic roles of synapsins at excitatory and inhibitory synapses. *J. Neurosci.* **24**, 11368–11380 (2004).
9. Pieribone, V. A. et al. Distinct pools of synaptic vesicles in neurotransmitter release. *Nature* **375**, 493–497 (1995).
10. Pechstein, A. et al. Vesicle clustering in a living synapse depends on a synapsin region that mediates phase separation. *Cell Rep.* **30**, 2594–2602.e3 (2020).
11. Shupliakov, O., Haucke, V. & Pechstein, A. How synapsin I may cluster synaptic vesicles. *Semin Cell Dev. Biol.* **22**, 393–399 (2011).
12. Zhang, M. & Augustine, G. J. Synapsins and the synaptic vesicle reserve pool: floats or anchors? *Cells* **10**, 658 (2021).
13. Wilhelm, B. G. et al. Composition of isolated synaptic boutons reveals the amounts of vesicle trafficking proteins. *Science* **344**, 1023–1028 (2014).
14. Milovanovic, D. & De Camilli, P. Synaptic vesicle clusters at synapses: a distinct liquid phase? *Neuron* **93**, 995–1002 (2017).
15. Sansevrino, R., Hoffmann, C. & Milovanovic, D. Condensate biology of synaptic vesicle clusters. *Trends Neurosci.* **46**, 293–306 (2023).
16. Park, D. et al. Cooperative function of synaptophysin and synapsin in the generation of synaptic vesicle-like clusters in non-neuronal cells. *Nat. Commun.* **12**, 263 (2021).
17. Zhang, X. M. et al. A proline-rich motif on VGLUT1 reduces synaptic vesicle super-pool and spontaneous release frequency. *Elife* **8**, e50401 (2019).
18. Hoffmann, C. et al. Synapsin condensates recruit alpha-synuclein. *J. Mol. Biol.* **433**, 166961 (2021).
19. Wei, M.-T. et al. Phase behaviour of disordered proteins underlying low density and high permeability of liquid organelles. *Nat. Chem.* **9**, 1118–1125 (2017).
20. Alshareedah, I., Moosa, M. M., Pham, M., Potoyan, D. A. & Banerjee, P. R. Programmable viscoelasticity in protein-RNA condensates with disordered sticker-spacer polypeptides. *Nat. Commun.* **12**, 6620 (2021).
21. Choi, J.-M., Holehouse, A. S. & Pappu, R. V. Physical principles underlying the complex biology of intracellular phase transitions. *Annu Rev. Biophys.* **49**, 1–27 (2020).
22. Wittig, S. et al. Cross-linking mass spectrometry uncovers protein interactions and functional assemblies in synaptic vesicle membranes. *Nat. Commun.* **12**, 858 (2021).
23. Pinot, M. et al. Polyunsaturated phospholipids facilitate membrane deformation and fission by endocytic proteins. *Science* **345**, 693–697 (2014).
24. Takamori, S. et al. Molecular anatomy of a trafficking organelle. *Cell* **127**, 831–846 (2006).
25. Gerth, F. et al. Intersectin associates with synapsin and regulates its nanoscale localization and function. *Proc. Natl Acad. Sci. USA* **114**, 12057–12062 (2017).
26. Raja, M. K. et al. Elevated synaptic vesicle release probability in synaptophysin/gyrin family quadruple knockouts. *Elife* **8**, e40744 (2019).
27. Südhof, T. C. et al. Synapsins: mosaics of shared and individual domains in a family of synaptic vesicle phosphoproteins. *Science* **245**, 1474–1480 (1989).
28. Hosaka, M. & Südhof, T. C. Homo- and heterodimerization of synapsins. *J. Biol. Chem.* **274**, 16747–16753 (1999).
29. Chi, P., Greengard, P. & Ryan, T. A. Synaptic vesicle mobilization is regulated by distinct synapsin I phosphorylation pathways at different frequencies. *Neuron* **38**, 69–78 (2003).
30. Bergeron-Sandoval, L.-P. et al. Endocytic proteins with prion-like domains form viscoelastic condensates that enable membrane remodeling. *Proc. Natl Acad. Sci. USA* **118**, e2113789118 (2021).
31. Day, K. J. et al. Liquid-like protein interactions catalyse assembly of endocytic vesicles. *Nat. Cell Biol.* **23**, 366–376 (2021).
32. Alabi, A. A. & Tsien, R. W. Synaptic vesicle pools and dynamics. *CSH Perspect. Biol.* **4**, a013680 (2012).
33. Rosahl, T. W. et al. Essential functions of synapsins I and II in synaptic vesicle regulation. *Nature* **375**, 488–493 (1995).
34. Hirokawa, N., Sobue, K., Kanda, K., Harada, A. & Yorifuji, H. The cytoskeletal architecture of the presynaptic terminal and molecular structure of synapsin 1. *J. Cell Biol.* **108**, 111–126 (1989).
35. Kamin, D. et al. High- and low-mobility stages in the synaptic vesicle cycle. *Biophys. J.* **99**, 675–684 (2010).
36. Orenbuch, A. et al. Synapsin selectively controls the mobility of resting pool vesicles at hippocampal terminals. *J. Neurosci.* **32**, 3969–3980 (2012).
37. Hilfiker, S. et al. Structural domains involved in the regulation of transmitter release by synapsins. *J. Neurosci.* **25**, 2658–69 (2005).
38. Hilfiker, S. et al. Two sites of action for synapsin domain E in regulating neurotransmitter release. *Nat. Neurosci.* **1**, 29–35 (1998).
39. Shupliakov, O. The synaptic vesicle cluster: a source of endocytic proteins during neurotransmitter release. *Neurosci.* **158**, 204–210 (2009).
40. Denker, A., Kröhnert, K., Bückers, J., Neher, E. & Rizzoli, S. O. The reserve pool of synaptic vesicles acts as a buffer for proteins involved in synaptic vesicle recycling. *Proc. Natl Acad. Sci. USA* **108**, 17183–17188 (2011).

41. Ziltener, P., Rebane, A. A., Graham, M., Ernst, A. M. & Rothman, J. E. The golgin family exhibits a propensity to form condensates in living cells. *FEBS Lett.* **594**, 3086–3094 (2020).
42. Gallo, R., Rai, A. & Pelkmans, L. DYRK3-controlled phase separation organizes the early secretory pathway. *bioRxiv* https://doi.org/10.1101/2020.02.10.941757 (2020).
43. Rodriguez, A. V., Frey, S. & Görlich, D. Engineered SUMO/protease system identifies Pdr6 as a bidirectional nuclear transport receptor. *J. Cell Biol.* **218**, 2006–2020 (2019).
44. Miesenböck, G., Angelis, D. A. D. & Rothman, J. E. Visualizing secretion and synaptic transmission with pH-sensitive green fluorescent proteins. *Nature* **394**, 192–195 (1998).
45. Granseth, B., Odermatt, B., Royle, S. J. & Lagnado, L. Clathrin-mediated endocytosis is the dominant mechanism of vesicle retrieval at hippocampal synapses. *Neuron* **51**, 773–786 (2006).
46. Nagy, A., Baker, R. R., Morris, S. J. & Whittaker, V. P. The preparation and characterization of synaptic vesicles of high purity. *Brain Res.* **109**, 285–309 (1976).
47. Huttner, W. B., Schiebler, W., Greengard, P. & De Camilli, P. Synapsin I (protein I), a nerve terminal-specific phosphoprotein. III. Its association with synaptic vesicles studied in a highly purified synaptic vesicle preparation. *J. Cell Biol.* **96**, 1374–1388 (1983).
48. Jiang, M. & Chen, G. High Ca2+-phosphate transfection efficiency in low-density neuronal cultures. *Nat. Protoc.* **1**, 695–700 (2006).
49. Sun, E. W. et al. Lipid transporter TMEM24/C2CD2L is a Ca 2+ -regulated component of ER–plasma membrane contacts in mammalian neurons. *Proc. Natl Acad. Sci. USA* **116**, 5775–5784 (2019).
50. Thompson, R. E., Larson, D. R. & Webb, W. W. Precise nanometer localization analysis for individual fluorescent probes. *Biophys. J.* **82**, 2775–2783 (2002).
51. Sbalzarini, I. F. & Koumoutsakos, P. Feature point tracking and trajectory analysis for video imaging in cell biology. *J. Struct. Biol.* **151**, 182–195 (2005).
52. Fujiwara, T. K. et al. Development of ultrafast camera-based single fluorescent-molecule imaging for cell biology. *J. Cell Biol.* **222**, e202110160 (2023).
53. Fujiwara, T. K. et al. Ultrafast single-molecule imaging reveals focal adhesion nano-architecture and molecular dynamics. *J. Cell Biol.* **222**, e202110162 (2023).
54. Fujiwara, T., Ritchie, K., Murakoshi, H., Jacobson, K. & Kusumi, A. Phospholipids undergo hop diffusion in compartmentalized cell membrane. *J. Cell Biol.* **157**, 1071–1082 (2002).
55. Fujiwara, T. K. et al. Confined diffusion of transmembrane proteins and lipids induced by the same actin meshwork lining the plasma membrane. *Mol. Biol. Cell* **27**, 1101–1119 (2016).
56. Koyama-Honda, I. et al. Fluorescence imaging for monitoring the colocalization of two single molecules in living cells. *Biophys. J.* **88**, 2126–2136 (2005).
57. Tsunoyama, T. A. et al. Super-long single-molecule tracking reveals dynamic-anchorage-induced integrin function. *Nat. Chem. Biol.* **14**, 497–506 (2018).
58. Dankovich, T. M. et al. Extracellular matrix remodeling through endocytosis and resurfacing of tenascin-R. *Nat. Commun.* **12**, 7129 (2021).
59. Crocker, J. C. & Grier, D. G. Methods of digital video microscopy for colloidal studies. *J. Colloid Inter. Sci.* **179**, 298–310 (1996).

Acknowledgements

We thank Advanced Medical Bioimaging Core Facility at Charité for the support; Kristina Jevdokimenko (UMG Göttingen) for the assistance with STED. The work is supported by the start-up funds from DZNE, as well as the grants from the European Research Council MemLessInterface–101078172 to DM; and the German Research Foundation SFB 1286/B10 and MI 2104 to DM; and SFB 1286/A03 to SOR. CH is supported by a fellowship of the Innovative Minds Program of the German Dementia Association; RC is supported by a fellowship from the Alexander von Humboldt Foundation. Schematics in Supplementary Data Fig. 2 and 14 are created with BioRender.com.

Author contributions

D.M. conceptualized the study. C.H. did all the reconstitution experiments and analyzed the data. T.A.T. and A.K. performed in-vitro single-molecule tracking and analyzed the data. J.R. and H.E. performed single-molecule tracking experiments in neurons and analyzed the data. R.C., A.H.S., and S.O.R. performed 3D STED microscopy. G.G. contributed to single-molecule microscopy. C.H., A.C., A.A.K., and M.G. performed partitioning measurements; G.A.P. and F.T. performed experiments in neurons. C.H., J.R., T.A.T., A.K., H.E., and D.M. wrote the paper. All the authors read and approved the final version of the paper.

Funding

Open Access funding enabled and organized by Projekt DEAL.

Competing interests

The authors declare no competing interests.

Additional information

Supplementary information The online version contains supplementary material available at https://doi.org/10.1038/s41467-023-42372-6.

Correspondence and requests for materials should be addressed to Dragomir Milovanovic.

Peer review information *Nature Communications* thanks Christian Eggeling and the other, anonymous, reviewer(s) for their contribution to the peer review of this work. A peer review file is available.

Reprints and permissions information is available at http://www.nature.com/reprints

Supplementary Information for:

Synapsin Condensation Controls Synaptic Vesicle Sequestering and Dynamics

Authors: Hoffmann Christian[1,*], Rentsch Jakob[2,*], Tsunoyama A. Taka[3,*], Chhabra Akshita[1], Aguilar Perez Gerard[1], Chowdhury Rajdeep[5], Trnka Franziska[1], Korobeinikov A. Aleksandr[1], Ali H. Shaib[5], Ganzella Marcelo[4], Giannone Gregory[6], Rizzoli O. Silvio[5], Kusumi Akihiro[3], Ewers Helge[2] & Milovanovic Dragomir[1*]

[1]Laboratory of Molecular Neuroscience, German Center for Neurodegenerative Diseases (DZNE), 10117 Berlin, Germany.
[2]Institute of Chemistry and Biochemistry, Freie Universität Berlin, 14195 Berlin, Germany.
[3]Membrane Cooperativity Unit, Okinawa Institute of Science and Technology Graduate University (OIST); Onna-son, Okinawa, 904-0495, Japan.
[4]Department of Neurobiology, Max Planck Institute for Multidisciplinary Sciences, 37077 Göttingen, Germany.
[5]University Medical Center Göttingen, Institute for Neuro- and Sensory Physiology, Germany; Biostructural Imaging of Neurodegeneration (BIN) Center, 37073 Göttingen, Germany; Excellence Cluster Multiscale Bioimaging, Göttingen, Germany.
[6]Interdisciplinary Institute for Neuroscience, University of Bordeaux, UMR 5297, F-33000 Bordeaux, France.

[*]These authors contributed equally to this work

✉Correspondence should be addressed to: dragomir.milovanovic@dzne.de

Supplementary Data contains:

- Supplementary Figures 1-14
- Supplementary Tables 1-2
- Supplementary Movies 1-3

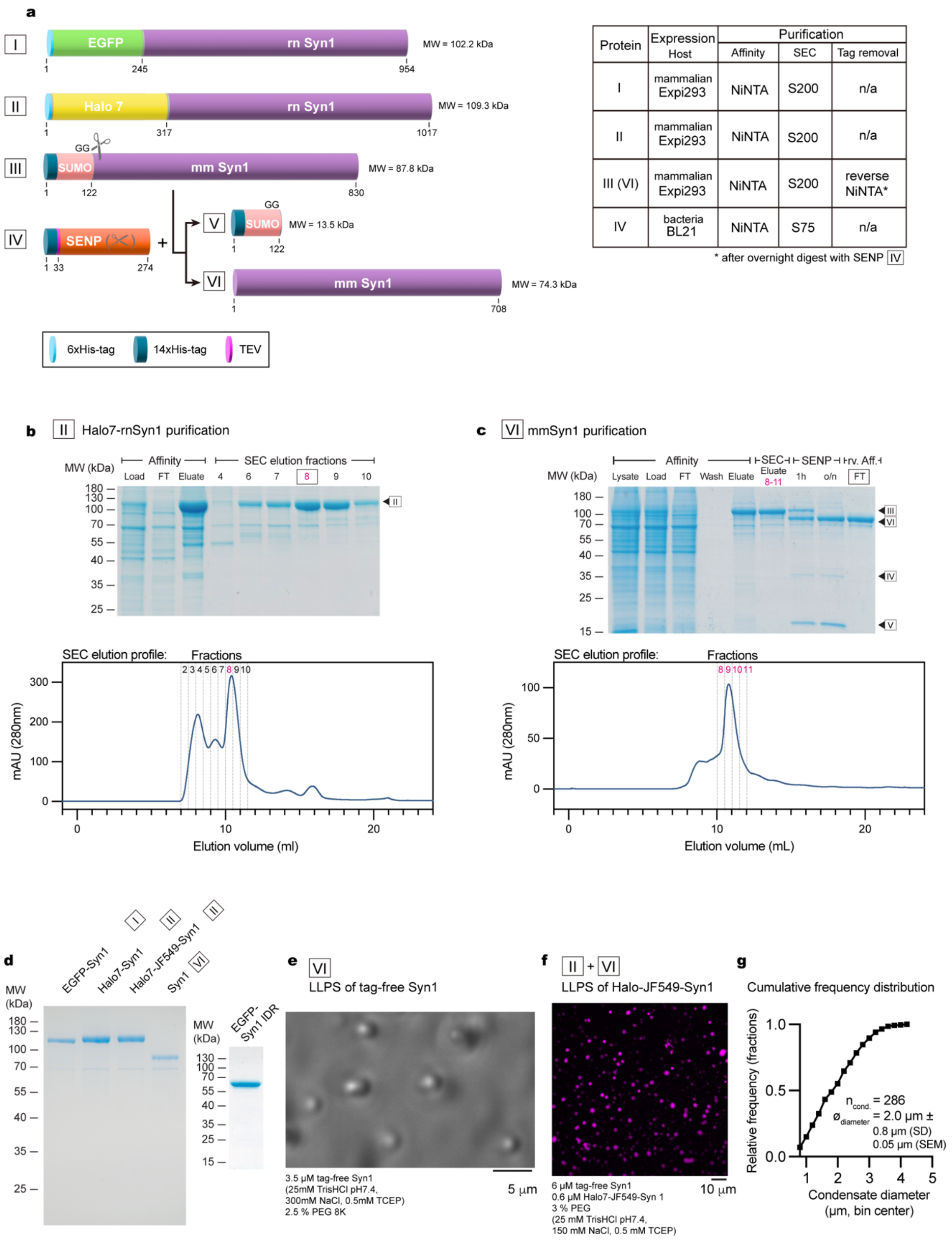

Protein	Expression Host	Purification		
		Affinity	SEC	Tag removal
I	mammalian Expi293	NiNTA	S200	n/a
II	mammalian Expi293	NiNTA	S200	n/a
III (VI)	mammalian Expi293	NiNTA	S200	reverse NiNTA*
IV	bacteria BL21	NiNTA	S75	n/a

* after overnight digest with SENP IV

Supplementary Figure 1 | Recombinant proteins used for reconstitution of synapsin condensates. a, Left: Schemes of synapsin 1 proteins variants used for reconstitution. The cartoons are to scale. Right: Overview of the purification strategy for each construct. For details, see Material and Methods. **b,** SDS-PAGE gel for recombinant purified Halo7-synapsin 1. **c,** SDS-PAGE gel showing the purification of tag-free synapsin 1. **d,** SDS-PAGE gel with all recombinant proteins used in this study (I: EGFP-synapsin 1; II: Halo7-synapsin 1; II*: Halo7*JF549-synapsin 1; VI: tag-free mmSynapsin 1). Right: EGFP-synapsin 1 IDR (amino acids: 416-705) **e,** Tag-free synapsin 1 forms condensates as visualized by phase contrast microscopy. **f,** JF549 labeled Halo7-synapsin 1 forms condensates. **g,** Cumulative size distribution of synapsin 1 condensates (mean 2 µm, standard deviation (SD) 0.8 µm, standard error of the mean (SEM) 0.05 µm).

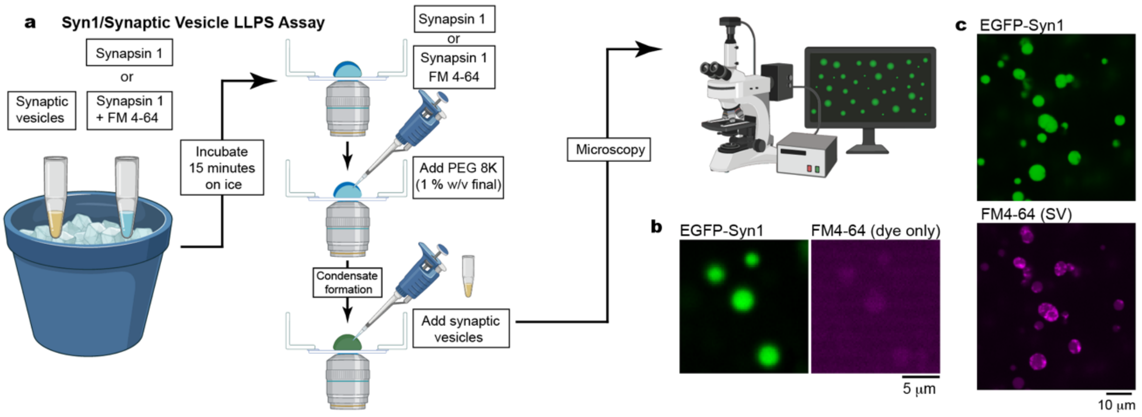

Supplementary Figure 2 | Reconstitution assay for visualizing SV/synapsin condensates. a, Scheme of the experimental pipeline. **b,** Exemplary fluorescence images of synapsin condensates with FM4-64 dye without SVs. **c**, Exemplary fluorescence images of synapsin 1/SV condensates.

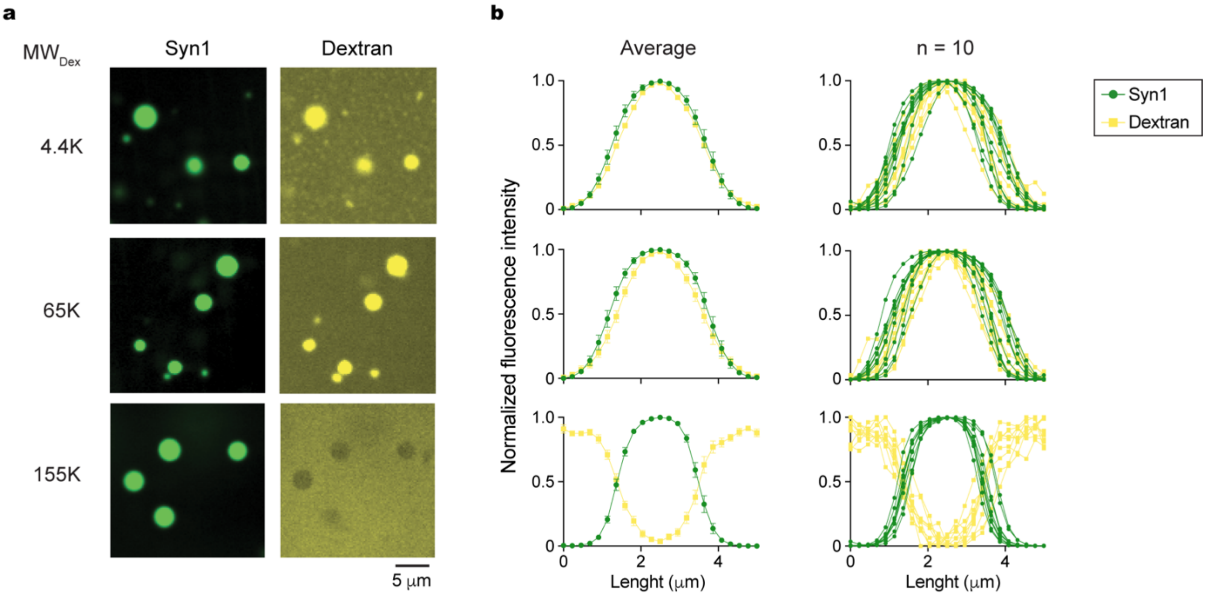

Supplementary Figure 3 | Synapsin condensates contain a meshwork that acts as a molecular sieve. a, Confocal images of EGFP-synapsin 1 condensates upon incubation with fluorescently-labeled dextran of 4.4 kDa (top), 65.85 kDa (middle), and 155 kDa (bottom) panels. Scale bar, 5 µm. **b**, Line profiles indicating either enrichment (for 4.4 kDa and 65.85 kDa) or exclusion (for 155 kDa) of fluorescently-labeled dextran. Left: an average line profile ± SEM; right: exemplary line profiles. For each condition ten condensates of similar size from three independent reconstitutions were analyzed.

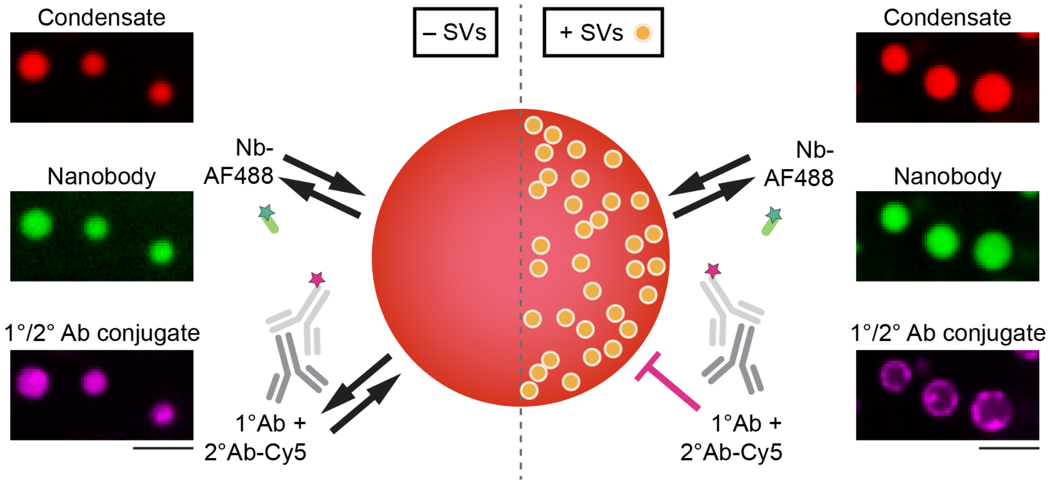

Supplementary Figure 4 | Differential partition of molecules into synapsin-drive condensates. Confocal images of Halo7*JF549-synapsin 1 condensates in the absence (left) or presence of synaptic vesicles (right). Condensates were co-incubated with a mixture of nanobody (Alexa Fluor 488-labeled nanobody against mouse IgG) and a primary/secondary antibody conjugate (primary: rabbit anti-LAMP1; secondary: Cy5-labeled goat-anti-rabbit). For each condition three independent reconstitutions were analyzed. Scale bars, 5 µm.

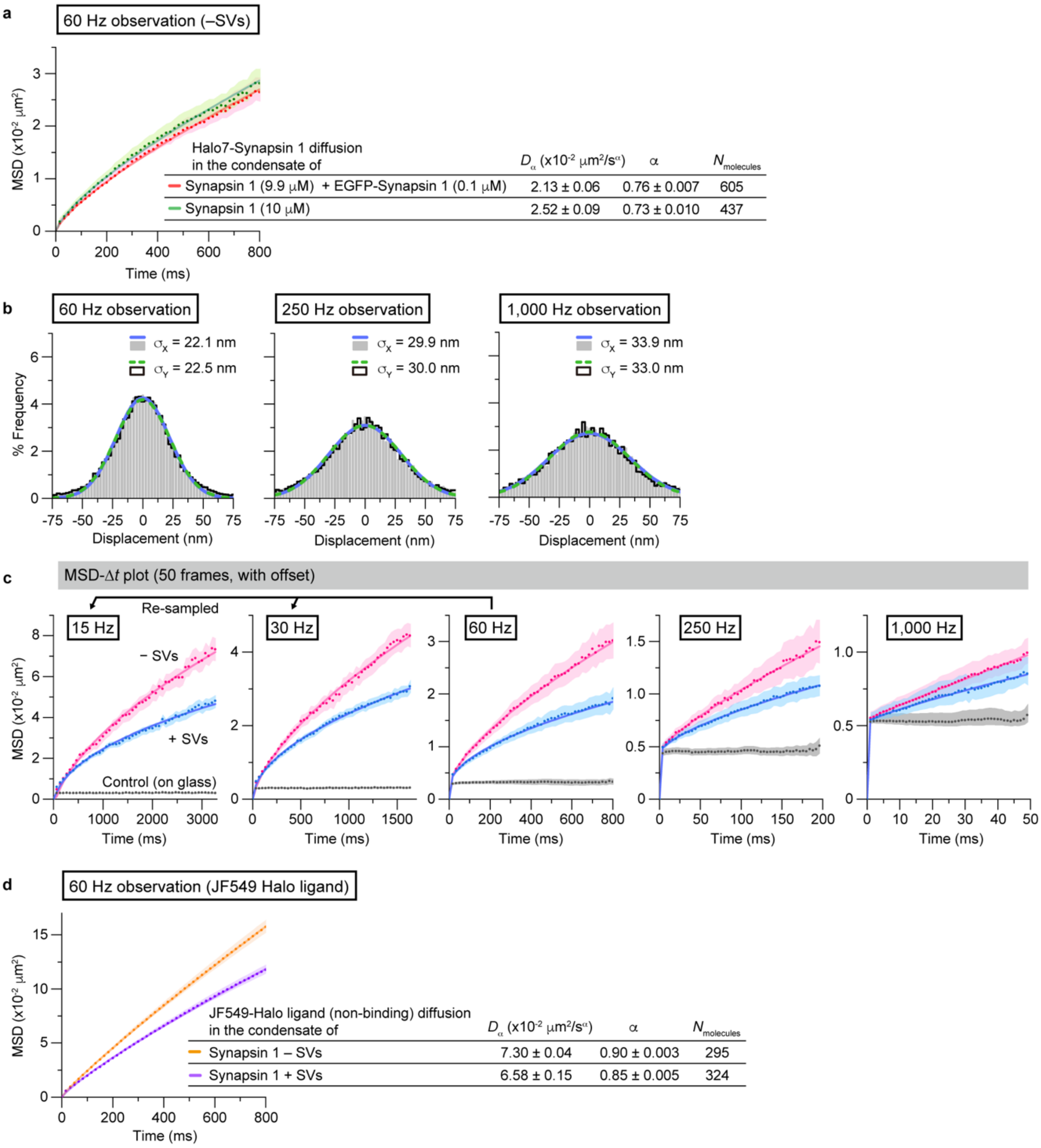

Supplementary Figure 5 | Control data for SMT employed for evaluating synapsin 1 diffusion in the SV/synapsin condensates. a, Halo7-synapsin 1 diffusion is not influenced by the presence of EGFP-synapsin 1 in the condensate (mean ± SEM). See Methods for details. **b,** Single-molecule localization precisions of JF549-labeled Halo7-synapsin 1 at three recording frame rates, determined for the molecules attached to the poly-L-lysine-coated glass-bottom dish. The standard deviations of the best-fit Gaussian functions provide the localization precisions. The number of observed spots were 23,800, 19,850, and 11,950 for frame rates of 60, 250, and 1,000 Hz, respectively. **c**, The MSD-Δt plots for Halo7-synapsin 1 located in the inner volume of the condensate (mean ± SEM). In these plots, the offset values are not subtracted data. The plots after subtraction are shown in *Fig. 2e.* **d**, The MSD-Δt plots for free JF549-Halo ligand molecules (not bound to Halo7 protein) located in the inner volume of the condensate (mean ± SEM). The diffusion is faster with less anomalies, compared with that of the synapsin 1-bound dyes, but the effect of the SV inclusion in the synapsin 1 condensate is clearly visible; a decrease of the diffusion coefficient and an increase of the diffusion anomaly.

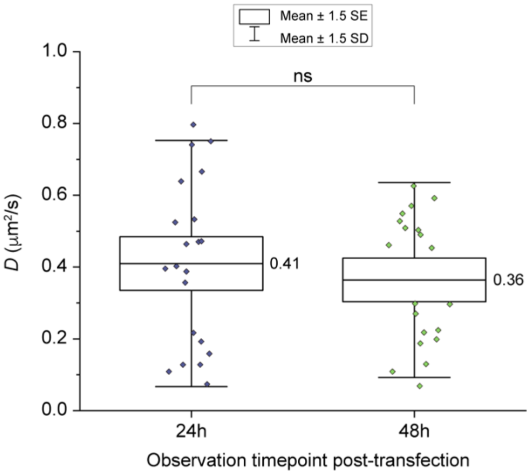

Supplementary Figure 6 | Confinement of expressed proteins in synaptic boutons is independent of the duration of expression. Mouse hippocampal neurons (14 days in culture) were transfected with mEOS3.2. Single-molecule tracking of mEOS3.2 was performed (100 Hz for 50 s) at either 24 h or 48 h post-transfection. Boxplot (mean ± 1.5 x SD (whiskers) and 1.5 x SE (box)) showing the geometric mean diffusion coefficients per tracking experiment (24 h, n = 21; 48 h, n = 20) of three independent neuronal preparations. Significance was tested using Mann-Whitney test ($p = 0.71$); ns = not significant.

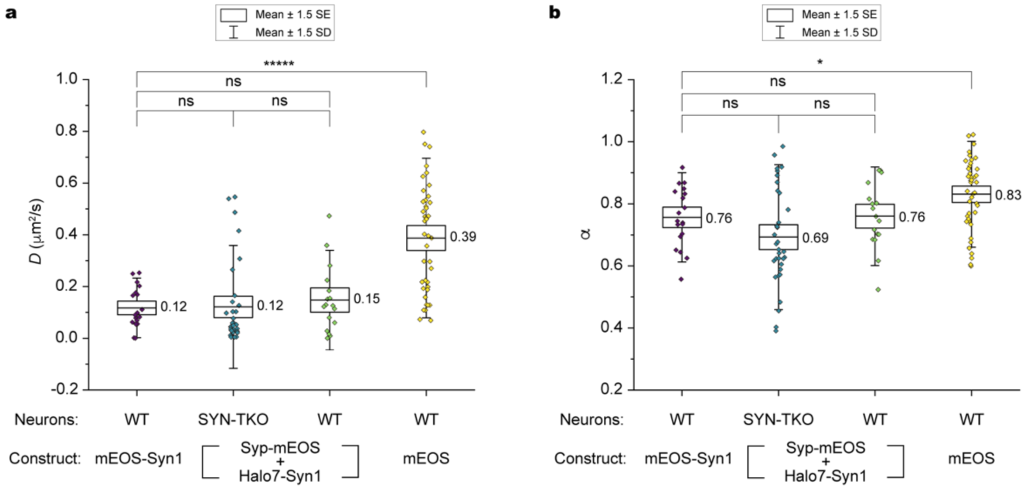

Supplementary Figure 7 | Synapsin confinement and diffusion rates are independent of synaptophysin/SVs. Single-molecule tracking experiments of synapsin 1 performed at 100 Hz for 50 s. (**a**) Boxplot (mean ± 1.5 x SD (whiskers) and 1.5 x SE (box)) showing the geometric mean diffusion coefficients per tracking experiment (WT mEos-Syn1, n = 19; SYN-TKO Syp-mEos and Halo7-Syn1, n = 33; WT Syp-mEos and Halo7-Syn1, n = 17, WT mEos, n = 41). Significance was tested using Mann-Whitney test (WT mEos-Syn1 vs WT mEos,

$p = 2.0\text{x}10^{-6}$; WT mEos-Syn1 vs WT Syp-mEos Halo7-Syn1, $p = 0.59$; WT mEos-Syn1 vs SYN-TKO Syp-mEos and Halo7-Syn1, $p = 0.12$; SYN-TKO Syp-mEos and Halo7-Syn1 vs WT Syp-mEos and Halo7-Syn, $p = 0.18$); asterisks indicate significance, ns = not significant. (**b**) Boxplot (mean ± 1.5 x SD (whiskers) and 1.5 x SE (box)) showing the mean coefficients of confinement (α) per tracking experiment (WT mEos-Syn1, n = 19; SYN-TKO Syp-mEos and Halo7-Syn1, n = 34; WT Syp-mEos and Halo7-Syn1, n = 17; WT mEos, n = 42). Significance was tested using Mann-Whitney test (WT mEos-Syn1 vs WT mEos, $p = 0.011$; WT mEos-Syn1 vs WT Syp-mEos Halo7-Syn1, $p = 0.95$; WT mEos-Syn1 vs SYN-TKO Syp-mEos Halo7-Syn1; $p = 0.083$; WT Syp-mEos and Halo7-Syn1 vs SYN-TKO Syp-mEos and Halo7-Syn1; $p = 0.084$); asterisks indicate significance, ns = not significant. Tracking data was acquired from at least three independent neuronal preparations. Mouse hippocampal neurons (14 days in culture) from wild-type (WT) or synapsin triple knockout (SynTKO) animals were transfected with mEOS3.2-synapsin 1. Rescue experiments were done by co-transfecting SynTKO neurons with synaptophysin-mEOS3.2 and Halo7-synapsin 1. Overexpression experiments were performed by co-transfecting wild-type neurons with Synaptophysin-mEOS3.2 and Halo7-synapsin 1. Additionally, neurons were transfected with soluble mEOS3.2 to assess the diffusion rate and confinement of a free diffusing protein in the axon. Of note, Halo7-synapsin 1 and mEOS3.2-synapsin 1 are significantly slower and more confined than soluble mEOS3.2 while not being affected by synaptophysin-mEOS3.2 expression. Thus, a molecular crowding alone is insufficient to account for the diffusion coefficients and coefficient of confinement of synapsin in synaptic boutons.

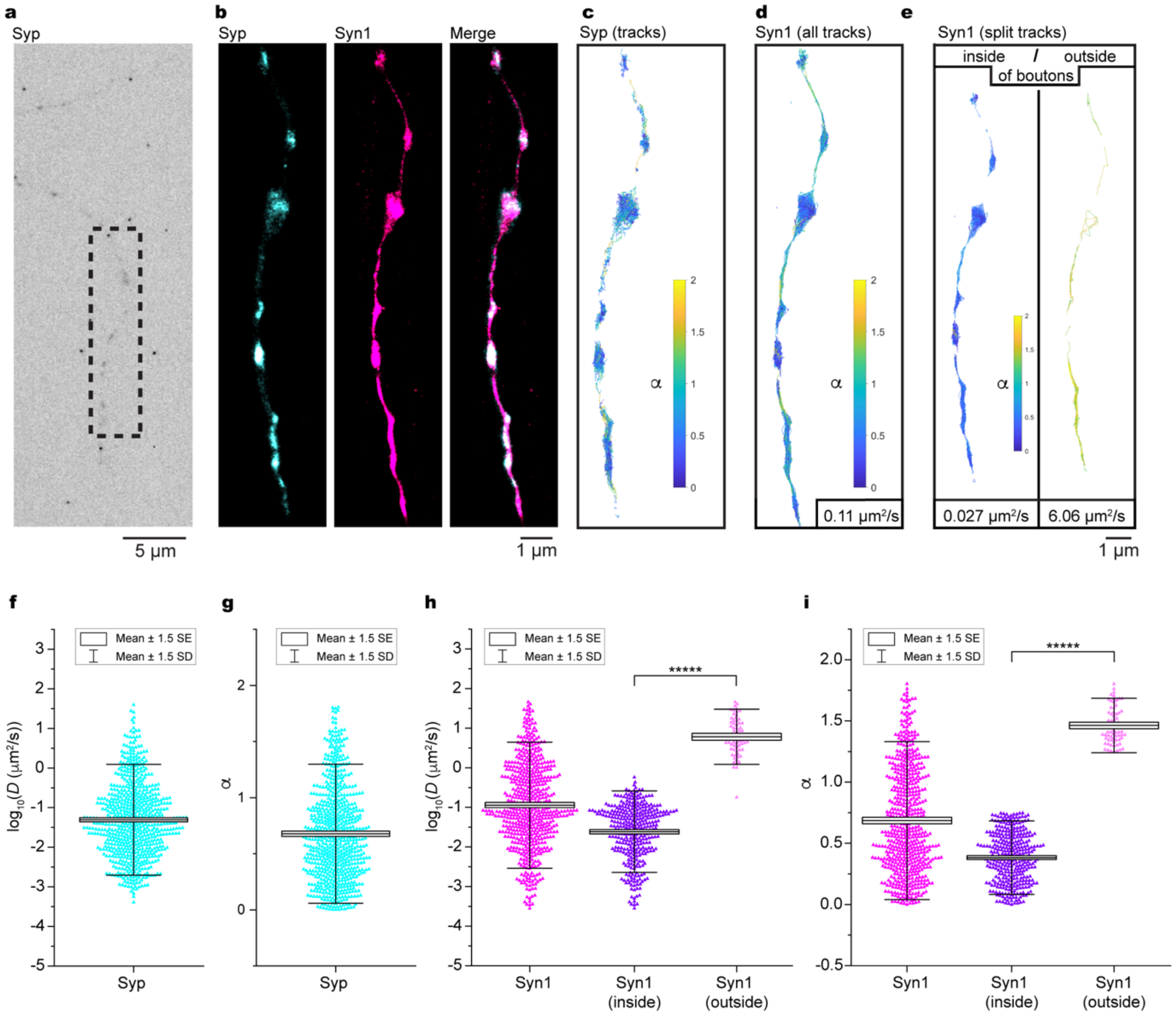

Supplementary Figure 8 | Synapsin 1 and synaptophysin are confined at synaptic boutons while maintaining their high motility. a, Widefield image of a neuron expressing synaptophysin-mEOS3.2. Mouse hippocampal neurons (14 days in culture) were transfected with Synaptophysin-mEOS3.2 (Syp) and Halo7-synapsin 1 (Syn1). **b**, Single-molecule localization reconstructions of proteins localized within dashed box in (*a*). Dual-color single-molecule tracking of Syp or Syn1 coupled to JF635 were performed at 100 Hz for 50 s. **c**, Map of all tracks (n = 690) of Syp within dashed box in (*a*) color-coded for coefficient of confinement (α). **d**, Map of Syn1 within dashed box in (*a*) color-coded for coefficient of confinement (α) (n = 596). **e**, Tracks of Syn1 filtered according to α (inside boutons (left, n = 355): 0.75> α > 0 or outside boutons (right, n = 68): 2 > α > 1.25. Values indicate the geometric mean diffusion coefficient for each panel. Boxplot (mean ± 1.5 x SD (whiskers) and 1.5 x SE (box)) showing diffusion coefficients (**f**) and α (**g**) for all tracks of Syp shown in (*c*). Boxplot (mean ± 1.5 x SD (whiskers) and 1.5 x SE (box)) showing diffusion coefficients (**h**) and α (**i**) for all tracks of Syn1 shown in (*d,e*). Significance was tested using Mann-Whtiney-Test; asterisks indicate significance; ns = not significant. Note that Syn1 is significantly slowed down (**h**, $p = 7.1\text{x}10^{-39}$) and confined (**i**, $p = 5.0\text{x}10^{-39}$) in synaptic boutons.

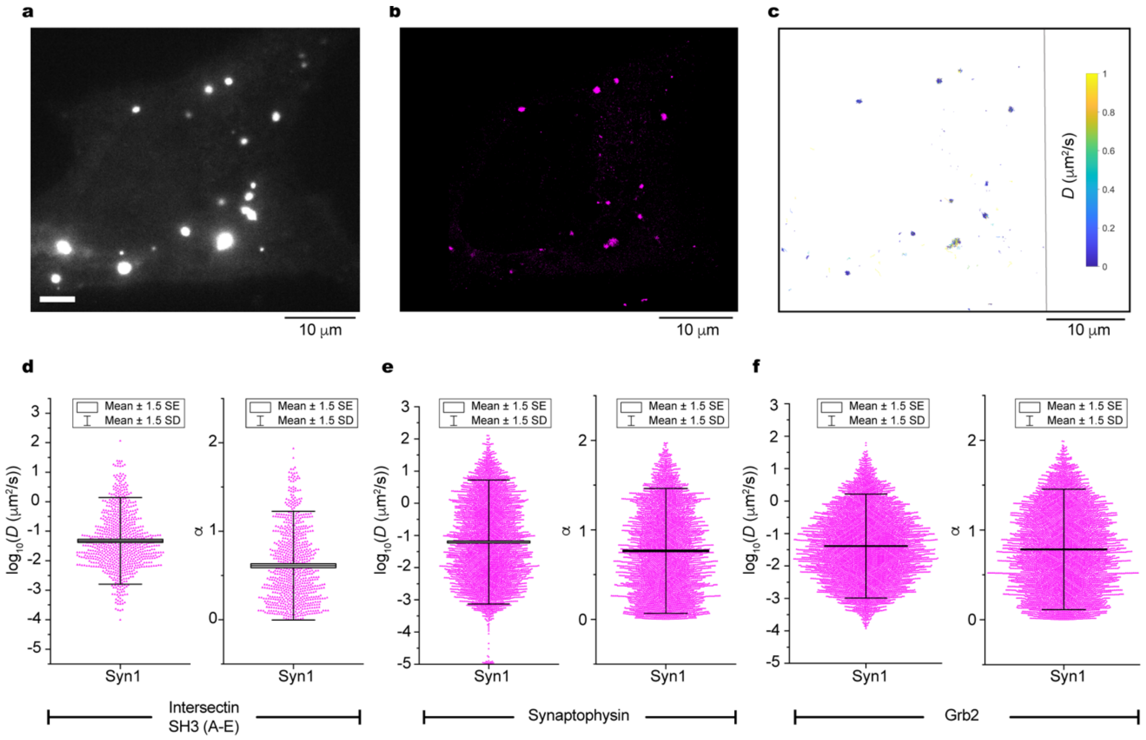

Supplementary Figure 9 | Synapsin 1-containing condensates reconstituted in non-neuronal cells recapitulate the motility pattern measured in synaptic boutons. CV-1 cells were transfected with EGFP-SH3(A-E) concatemer of Intersectin and mEOS3.2-synapsin 1 (Syn1). **a**, Widefield fluorescence image of synapsin 1-containing condensates in the cytosol. Single-molecule tracking measurements of Syn1 were performed at 100 Hz for 50 s. **b**, Reconstruction of proteins localized for cell in (*a*). **c**, Map of all tracks (n=768) for cell in (*a*) color-coded for diffusion coefficient. **d**, Boxplots (mean ± 1.5 x SD (whiskers) and 1.5 x SE (box)) showing diffusion coefficients (left) and the coefficient of confinement (α) (right) for all tracks of Syn1 shown in (c). **e**, the as in *d* but for the cells co-expressing Syn1 and untagged synaptophysin, **f**, the same as in *d* but for the cells co-expressing Syn1 and Grb2.

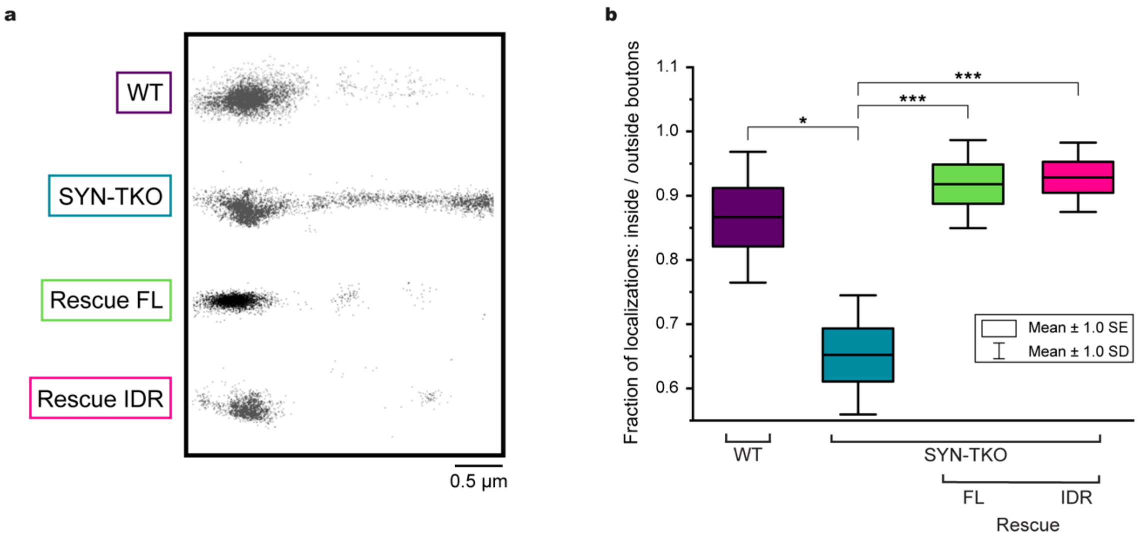

Supplementary Figure 10 | Quantification of the synaptic vesicle accumulation inside boutons. a, Representative single-molecule localization reconstructions of mouse hippocampal neurons (14 days *in vitro*) expressing synaptophysin-mEos3.2 (5000 frames, 10 ms exposure time) in neurons with different synapsin expressions: wild-type (WT), synapsin triple knock out neurons (SYN-TKO), SYN-TKO neurons rescued by expressing mCherry-synapsin 1 full-length (Rescue FL) or mCherry-synapsin 1 intrinsically disordered region amino acids 416-705 (Rescue IDR). Scale bar, 0.5 µm. **b**, Ratios of total number of single-molecule localizations of synaptophysin-mEos3.2 inside and up to 2 µm outside of boutons shown as a boxplot (mean ± 1.0 x SD (whiskers) and 1.0 x SE (box)) under the same synapsin expression patterns described in *a*. Significance was tested using unpaired *t-test* with equal variance assumed (WT vs SYN-TKO, $p = 8.3\text{x}10^{-3}$; SYN-TKO vs Rescue-FL, $p = 8.8\text{x}10^{-4}$; SYN-TKO vs Rescue-IDR; $p = 4.3\text{x}10^{-4}$); n = 5 independent neuronal preparation for each expression pattern; asterisks indicate significance; ns = not significant.

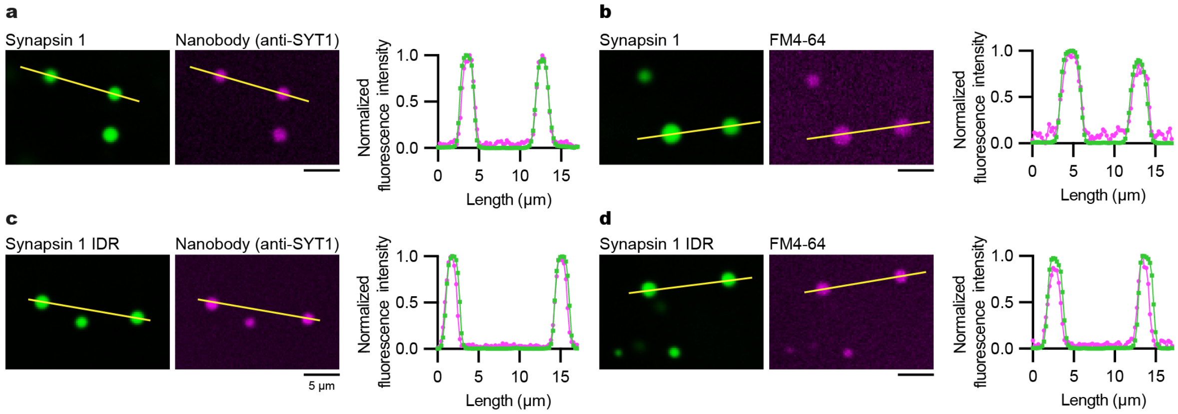

Supplementary Figure 11 | The full-length and the intrinsically disordered region of synapsin 1 sequester synaptic vesicles. a, Representative confocal images of the recombinant full-length synapsin 1 (10 µM) coincubated with synaptic vesicles (SVs, 3 nM) visualized using fluorescently-labeled Abberior STAR 635P nanobody against synaptotagmin 1 (anti-SYT1). Left: Images, right: line profiles. **b,** The same as in *a* but SVs were visualized with lipophilic dye FM4-64. **c,** Representative confocal images of the recombinant intrinsically disordered region (IDR, amino acids 416-705) of synapsin 1 (10 µM) coincubated with synaptic vesicles (SVs, 3 nM) visualized using fluorescently-labeled Abberior STAR 635P nanobody against synaptotagmin 1 (anti-SYT1). Left: Images, right: line profiles. **d,** The same as in *c* but SVs visualized with lipophilic dye FM4-64**.** Scale bars, 5 µm. All reconstitutions have been independently performed at least three times.

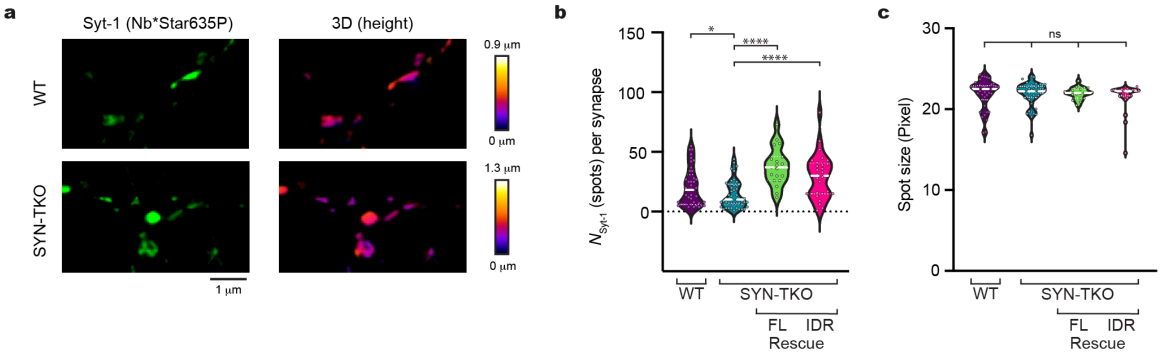

Supplementary Figure 12 | Quantification of the synaptic vesicle accumulation using 3D STED microscopy. a, Representative STED images of primary mouse hippocampal neurons stained with Aberrior STAR 635P-labeled nanobodies (Nb*Star635P) against synaptotagmin-1 (Syt-1), a *bona fide* synaptic vesicle protein. **b**, Quantification of number of Syt-1 positive spots in boutons of wild-type (WT; N = 41) neurons or synapsin triple knock-out (SYN-TKO; N = 48) neurons transfected with mCherry-synapsin 1 full-length (Rescue FL; N = 19) or mCherry-synapsin 1 intrinsically disordered region (IDR, amino acids 416-705; N = 28). **c**, Spot size distribution in all conditions analyzed in *b* indicating the consistent labeling pattern of Syt-1 nanobody. Significance was tested using unpaired, two-tailed *t-test*. Asterisks, significance; *, $p < 0.05$; ****, $p < 0.0001$; ns, not significant.

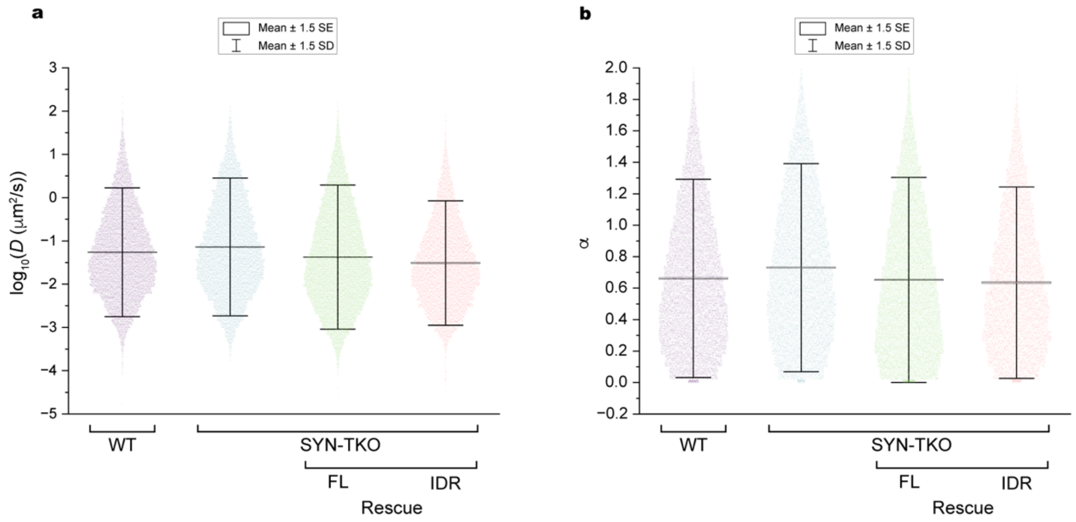

Supplementary Figure 13 | Analysis of all tracks confirms that synapsin determines the confinement and diffusion rates of synaptic vesicles (SVs). Single-molecule tracking experiments of synaptophysin-mEOS3.2 (Syp) performed at 100 Hz for 50 s. Mouse hippocampal neurons (14 days in culture) from wild-type or synapsin triple knockout (SYN-TKO) animals were transfected with Syp. Rescue experiments were done by co-transfecting SYN-TKO neurons with Syp and either full-length synapsin 1 (Rescue FL) or the intrinsically disordered region of synapsin 1 (Rescue IDR). Boxplots (mean ± 1.5 x SD (whiskers) and 1.5 x SE (box)) showing the diffusion coefficients (**a**) and the coefficient of confinement (α) (**b**) of all tracks (N = 77,675) of at least four independent neuronal preparations per condition.

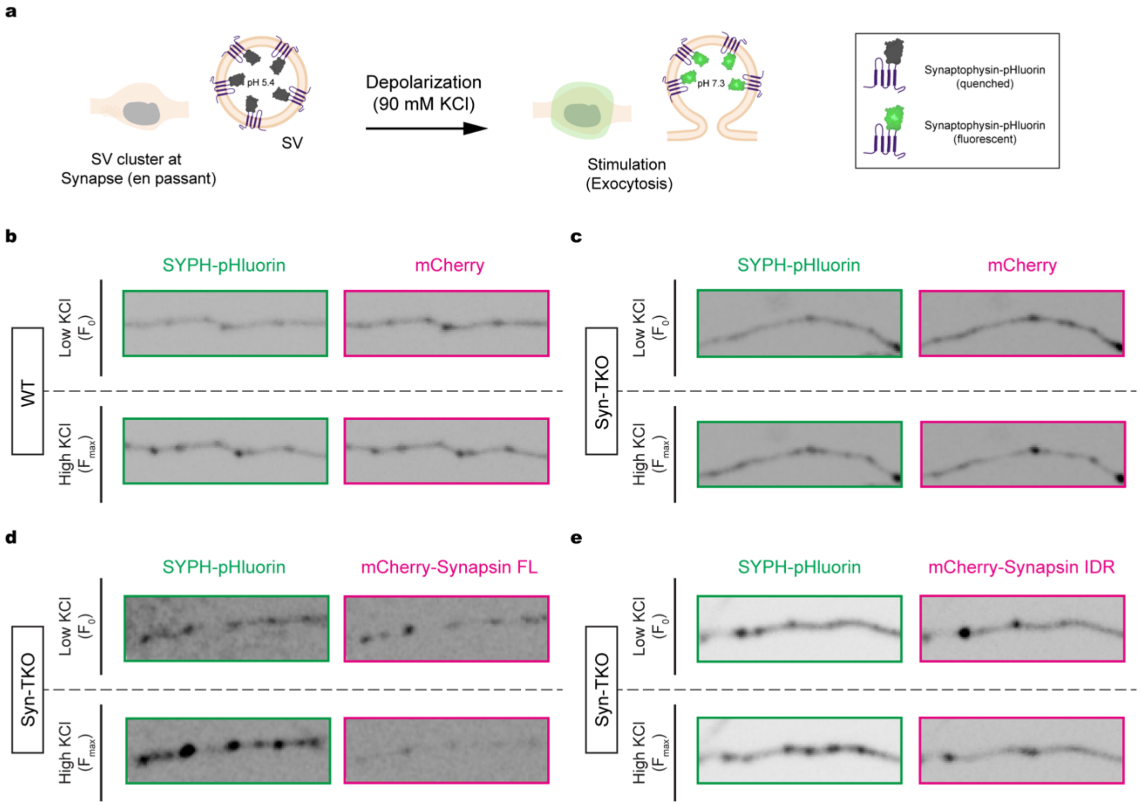

Supplementary Figure 14 | Functional assay for measuring SV release. a, Scheme of the assay. SV release measured as an increase in fluorescence of pH-sensitive EGFP variant tagged to the luminal region of synaptophysin (SYPH-pHluorin) upon chemical stimulation with KCl (90 mM). Representative images of wild-type neurons co-transfected with only a soluble red fluorophore (**b**) or SYN-TKO neurons co-transfected with a soluble red fluorophore (**c**), synapsin FL (**d**) or the synapsin IDR (**e**).

Supplementary Table 1. DNA sequences of (a) His14-SUMO_Eu1-mmSynapsin1a and (b) SYPH-pHluorin expression cassettes

a) …cmv-***Age*I**-His14-**SUMO_Eu1**-***Bgl*II-**mmSyn1a-*SV40*…

…cgccccattgacgcaaatgggcggtaggcgtgtacggtgggaggtctatataagcagagc
tGGTTTAGTGAACCGTCAGATCCGCTAGCGCT***ACCGGT***CGCCACCATGAGCAAGCATCACC
ATCATTCAGGCCATCACCATACCGGACACCACCATCATTCAGGCAGTCATCACCATTCCGG
A**TCTGCTGCGGGTGGCGAAGAAGATAAGAAACCGGCAGGTGGCGAAGGTGGCGGTGCCCAT**
ATCAACCTGAAAGTGAAAGGTCAAGACGGCAACGAAGTCTTTTTCCGCATCAAACGTTCTA
CCCAGCTGAAAAAGCTGATGAACGCATACTGTGACCGTCAGTCTGTAGACATGAAGGCAAT
TGCTTTCCTCTTTAAGGGTCGTCGCCTACGTGCGGAAAGGACCCCGGATGAACTGGAAATG
GAAGATGGCGACGAAATCGACGCAATGCTGCACCAGACTGGAGGC*AGATCT*ATGAACTACC
TGCGGCGCCGCCTGTCGGACAGCAACTTCATGGCCAATCTGCCGAATGGGTACATGACAGA
CCTGCAGCGCCCGCAACCGCCCCCGCCGCCTCCCTCGGCCGCCAGCCCTGGGGCCACGCCC
GGCTCCGCGACAGCCTCTGCCGAGAGGGCCTCCACAGCTGCTCCAGTGGCTTCTCCAGCAG
CCCCTAGTCCTGGGTCCTCGGGGGGCGGCGGCTTCTTCTCGTCGCTGTCTAACGCGGTCAA
GCAAACCACAGCAGCCGCAGCCGCCACCTTCAGCGAGCAGGTGGGCGGTGGCTCTGGGGGC
GCAGGCCGCGGGGGCGCCGCCGCCAGGGTGCTGCTGGTCATCGACGAACCGCACACCGACT
GGGCAAAATACTTCAAAGGAAGAAGATCCATGGAGAAATTGACATTAAAGTAGAGCAAGC
TGAATTCTCTGATCTCAATCTTGTGGCTCATGCCAATGGTGGATTCTCTGTGGACATGGAA
GTTCTTCGGAATGGAGTCAAAGTTGTGAGGTCTCTGAAGCCAGACTTTGTGCTGATCCGCC
AGCATGCCTTCAGCATGGCACGTAATGGAGACTACCGAAGTTTGGTCATTGGGCTGCAGTA
TGCTGGAATCCCCAGTGTAAACTCTTTGCATTCTGTCTACAACTTCTGTGACAAACCCTGG
GTGTTTGCCCAGATGGTTCGACTACACAAGAAGCTTGGAACAGAGGAATTCCCTCTGATTG
ATCAGACTTTCTATCCTAATCACAAAGAGATGCTCAGCAGCACAACATACCCTGTGGTTGT
GAAGATGGGCCACGCACATTCTGGGATGGGCAAGGTCAAGGTAGACAACCAACATGACTTC
CAGGATATTGCAAGTGTTGTGGCACTGACTAAGACATATGCCACTGCTGAGCCCTTCATTG
ATGCTAAATATGATGTGCGTGTCCAGAAGATTGGGCAGAACTACAAGGCCTACATGAGGAC
ATCAGTGTCGGGTAACTGGAAGACCAATACAGGTTCTGCTATGCTTGAGCAGATTGCCATG
TCTGACAGGTACAAGTTGTGGGTAGACACGTGCTCAGAGATTTTTGGGGGACTTGACATCT
GCGCAGTGGAAGCGCTGCATGGCAAGGACGGAAGGGATCACATTATTGAGGTGGTGGGCTC
CTCCATGCCACTCATTGGTGATCACCAGGATGAAGACAAGCAGCTCATCGTGGAACTTGTG
GTCAACAAGATGACTCAGGCTCTGCCTCGGCAGCCGCAGCGGGATGCTTCCCCTGGCAGGG
GCTCCCACAGCCAGTCTTCATCCCCAGGAGCCCTGACCTTGGGCCGCCAGACCTCCCAGCA
GCCTGCAGGTCCTCCTGCTCAACAACGACCCCCACCCCAGGGAGGCCCTCCACAGCCAGGC
CCAGGACCTCAGCGCCAGGGACCCCCGCTGCAGCAGCGCCCACCCCCACAAGGCCAGCAAC
ATCTTTCTGGCCTTGGACCGCCAGCTGGCAGCCCTCTGCCTCAGCGCCTACCAAGTCCCAC
CGCAGCACCTCAGCAGTCTGCCTCTCAGGCCACACCAGTGACCCAGGGTCAAGGCCGCCAG
TCGCGGCCAGTGGCAGGAGGCCCTGGAGCACCTCCAGCAGCGCCCACCAGCCTCCCCAT
CTCCACAGCGTCAGGCGGGGGCCCCGCAGGCTACCCGTCAGGCATCTATCTCTGGTCCAGC
TCCAACGAAGGCCTCAGGAGCCCCACCCGGAGGGCAGCAGCGCCAGGGCCCTCCCCAAAAA
CCCCCAGGCCCTGCTGGTCCCACTCGTCAGGCCAGTCAGGCAGGTCCCGGACCTCGCACTG
GGCCTCCCACCACACAGCAGCCCCGGCCCAGCGGCCCAGGTCCTGCTGGACGTCCCGCCAA
ACCACAGCTGGCCCAGAAACCCAGCCAGGATGTGCCACCACCCATCACCGCCGCTGCCGGG
GGACCCCCGCACCCCCAGCTCAACAAATCCCAGTCTCTGACCAATGCCTTCAACCTTCCAG
AGCCAGCCCCTCCCAGGCCCAGCCTTAGCCAGGACGAGGTGAAAGCTGAGACCATCCGCAG
CCTGAGGAAGTCTTTCGCCAGCCTCTTCTCCGACTGAGAGCTCAAGCTTCGAATTCTGCAG
TCGACGGTACCGCGGGCCCGGGATCCACCGGATCTAGATAACTGATCATAATCAGCCATAC
CACATTTGTAGAGGTTTTACTTGCTTTAAAAAACCTCCCACACCTCCCCCTGAACCTGAAA
CATAAAATGAATGCAATTGTTGTTGTT*AACTTGTTTATTGCAGCTTATAATGGTTACAAAT*
AAAGCAATAGCATCACAAATTTCACA…

b) …cmv-SYPH(M1-T190)-**pHluorin**-SYPH(C191-A240)-Linker-*SV40*…
…cgccccattgacgcaaatgggcggtaggcgtgtacggtgggaggtctatataagcagagctggtt tagtgaaccgtcagatcCGCTAGCGCTACCGGACTCAGATCTCGAGCTCAAGCTTGCCACCATGGA CGTGGTGAATCAGCTGGTGGCTGGGGGTCAGTTCCGGGTGGTCAAGGAGCCCCTTGGCTTC GTGAAGGTGCTGCAGTGGGTCTTTGCCATCTTCGCCTTTGCTACGTGCGGCAGCTACACCG GAGAGCTTCGGCTGAGCGTGGAGTGTGCCAACAAGACGGAGAGTGCCCTCAACATCGAAGT CGAATTTGAGTACCCATTCAGGCTGCACCAAGTGTACTTTGATGCACCCTCCTGCGTTAAA GGGGGCACTACCAAGATCTTCCTAGTTGGTGACTACTCCTCCTCGGCTGAATTCTTTGTCA CCGTGGCTGTGTTTGCCTTCCTCTACTCCATGGGGGCCCTGGCCACCTACATCTTCCTGCA GAACAAGTACCGAGAGAACAACAAAGGGCCAATGATGGACTTCCTGGCCACAGCAGTGTTC GCTTTCATGTGGCTAGTTAGCTCATCCGCCTGGGCCAAAGGCCTGTCCGATGTGAAGATGG CCACTGACCCAGAGAACATTATCAAGGAGATGCCTATGTGCCGCCAGACAGGAAACACA**GG** **CGGAAGTAAAGGAGAAGAACTTTTCACTGGAGTTGTCCCAATTCTTGTTGAATTAGATGGTGATGT** **TAATGGGCACAAATTTTCTGTCAGTGGAGAGGGTGAAGGTGATGCAACATACGGAAAACTTACCCT** **TAAATTTATTTGCACTACTGGAAAACTACCTGTTCCTTGGCCAACACTTGTCACTACTTTAACTTA** **TGGTGTTCAATGCTTTTCAAGATACCCAGATCATATGAAACGGCATGACTTTTTCAAGAGTGCCAT** **GCCCGAAGGTTATGTACAGGAAAGAACTATATTTTTCAAAGATGACGGGAACTACAAGACACGTGC** **TGAAGTCAAGTTTGAAGGTGATACCCTTGTTAATAGAATCGAGTTAAAAGGTATTGATTTTAAAGA** **AGATGGAAACATTCTTGGACACAAATTGGAATACAACTATAACGATCACCAGGTGTACATCATGGC** **AGACAAACAAAAGAATGGAATCAAAGCTAACTTCAAAATTAGACACAACATTGAAGATGGAGGCGT** **TCAACTAGCAGACCATTATCAACAAAATACTCCAATTGGCGATGGGCCCGTCCTTTTACCAGACAA** **CCATTACCTGTTTACAACTTCTACTCTTTCGAAAGATCCCAACGAAAAGAGAGACCACATGGTCCT** **TCTTGAGTTTGTAACAGCTGCTGGGATTACACATGGCATGGATGAACTATACAAAACCGGTCGCCA** **GACAGGGAACACA**TGCAAGGAACTGAGGGACCCTGTGACTTCAGGACTCAACACCTCGGTGG TGTTTGGCTTCCTGAACCTGGTGCTCTGGGTTGGCAACCTATGGTTCGTGTTCAAGGAGAC AGGCTGGGCCGCCCCATTCATGCGCGCACCTCCAGGCGCCAGCGGCGGTTCCGGGGGTAGCGG TGGCAGCTCCGGACTCAGATCTCGAGCTCAAGCTTCGAATTCTGCAGTCGACGGTACCGCGGGCCC GGGATCCACCGGATCTAGATAA*AGCGGCCGCGACTCTAGATCATAATCAGCCATACCACATT* *TGTAGAGGTTTTACTTGCTTTAAAAAACCTCCCACACCTCCCCCTGAACCTGAAACATAAA* *ATGAATGCAATTGTTGTTGTTAACTTGTTTATTGCAGCTTATAATGGTTACAAATAAAGCA* *ATAGCATCACAAATTTCAC…*

Supplementary Table 2. Primer sequences for plasmid construction

#DML0331+0332 **(*Age*I, *Bgl*II)**	**FW:** ATCA**ACCGGT**CGCCACCATGAGCAAGCATCACCATCATTCAGGCC **RV:** ATCA**AGATCT**GCCTCCAGTCTGGTGCAG
#DML0195+0196 **(*Age*I, *Bgl*II)**	**FW:** ATCA**ACCGGT**GCCACCATGGCAGAAATCGGTACTGG **RV:** TGAT**AGATCT**GCTGCCGCTGCCGGAAATCTCGAGCGTC
#DML0438+0439 **(*Nhe*I, *Age*I)**	**FW:** **CTAGC**GCCACCATGCATCACCATCACCATCAC**A** **RV:** **CCGGT**GTGATGGTGATGGTGATGCATGGTGGC**G**

6. Summary

This work focused on the exploration of compartmentalized systems in neuronal cells. To that end, a combinatorial approach of different super-resolution microscopy techniques was employed.

One such compartmentalized system exists in the PM of neuronal cells. Here, membrane compartmentalization had been observed into ~200 nm spaced periodic membrane domains, confined between actin rings.[30] Importantly, the molecular cause of the observed compartmentalization remained elusive. Two main hypotheses emerged as the cause for the compartmentalization: actin rings or large voltage-gated channel densities. This work now showed that periodic actin ring structures are indeed the cause of the membrane compartmentalization. This was shown, by first investigating models of membrane compartmentalization mathematically. To that end, *in silico* SPT experiments of membrane molecules diffusing either over geometries mimicking actin rings or channel protein densities were performed. Actin rings geometries clearly formed membrane compartments that were similar to previously observed membrane domains. Geometries mimicking channel proteins densities formed no such domains. Additionally, *in silico* SPT experiments were performed to test the permeability of the actin barrier. It was found that a coverage of 30% of the actin rings with transmembrane protein pickets would be sufficient to induce membrane compartmentalization.

Additionally, this work investigated the distance of actin rings to the PM. If actin rings are indeed the cause of the observed compartmentalization it stands to reason that they must be close to the PM. Using live-cell STED microscopy it was found that the rings were indeed close to the membrane (~20 nm). Additionally, membrane compartments were detected by performing SPT of the outer leaflet membrane protein GPI-GFP in other cells of the neuronal lineage without channel protein densities.[52] This finding further excluded channel protein densities as the cause for the observed compartmentalization. Similar compartments were detected for the inner leaflet protein SRC-Halo and the transmembrane protein YFP-CB1. Moreover, by performing correlative SPT and immunostainings of neuronal markers, membrane domains formed by GPI-GFP could be confirmed in neurons, astrocytes, and oligodendrocytes. Both discoveries highlight the ubiquity of membrane compartmentalization in the neuronal lineage.

Next, the nanoscopic location of the domains in relation to actin rings was investigated. To that end, correlative SPT of GPI-GFP and dSTORM of actin was performed in progenitor-derived neuronal cells. It was found that GPI-GFP is more likely to localize between actin rings (similar to what was previously observed specifically in the AIS of neurons)[30]. This discovery also corroborated findings acquired by *in silico* SPT experiments described above. Lastly, the effect of actin disruption on membrane compartmentalization was investigated. This work could show that actin rings in progenitor-derived neuronal cells are disrupted by the actin inhibitor Swin A. Furthermore, a software was developed by Selle Bandstra, Mohsen Sadeghi and Frank Noé to detect periodic regions in SPT data (Stripefinder). The Stripefinder was confirmed to reliably detect periodicity in synthetic periodic SPT data. The software did not detect such patterns in random synthetic SPT data and in SPT data of CV-1 cells (without periodic actin structures)[38]. The Stripefinder was then used to quantify the magnitude of compartmentalization ("stripe score") in cells with disrupted actin rings. To that end, GPI-GFP was tracked in the same progenitor-derived neuronal cells before and after treatment of actin with Swin A. A significant reduction in the stripe score was detected as compared to cells that were treated with DMSO.

Overall, this part of the thesis showed that membrane proximal actin rings induce membrane compartmentalization. This discovery lends support to a long-standing theory of membrane organization: the picket-fence model (3.2.2).[6] Direct evidence for the model had been previously difficult to obtain, as most cytoskeletal proteins are highly dynamic. From the findings of this thesis, it can be concluded that actin generates nanometer-sized domains that exist wherever periodic actin rings are present.

This work also explored another compartmentalized system located in the cytosol of neurons: SV clusters at synaptic boutons. It had been shown previously that the soluble phosphoprotein synapsin is acting as the master regulator by being necessary and sufficient for SV cluster formation (3.3.4),[3] however the molecular mechanism remained elusive. By performing PALM in live hippocampal neurons this work now found that synapsin 1 co-localizes with synaptophysin 1 (a SV marker) at synaptic boutons. Furthermore, while synaptophysin molecules (or SVs) are almost exclusively located inside boutons, synapsin 1 is present along the entire axon. The stereotypical localization of synaptophysin 1 (WT) was lost in triple synapsin KO neurons (KO) but could be rescued in KO neurons expressing full length synapsin 1 (full length rescue) and also in neurons expressing only the IDR of synapsin 1 (differential rescue, the IDR is known to be necessary and sufficient to induce LLPS[3]). These results suggest that synapsin 1 controls the confinement of SV cluster at synaptic boutons trough LLPS.

Furthermore, by performing dual-color SMT in live hippocampal neurons this work found that both synapsin 1 and synaptophysin 1 maintain a high mobility at synaptic boutons. Two populations of synapsin 1 could be identified. One that is slow and confined at boutons and one that is fast and much less confined between boutons. By comparing the number of trajectories inside and outside synaptic boutons, this work found a three-fold enrichment of synapsin 1 inside boutons compared to outside synaptic boutons.

The mobility of synapsin was not affected by its own expression level, as mobility remained unchanged in 24h or 48h post-transfection cells. Too investigate whether the slowdown of synapsin 1 at synaptic boutons was due to unspecific molecular crowding or due to LLPS, the mobility of synapsin 1 was compared with the mobility of soluble mEos. Synapsin 1 was found to be more confined and less mobile inside synaptic boutons even though both molecules have similar molecular weights. Furthermore, the level of confinement of the fast-moving population of synapsin 1 was comparable to that of soluble mEos. Therefore, this work shows that the slowdown of synapsin 1 at synaptic boutons cannot be explained by molecular crowding alone. To avoid any bias in the analysis, dual-color SMT data of synapsin 1 and synaptophysin in the axon of neurons were analyzed again. Tracks were filtered according to the exponent of confinement. With this analysis method, again two populations of synapsin 1 were observed: confined tracks were located at synaptic boutons, while tracks displaying active transport were located between boutons.

Furthermore, this work showed that synapsin 1 can form condensates without SVs in an ectopic system. To that end, synapsin 1 was co-expressed in CV-1 cells with different interaction partners (SH3-concatemer, Grb2, synaptophysin 1). Condensates similar to those found in neurons were present under all conditions with similar diffusive properties of synapsin 1.

Additionally, this work showed that the mobility of SVs is controlled by synapsin 1. Here, synaptophysin 1 was expressed in different genetic backgrounds of synapsin 1 (WT, KO of synapsin 1-3, rescue with full-length synapsin 1, rescue with the only IDR of synapsin 1). Again, SPT of synaptophysin 1 was used as a proxy for the mobility of SVs. It was found that SV mobility (diffusion coefficient and exponent of confinement) was significantly reduced in the presence of synapsin 1. This was true when comparing WT and KO conditions but also when comparing KO with rescue conditions. The same result of the effect of synapsin 1 on SV mobility was obtained when analyzing the data in three different ways (by treating each tracking experiment as a data point, by treating each track as a data point or by calculating MSD-lagtime-curves). Importantly, neither the expression level of synaptophysin 1 (WT vs. overexpression) nor the tags (Halo vs. GFP) used had a significant effect on the diffusion coefficient or the exponent of confinement of synapsin 1. Crucially, the IDR of synapsin 1 was sufficient to rescue the diffusive properties of SVs of the WT. Since the IDR of synapsin 1 is sufficient to trigger LLPS[3] (3.3.4), it can be concluded here that synapsin 1 controls the mobility of SVs via LLPS.

This finding was confirmed by 3D-STED microscopy performed by Rajdeep Chowdhury, Ali H. Shaib, and Silvio O. Rizzoli in synapsin triple KO neurons, showing that the IDR of synapsin 1 is indeed sufficient to rescue SV clustering. That this is of functional relevance was shown by employing an exocytosis assay performed by Gerard Aguilar Perez and Franziska Trnka. Here, the fluorescence of a pH sensitive probe (pHluorin-tagged synaptophysin) inside SVs in different genetic backgrounds (WT, KO of synapsin 1-3, rescue with full-length synapsin 1, rescue with the only IDR of synapsin 1) was recorded. Changes in fluorescence indicated that both the IDR of synapsin 1 and full length synapsin 1 rescued SV release in synapsin triple KO neurons.

Furthermore, Christian Hoffmann performed *in vitro* reconstitutions of native SVs from murine brains and purified synapsin 1. Synapsin 1 and SVs readily formed condensates as shown by fluorescence microscopy. Additionally, by incubating synapsin 1 / SV complexes with biomolecules of different sizes, it was shown that SVs modulate the meshwork pore size of synapsin 1 / SV condensates.

Findings of SPT in mouse hippocampal neurons described above were also confirmed by ultrafast SPT experiments. Taka A. Tsunoyama and Akihiro Kusumi tracked synapsin 1 and SVs in *in vitro* reconstituted condensates. Here, it was shown that mobility (diffusion coefficient and exponent of confinement) of synapsin 1 is significantly reduced in the presence of SVs, independent of the timescale of the measurement.

Overall, this part of the thesis established synapsin 1 as the master regulator of SV mobility. The findings suggest that condensation of synapsin is sufficient to induce compartmentalization of SVs into clusters inside synaptic boutons.

In summary, this thesis investigated two compartmentalized systems in neuronal cells in the PM and in the cytosol. In the PM, two-dimensional compartments are formed by direct interactions with sub-membranous actin rings, that form semi-permeable diffusion barriers. In the cytosol, specifically in synaptic boutons, condensate formation is enabled by the phosphoprotein synapsin 1 via liquid liquid phase separation. The formed condensates act as three-dimensional compartments that sequester SVs. In the following chapter the findings of this work will be discussed in the context of the wider research field.

7. Discussion and outlook

This thesis found that compartmentalization is a general principle for the organization of complex fluid systems in neurons. In the PM, two-dimensional compartments are formed by direct interactions of membrane proteins with sub-membranous actin rings. Here, actin rings act as a semi-permeable barrier, which causes the formation of membrane domains located between actin rings. In the cytosol, compartmentalization does not require cytoskeletal proteins directly. Specifically in synaptic boutons, condensate formation through liquid liquid phase separation enables the generation of three-dimensional compartments. Phase separation in the synaptic bouton is conferred by the phosphoprotein synapsin 1 through its IDR. Crucially, synapsin 1 condensates then form an embedding medium around SVs, thereby sequestering SVs into dense clusters and controlling the dynamics of SVs inside clusters (Figure 15).

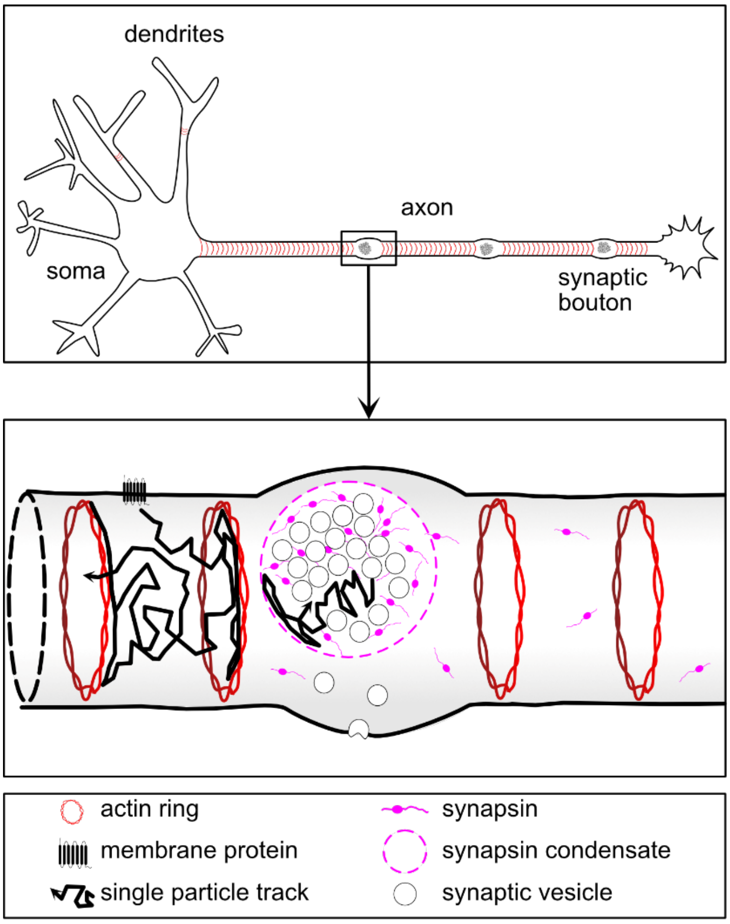

Figure 15 Two molecular mechanisms of compartmentalization in neuronal cells.

This work investigated fluid systems in of both the PM and the cytosol of neuronal cells. In the PM compartmentalization is conferred by direct interactions of membrane proteins with the cytoskeleton, which leads to the formation of two-dimensional membrane domains located between actin rings. In the cytosol, specifically inside synaptic boutons, liquid liquid phase separation driven by synapsin 1, enables the generation of three-dimensional condensates. These condensates form an embedding medium around SVs, thereby sequestering SVs into dense clusters.

Importantly, both the two-dimensional compartments in the PM and the three-dimensional compartments in the cytosol of neurons do not have a hard boundary, rather both types of compartments are in constant exchange with the surrounding medium. In the case of the PM, this is clearly shown by the data presented in this work, as all investigated membrane proteins are able to pass the actin barrier (in agreement with the literature)[30]. For synapsin condensates this work has found two populations of synapsin 1 (one inside the synaptic boutons, one distributed along the axon), suggesting a lack of complete confinement of synapsin 1 to condensates. Also, this work has shown via *in vitro* ultrafast SMT performed by Taka A. Tsunoyama that synapsin 1 is recruited to condensates from the surrounding medium. This is in agreement with previous FRAP experiments both *in vitro* and *in vivo,* where synapsin condensates recover quickly after a photo bleaching event.[3,91] Taking together, this work highlights the transient nature of the studied compartments, which makes understanding the dynamics of these systems essential. Precisely by investigating these dynamics, this work has uncovered two possible molecular mechanisms of compartmentalized systems, however important questions remain.

In the PM of neuronal cells, this work has shown the compartmentalization of the PM by actin rings for inner-leaflet, transmembrane and outer-leaflet proteins. Inner-leaflet and transmembrane proteins are plausibly in contact with actin rings. This begs the questions: How is the compartmentalization effect of the actin rings communicated to outer-leaflet membrane proteins, not in contact with sub-membranous actin? According to the picket-fence model (3.2.2), this is likely achieved by transmembrane pickets immobilized on the actin rings. The identity of the pickets so far remains elusive. A possible candidate might be cluster of differentiation 44 (CD44), which has been shown to be immobilized on cortical actin filaments in macrophages and thereby act as a barrier to the diffusion of phagocytic receptors.[222] CD44 is expressed in neuronal cells,[223,224] however it remains unclear how and if it interacts with neuronal actin structures (especially actin rings). Further research into the nanoscopic organization of CD44 in neurons is therefore needed.

Another potential picket protein is the voltage gated potassium channel 1.2 (KV1.2), which has been identified to directly localize to actin rings.[225] While KV1.2 is present in both the AIS and the distal axon,[226] it is detectable only very late during neuronal maturation (after DIV14)[227].

The neurons investigated in this work where no older than DIV14. Furthermore, KV1.2 is not expressed ubiquitously in astrocytes and oligodendrocytes.[228,229] Hence, KV1.2 is not sufficient to explain the pervasive compartmentalization of the PM in many cell types of the neuronal lineage found in this work.

Other candidates to explain confinement of out-leaflet membrane molecules are cell adhesion proteins extending from the inside of the cell to the extracellular maxtrix.[230] Interestingly, Hauser *et al.* have shown in primary neurons and in progenitor-derived neuronal cells that neurites in direct contact with each other, show an alignment in their MPS.[52] Although the mechanism of the alignment is unknown, it is likely that cell adhesion molecules are involved as they are responsible for intercellular binding.[230] Recently, Zhou *et al.* have shown that such adhesion molecules (e.g. neurofascin) show a periodic organization in neurites, suggesting an association with the neuronal MPS,[231] likely conferred by an ankyrin-binding domain.[232] Critically, ankyrins are located between actin rings (3.2.3),[46,225] therefore cell adhesion molecules associated to ankyrins are also located between actin rings.[49] Hence, it is likely that cell adhesion molecules associated to ankyrins would restrict the motion of membrane molecules in a similar way as channel proteins associated with ankyrins investigated in this work via *in silico* SPT experiments. Channel protein densities did not accurately predict the experimentally observed confinement. It is therefore unlikely that adhesion molecules in the extracellular matrix are the cause of the observed membrane compartmentalization. In addition, the progenitor-derived neuronal cells investigated in this work did not show a stereotypical organization of AnkG. It is therefore unclear if and how adhesion molecules are associated with the MPS in these cells, which further sheds doubt on the hypotheses that adhesion molecules could explain the observed membrane compartmentalization. Since neither known picket proteins, nor adhesion molecules sufficiently explain the confinement of outer-leaflet membrane probes observed here, research into the identity of membrane pickets associated with actin rings and other cytoskeletal structures is needed.

This work measured the distance of actin rings and the PM to be ~20 nm. While this means that actin rings are certainly close to the inner leaflet of the PM, it also shows that actin rings do not seem to be in direct contact with the PM. Therefore, this raises the question if and how actin rings are anchored to the PM. Possible candidates include members of the septin family. Septins have been shown to both interact with membranes[233] and with actin[234,235]. Specifically

Septin 7 forms a diffusion barrier in dendritic spines of neurons.[236] As actin rings are present in spine necks[54] this barrier might be constructed by the interaction of septin 7 with actin rings. Furthermore, septins 5, 6, 7, and 11 have been shown to form a detergent-resistant pool that colocalizes with AnkG in the AIS of neurons.[237] Components of the MPS (like spectrin[48]) have been found to form a similar detergent resistant pool. Therefore, this finding might indicate, that septins are also part of the MPS, where one of their roles potentially includes the anchoring of actin rings to the PM. Further research to elucidate the role of septins for anchoring of actin to the PM or to identify other components of the MPS with a similar function is needed.

What is the functional role of the actin ring diffusion barrier? Recently, Zhou *et al.* have shown that the MPS serves as a structural platform for signaling molecules (e.g. CB-1, Src), enabling downstream intracellular signaling.[4] Importantly, Zhou *et al.* employed dual-color STORM to show that signaling molecules are localized between actin rings upon stimulation. While very insightful, this work only contains end-point measurements, hence the dynamics of the molecular interactions remain underexplored. Therefore, future research in living cells employing SPT techniques could shed new light on the function of the MPS.

The MPS is highly regular and periodic (3.2.3). Therefore, it likely enables consistent responses to stimuli all along the axon by distributing important signaling molecules associated with the MPS. Concentrating specific molecules between actin rings via a diffusion barrier might enable the formation of specialized signaling hubs at different sections of the axon (e.g. AIS, nodes of Ranvier). Actin rings could serve a similar function in the processes of other cells of the neuronal lineage. Furthermore, actin rings might influence the fluidity and viscosity of the PM locally. This raises the interesting possibility that actin rings and associated molecules induce phase separation of membrane proteins.[4] Such phase separation potentially enhances the effect of the physical actin diffusion barrier by allowing the local concentration of membrane proteins at or between actin rings, but this remains to be explored in future work. Especially, in the context of phase separation, the lipid composition of the PM is likely to play a crucial role. The role of lipids in the diffusion barrier at actin rings has been underexplore. Future research should focus on the interaction of the cytoskeleton with lipid / protein complexes (lipid rafts)[26] in the PM.

Furthermore, stable periodic cytoskeletal structures are not only present in the neuronal lineage but also in other cell types such as erythrocytes[40] and cardiomyocytes[238].

Consequently, exploring the effect of the cytoskeleton on the PM in these cell types could prove insightful.

Recently, Fujiwara *et al.* developed an ultra-fast camera that can record single fluorophores with up to 10 kHz framerate.[239] They used this camera system to show that transmembrane proteins undergo hop-diffusion inside focal adhesions and that compartments are smaller than in the rest of the PM.[29] MINFLUX microscopy (3.4.1) achieves similar resolutions and can be used in 3D to infer detailed information about the nanostructure of biological systems.[172,240] Applying these cutting edge imaging techniques to the diffusion barrier at actin rings described in this work is likely to generate new insights into the molecular dynamics of this system.

Additionally, cortical actin structures should be investigated with cutting edge ultra-fast SPT techniques. The investigation of the influence of cortical actin on PM organization has been held back by the highly dynamic nature of the cortical actin cytoskeleton.[39] Employing ultra-fast SPT techniques now enables the observation of the PM and its underlying cytoskeletal cortex on physiological relevant time scales, thereby possibly uncovering the nanometer scale organization of the PM.

This works has shown that synapsin 1 controls the mobility of SVs inside synaptic boutons by inducing compartmentalization into liquid liquid phase separated condensates. Previously, synapsins were thought to induce vesicle clustering by crosslinking vesicles via short, thin filaments.[111] In this model, synapsin 1 acts as a tether for SVs. This thesis has shown that synapsin 1 and SVs remain highly mobile inside SV condensates. Therefore, an alternative hypothesis of how synapsin 1 induces SV clustering[3] can be proposed: In this scenario, synapsins instead acts as an ensnaring medium surrounding SVs, thereby inducing clustering. Since SVs are not tethered, they could consequently move relatively freely inside the condensate (maintaining high mobility). Of note, both hypotheses (synapsin as tether, synapsin as medium) are not necessarily mutually exclusive. Hirokawa *et al.* identified synapsin 1 tethers between SVs via quick-freeze deep-etch EM.[111] Though a powerful technique, it is likely that dynamic structures dominated by weak interactions such as synapsin condensates are not well preserved during sample preparation, while stable structures like filamentous synapsin 1 tethers are. Consequently, synapsin condensates might not have been readily observable. At least a fraction of synapsin 1 is likely to be aggregated under physiological conditions, as indicated by a large immobile fraction observed in FRAP experiments of synapsin 1 condensates.[91]

Liquid liquid phase separated condensates have been shown to be metastable[86,87] (3.3.1), i.e. initial liquid structures transition into solid like aggregates over time (under certain conditions reversibly)[1]. This feature of condensates might function here to control the viscosity of SV clusters. By increasing the fraction of aggregated synapsin 1, viscosity inside clusters might increase in response to stress or other stimuli (conversely an increase in the soluble fraction of synapsin 1 might reduce viscosity inside SV clusters).

Liquid condensates have been shown to be strongly affected by changes in temperature and pH near the physiological range.[101] So synapsin 1 aggregation in response to an increase in temperature might prevent the dispersal of SV clusters. Similarly, controlled synapsin 1 aggregation might function as a buffer against other factors that affect SV cluster viscosity such as local ion concentration and pH, which are changing during depolarization. To address this, further research into the effect of changes in physiological conditions on synapsin 1 condensate formation in living systems is needed.

The work presented in this thesis used the diffusion of synaptophysin as a proxy for the movement of SVs. Importantly, synaptophysin is a tetra-span transmembrane protein highly abundant in the PM of SVs (3.3.3).[124] It is likely that synaptophysin is not immobile in the membrane. This work achieved a spatial resolution of 20 nm for 3D-SPT of synaptophysin. Considering the diameter of SVs of ~45 nm[124], it was impossible to distinguish between the motion of individual SVs and of synaptophysin inside the PM of SVs. In future work, insights into the dynamics of synaptophysin inside SVs could be gained by employing MINFLUX microscopy. MINFLUX microscopy recently achieved a 3D spatial resolution below 3 nm in fixed neurons.[240] Though likely to be more challenging to achieve in a live-cell setting (due to among other things internal motion of the sample), spatial resolutions in this order of magnitude are likely to allow for a sub SV study of the interaction of synapsin with synaptophysin and other SV membrane proteins.

This thesis focused on the effect of synapsin on the mobility of SVs. In future work, other soluble proteins present in SV clusters should also be considered. For example, synucleins have been shown to reduce SV packing density (3.3.3) in stark contrast to synapsin.[3,118] Therefore, it can be hypothesized that synuclein presence in synaptic boutons is likely to increase SV mobility. To address this, SMT of SVs in the presence and absence of synucleins should be performed in live neurons in future work. Synucleins and synapsins have been proposed to control the packing density of SV clusters in tandem, where a physiological equilibrium of synapsins and synucleins in the boutons stabilizes SV cluster density.[2] Hence, it is likely that a similar equilibrium exists for SV mobility, which should be investigated in future research.

The clustering of SV-like structures by synapsin 1 does not require cytoskeletal proteins *in vitro*.[3] Importantly this does not exclude the involvement of cytoskeletal proteins completely. SVs have been shown to polymerize actin[112] but the exact mechanism remains unknown. Hence, future research should focus on the effect of synapsin condensates on actin polymerization inside synaptic boutons. This could be achieved by investigating if bouton specific actin nanostructures[113] require the presence of synapsin 1.

Furthermore, the role of actin structures on the organization of SV condensates should be investigated further. The role of actin in boutons likely includes anchoring SV condensates to prevent dispersal along the length of the axon. Additionally, actin might acts as a tether between SVs similar to what had been proposed for synapsin 1 previously,[111] but this remains to be explored in future research.

Actin rings are absent inside synaptic boutons.[113] This raises the question if and how the PM is compartmentalized there. Bouton specific nanostructures might play a similar role as actin rings along neuronal processes. Recently, Ogunmowo *et al.* identified a torus like actin structure around SV clusters.[114] Importantly, these structures are perpendicular to the actin rings found along neuronal processes. Furthermore, the torus structures appear much thicker than actin rings, so they are likely to be structurally distinct.[47,114] Nevertheless, if the torus structures are close to the PM, they might act as a diffusion barrier, restricting the entry of membrane molecules from the rest of the axon towards the active zone. KV channels are likely to be present in the PM of synaptic boutons.[241] If they act as membrane pickets bound to actin as hypothesized above, they might form a ring-like structure around SV clusters. Interestingly, such a ring-like structure has been found in the immunological synapse for KV1.3,[242] though it remains unclear if it acts as a diffusion barrier.

Finally, future research should focus on the interactions of the compartments investigated in this thesis. Neuronal transmission requires a complex interplay of cytosolic entities (SVs, soluble proteins, the cytoskeleton…) and membrane molecules (receptors, channels, transporters…). It is therefore highly likely that both membrane compartments and intracellular condensates are tightly regulated together and influence one another directly. Understanding these interactions is crucial for deepening our understanding of neuronal function. This thesis has made important strides towards this goal by uncovering the molecular mechanisms of how compartmentalization operates in both the PM and the cytosol of neuronal cells.

8. Appendix

8.1 Curriculum Vitae

Personal information

Name	Jakob Rentsch

Education

2012	High school graduation (final grade 1.0)
2012-2015	**B. Sc. Biochemistry** Freie Universität Berlin (final grade 1.6) Thesis topic: “Effect of novel PI3K-inhibitors on viability and cell cycle in gastroenteropancreatic neuroendocrine neoplasia (GEP-NEN)“ Supervisor: PD. Grabowski at Charité, Berlin, Germany
2015-2018	**M. Sc. Biochemistry** Freie Universität Berlin (final grade 1.3) Thesis topic: “Mapping intracellular diffusion of inner leaflet peripheral membrane proteins using single particle tracking of quantum dot nanocrystals“ Supervisor: Prof. Helge Ewers at Freie Universität Berlin, Germany
09/16-03/17	Erasmus semester, Universidat de Barcelona, Spain
2018-2024	**Doctoral student in Biochemistry** Freie Universität Berlin (final grade summa cum laude) Thesis topic: “Uncovering the molecular basis of compartmentalization as a principle of neuronal organization” Supervisor: Prof. Helge Ewers at Freie Universität Berlin, Germany Methods: single particle tracking, single molecule localisation microscopy, STED, culturing and differentiation of neuronal progenitor cells, molecular simulations

Work experience

2018-2024	Scientific assistant Freie Universität Berlin, Germany Laboratory of Prof. Helge Ewers

Conference talks

02/2023	Biophysical Society Meeting 2023, San Diego
03/2023	German Neuroscience Meeting 2023, Göttingen

Teaching

2019	Teaching assistant for undergraduate biochemistry practical: “Basic methods in biochemistry”
2020-2022	Teaching assistant for master level biochemistry practical: “Quantitative fluorescence microscopy” Methods: single particle tracking, fluorescence recovery after photobleaching
10/2021	Instructor at CAJAL Advanced Imaging Methods for Cellular Neuroscience 2021 Université de Bordeaux, France Topic: “Nanoscale organization and dynamics of synapsin condensates”

Languages

English	fluent, level C1
Spanish	fluent, level B2
French	basic, level A1

Programming skills

Coding	Matlab, R, ImageJ, Python

Publications

1. Rentsch, J., Bandstra, S., Sezen, B., Sigrist, P., Bottanelli, F., Schmerl, B., Shoichet, S., Noé, F., Sadeghi, M., and Ewers, H. (2024). Sub-membrane actin rings compartmentalize the plasma membrane. Journal of Cell Biology *223*, e202310138. 10.1083/jcb.202310138.
2. Hoffmann, C., Rentsch, J., Tsunoyama, T.A., Chhabra, A., Aguilar Perez, G., Chowdhury, R., Trnka, F., Korobeinikov, A.A., Shaib, A.H., Ganzella, M., et al. (2023). Synapsin condensation controls synaptic vesicle sequestering and dynamics. Nature Communications *14*, 6730. 10.1038/s41467-023-42372-6.
3. Thielhorn, R., Heing-Becker, I., Humpfer, N., Rentsch, J., Haag, R., Licha, K., and Ewers, H. (2023). Controlled Grafting Expansion Microscopy. Angew Chem Int Ed Engl, e202302318. 10.1002/anie.202302318.
4. Schmerl, B., Gimber, N., Kuropka, B., Stumpf, A., Rentsch, J., Kunde, S.A., von Sivers, J., Ewers, H., Schmitz, D., Freund, C., et al. (2022). The synaptic scaffold protein MPP2 interacts with GABAA receptors at the periphery of the postsynaptic density of glutamatergic synapses. PLoS Biol *20*, e3001503. 10.1371/journal.pbio.3001503.
5. Zehtabian, A., Muller, P.M., Goisser, M., Obendorf, L., Janisch, L., Humpfer, N., Rentsch, J., and Ewers, H. (2022). Precise measurement of nanoscopic septin ring structures with deep learning-assisted quantitative superresolution microscopy. Mol Biol Cell *33*, ar76. 10.1091/mbc.E22-02-0039.
6. Kutz, S., Zehrer, A.C., Svetlitckii, R., Gülcüler Balta, G.S., Galli, L., Kleber, S., Rentsch, J., Martin-Villalba, A., and Ewers, H. (2021). An Efficient GUI-Based Clustering Software for Simulation and Bayesian Cluster Analysis of Single-Molecule Localization Microscopy Data. Frontiers in Bioinformatics.
7. Gao, M., Thielhorn, R., Rentsch, J., Honigmann, A., and Ewers, H. (2021). Expansion STED microscopy (ExSTED). Methods in Cell Biology. 1 ed. Elsevier Inc.
8. Li, J.H., Santos-Otte, P., Au, B., Rentsch, J., Block, S., and Ewers, H. (2020). Directed manipulation of membrane proteins by fluorescent magnetic nanoparticles. Nature Communications *11*, 1-7. 10.1038/s41467-020-18087-3.
9. Mikhaylova, M., Rentsch, J., and Ewers, H. (2020). Actomyosin Contractility in the Generation and Plasticity of Axons and Dendritic Spines. Cells *9*, 1-14. 10.3390/cells9092006.
10. Nölting, S., Rentsch, J., Freitag, H., Detjen, K., Briest, F., Möbs, M., Weissmann, V., Siegmund, B., Auernhammer, C.J., Aristizabal Prada, E.T., et al. (2017). The selective PI3Kα inhibitor BYL719 as a novel therapeutic option for neuroendocrine tumors: Results from multiple cell line models. PLoS ONE.

8.2 References

1 Shin, Y. & Brangwynne, C. P. Liquid phase condensation in cell physiology and disease. *Science* **357** (2017). https://doi.org:10.1126/science.aaf4382

2 Sansevrino, R., Hoffmann, C. & Milovanovic, D. Condensate biology of synaptic vesicle clusters. *Trends Neurosci* **46**, 293-306 (2023). https://doi.org:10.1016/j.tins.2023.01.001

3 Milovanovic, D., Wu, Y., Bian, X. & De Camilli, P. A liquid phase of synapsin and lipid vesicles. *Science* **361**, 604-607 (2018). https://doi.org:10.1126/science.aat5671

4 Zhou, R., Han, B., Xia, C. & Zhuang, X. Membrane-associated periodic skeleton is a signaling platform for RTK transactivation in neurons. *Science* **365**, 929-934 (2019). https://doi.org:10.1126/science.aaw5937

5 Kusumi, A., Suzuki, K. G. N., Kasai, R. S., Ritchie, K. & Fujiwara, T. K. Hierarchical mesoscale domain organization of the plasma membrane. *Trends in Biochemical Sciences* **36**, 604-615 (2011). https://doi.org:https://doi.org/10.1016/j.tibs.2011.08.001

6 Kusumi, A. *et al.* Paradigm Shift of the Plasma Membrane Concept from the Two-Dimensional Continuum Fluid to the Partitioned Fluid: High-Speed Single-Molecule Tracking of Membrane Molecules. *Annual Review of Biophysics and Biomolecular Structure* **34**, 351-378 (2005). https://doi.org:10.1146/annurev.biophys.34.040204.144637

7 Mukherjee, S. & Maxfield, F. R. Membrane Domains. *Annual Review of Cell and Developmental Biology* **20**, 839-866 (2004). https://doi.org:10.1146/annurev.cellbio.20.010403.095451

8 Singer, S. J. J. Structure and function of biological membranes. 145 (1971).

9 Van Meer, G., Voelker, D. R. & Feigenson, G. W. Membrane lipids: Where they are and how they behave. *Nature Reviews Molecular Cell Biology* **9**, 112-124 (2008). https://doi.org:10.1038/nrm2330

10 Branton, D. Fracture faces of frozen membranes. *Proc Natl Acad Sci U S A* **55**, 1048-1056 (1966).

11 Guidotti, G. Membrane proteins. *Annu. Rev. Biochem.* **41**, 731-752 (1972).

12 Singer, S. J. J. & Nicolson, G. L. L. The fluid mosaic model of the structure of cell membranes. *Science* **175**, 720-731 (1972). https://doi.org:10.1126/science.175.4023.720

13 Killian, J. A. & Von Heijne, G. How proteins adapt to a membrane-water interface. *Trends in Biochemical Sciences* **25**, 429-434 (2000). https://doi.org:10.1016/S0968-0004(00)01626-1

14 Johnson, J. E. & Cornell, R. B. Amphitropic proteins: Regulation by reversible membrane interactions. *Molecular Membrane Biology* (1999). https://doi.org:10.1080/096876899294544

15 Paulick, M. G. & Bertozzi, C. R. The glycosylphosphatidylinositol anchor: A complex membrane-anchoring structure for proteins. *Biochemistry* **47**, 6991-7000 (2008). https://doi.org:10.1021/bi8006324

16 Cho, W. & Stahelin, R. V. Membrane-Protein Interactions in Cell Signaling and Membrane Trafficking. *Annual Review of Biophysics and Biomolecular Structure* (2005). https://doi.org:10.1146/annurev.biophys.33.110502.133337

17 Hanakam, F., Gerisch, G., Lotz, S., Alt, T. & Seelig, A. Binding of hisactophilin I and II to lipid membranes is controlled by a pH-dependent myristoyl-histidine switch. *Biochemistry* (1996). https://doi.org:10.1021/bi960789j

18 Frye, L. D. & Edidin, M. The Rapid Intermixing of Cell Surface Antigens After Formation of Mouse-Human Heterokaryons. *Journal of Cell Science* **7**, 319-335 (1970).

19 Grasberger, B., Minton, A. P., DeLisi, C. & Metzger, H. Interaction between proteins localized in membranes. *Proceedings of the National Academy of Sciences* **83**, 6258-6262 (1986). https://doi.org:10.1073/pnas.83.17.6258

20 Saffman, P. G., Delbruck, M. & Delbrück, M. Brownian motion in biological membranes. *Proc Natl Acad Sci USA* **72**, 3111-3113 (1975). https://doi.org:10.1073/pnas.72.8.3111

21 Weiß, K. *et al.* Quantifying the Diffusion of Membrane Proteins and Peptides in Black Lipid Membranes with 2-Focus Fluorescence Correlation Spectroscopy. *Biophysical Journal* **105**, 455-462 (2013). https://doi.org:https://doi.org/10.1016/j.bpj.2013.06.004

22 Hegener, O. *et al.* Dynamics of beta2-adrenergic receptor-ligand complexes on living cells. *Biochemistry* **43**, 6190-6199 (2004). https://doi.org:10.1021/bi035928t

23 Koppel, D. E., Sheetz, M. P. & Schindler, M. Matrix control of protein diffusion in biological membranes. *Proc Natl Acad Sci U S A* **78**, 3576-3580 (1981).

24 Kusumi, A., Sako, Y. & Yamamoto, M. Confined lateral diffusion of membrane receptors as studied by single particle tracking (nanovid microscopy). Effects of calcium-induced differentiation in cultured epithelial cells. *Biophysical Journal* **65**, 2021-2040 (1993). https://doi.org:10.1016/S0006-3495(93)81253-0

25 Tomishige, M. & Kusumi, A. Compartmentalization of the erythrocyte membrane by the membrane skeleton: intercompartmental hop diffusion of band 3. *Molecular biology of the cell* **10**, 2475-2479 (1999). https://doi.org:10.1091/mbc.10.8.2475

26 Suzuki, K. G. N. & Kusumi, A. Refinement of Singer-Nicolson fluid-mosaic model by microscopy imaging: Lipid rafts and actin-induced membrane compartmentalization. *Biochimica et Biophysica Acta (BBA) - Biomembranes* **1865**, 184093 (2023). https://doi.org:https://doi.org/10.1016/j.bbamem.2022.184093

27 Fujiwara, T., Ritchie, K., Murakoshi, H., Jacobson, K. & Kusumi, A. Phospholipids undergo hop diffusion in compartmentalized cell membrane. *Journal of Cell Biology* **157**, 1071-1081 (2002). https://doi.org:10.1083/jcb.200202050

28 Suzuki, K., Ritchie, K., Kajikawa, E., Fujiwara, T. & Kusumi, A. Rapid hop diffusion of a G-protein-coupled receptor in the plasma membrane as revealed by single-molecule techniques. *Biophysical Journal* **88**, 3659-3680 (2005). https://doi.org:10.1529/biophysj.104.048538

29 Fujiwara, T. K. *et al.* Ultrafast single-molecule imaging reveals focal adhesion nano-architecture and molecular dynamics. *Journal of Cell Biology* **222**, e202110162 (2023). https://doi.org:10.1083/jcb.202110162

30 Albrecht, D. *et al.* Nanoscopic compartmentalization of membrane protein motion at the axon initial segment. *Journal of Cell Biology* **215**, 37-46 (2016). https://doi.org:10.1083/jcb.201603108

31 Fujiwara, T. K. *et al.* Confined diffusion of transmembrane proteins and lipids induced by the same actin meshwork lining the plasma membrane. *Molecular biology of the cell* **27**, 1101-1119 (2016). https://doi.org:10.1091/mbc.e15-04-0186

32 Andrade, D. M. *et al.* Cortical actin networks induce spatio-temporal confinement of phospholipids in the plasma membrane--a minimally invasive investigation by STED-FCS. *Sci Rep* **5**, 11454 (2015). https://doi.org:10.1038/srep11454

33 Xu, K., Babcock, H. P. & Zhuang, X. Dual-objective STORM reveals three-dimensional filament organization in the actin cytoskeleton. *Nature Methods* **9**, 185-188 (2012). https://doi.org:10.1038/nmeth.1841

34 Clausen, M. P., Colin-York, H., Schneider, F., Eggeling, C. & Fritzsche, M. Dissecting the actin cortex density and membrane-cortex distance in living cells by super-resolution microscopy. *Journal of Physics D: Applied Physics* **50**, 064002 (2017). https://doi.org:10.1088/1361-6463/aa52a1

35 Bisaria, A., Hayer, A., Garbett, D., Cohen, D. & Meyer, T. Membrane-proximal F-actin restricts local membrane protrusions and directs cell migration. *Science* **368**, 1205-1210 (2020). https://doi.org:10.1126/science.aay7794

36 Kastrup, L., Blom, H., Eggeling, C. & Hell, S. W. Fluorescence fluctuation spectroscopy in subdiffraction focal volumes. *Phys Rev Lett* **94**, 178104 (2005). https://doi.org:10.1103/PhysRevLett.94.178104

37 Bovellan, M. *et al.* Cellular Control of Cortical Actin Nucleation. *Current Biology* **24**, 1628-1635 (2014). https://doi.org:10.1016/j.cub.2014.05.069

38 Li, J. H. *et al.* Directed manipulation of membrane proteins by fluorescent magnetic nanoparticles. *Nature Communications* **11**, 1-7 (2020). https://doi.org:10.1038/s41467-020-18087-3

39 Gowrishankar, K. *et al.* Active Remodeling of Cortical Actin Regulates Spatiotemporal Organization of Cell Surface Molecules. *Cell* **149**, 1353-1367 (2012).

40 Pan, L., Yan, R., Li, W. & Xu, K. Super-Resolution Microscopy Reveals the Native Ultrastructure of the Erythrocyte Cytoskeleton Report Super-Resolution Microscopy Reveals the Native Ultrastructure of the Erythrocyte Cytoskeleton. 1151-1158 (2018). https://doi.org:10.1016/j.celrep.2017.12.107

41 Han, B., Zhou, R., Xia, C. & Zhuang, X. Structural organization of the actin-spectrin-based membrane skeleton in dendrites and soma of neurons. *Proc Natl Acad Sci U S A* **114**, E6678-e6685 (2017). https://doi.org:10.1073/pnas.1705043114

42 Xu, K., Zhong, G. & Zhuang, X. Actin, Spectrin, and Associated Proteins Form a Periodic Cytoskeletal Structure in Axons. *Science* **339**, 452-456 (2013). https://doi.org:10.1126/science.1232251

43 Mikhaylova, M., Rentsch, J. & Ewers, H. Actomyosin Contractility in the Generation and Plasticity of Axons and Dendritic Spines. *Cells* **9**, 1-14 (2020). https://doi.org:10.3390/cells9092006

44 He, J. *et al.* Prevalent presence of periodic actin-spectrin-based membrane skeleton in a broad range of neuronal cell types and animal species. *Proceedings of the National Academy of Sciences of the United States of America* **113**, 6029-6034 (2016). https://doi.org:10.1073/pnas.1605707113

45 Gao, M. *et al.* Expansion Stimulated Emission Depletion Microscopy (ExSTED). *ACS Nano* **12**, 4178-4185 (2018). https://doi.org:10.1021/acsnano.8b00776

46 Leterrier, C. *et al.* Nanoscale Architecture of the Axon Initial Segment Reveals an Organized and Robust Scaffold. *Cell Reports* **13**, 2781-2793 (2015). https://doi.org:10.1016/j.celrep.2015.11.051

47 Vassilopoulos, S., Gibaud, S., Jimenez, A., Caillol, G. & Leterrier, C. Ultrastructure of the axonal periodic scaffold reveals a braid-like organization of actin rings. *Nature Communications* **10** (2019). https://doi.org:10.1038/s41467-019-13835-6

48 Yu, C. *et al.* αII spectrin forms a periodic cytoskeleton at the axon initial segment and is required for nervous system function. *The Journal of Neuroscience* **37**, 11311-11322 (2017). https://doi.org:10.1523/JNEUROSCI.2112-17.2017

49 D'Este, E., Kamin, D., Göttfert, F., El-Hady, A. & Hell, S. W. STED Nanoscopy Reveals the Ubiquity of Subcortical Cytoskeleton Periodicity in Living Neurons. *Cell Reports* **10**, 1246-1251 (2015). https://doi.org:10.1016/j.celrep.2015.02.007

50 D'Este, E. *et al.* Subcortical cytoskeleton periodicity throughout the nervous system. *Sci Rep* **6**, 22741 (2016). https://doi.org:10.1038/srep22741

51 Costa, A. C. R. *et al.* The membrane periodic skeleton is an actomyosin network that regulates axonal diameter and conduction. *eLife* **9**, 1-20 (2020). https://doi.org:10.7554/eLife.55471

52 Hauser, M. *et al.* The Spectrin-Actin-Based Periodic Cytoskeleton as a Conserved Nanoscale Scaffold and Ruler of the Neural Stem Cell Lineage. *Cell Reports* **24**, 1512-1522 (2018). https://doi.org:10.1016/j.celrep.2018.07.005

53 Winterflood, C. M., Platonova, E., Albrecht, D. & Ewers, H. Dual-Color 3D Superresolution Microscopy by Combined Spectral-Demixing and Biplane Imaging. *Biophysical Journal* **109**, 3-6 (2015). https://doi.org:10.1016/j.bpj.2015.05.026

54 Bär, J., Kobler, O., Van Bommel, B. & Mikhaylova, M. Periodic F-actin structures shape the neck of dendritic spines. *Scientific Reports* **6**, 1-9 (2016). https://doi.org:10.1038/srep37136

55 Carmely, S. & Kashman, Y. Structure of swinholide-a, a new macrolide from the marine sponge theonella swinhoei. *Tetrahedron Letters* **26**, 511-514 (1985). https://doi.org:https://doi.org/10.1016/S0040-4039(00)61925-1

56 Spector, I., Braet, F., Shochet, N. R. & Bubb, M. R. New anti-actin drugs in the study of the organization and function of the actin cytoskeleton. *Microscopy Research and Technique* **47**, 18-37 (1999). https://doi.org:https://doi.org/10.1002/(SICI)1097-0029(19991001)47:1<18::AID-JEMT3>3.0.CO;2-E

57 Klenchin, V. A., King, R., Tanaka, J., Marriott, G. & Rayment, I. Structural basis of swinholide a binding to actin. *Chemistry and Biology* **12**, 287-291 (2005). https://doi.org:10.1016/j.chembiol.2005.02.011

58 Bubb, M. R., Spector, I., Bershadsky, A. D. & Korn, E. D. Swinholide A Is a Microfilament Disrupting Marine Toxin That Stabilizes Actin Dimers and Severs Actin Filaments (∗). *Journal of Biological Chemistry* **270**, 3463-3466 (1995). https://doi.org:10.1074/jbc.270.8.3463

59 Efimova, N. *et al.* Biii Spectrin Is Necessary for Formation of the Constricted Neck of Dendritic Spines and Regulation of Synaptic Activity in Neurons. *Journal of Neuroscience* **37**, 6442-6459 (2017). https://doi.org:10.1523/JNEUROSCI.3520-16.2017

60 Hammarlund, M., Jorgensen, E. M. & Bastiani, M. J. Axons break in animals lacking β-spectrin. *Journal of Cell Biology* **176**, 269-275 (2007). https://doi.org:10.1083/jcb.200611117

61 Dubey, S. *et al.* The axonal actin-spectrin lattice acts as a tension buffering shock absorber. *eLife* **9**, 1-22 (2020). https://doi.org:10.7554/eLife.51772

62 Abouelezz, A. *et al.* Tropomyosin Tpm3.1 Is Required to Maintain the Structure and Function of the Axon Initial Segment. *iScience* **23**, 101053 (2020). https://doi.org:10.1016/j.isci.2020.101053

63 Yoshimura, T. & Rasband, M. N. Axon initial segments: Diverse and dynamic neuronal compartments. *Current Opinion in Neurobiology* **27**, 96-102 (2014). https://doi.org:10.1016/j.conb.2014.03.004

64 Rasband, M. N. in *Nature reviews. Neuroscience* Vol. 11 552-562 (2010).

65 Sobotzik, J. M. *et al.* AnkyrinG is required to maintain axo-dendritic polarity in vivo. *Proceedings of the National Academy of Sciences of the United States of America* **106**, 17564-17569 (2009). https://doi.org:10.1073/pnas.0909267106

66 Hedstrom, K. L., Ogawa, Y. & Rasband, M. N. AnkyrinG is required for maintenance of the axon initial segment and neuronal polarity. *The Journal of Cell Biology* **183**, 635-640 (2008). https://doi.org:10.1083/jcb.200806112

67 Gasser, A. *et al.* An AnkyrinG-Binding Motif Is Necessary and Sufficient for Targeting Na v 1 . 6 Sodium Channels to Axon Initial Segments and Nodes of Ranvier. **32**, 7232-7243 (2012). https://doi.org:10.1523/JNEUROSCI.5434-11.2012

68 Hedstrom, K. L. *et al.* Neurofascin assembles a specialized extracellular matrix at the axon initial segment. *Journal of Cell Biology* **178**, 875-886 (2007). https://doi.org:10.1083/jcb.200705119

69 Rasband, M. N. The axon initial segment and the maintenance of neuronal polarity. *Nature Reviews Neuroscience* **11**, 552-562 (2010). https://doi.org:10.1038/nrn2852

70 Hinman, J. D., Rasband, M. N. & Carmichael, S. T. Remodeling of the axon initial segment after focal cortical and white matter stroke. *Stroke* **44**, 182-189 (2013). https://doi.org:10.1161/strokeaha.112.668749

71 Schafer, D. P. *et al.* in *Journal of Neuroscience* Vol. 29 13242-13254 (2009).

72 Dotti, C. G. & Simons, K. Polarized sorting of viral glycoproteins to the axon and dendrites of hippocampal neurons in culture. *Cell* **62**, 63-72 (1990). https://doi.org:10.1016/0092-8674(90)90240-f

73 Dotti, C. G., Parton, R. G. & Simons, K. Polarized sorting of glypiated proteins in hippocampal neurons. *Nature* **349**, 158-161 (1991). https://doi.org:10.1038/349158a0

74 Kobayashi, T., Storrie, B., Simons, K. & Dotti, C. G. A functional barrier to movement of lipids in polarized neurons. *Nature* **359**, 647-650 (1992). https://doi.org:10.1038/359647a0

75 Bettina Winckler, P. F., Ira Mellman. A diffusion barrier maintains distribution of membrane proteins in polarized neurons. *Nature* **397**, 698-701 (1999).

76 Nakada, C. *et al.* Accumulation of anchored proteins forms membrane diffusion barriers during neuronal polarization. *Nature Cell Biology* **5**, 626-632 (2003). https://doi.org:10.1038/ncb1009

77 Rust, M. J., Bates, M. & Zhuang, X. W. Sub-diffraction-limit imaging by stochastic optical reconstruction microscopy (STORM). *Nat Methods* **3**, 793-795 (2006). https://doi.org:Doi 10.1038/Nmeth929

78 Luby-Phelps, K. The physical chemistry of cytoplasm and its influence on cell function: an update. *Mol Biol Cell* **24**, 2593-2596 (2013). https://doi.org:10.1091/mbc.E12-08-0617

79 Wilson, E. B. The structure of protoplasm. *Science*, 33-45 (1899). https://doi.org:10.1126/science.10.237.33

80 Runnström, J. Sperm-induced protrusions in sea urchin oocytes: A study of phase separation and mixing in living cytoplasm. *Developmental Biology* **7**, 38-50 (1963). https://doi.org:https://doi.org/10.1016/0012-1606(63)90105-2

81 Walter, H. & Brooks, D. E. Phase separation in cytoplasm, due to macromolecular crowding, is the basis for microcompartmentation. *FEBS Letters* **361**, 135-139 (1995). https://doi.org:https://doi.org/10.1016/0014-5793(95)00159-7

82 Brangwynne, C. P. *et al.* Germline P Granules Are Liquid Droplets That Localize by Controlled Dissolution/Condensation. *Science* **324**, 1729-1732 (2009). https://doi.org:10.1126/science.1172046

83 Schwarz-Romond, T., Merrifield, C., Nichols, B. J. & Bienz, M. The Wnt signalling effector Dishevelled forms dynamic protein assemblies rather than stable associations with cytoplasmic vesicles. *J Cell Sci* **118**, 5269-5277 (2005). https://doi.org:10.1242/jcs.02646

84 Grakoui, A. *et al.* The Immunological Synapse: A Molecular Machine Controlling T Cell Activation. *Science* **285**, 221-227 (1999). https://doi.org:10.1126/science.285.5425.221

85 Kedersha, N. *et al.* Dynamic Shuttling of Tia-1 Accompanies the Recruitment of mRNA to Mammalian Stress Granules. *Journal of Cell Biology* **151**, 1257-1268 (2000). https://doi.org:10.1083/jcb.151.6.1257

86 Patel, A. *et al.* A Liquid-to-Solid Phase Transition of the ALS Protein FUS Accelerated by Disease Mutation. *Cell* **162**, 1066-1077 (2015). https://doi.org:https://doi.org/10.1016/j.cell.2015.07.047

87 Molliex, A. *et al.* Phase Separation by Low Complexity Domains Promotes Stress Granule Assembly and Drives Pathological Fibrillization. *Cell* **163**, 123-133 (2015). https://doi.org:https://doi.org/10.1016/j.cell.2015.09.015

88 Brangwynne, Clifford P., Tompa, P. & Pappu, Rohit V. Polymer physics of intracellular phase transitions. *Nature Physics* **11**, 899-904 (2015). https://doi.org:10.1038/nphys3532

89 Hyman, A. A., Weber, C. A. & Julicher, F. Liquid-liquid phase separation in biology. *Annu Rev Cell Dev Biol* **30**, 39-58 (2014). https://doi.org:10.1146/annurev-cellbio-100913-013325

90 Kajetan, K., Laurie, D., Olaf, M. & Pietro De, C. Mobility of Synaptic Vesicles in Nerve Endings Monitored by Recovery from Photobleaching of Synaptic Vesicle-Associated Fluorescence. *The Journal of Neuroscience* **16**, 5905 (1996). https://doi.org:10.1523/JNEUROSCI.16-19-05905.1996

91 Hoffmann, C. *et al.* Synapsin Condensates Recruit alpha-Synuclein. *J Mol Biol* **433**, 166961 (2021). https://doi.org:10.1016/j.jmb.2021.166961

92 Brangwynne, C. P., Mitchison, T. J. & Hyman, A. A. Active liquid-like behavior of nucleoli determines their size and shape in Xenopus laevis oocytes. *Proc Natl Acad Sci U S A* **108**, 4334-4339 (2011). https://doi.org:10.1073/pnas.1017150108

93 Anderson, P. & Kedersha, N. RNA granules: post-transcriptional and epigenetic modulators of gene expression. *Nat Rev Mol Cell Biol* **10**, 430-436 (2009). https://doi.org:10.1038/nrm2694

94 Pawson, T. & Nash, P. Assembly of Cell Regulatory Systems Through Protein Interaction Domains. *Science* **300**, 445-452 (2003). https://doi.org:10.1126/science.1083653

95 Li, P. *et al.* Phase transitions in the assembly of multivalent signalling proteins. *Nature* **483**, 336-340 (2012). https://doi.org:10.1038/nature10879

96 Holehouse, A. S. & Pappu, R. V. Protein polymers: Encoding phase transitions. *Nat Mater* **14**, 1083-1084 (2015). https://doi.org:10.1038/nmat4459

97 Romero, P. *et al.* Sequence complexity of disordered protein. *Proteins* **42**, 38-48 (2001). https://doi.org:10.1002/1097-0134(20010101)42:1<38::aid-prot50>3.0.co;2-3

98 Aumiller, W. M., Jr. & Keating, C. D. Phosphorylation-mediated RNA/peptide complex coacervation as a model for intracellular liquid organelles. *Nat Chem* **8**, 129-137 (2016). https://doi.org:10.1038/nchem.2414

99 Misteli, T. *et al.* Serine Phosphorylation of SR Proteins Is Required for Their Recruitment to Sites of Transcription In Vivo. *Journal of Cell Biology* **143**, 297-307 (1998). https://doi.org:10.1083/jcb.143.2.297

100 Wang, J. T. *et al.* Regulation of RNA granule dynamics by phosphorylation of serine-rich, intrinsically disordered proteins in C. elegans. *Elife* **3**, e04591 (2014). https://doi.org:10.7554/eLife.04591

101 Nott, Timothy J. *et al.* Phase Transition of a Disordered Nuage Protein Generates Environmentally Responsive Membraneless Organelles. *Molecular Cell* **57**, 936-947 (2015). https://doi.org:10.1016/j.molcel.2015.01.013

102 Altmeyer, M. *et al.* Liquid demixing of intrinsically disordered proteins is seeded by poly(ADP-ribose). *Nat Commun* **6**, 8088 (2015). https://doi.org:10.1038/ncomms9088

103 Rizzoli, S. O. Synaptic vesicle recycling: steps and principles. *The EMBO Journal* **33**, 788-822 (2014). https://doi.org:https://doi.org/10.1002/embj.201386357

104 Heuser, J. E. & Reese, T. S. Evidence for recycling of synaptic vesicle membrane during transmitter release at the frog neuromuscular junction. *Journal of Cell Biology* **57**, 315-344 (1973). https://doi.org:10.1083/jcb.57.2.315

105 Betz, W. J., Bewick, G. S. & Ridge, R. M. A. P. Intracellular movements of fluorescently labeled synaptic vesicles in frog motor nerve terminals during nerve stimulation. *Neuron* **9**, 805-813 (1992). https://doi.org:https://doi.org/10.1016/0896-6273(92)90235-6

106 Denker, A. *et al.* A small pool of vesicles maintains synaptic activity in vivo. *Proceedings of the National Academy of Sciences* **108**, 17177-17182 (2011). https://doi.org:10.1073/pnas.1112688108

107 Denker, A., Kröhnert, K., Bückers, J., Neher, E. & Rizzoli, S. O. The reserve pool of synaptic vesicles acts as a buffer for proteins involved in synaptic vesicle recycling. *Proceedings of the National Academy of Sciences* **108**, 17183-17188 (2011). https://doi.org:doi:10.1073/pnas.1112690108

108 Rey, S., Marra, V., Smith, C. & Staras, K. Nanoscale Remodeling of Functional Synaptic Vesicle Pools in Hebbian Plasticity. *Cell Reports* **30**, 2006-2017.e2003 (2020). https://doi.org:https://doi.org/10.1016/j.celrep.2020.01.051

109 Reshetniak, S. *et al.* A comparative analysis of the mobility of 45 proteins in the synaptic bouton. *EMBO J* **39**, e104596 (2020). https://doi.org:10.15252/embj.2020104596

110 Sankaranarayanan, S., Atluri, P. P. & Ryan, T. A. Actin has a molecular scaffolding, not propulsive, role in presynaptic function. *Nat Neurosci* **6**, 127-135 (2003). https://doi.org:10.1038/nn1002

111 Hirokawa, N., Sobue, K., Kanda, K., Harada, A. & Yorifuji, H. The cytoskeletal architecture of the presynaptic terminal and molecular structure of synapsin 1. *Journal of Cell Biology* **108**, 111-126 (1989). https://doi.org:10.1083/jcb.108.1.111

112 Chieregatt, E., Ceccaldi, P. E., Benfenati, F. & Valtorta, F. Effects of synaptic vesicles on actin polymerization. *FEBS Letters* **398**, 211-216 (1996). https://doi.org:https://doi.org/10.1016/S0014-5793(96)01240-9

113 Bingham, D. *et al.* Presynapses contain distinct actin nanostructures. *Journal of Cell Biology* **222** (2023). https://doi.org:10.1083/jcb.202208110

114 Ogunmowo, T. H. *et al.* Membrane compression by synaptic vesicle exocytosis triggers ultrafast endocytosis. *Nat Commun* **14**, 2888 (2023). https://doi.org:10.1038/s41467-023-38595-2

115 Südhof, T. C. *et al.* Synapsins: Mosaics of Shared and Individual Domains in a Family of Synaptic Vesicle Phosphoproteins. *Science* **245**, 1474-1480 (1989). https://doi.org:10.1126/science.2506642

116 Clayton, D. F. & George, J. M. The synucleins: a family of proteins involved in synaptic function, plasticity, neurodegeneration and disease. *Trends in Neurosciences* **21**, 249-254 (1998). https://doi.org:https://doi.org/10.1016/S0166-2236(97)01213-7

117 Chandra, S., Chen, X., Rizo, J., Jahn, R. & Südhof, T. C. A broken alpha -helix in folded alpha -Synuclein. *J Biol Chem* **278**, 15313-15318 (2003). https://doi.org:10.1074/jbc.m213128200

118 Vargas, K. J. *et al.* Synucleins Have Multiple Effects on Presynaptic Architecture. *Cell Reports* **18**, 161-173 (2017). https://doi.org:https://doi.org/10.1016/j.celrep.2016.12.023

119 Fouke, K. E. *et al.* Synuclein Regulates Synaptic Vesicle Clustering and Docking at a Vertebrate Synapse. *Front Cell Dev Biol* **9**, 774650 (2021). https://doi.org:10.3389/fcell.2021.774650

120 Burré, J., Sharma, M. & Südhof, T. C. α-Synuclein assembles into higher-order multimers upon membrane binding to promote SNARE complex formation. *Proc Natl Acad Sci U S A* **111**, E4274-4283 (2014). https://doi.org:10.1073/pnas.1416598111

121 Fernández-Busnadiego, R. *et al.* Quantitative analysis of the native presynaptic cytomatrix by cryoelectron tomography. *Journal of Cell Biology* **188**, 145-156 (2010). https://doi.org:10.1083/jcb.200908082

122 Diao, J. *et al.* Native α-synuclein induces clustering of synaptic-vesicle mimics via binding to phospholipids and synaptobrevin-2/VAMP2. *eLife* **2**, e00592 (2013). https://doi.org:10.7554/eLife.00592

123 Siksou, L. *et al.* A role for vesicular glutamate transporter 1 in synaptic vesicle clustering and mobility. *Eur J Neurosci* **37**, 1631-1642 (2013). https://doi.org:10.1111/ejn.12199

124 Takamori, S. *et al.* Molecular Anatomy of a Trafficking Organelle. *Cell* **127**, 831-846 (2006). https://doi.org:10.1016/j.cell.2006.10.030

125 Raja, M. K. *et al.* Elevated synaptic vesicle release probability in synaptophysin/gyrin family quadruple knockouts. *eLife* **8**, e40744 (2019). https://doi.org:10.7554/eLife.40744

126 Wilhelm, B. G. *et al.* Composition of isolated synaptic boutons reveals the amounts of vesicle trafficking proteins. *Science* **344**, 1023-1028 (2014). https://doi.org:10.1126/science.1252884

127 Hilfiker, S. *et al.* Two sites of action for synapsin domain E in regulating neurotransmitter release. *Nature Neuroscience* **1**, 29-35 (1998). https://doi.org:10.1038/229

128 Cavalleri, G. L. *et al.* Multicentre search for genetic susceptibility loci in sporadic epilepsy syndrome and seizure types: a case-control study. *The Lancet Neurology* **6**, 970-980 (2007). https://doi.org:https://doi.org/10.1016/S1474-4422(07)70247-8

129 Mirnics, K., Middleton, F. A., Lewis, D. A. & Levitt, P. Analysis of complex brain disorders with gene expression microarrays: schizophrenia as a disease of the

synapse. *Trends Neurosci* **24**, 479-486 (2001). https://doi.org:10.1016/s0166-2236(00)01862-2

130 Kao, H.-T. *et al.* Molecular evolution of the synapsin gene family. *The Journal of Experimental Zoology* **285**, 360-377 (1999). https://doi.org:10.1002/(sici)1097-010x(19991215)285:4<360::Aid-jez4>3.0.Co;2-3

131 Südhof, T. C. The structure of the human synapsin I gene and protein. *Journal of Biological Chemistry* **265**, 7849-7852 (1990). https://doi.org:https://doi.org/10.1016/S0021-9258(19)39008-8

132 Song, S.-H. & Augustine, G. Synapsin Isoforms and Synaptic Vesicle Trafficking. *Molecules and cells* **38**, 936-940 (2015). https://doi.org:10.14348/molcells.2015.0233

133 Hosaka, M., Hammer, R. E. & Südhof, T. C. A Phospho-Switch Controls the Dynamic Association of Synapsins with Synaptic Vesicles. *Neuron* **24**, 377-387 (1999). https://doi.org:https://doi.org/10.1016/S0896-6273(00)80851-X

134 Jovanovic, J. N. *et al.* Neurotrophins stimulate phosphorylation of synapsin I by MAP kinase and regulate synapsin I-actin interactions. *Proc Natl Acad Sci U S A* **93**, 3679-3683 (1996). https://doi.org:10.1073/pnas.93.8.3679

135 Hosaka, M. & Südhof, T. C. Synapsins I and II Are ATP-binding Proteins with Differential Ca2+ Regulation*. *Journal of Biological Chemistry* **273**, 1425-1429 (1998). https://doi.org:https://doi.org/10.1074/jbc.273.3.1425

136 Monaldi, I. *et al.* The highly conserved synapsin domain E mediates synapsin dimerization and phospholipid vesicle clustering. *The Biochemical journal* **426 1**, 55-64 (2010).

137 Hosaka, M. & Südhof, T. C. Synapsin III, a Novel Synapsin with an Unusual Regulation by Ca2+*. *Journal of Biological Chemistry* **273**, 13371-13374 (1998). https://doi.org:https://doi.org/10.1074/jbc.273.22.13371

138 Kao, H.-T. *et al.* A third member of the synapsin gene family. *Proceedings of the National Academy of Sciences* **95**, 4667-4672 (1998). https://doi.org:doi:10.1073/pnas.95.8.4667

139 Czernik, A. J., Pang, D. T. & Greengard, P. Amino acid sequences surrounding the cAMP-dependent and calcium/calmodulin-dependent phosphorylation sites in rat and bovine synapsin I. *Proceedings of the National Academy of Sciences* **84**, 7518-7522 (1987). https://doi.org:10.1073/pnas.84.21.7518

140 Jovanovic, J. N., Czernik, A. J., Fienberg, A. A., Greengard, P. & Sihra, T. S. Synapsins as mediators of BDNF-enhanced neurotransmitter release. *Nature Neuroscience* **3**, 323-329 (2000). https://doi.org:10.1038/73888

141 Matsubara, M. *et al.* Site-specific Phosphorylation of Synapsin I by Mitogen-activated Protein Kinase and Cdk5 and Its Effects on Physiological Functions *. *Journal of Biological Chemistry* **271**, 21108-21113 (1996). https://doi.org:10.1074/jbc.271.35.21108

142 Jasmina, N. J. *et al.* Opposing Changes in Phosphorylation of Specific Sites in Synapsin I During Ca²⁺-Dependent Glutamate Release in Isolated Nerve Terminals. *The Journal of Neuroscience* **21**, 7944 (2001). https://doi.org:10.1523/JNEUROSCI.21-20-07944.2001

143 Llinás, R., Gruner, J. A., Sugimori, M., McGuinness, T. L. & Greengard, P. Regulation by synapsin I and Ca(2+)-calmodulin-dependent protein kinase II of the transmitter release in squid giant synapse. *J Physiol* **436**, 257-282 (1991). https://doi.org:10.1113/jphysiol.1991.sp018549

144 Gitler, D. *et al.* Different Presynaptic Roles of Synapsins at Excitatory and Inhibitory Synapses. *The Journal of Neuroscience* **24**, 11368-11380 (2004). https://doi.org:10.1523/jneurosci.3795-04.2004

145 Pieribone, V. A. *et al.* Distinct pools of synaptic vesicles in neurotransmitter release. *Nature* **375**, 493-497 (1995). https://doi.org:10.1038/375493a0

146 Pechstein, A. *et al.* Vesicle Clustering in a Living Synapse Depends on a Synapsin Region that Mediates Phase Separation. *Cell Reports* **30**, 2594-2602.e2593 (2020). https://doi.org:10.1016/j.celrep.2020.01.092

147 Milovanovic, D. & De Camilli, P. Synaptic Vesicle Clusters at Synapses: A Distinct Liquid Phase? *Neuron* **93**, 995-1002 (2017). https://doi.org:10.1016/j.neuron.2017.02.013

148 Rizzoli, S. O. & Betz, W. J. The Structural Organization of the Readily Releasable Pool of Synaptic Vesicles. *Science* **303**, 2037-2039 (2004). https://doi.org:10.1126/science.1094682

149 Darcy, K. J., Staras, K., Collinson, L. M. & Goda, Y. Constitutive sharing of recycling synaptic vesicles between presynaptic boutons. *Nat Neurosci* **9**, 315-321 (2006). https://doi.org:10.1038/nn1640

150 Hosaka, M. & Südhof, T. C. Homo- and Heterodimerization of Synapsins*. *Journal of Biological Chemistry* **274**, 16747-16753 (1999). https://doi.org:https://doi.org/10.1074/jbc.274.24.16747

151 Yang, P. *et al.* G3BP1 Is a Tunable Switch that Triggers Phase Separation to Assemble Stress Granules. *Cell* **181**, 325-345.e328 (2020). https://doi.org:10.1016/j.cell.2020.03.046

152 Gerth, F. *et al.* Intersectin associates with synapsin and regulates its nanoscale localization and function. *Proc Natl Acad Sci U S A* **114**, 12057-12062 (2017). https://doi.org:10.1073/pnas.1715341114

153 Ogunmowo, T. *et al.* Intersectin and Endophilin condensates prime synaptic vesicles for release site replenishment. *bioRxiv* (2023). https://doi.org:10.1101/2023.08.22.554276

154 Benfenati, F., Bähler, M., Jahn, R. & Greengard, P. Interactions of synapsin I with small synaptic vesicles: distinct sites in synapsin I bind to vesicle phospholipids and vesicle proteins. *Journal of Cell Biology* **108**, 1863-1872 (1989). https://doi.org:10.1083/jcb.108.5.1863

155 Ohsawa, K., Oshima, H. & Ohki, S. Surface potential and surface charge density of the cerebral-cortex synaptic vesicle and stability of vesicle suspension. *Biochimica et Biophysica Acta (BBA) - Biomembranes* **648**, 206-214 (1981). https://doi.org:https://doi.org/10.1016/0005-2736(81)90036-5

156 Kim, G. *et al.* Multivalent electrostatic pi–cation interaction between synaptophysin and synapsin is responsible for the coacervation. *Molecular Brain* **14**, 137 (2021). https://doi.org:10.1186/s13041-021-00846-y

157 Park, D. *et al.* Cooperative function of synaptophysin and synapsin in the generation of synaptic vesicle-like clusters in non-neuronal cells. *Nature Communications* **12**, 263 (2021). https://doi.org:10.1038/s41467-020-20462-z

158 Ludwig, K. *et al.* Synapsin I Senses Membrane Curvature by an Amphipathic Lipid Packing Sensor Motif. *The Journal of Neuroscience* **31**, 18149 (2011). https://doi.org:10.1523/JNEUROSCI.4345-11.2011

159 Abbe, E. Beiträge zur Theorie des Mikroskops und der mikroskopischen Wahrnehmung. *Archiv für Mikroskopische Anatomie* **9**, 413-468 (1873). https://doi.org:10.1007/BF02956173

160 Hink, M. A. *et al.* Structural Dynamics of Green Fluorescent Protein Alone and Fused with a Single Chain Fv Protein*. *Journal of Biological Chemistry* **275**, 17556-17560 (2000). https://doi.org:https://doi.org/10.1074/jbc.M001348200

161 Vangindertael, J. *et al.* An introduction to optical super-resolution microscopy for the adventurous biologist. *Methods and Applications in Fluorescence* **6** (2018). https://doi.org:10.1088/2050-6120/aaae0c

162 Gustafsson, M. G. L. Surpassing the lateral resolution limit by a factor of two using structured illumination microscopy. *Journal of Microscopy* **198**, 82-87 (2000). https://doi.org:https://doi.org/10.1046/j.1365-2818.2000.00710.x

163 Hell, S. W. & Wichmann, J. Breaking the diffraction resolution limit by stimulated emission: stimulated-emission-depletion fluorescence microscopy. *Opt. Lett.* **19**, 780 (1994). https://doi.org:10.1364/ol.19.000780

164 Moerner, W. E. & Kador, L. Optical detection and spectroscopy of single molecules in a solid. *Physical Review Letters* **62**, 2535-2538 (1989). https://doi.org:10.1103/PhysRevLett.62.2535

165 Betzig, E. *et al.* Imaging Intracellular Fluorescent Proteins at Nanometer Resolution. *Science* **313**, 1642-1645 (2006). https://doi.org:10.1126/science.1127344

166 Jungmann, R. *et al.* Super-Resolution Microscopy by Fluorescence Imaging of Transient Binding on DNA Origami. *Nano Letters*, 4756-4761 (2010). https://doi.org:10.1021/nl103427w

167 Heilemann, M. *et al.* Subdiffraction-resolution fluorescence imaging with conventional fluorescent probes. *Angewandte Chemie - International Edition* **47**, 6172-6176 (2008). https://doi.org:10.1002/anie.200802376

168 Balzarotti, F. *et al.* Nanometer resolution imaging and tracking of fluorescent molecules with minimal photon fluxes. *Science* **355**, 606-612 (2017). https://doi.org:10.1126/science.aak9913

169 Geerts, H. *et al.* Nanovid tracking: a new automatic method for the study of mobility in living cells based on colloidal gold and video microscopy. *Biophysical Journal* **52**, 775-782 (1987). https://doi.org:10.1016/S0006-3495(87)83271-X

170 Shen, H. *et al.* Single Particle Tracking: From Theory to Biophysical Applications. *Chemical Reviews* **117**, 7331-7376 (2017). https://doi.org:10.1021/acs.chemrev.6b00815

171 Tsunoyama, T. A. *et al.* Super-long single-molecule tracking reveals dynamic-anchorage-induced integrin function. *Nature Chemical Biology* **14**, 497-506 (2018). https://doi.org:10.1038/s41589-018-0032-5

172 Wolff, J. O. *et al.* MINFLUX dissects the unimpeded walking of kinesin-1. *Science* **379**, 1004-1010 (2023). https://doi.org:10.1126/science.ade2650

173 Betzig, E. Proposed method for molecular optical imaging. *Opt. Lett.* **20**, 237-239 (1995). https://doi.org:10.1364/OL.20.000237

174 Wiedenmann, J. *et al.* EosFP, a fluorescent marker protein with UV-inducible green-to-red fluorescence conversion. *Proc Natl Acad Sci U S A* **101**, 15905-15910 (2004). https://doi.org:10.1073/pnas.0403668101

175 Nienhaus, K., Nienhaus, G. U., Wiedenmann, J. & Nar, H. Structural basis for photo-induced protein cleavage and green-to-red conversion of fluorescent protein EosFP. *Proceedings of the National Academy of Sciences* **102**, 9156-9159 (2005). https://doi.org:doi:10.1073/pnas.0501874102

176 van de Linde, S. *et al.* Direct stochastic optical reconstruction microscopy with standard fluorescent probes. *Nature Protocols* **6**, 991-1009 (2011). https://doi.org:10.1038/nprot.2011.336

177 Einstein, A. Strahlungs-Emission und -Absorption nach der Quantentheorie. *Deutsche Physikalische Gesellschaft* **18**, 318-323 (1916).

178 Klar, T. A., Jakobs, S., Dyba, M., Egner, A. & Hell, S. W. Fluorescence microscopy with diffraction resolution barrier broken by stimulated emission. *Proceedings of the National Academy of Sciences* **97**, 8206-8210 (2000). https://doi.org:doi:10.1073/pnas.97.15.8206

179 Reuss, M., Engelhardt, J. & Hell, S. W. Birefringent device converts a standard scanning microscope into a STED microscope that also maps molecular orientation. *Opt. Express* **18**, 1049-1058 (2010). https://doi.org:10.1364/OE.18.001049

180 Klar, T. A., Engel, E. & Hell, S. W. Breaking Abbe's diffraction resolution limit in fluorescence microscopy with stimulated emission depletion beams of various shapes. *Physical Review E* **64**, 066613 (2001). https://doi.org:10.1103/PhysRevE.64.066613

181 Göttfert, F. *et al.* Strong signal increase in STED fluorescence microscopy by imaging regions of subdiffraction extent. *Proceedings of the National Academy of Sciences* **114**, 2125-2130 (2017). https://doi.org:doi:10.1073/pnas.1621495114

182 Dyba, M. & Hell, S. W. Photostability of a fluorescent marker under pulsed excited-state depletion through stimulated emission. *Appl. Opt.* **42**, 5123-5129 (2003). https://doi.org:10.1364/AO.42.005123

183 Bottanelli, F. *et al.* Two-colour live-cell nanoscale imaging of intracellular targets. *Nature Communications* **7**, 1-5 (2016). https://doi.org:10.1038/ncomms10778

184 Wegner, W. *et al.* In vivo mouse and live cell STED microscopy of neuronal actin plasticity using far-red emitting fluorescent proteins. *Scientific Reports* **7**, 11781 (2017). https://doi.org:10.1038/s41598-017-11827-4

185 Wegner, W., Mott, A. C., Grant, S. G. N., Steffens, H. & Willig, K. I. In vivo STED microscopy visualizes PSD95 sub-structures and morphological changes over several hours in the mouse visual cortex. *Sci Rep* **8**, 219 (2018). https://doi.org:10.1038/s41598-017-18640-z

186 Sheetz, M. P., Turney, S., Qian, H. & Elson, E. L. Nanometre-level analysis demonstrates that lipid flow does not drive membrane glycoprotein movements. *Nature* **340**, 284-288 (1989). https://doi.org:10.1038/340284a0

187 Grimm, J. B. *et al.* A general method to improve fluorophores for live-cell and single-molecule microscopy. *Nature Methods* **12**, 244-250 (2015). https://doi.org:10.1038/nmeth.3256

188 Grimm, J. B. *et al.* Bright photoactivatable fluorophores for single-molecule imaging. *Nature Methods* (2016). https://doi.org:10.1038/nmeth.4034

189 Wöll, D., Kölbl, C., Stempfle, B. & Karrenbauer, A. A novel method for automatic single molecule tracking of blinking molecules at low intensities. *Physical Chemistry Chemical Physics* **15**, 6196-6205 (2013). https://doi.org:10.1039/C3CP44693J

190 Hughes, L. D., Rawle, R. J. & Boxer, S. G. Choose your label wisely: Water-soluble fluorophores often interact with lipid bilayers. *PLoS ONE* **9** (2014). https://doi.org:10.1371/journal.pone.0087649

191 Ries, J., Kaplan, C., Platonova, E., Eghlidi, H. & Ewers, H. A simple, versatile method for GFP-based super-resolution microscopy via nanobodies. *Nature Methods* **9**, 582-584 (2012). https://doi.org:10.1038/nmeth.1991

192 Albrecht, D., Winterflood, C. M. & Ewers, H. Dual color single particle tracking via nanobodies. *Methods and Applications in Fluorescence* **3** (2015). https://doi.org:10.1088/2050-6120/3/2/024001

193 Chen, Z. *et al.* Nanopore-mediated protein delivery enabling three-color single-molecule tracking in living cells. *Proc Natl Acad Sci U S A* **118** (2021). https://doi.org:10.1073/pnas.2012229118

194 Los, G. V. *et al.* HaloTag: A Novel Protein Labeling Technology for Cell Imaging and Protein Analysis. *ACS Chemical Biology* **3**, 373-382 (2008). https://doi.org:10.1021/cb800025k

195 Manley, S. *et al.* High-density mapping of single-molecule trajectories with photoactivated localization microscopy. *Nature Methods* **5**, 155-157 (2008). https://doi.org:10.1038/nmeth.1176

196 Zhang, M. *et al.* Rational design of true monomeric and bright photoactivatable fluorescent proteins. *Nature Methods* **9**, 727-729 (2012). https://doi.org:10.1038/nmeth.2021

197 Zorman, B., Ramakrishna, M. V. & Friesner, R. A. Quantum Confinement Effects in CdSe Quantum Dots. *The Journal of Physical Chemistry* **99**, 7649-7653 (1995). https://doi.org:10.1021/j100019a052

198 Bajorowicz, B. *et al.* Quantum dot-decorated semiconductor micro- and nanoparticles: A review of their synthesis, characterization and application in photocatalysis. (2018). https://doi.org:10.1016/j.cis.2018.02.003

199 Efros, A. L. & Brus, L. E. Nanocrystal Quantum Dots: From Discovery to Modern Development. *ACS Nano* **15**, 6192-6210 (2021). https://doi.org:10.1021/acsnano.1c01399

200 Ghasemi, Y., Peymani, P. & Afifi, S. Quantum dot: Magic nanoparticle for imaging, detection and targeting. *Acta Biomedica de l'Ateneo Parmense* **80**, 156-165 (2009). https://doi.org:19848055

201 Chan, W. C. W. *et al.* Luminescent quantum dots for multiplexed biological detection and imaging. *Current Opinion in Biotechnology* **13**, 40-46 (2002). https://doi.org:10.1016/S0958-1669(02)00282-3

202 Clausen, M. P. & Lagerholm, B. C. The probe rules in single particle tracking. *Current protein & peptide science* **12**, 699-713 (2011). https://doi.org:10.2174/138920311798841672

203 Chen, F. & Gerion, D. Fluorescent CdSe/ZnS nanocrystal-peptide conjugates for long-term, nontoxic imaging and nuclear targeting in living cells. *Nano Letters* **4**, 1827-1832 (2004). https://doi.org:10.1021/nl049170q

204 Delehanty, J. B., Mattoussi, H. & Medintz, I. L. Delivering quantum dots into cells: Strategies, progress and remaining issues. *Analytical and Bioanalytical Chemistry* **393**, 1091-1105 (2009). https://doi.org:10.1007/s00216-008-2410-4

205 Derfus, A. M., Chan, W. C. W. W. & Bhatia, S. N. Intracellular delivery of quantum dots for live cell labeling and organelle tracking. *Advanced Materials* **16**, 961-966 (2004). https://doi.org:10.1002/adma.200306111

206 Derivery, E., Bartolami, E., Matile, S., Gonzalez-Gaitan, M. & Id, P. D. B. Efficient Delivery of Quantum Dots into the Cytosol of Cells Using Cell-Penetrating Poly(disulfide)s. *Journal of the American Chemical Society* **139**, 10172-10175 (2017). https://doi.org:10.1021/jacs.7b02952

207 Katrukha, E. A. *et al.* Probing cytoskeletal modulation of passive and active intracellular dynamics using nanobody-functionalized quantum dots. *Nature Communications* **8**, 14772 (2017). https://doi.org:10.1038/ncomms14772

208 Li, H. *et al.* Mapping intracellular diffusion distribution using single quantum dot tracking: Compartmentalized diffusion defined by endoplasmic reticulum. *Journal of the American Chemical Society* **137**, 436-444 (2015). https://doi.org:10.1021/ja511273c

209 Medepalli, K., Alphenaar, B. W., Keynton, R. S. & Sethu, P. A new technique for reversible permeabilization of live cells for intracellular delivery of quantum dots. *Nanotechnology* **24** (2013). https://doi.org:10.1088/0957-4484/24/20/205101

210 Medintz, I. L. *et al.* Intracellular delivery of quantum dot-protein cargos mediated by cell penetrating peptides. *Bioconjugate Chemistry* (2008). https://doi.org:10.1021/bc800089r

211 Varela, J. A. *et al.* Targeting neurotransmitter receptors with nanoparticles in vivo allows single-molecule tracking in acute brain slices. *Nat Commun* **7**, 10947 (2016). https://doi.org:10.1038/ncomms10947

212 Echarte, M. M., Bruno, L., Arndt-Jovin, D. J., Jovin, T. M. & Pietrasanta, L. I. Quantitative single particle tracking of NGF–receptor complexes: Transport is bidirectional but biased by longer retrograde run lengths. *FEBS Letters* **581**, 2905-2913 (2007). https://doi.org:https://doi.org/10.1016/j.febslet.2007.05.041

213 Fichter, K. M., Flajolet, M., Greengard, P. & Vu, T. Q. Kinetics of G-protein–coupled receptor endosomal trafficking pathways revealed by single quantum dots. *Proceedings of the National Academy of Sciences* **107**, 18658-18663 (2010). https://doi.org:doi:10.1073/pnas.1013763107

214 Biju, V., Itoh, T. & Ishikawa, M. Delivering quantum dots to cells: bioconjugated quantum dots for targeted and nonspecific extracellular and intracellular imaging. *Chemical Society Reviews* **39**, 3031 (2010). https://doi.org:10.1039/b926512k

215 Einstein, A. Über die von der molekularkinetischen Theorie der Wärme geförderte Bewegung von in ruhenden Flüssigkeiten suspendierten Teilchen. *Ann. Phys. (Leipzig)* **17**, 549-560-560 (1905). https://doi.org:10.1002/andp.19053220806

216 Brown, R. XXVII. A brief account of microscopical observations made in the months of June, July and August 1827, on the particles contained in the pollen of plants; and on the general existence of active molecules in organic and inorganic bodies. *The Philosophical Magazine* **4**, 161-173 (1828). https://doi.org:10.1080/14786442808674769

217 Zhang, M. L., Ti, H. Y., Wang, P. Y. & Li, H. Intracellular transport dynamics revealed by single-particle tracking. *Biophys Rep* **7**, 413-427 (2021). https://doi.org:10.52601/bpr.2021.210035

218 Daumas, F. *et al.* Confined diffusion without fences of a G-protein-coupled receptor as revealed by single particle tracking. *Biophysical Journal* **84**, 356-366 (2003). https://doi.org:10.1016/S0006-3495(03)74856-5

219 Lagardere, M., Chamma, I., Bouilhol, E., Nikolski, M. & Thoumine, O. FluoSim: simulator of single molecule dynamics for fluorescence live-cell and super-resolution imaging of membrane proteins. *Sci Rep* **10**, 19954 (2020). https://doi.org:10.1038/s41598-020-75814-y

220 Peltier, J., Agrawal, S., Robertson, M. J. & Schaffer, D. V. In Vitro Culture and Analysis of Adult Hippocampal Neural Progenitors. 65-87 (2014). https://doi.org:10.1007/978-1-60761-063-2

221 Reshetniak, S. & Rizzoli, S. O. The vesicle cluster as a major organizer of synaptic composition in the short-term and long-term. *Curr Opin Cell Biol* **71**, 63-68 (2021). https://doi.org:10.1016/j.ceb.2021.02.007

222 Freeman, S. A. *et al.* Transmembrane Pickets Connect Cyto- and Pericellular Skeletons Forming Barriers to Receptor Engagement. *Cell* **172**, 305-317.e310 (2018). https://doi.org:10.1016/j.cell.2017.12.023

223 Roszkowska, M. *et al.* CD44: a novel synaptic cell adhesion molecule regulating structural and functional plasticity of dendritic spines. *Mol Biol Cell* **27**, 4055-4066 (2016). https://doi.org:10.1091/mbc.E16-06-0423

224 Naruse, M., Shibasaki, K., Yokoyama, S., Kurachi, M. & Ishizaki, Y. Dynamic changes of CD44 expression from progenitors to subpopulations of astrocytes and neurons in developing cerebellum. *PLoS One* **8**, e53109 (2013). https://doi.org:10.1371/journal.pone.0053109

225 D'Este, E., Kamin, D., Balzarotti, F. & Hell, S. W. Ultrastructural anatomy of nodes of Ranvier in the peripheral nervous system as revealed by STED microscopy. *Proceedings of the National Academy of Sciences* **114**, E191-E199 (2017). https://doi.org:doi:10.1073/pnas.1619553114

226 Duménieu, M., Oulé, M., Kreutz, M. R. & Lopez-Rojas, J. The Segregated Expression of Voltage-Gated Potassium and Sodium Channels in Neuronal Membranes: Functional Implications and Regulatory Mechanisms. *Front Cell Neurosci* **11**, 115 (2017). https://doi.org:10.3389/fncel.2017.00115

227 Gu, C. *et al.* The Microtubule Plus-End Tracking Protein EB1 Is Required for Kv1 Voltage-Gated K+ Channel Axonal Targeting. *Neuron* **52**, 803-816 (2006). https://doi.org:10.1016/j.neuron.2006.10.022

228 Seifert, G., Henneberger, C. & Steinhäuser, C. Diversity of astrocyte potassium channels: An update. *Brain Res Bull* **136**, 26-36 (2018). https://doi.org:10.1016/j.brainresbull.2016.12.002

229 Chow, L. W. C. & Leung, Y. M. The versatile Kv channels in the nervous system: actions beyond action potentials. *Cell Mol Life Sci* **77**, 2473-2482 (2020). https://doi.org:10.1007/s00018-019-03415-8

230 Maness, P. F. & Schachner, M. Neural recognition molecules of the immunoglobulin superfamily: signaling transducers of axon guidance and neuronal migration. *Nat Neurosci* **10**, 19-26 (2007). https://doi.org:10.1038/nn1827

231 Zhou, R. *et al.* Proteomic and functional analyses of the periodic membrane skeleton in neurons. *Nat Commun* **13**, 3196 (2022). https://doi.org:10.1038/s41467-022-30720-x

232 Davis, J. Q., Lambert, S. & Bennett, V. Molecular composition of the node of Ranvier: identification of ankyrin-binding cell adhesion molecules neurofascin (mucin+/third FNIII domain-) and NrCAM at nodal axon segments. *J Cell Biol* **135**, 1355-1367 (1996). https://doi.org:10.1083/jcb.135.5.1355

233 Tanaka-Takiguchi, Y., Kinoshita, M. & Takiguchi, K. Septin-Mediated Uniform Bracing of Phospholipid Membranes. *Current Biology* **19**, 140-145 (2009). https://doi.org:10.1016/j.cub.2008.12.030

234 Hagiwara, A. *et al.* Submembranous septins as relatively stable components of actin-based membrane skeleton. *Cytoskeleton (Hoboken)* **68**, 512-525 (2011). https://doi.org:10.1002/cm.20528

235 Kinoshita, M., Field, C. M., Coughlin, M. L., Straight, A. F. & Mitchison, T. J. Self- and actin-templated assembly of Mammalian septins. *Dev Cell* **3**, 791-802 (2002). https://doi.org:10.1016/s1534-5807(02)00366-0

236 Ewers, H. *et al.* A septin-dependent diffusion barrier at dendritic spine necks. *PLoS ONE* **9**, 1-19 (2014). https://doi.org:10.1371/journal.pone.0113916

237 Hamdan, H. *et al.* Mapping axon initial segment structure and function by multiplexed proximity biotinylation. *Nature Communications* **11**, 368 (2020). https://doi.org:10.1038/s41467-019-13658-5

238 Burbaum, L. *et al.* Molecular-scale visualization of sarcomere contraction within native cardiomyocytes. *Nat Commun* **12**, 4086 (2021). https://doi.org:10.1038/s41467-021-24049-0

239 Fujiwara, T. K. *et al.* Development of ultrafast camera-based single fluorescent-molecule imaging for cell biology. *J Cell Biol* **222** (2023). https://doi.org:10.1083/jcb.202110160

240 Gwosch, K. C. *et al.* MINFLUX nanoscopy delivers multicolor nanometer 3D-resolution in (living) cells. *bioRxiv*, 734251 (2019). https://doi.org:10.1101/734251

241 Meneses, D., Vega, A. V., Torres-Cruz, F. M. & Barral, J. KV1 and KV3 Potassium Channels Identified at Presynaptic Terminals of the Corticostriatal Synapses in Rat. *Neural Plast* **2016**, 8782518 (2016). https://doi.org:10.1155/2016/8782518

242 Capera, J. *et al.* Dynamics and spatial organization of Kv1.3 at the immunological synapse of human CD4+ T cells. *Biophysical Journal* (2023). https://doi.org:https://doi.org/10.1016/j.bpj.2023.08.011